Theoretical Aspects of Electrodeposition in Charged Porous Media

by

Edwin Sze Lun Khoo

B.S., Stanford University (2010)
S.M., Massachusetts Institute of Technology (2012)

Submitted to the Department of Chemical Engineering
in partial fulfillment of the requirements for the degree of

Doctor of Philosophy in Chemical Engineering

at the

MASSACHUSETTS INSTITUTE OF TECHNOLOGY

February 2019

Author .....
Department of Chemical Engineering
January 4, 2019

Certified by .....
Martin Z. Bazant
E. G. Roos (1944) Professor of Chemical Engineering
Executive Officer, Chemical Engineering
Professor of Mathematics
Thesis Supervisor

Accepted by .....
Patrick S. Doyle
Robert T. Haslam (1911) Professor of Chemical Engineering
Singapore Research Professor
Chairman, Committee for Graduate Students

Theoretical Aspects of Electrodeposition in Charged Porous Media

by

Edwin Sze Lun Khoo

Submitted to the Department of Chemical Engineering
on January 4, 2019, in partial fulfillment of the
requirements for the degree of
Doctor of Philosophy in Chemical Engineering

Abstract

Electrodeposition is a fascinating electrochemical phenomenon that contains deep physical insights and has broad practical applications. At the heart of the physics governing electrodeposition is a competition between a destabilizing force caused by surface crests growing more rapidly than surface troughs in a positive feedback loop and a stabilizing force arising from surface energy effects that prevent the surface from roughening excessively. The physical manifestation of this surface instability is the formation and propagation of dendrites. Some applications of electrodeposition include electroplating of metals such as copper and charging of next-generation high-energy-density metal batteries such as lithium metal batteries.

From both theoretical and practical standpoints, it is important to understand how to control and exploit electrodeposition. In this thesis, we explore electrodeposition in a homogenized charged porous medium that contains a fixed background charge density, which affords us a new knob for controlling electrodeposition. In practice, such a background charge density can either naturally arise from ionization of surface functional groups or be generated through experimental techniques such as layer-by-layer deposition of polyelectrolytes on the pore surfaces.

We investigate the theoretical aspects of electrodeposition in charged porous media in three different ways. First, we introduce a simple transport model that accounts for the background charge density and couple it with electrochemical reaction kinetics for electrodeposition. We then validate the coupled model by comparing predicted steady state current-voltage relations and linear sweep voltammetry with experimental data for copper electrodeposition in a variety of nanoporous media. Second, we perform linear stability analysis on the model to understand how key system parameters such as the background charge density affect the linear stability of the metal surface. We then show good agreement between theoretical predictions and experimental observations of the critical and instability wavelengths for copper electrodeposition in cellulose nitrate membranes. Third, we carry out impedance analysis on the model and explain some intriguing features in the experimental impedance spectra for copper electrodeposition in anodic aluminum oxide membranes. Through these

three different types of analysis, we demonstrate the predictive power and robustness of the theory despite its simplicity.

Thesis Supervisor: Martin Z. Bazant
Title: E. G. Roos (1944) Professor of Chemical Engineering
Executive Officer, Chemical Engineering
Professor of Mathematics

Acknowledgments

I would like to first thank my advisor Martin Bazant for being incredibly supportive and patient throughout my PhD journey. His infectious enthusiasm for rigorous research and deep physical and mathematical insights into open problems have been a major driving force behind the work done in this thesis. I also would like to thank my thesis committee members Fikile Brushett, Klavs Jensen and Qiqi Wang for their thought-provoking questions that have significantly improved this thesis.

I have been tremendously fortunate to have interacted with many friends and colleagues in the Bazant group professionally and socially through the years. Todd Ferguson and Sven Schlumpberger have been very helpful with easing my transition into graduate school. Raymond Smith has always been and still is a constant source of inspiration and clarity for research ideas and I owe to him a lot of what little I do know about research. He also introduced me to Linux and Git, which form the technological foundation of this thesis. Kameron Conforti, together with Raymond Smith, have been through the ups and downs of this journey with me and I thank them for their optimism. Hongbo Zhao has been a wonderful person to brainstorm and discuss research ideas with. I would like to thank Ji-Hyung Han and Peng Bai for being great experimentalists and collaborators who have provided most of the experimental data that this thesis looks at. I would also like to thank Juhyun Song for his collaboration and unique experiences that he has shared.

Outside of MIT, I am extremely grateful for the company of many friends. In particular, I would like to thank Danqing Wang, Kaicheng Liang, Ronald Chan and Hongwan Liu for their unwavering support, friendship and wisdom on all matters. In addition, I am been fortunate to be a part of several online communities and I appreciate Bryan Dunyak, Michael Susman, Elizabeth Crocker, Rachael Holloway and Zanna for sharing their knowledge and greatly broadening my perspectives.

Last but not least, I appreciate my family for being constantly supportive of all my choices, including doing this PhD, no matter how difficult the journey is and for tolerating my long absence from home.

Contents

List of Figures

List of Tables

Chapter 1

Introduction

Both the fundamental and practical aspects of electrodeposition have been extensively studied for a long time. The fundamental aspect concerns the inherent instability of the physics governing electrodeposition in which the main destabilizing effect originates from the amplification of surface protrusions by diffusive fluxes while the main stabilizing effect arises from the surface energy penalty incurred in the creation of additional surface area. The competition between these two effects sets a characteristic length scale for the surface instability, which manifests in the form of dendrites that have been greatly investigated theoretically and experimentally. One common theoretical tool to investigate the stability characteristics of electrodeposition, which is a highly nonlinear electrochemical system, is the linear stability analysis performed in the style of the classic Mullins-Sekerka analysis [168, 169]. Such a linear stability analysis linearizes the nonlinear system around a base state in order to derive a dispersion relation that relates the perturbation growth rate to the perturbation wavenumber or wavelength, providing physical insights into how to control the surface instability.

The practical aspect of electrodeposition concerns applications such as electroplating of metals [74, 58] and charging of batteries such as lithium metal batteries and lithium-ion batteries [137, 191, 190, 276, 116, 226, 216, 158, 18]. For these applications, it would be very beneficial to perform them at a large current or voltage without causing the formation and propagation of dendrites that may result in

internal short circuits. Hence, it behooves us to understand the possible mechanisms for an electrochemical system to sustain a large current or voltage and how they affect electrodeposition. In a classical neutral channel or porous medium, there exists a maximum current that the system can sustain under diffusion and electromigration that is called the limiting current [172, 24]. However, it has long been observed experimentally that it is possible to achieve an overlimiting current in ion-exchange membranes [207, 211, 126, 125, 203, 208, 72, 221, 176, 175, 235] and microchannels and nanochannels [123, 269, 271, 273, 272, 170, 218, 229]. While there are many possible physical and chemical mechanisms for overlimiting current, the mechanism that is expected to be dominant in nanoscale pores [77] is surface conduction [271, 273, 272, 155, 154, 76], which is the electromigration of counterions in the electric double layers next to the charged pore surfaces. One simple model for describing surface conduction is the leaky membrane model [77, 154, 76] in which the charges on the pore surfaces are homogenized and represented as a volume-averaged background charge density.

In this thesis, we couple the leaky membrane model for surface conduction [77, 154, 76] with Butler-Volmer kinetics [31, 84, 172, 24] for electrochemical reactions such as electrodeposition and analyze this coupled model in three different ways. First, in Chapter 2, we study the steady state current-voltage relations and linear sweep voltammetry predicted by the model and compare them with experimental data for copper electrodeposition in a variety of nanoporous media. This serves as a way to validate the model before we proceed with more sophisticated analysis and provides a foundation on which the results in the following chapters rest on. Second, in Chapter 3, we perform linear stability analysis on the model with respect to a time-dependent base state and investigate the dispersion relation via parameter sweeps over key system parameters of interest, in particular the volume-averaged background charge density. We also compare the critical and instability wavelengths predicted by the model with experimental data for copper electrodeposition in cellulose nitrate membranes to further validate the theory. Third, in Chapter 4, we carry out impedance analysis on the model and explain some intriguing features in

the experimental impedance spectra observed for copper electrodeposition in anodic aluminum oxide membranes. This also serves as yet another method for validating the model and demonstrates the robustness of the theory despite its simplicity.

Chapter 2

Theory of voltammetry in charged porous media

Except for some minor edits, the contents of this chapter have been published in [122].

2.1 Abstract

We couple the Leaky Membrane Model, which describes the diffusion and electromigration of ions in a homogenized porous medium of fixed background charge, with Butler-Volmer reaction kinetics for flat electrodes separated by such a medium in a simple mathematical theory of voltammetry. The model is illustrated for the prototypical case of copper electro-deposition/dissolution in aqueous charged porous media. We first consider the steady state with three different experimentally relevant boundary conditions and derive analytical or semi-analytical expressions for concentration profiles, electric potential profiles, current-voltage relations and overlimiting conductances. Next, we perform nonlinear least squares fitting on experimental data, consider the transient response for linear sweep voltammetry and demonstrate good agreement of the model predictions with experimental data. The experimental datasets are for copper electrodeposition from copper(II) sulfate solutions in a variety of nanoporous media, such as anodic aluminum oxide, cellulose nitrate and polyethylene battery separators, whose internal surfaces are functionalized with positively and

negatively charged polyelectrolyte polymers.

2.2 Introduction

In recent years, there is a growing need to extend electrochemical methods and devices to include charged porous media, which are macroscopically neutral, but contain charged internal surfaces or sites that provide a significant total charge per volume, comparable to the additional neutral salt concentration. Transport in a neutral confined channel or porous medium is described by the classical Nernst-Planck equations for diffusion and electromigration (also collectively known as electrodiffusion), which predict a diffusion-limited current that the current in the system cannot exceed [172, 24]. Under potentiostatic conditions, an infinite voltage is required for the current to reach its diffusion-limited value. Under galvanostatic conditions, applying a current that is larger than its diffusion-limited value results in negative concentrations and singularities at Sand's time [215]. However, experiments for electrodialysis in ion-exchange membranes [207, 211, 126, 125, 203, 208, 72, 221, 176, 175, 235] and for microchannels and nanochannels [123, 269, 271, 273, 272, 170, 218] have demonstrated that it is possible for an electrochemical system to exceed the diffusion-limited current and achieve overlimiting current (OLC) beyond bulk electrodiffusion.

In a confined channel or a porous medium, there are three physical mechanisms for OLC [77]: surface conduction (SC) [155, 271, 273, 272, 154, 76], electroosmotic flow (EOF) [268, 206] and electroosmotic instability (EOI) [205, 270]. These mechanisms are a strong function of the pore size and for pore sizes in the nanometer scale, surface conduction is expected to be the dominant OLC mechanism [77]. When surface charges are present on the pore walls in a charged nanoporous medium and a sufficiently large current or voltage is applied to deplete the coions at an ion-selective interface such as an electrode or ion-exchange membrane, a large electric field develops in the depletion region that drives electromigration of the counterions in the electric double layers, i.e., surface conduction. In the depletion region, because the concentration gradients of the coions and counterions are very small, surface conduction is respon-

sible for carrying most of the current. Surface conduction therefore sustains the OLC beyond bulk electrodiffusion and causes the formation and propagation of a deionization shock where ions are depleted behind the shock in porous media [154, 267, 76] and in microchannels and nanochannels [77, 155, 271, 273, 272, 173]. In addition, there are also chemical mechanisms for OLC such as water splitting [176, 175] and current-induced membrane discharge caused by membrane deprotonation and water self-ionization [6].

The key mathematical concept in the leaky membrane model for describing OLC due to surface conduction is the addition of a volume-averaged background charge density term to the macroscopic electroneutrality equation for an electrolyte containing two or more mobile charge carriers so that one of the charge carriers can be depleted. This concept also appears in closely related fields such as electrodialysis in ion-exchange membranes and semiconductor physics. For describing ion transport in ion-exchange membranes, a spatially averaged background charge density is commonly added to macroscopic electroneutrality in order to account for the fixed ions present in the membranes [109, 251, 250, 43]; this simplification, as opposed to using Poisson's equation for electrostatics to describe space charge, is also known as the Teorell-Meyer-Sievers (TMS) theory [257, 186]. In doped semiconductors, the dopant concentration is analogous to the volume-averaged background charge density while the electrons and holes are analogous to the anions and cations of a binary electrolyte respectively [187, 204, 194, 237].

We first derive the governing equations for describing transport and electrochemical reaction kinetics in a charged nanoporous medium. To predict OLC due to surface conduction, we use the leaky membrane model to describe transport [77, 154, 76]. For electrochemical reaction kinetics, we use Butler-Volmer reaction kinetics [31, 84, 172, 24] and focus on copper electrodeposition and electrodissolution as a classic example whose reaction mechanism and parameters are well studied [172, 157, 45, 54]. There are more sophisticated reaction models for copper electrodeposition and electrodissolution that, for example, take into account the adsorption of copper(I) ions on the electrode surface and do not assume any rate-determining step [113, 133, 114]. In the

interest of being able to derive analytical or semi-analytical expressions for quantities of interest, we do not account for these additional complications in the reaction model. We first study the model at steady state under three different experimentally relevant boundary conditions, including the Butler-Volmer boundary conditions. We then use the model to study copper electrodeposition and electrodissolution under linear sweep voltammetry (LSV) in charged nanoporous anodic aluminum oxide (AAO) membranes, which are ordered membranes, and cellulose nitrate (CN) and polyethylene (PE) membranes, which are random membranes, to demonstrate that the model can fit published experimental results [105, 106] for a variety of membranes with sufficient accuracy. In these porous membranes, the surface charge density on the pore walls is tuned by using the layer-by-layer technique of depositing multiple layers of negatively or positively charged polyelectrolytes [104].

Table 2.5 in Appendix 2.8.1 provides the symbols for variables, parameters and constants that are used throughout the paper. Superscripted "a" and "c" refer to quantities evaluated at the anode and cathode respectively, superscripted Θ denotes standard state, and superscripted "eq" denotes equilibrium.

2.3 Model

2.3.1 Transport in leaky membrane model

As illustrated in Figure 2-1, we consider a charged nanoporous medium with a porosity $\epsilon_{\mathrm{p}}(r,t)$, an internal pore surface area/volume ratio $a_{\mathrm{p}}(r,t)$ and a pore surface charge/area ratio $\sigma_{\mathrm{s}}(r,t)$ where r denotes the position vector. The porous medium is filled with a binary asymmetric electrolyte with unequal diffusivities. The chemical formula of the neutral salt is written as $\mathrm{c}_{\nu_+}^{z+}\mathrm{a}_{\nu_-}^{z-}$ where c^{z+} and a^{z-} represent the cations and anions respectively and ν_+ and ν_- are the numbers of cations and anions produced respectively by the complete dissociation of 1 molecule of neutral salt. The anode and cathode are located on the left and right ends of the system respectively, therefore the current I in the system flows from left to right.

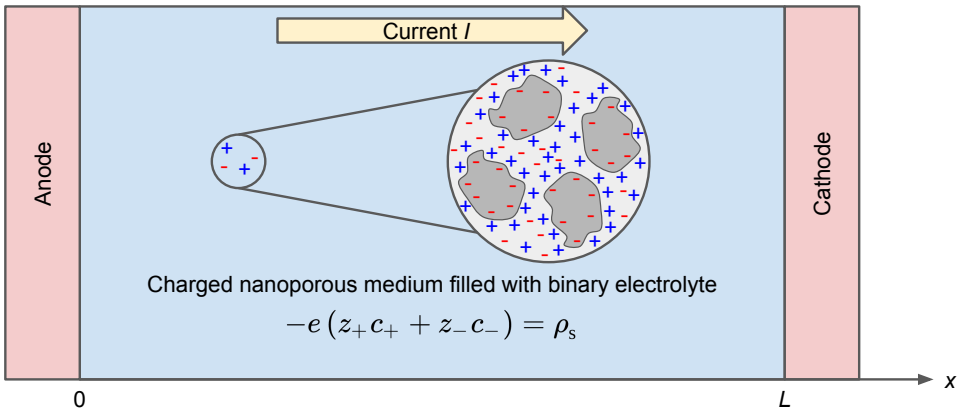

Figure 2-1: Schematic of system considered: charged nanoporous medium filled with binary electrolyte flanked on the left by anode and right by cathode. Current I in system flows from left to right. The equation shown describes macroscopic electroneutrality given by Equation 2.4 where ρ_s is the volume-averaged background charge density.

Based on linear irreversible thermodynamics [31, 84], the diffusional molar flux F_i of species $i \in \{+, -\}$ is given by

$$F_i = -\frac{\epsilon_p D_i^m c_i}{\tau k_B T} \nabla \mu_i, \quad \mu_i = k_B T \ln a_i + z_i e \phi + \mu_i^\Theta, \tag{2.1}$$

where $a_i = \gamma_i \hat{c}_i$ is the activity of species i and $\hat{c}_i \equiv \frac{c_i}{c_i^\Theta}$ is the concentration of species i, c_i, normalized by its standard concentration c_i^Θ, and the Θ superscript denotes standard state. T and ϕ are the temperature and electric potential of the electrolyte respectively and k_B is the Boltzmann constant. A natural scale for electric potentials is the thermal voltage given by $\frac{k_B T}{e} = \frac{RT}{F} \approx 26\,\text{mV}$ at $T = 298\,\text{K}$ (room temperature) where $F = N_A e$ and $R = N_A k_B$. D_i^m, μ_i, z_i, μ_i^Θ and γ_i are the molecular (free solution) tracer diffusivity, electrochemical potential, charge number, standard electrochemical potential and activity coefficient of species i respectively. We account for corrections due to the porosity ϵ_p and tortuosity τ of the charged nanoporous medium in F_i and we ignore dispersion effects. We assume isothermal conditions, i.e., T is constant, and that the material properties ϵ_p and τ are uniform and constant.

$\gamma_\pm$ is generally a function of $c_\pm$. Modeling diffusion as an activated process, $D_i^m = D_{i0}^m \frac{\gamma_i}{\gamma_{\ddagger,i}^d}$ where D_{i0}^m and $\gamma_{\ddagger,i}^d$ are the molecular (free solution) tracer diffusivity

in the dilute limit and the activity coefficient of the transition state for activated diffusion of species $i \in \{+,-\}$ respectively [31]. Throughout this paper, we set all activity coefficients to 1 and ignore non-ideal effects because we are primarily interested in studying the effects of coupling Butler-Volmer reaction kinetics with the leaky membrane model, therefore we set $D_{\pm}^{\mathrm{m}} = D_{\pm 0}^{\mathrm{m}}$.

The macroscopic diffusivities need to account for corrections due to the tortuosity of the charged nanoporous medium τ. Following [84], we define the macroscopic tracer diffusivity in the dilute limit of species $i \in \{+,-\}$, D_{i0}, as $D_{i0} \equiv \frac{D_{i0}^{\mathrm{m}}}{\tau}$. Thus, $F_{\pm}$ becomes

$$F_{\pm} = -\epsilon_{\mathrm{p}} D_{\pm 0} \left(\nabla c_{\pm} + \frac{z_{\pm} e c_{\pm}}{k_{\mathrm{B}} T} \nabla \phi \right). \tag{2.2}$$

For AAO membranes that have parallel straight cylindrical pores with a constant pore radius, $\tau = 1$ while for random porous membranes such as CN and PE membranes, we can use the Bruggeman relation given by $\tau = \epsilon_{\mathrm{p}}^{-\frac{1}{2}}$ to estimate their tortuosities as a function of porosity.

The leaky membrane model consists of the Nernst-Planck equations that are coupled with the algebraic constraint given by macroscopic electroneutrality. Assuming no convection, the Nernst-Planck equations are given by

$$\epsilon_{\mathrm{p}} \frac{\partial c_{\pm}}{\partial t} + \nabla \cdot F_{\pm} = 0, \tag{2.3}$$

where we account for corrections due to the porosity of the charged nanoporous medium ϵ_{p} and assume that there are no homogeneous reactions. Macroscopic electroneutrality implies that

$$\rho_{\mathrm{s}} \equiv \frac{\sigma_{\mathrm{s}}}{h_{\mathrm{p}}} = \frac{a_{\mathrm{p}} \sigma_{\mathrm{s}}}{\epsilon_{\mathrm{p}}} = -e(z_{+} c_{+} + z_{-} c_{-}) \tag{2.4}$$

where we define the effective pore size $h_{\mathrm{p}} \equiv \frac{\epsilon_{\mathrm{p}}}{a_{\mathrm{p}}}$ and ρ_{s} is the volume-averaged background charge density. We assume that the material properties a_{p}, h_{p}, σ_{s}, ρ_{s} are uniform and constant. Since we are invoking macroscopic electroneutrality, the electric double layers are assumed to be at equilibrium and their structures are not explic-

itly considered. For the electroneutrality of 1 molecule of neutral salt, we require $z_+\nu_+ + z_-\nu_- = 0$. The current density J is given by the linear combination of the diffusional molar fluxes of all species weighted by their charges, i.e.,

$$J = e(z_+F_+ + z_-F_-). \tag{2.5}$$

Multiplying z_ie to the Nernst-Planck equation of each species $i \in \{+, -\}$ and summing all such equations gives the charge conservation equation

$$\nabla \cdot J = 0. \tag{2.6}$$

We denote the positions of the anode/electrolyte and cathode/electrolyte interfaces as $r_{\mathrm{m}}^{\mathrm{a}}(t)$ and $r_{\mathrm{m}}^{\mathrm{c}}(t)$ respectively and the "a" and "c" superscripts denote the anode and cathode respectively. The current I is given by

$$I = \int \hat{n} \cdot J|_{r=r_{\mathrm{m}}^{\mathrm{c}}} \, \mathrm{d}S^{\mathrm{c}} = \int -\hat{n} \cdot J|_{r=r_{\mathrm{m}}^{\mathrm{a}}} \, \mathrm{d}S^{\mathrm{a}} \tag{2.7}$$

where we define $\hat{n}$ as the unit normal that points outwards from the electrolyte and the surface integral is performed over the total surface area of the anode or cathode, i.e., including both the electrolyte and matrix phases. Because of charge conservation, the current entering the cathode must be equal to the current leaving the anode, which is enforced in Equation 2.7. We will use Butler-Volmer reaction kinetics to describe electrochemical reactions at the electrodes and we denote the Faradaic current densities at the anode and cathode as $J_{\mathrm{F}}^{\mathrm{a}}$ and $J_{\mathrm{F}}^{\mathrm{c}}$ respectively. Because of the conservation of charges across the anode/electrolyte and cathode/electrolyte interfaces and because the volumetric porosity of a porous medium is equal to its areal porosity [33], we require

$$\hat{n} \cdot J|_{r=r_{\mathrm{m}}^{\mathrm{a,c}}} = \epsilon_{\mathrm{p}} J_{\mathrm{F}}^{\mathrm{a,c}}|_{r=r_{\mathrm{m}}^{\mathrm{a,c}}}. \tag{2.8}$$

The boundary condition given by Equation 2.8 describes the coupling between transport in the charged nanoporous medium and electrochemical reaction kinetics at the

electrode/electrolyte interfaces.

For a binary electrolyte, we define the neutral salt bulk concentration, which is denoted by c, that can be depleted, i.e., reach 0. Regardless of the sign of ρ_{s}, the concentration of the ions whose charge has the same sign as ρ_{s}, i.e., the coions, can be depleted. For $\rho_{\mathrm{s}} \leq 0$, c_- can reach 0 while for $\rho_{\mathrm{s}} \geq 0$, c_+ can reach 0. Therefore, we define

$$c \equiv \begin{cases} \frac{c_-}{\nu_-}, & \rho_{\mathrm{s}} \leq 0 \\ \frac{c_+}{\nu_+}, & \rho_{\mathrm{s}} \geq 0. \end{cases} \tag{2.9}$$

Hence, rearranging Equation 2.9,

$$c_- = \nu_- c - \frac{\rho_{\mathrm{s}} + |\rho_{\mathrm{s}}|}{2 z_- e}. \tag{2.10}$$

The initial neutral salt bulk concentration $c(t = 0)$ is specified as an initial condition and we determine $c_-(t = 0)$ from Equation 2.10.

2.3.2 Electrochemical reaction kinetics

Generally, for an electron transfer reaction involving n electrons, the Faradaic current density J_{F} can be written in terms of the exchange current density J_0 and overpotential η as

$$J_{\mathrm{F}} = J_0 \left[\exp\left(-\frac{\alpha_{\mathrm{c}} n e \eta}{k_{\mathrm{B}} T} \right) - \exp\left(\frac{\alpha_{\mathrm{a}} n e \eta}{k_{\mathrm{B}} T} \right) \right], \quad \alpha_{\mathrm{c}} + \alpha_{\mathrm{a}} = 1, \tag{2.11}$$

where α_{c} and α_{a} are the cathodic and anodic charge transfer coefficients respectively [31, 84] and J_0 is generally a function of the activities of the oxidized and reduced species and electrons. We define $\eta = \Delta\phi - \Delta\phi^{\mathrm{eq}}$ where $\Delta\phi = \phi_{\mathrm{e}} - \phi$ is the interfacial electric potential difference, ϕ_{e} is the electric potential of the electrode and $\Delta\phi^{\mathrm{eq}}$ is the Nernst potential, which is generally a function of the activities of the oxidized and reduced species and electrons. The overpotential provides the driving force for a Faradaic reaction to go out of equilibrium and results in a nonzero Faradaic current density.

As a prototypical example of electrochemical reaction kinetics, we consider copper electrodeposition and electrodissolution, which have been studied extensively in literature [172, 157, 45, 54]. A more general theoretical treatment of electrochemical reaction kinetics based on nonequilibrium thermodynamics can be found at [31, 84]. All variables here are evaluated at the electrode/electrolyte interface ($r = r_{\mathrm{m}}^{\mathrm{a,c}}$). We assume that only ions exist in the electrolyte while only electrons and neutral atoms exist in the solid electrode, i.e., we do not consider mixed ion-electron conductors that are used in applications such as solid oxide fuel cells.

The reaction mechanism for copper electrodeposition and electrodissolution [172, 157, 45, 54] can be written as

$$\mathrm{Cu^{2+}(aq) + e^- \rightleftharpoons Cu^+(ads)}, \tag{2.12}$$

$$\mathrm{Cu^{+}(ads) + e^- \rightleftharpoons Cu(s)}, \tag{2.13}$$

where (aq) indicates aqueous, (ads) indicates adsorbed on the electrode surface, (s) indicates solid, and the mechanism involves the overall transfer of $n = 2$ electrons. We assume that the first step is the rate-determining step (RDS) while the second step is at equilibrium and that Butler-Volmer reaction kinetics [31, 84, 172, 24] applies to both steps. We also assume that the activity of the electrons is 1, i.e., we ignore non-ideal effects associated with the electrons. Denoting $J_{\mathrm{F},1}$ and $J_{\mathrm{F},2}$ as the Faradaic current densities for the first and second steps respectively, in terms of $\Delta\phi$, we obtain

$$J_{\mathrm{F},1} = \frac{e}{\gamma_{\ddagger,1}^{\mathrm{r}}}\left\{k_{\mathrm{c},1} a_{\mathrm{Cu^{2+}}} \exp\left(-\frac{\alpha_1 e\Delta\phi}{k_{\mathrm{B}}T}\right) - k_{\mathrm{a},1} a_{\mathrm{Cu^{+}}} \exp\left[\frac{(1-\alpha_1)e\Delta\phi}{k_{\mathrm{B}}T}\right]\right\}, \tag{2.14}$$

$$J_{\mathrm{F},2} = \frac{e}{\gamma_{\ddagger,2}^{\mathrm{r}}}\left\{k_{\mathrm{c},2} a_{\mathrm{Cu^{+}}} \exp\left(-\frac{\alpha_2 e\Delta\phi}{k_{\mathrm{B}}T}\right) - k_{\mathrm{a},2} \exp\left[\frac{(1-\alpha_2)e\Delta\phi}{k_{\mathrm{B}}T}\right]\right\}, \tag{2.15}$$

where $\gamma_{\ddagger,i}^{\mathrm{r}}$, $k_{\mathrm{c},i}$, $k_{\mathrm{a},i}$ and α_i are the activity coefficient of the transition state for the Faradaic reaction, cathodic rate constant, anodic rate constant and charge transfer coefficient of step $i \in \{1, 2\}$ respectively. We assume that a_{Cu} remains constant at 1 in $J_{\mathrm{F},2}$ because Cu(s) is a solid metal at room temperature. Because we assume that the first step is the RDS while the second step is at equilibrium, $J_{\mathrm{F}} = 2J_{\mathrm{F},1}$,

where the factor of 2 accounts for the overall transfer of 2 electrons, and $J_{\mathrm{F},2} \approx 0$. Like in Section 2.3.1, we assume that all activity coefficients are equal to 1 and ignore non-ideal effects. Therefore,

$$J_{\mathrm{F}} = 2e\left\{k_{\mathrm{c},1}\hat{c}_{\mathrm{Cu}^{2+}} \exp\left(-\frac{\alpha_1 e\Delta\phi}{k_{\mathrm{B}}T}\right) - \frac{k_{\mathrm{a},1}k_{\mathrm{a},2}}{k_{\mathrm{c},2}} \exp\left[\frac{(2-\alpha_1)e\Delta\phi}{k_{\mathrm{B}}T}\right]\right\}. \tag{2.16}$$

At equilibrium, $J_{\mathrm{F}} = 0$ and $\Delta\phi = \Delta\phi^{\mathrm{eq}}$ and we recover the Nernst equation given by

$$\Delta\phi^{\mathrm{eq}} = \frac{k_{\mathrm{B}}T}{2e} \ln\left(\frac{k_{\mathrm{c},1}k_{\mathrm{c},2}\hat{c}_{\mathrm{Cu}^{2+}}}{k_{\mathrm{a},1}k_{\mathrm{a},2}}\right). \tag{2.17}$$

where the "eq" superscript denotes equilibrium. At standard conditions, $\hat{c}_{\mathrm{Cu}^{2+}} = 1$ and we obtain

$$E^{\Theta} \equiv \Delta\phi^{\mathrm{eq},\Theta} = \frac{k_{\mathrm{B}}T}{2e} \ln\left(\frac{k_{\mathrm{c},1}k_{\mathrm{c},2}}{k_{\mathrm{a},1}k_{\mathrm{a},2}}\right), \quad \Delta\phi^{\mathrm{eq}} = \frac{k_{\mathrm{B}}T}{2e} \ln \hat{c}_{\mathrm{Cu}^{2+}} + E^{\Theta}, \tag{2.18}$$

where E^{Θ} is the standard electrode potential for Cu^{2+} ions. We express J_{F} in terms of J_0 and η as

$$J_{\mathrm{F}} = J_0\left\{\exp\left(-\frac{\alpha_1 e\eta}{k_{\mathrm{B}}T}\right) - \exp\left[\frac{(2-\alpha_1)e\eta}{k_{\mathrm{B}}T}\right]\right\}, \quad J_0 = 2e(k_{\mathrm{c},1}\hat{c}_{\mathrm{Cu}^{2+}})^{1-\frac{\alpha_1}{2}}\left(\frac{k_{\mathrm{a},1}k_{\mathrm{a},2}}{k_{\mathrm{c},2}}\right)^{\frac{\alpha_1}{2}}. \tag{2.19}$$

Comparing Equation 2.19 with Equation 2.11, we identify

$$\alpha_{\mathrm{c}} = \frac{\alpha_1}{2}, \quad \alpha_{\mathrm{a}} = 1 - \frac{\alpha_1}{2}. \tag{2.20}$$

Given the value of J_0 at a given reference value $\hat{c}^{\mathrm{ref}}_{\mathrm{Cu}^{2+}}$ and denoting this value of J_0 as J_0^{ref}, we can rewrite J_0 as

$$J_0 = J_0^{\mathrm{ref}}\left(\frac{\hat{c}_{\mathrm{Cu}^{2+}}}{\hat{c}^{\mathrm{ref}}_{\mathrm{Cu}^{2+}}}\right)^{1-\frac{\alpha_1}{2}} = 2ek_0\hat{c}_{\mathrm{Cu}^{2+}}^{1-\frac{\alpha_1}{2}}, \quad k_0 = \frac{J_0^{\mathrm{ref}}}{2e\left(\hat{c}^{\mathrm{ref}}_{\mathrm{Cu}^{2+}}\right)^{1-\frac{\alpha_1}{2}}}, \tag{2.21}$$

where k_0 is the overall reaction rate constant.

To compare the reaction rate with the diffusion rate, we define the Damköhler

number Da as the ratio of these two rates. Taking Equation 2.8 into consideration, the scale for the Faradaic current density can be estimated as $e\epsilon_{\mathrm{p}}k_0$ while the scale for the current density in the electrolyte due to diffusion and electromigration is set by the limiting current density J_{lim}, which is given in Equation 2.23. Therefore, the Damköhler number Da is given by the ratio of these two scales:

$$\mathrm{Da} = \frac{e\epsilon_{\mathrm{p}}k_0}{J_{\mathrm{lim}}}. \tag{2.22}$$

A large Da, i.e., $\mathrm{Da} \gg 1$, means that the system is diffusion-limited while a small Da, i.e., $\mathrm{Da} \ll 1$, means that the system is reaction-limited.

2.3.3 Boundary conditions, constraints and initial conditions

For this paper, because we are interested in a 1D model where the electrodes are located at the endpoints of the 1D domain, we prescribe boundary conditions only at these endpoints. For 2D and 3D models, we would need to prescribe appropriate boundary conditions at boundaries that are not electrode/electrolyte interfaces.

2.3.3.1 Boundary conditions

We denote the anode and cathode electric potentials as $\phi_{\mathrm{e}}^{\mathrm{a,c}}$. We arbitrarily choose the anode to be on the left end of the system and the cathode to be on the right end of the system and ground the anode at all times, i.e., $\phi_{\mathrm{e}}^{\mathrm{a}} = 0$.

We assume that the electrode/electrolyte interfaces are stationary. In reality, these interfaces move because of copper electrodeposition and electrodissolution, therefore we can relate their normal velocities to the normal current densities using mass conservation and the mass-average velocity of the liquid electrolyte is nonzero [236, 78, 71]. Nonetheless, these velocities are usually negligible and will be ignored in this paper. Mass conservation of the inert anions implies that $\hat{n} \cdot F_{-}(r = r_{\mathrm{m}}^{\mathrm{a,c}}) = 0$. Conservation of charges across the electrode/electrolyte interfaces requires $\hat{n} \cdot J(r = r_{\mathrm{m}}^{\mathrm{a,c}}) = \epsilon_{\mathrm{p}} J_{\mathrm{F}}^{\mathrm{a,c}}$ as discussed in Section 2.3.1.

2.3.3.2 Constraints from galvanostatic and potentiostatic conditions and linear sweep voltammetry

For galvanostatic conditions where we impose a current I_{applied} on the system, we require $\int \hat{n} \cdot J(r = r_{\text{m}}^{\text{c}})\,\mathrm{d}S^{\text{c}} = \int -\hat{n} \cdot J(r = r_{\text{m}}^{\text{a}})\,\mathrm{d}S^{\text{a}} = I_{\text{applied}}$. For potentiostatic conditions where we impose an electric potential V on the cathode, we set $\phi_{\text{e}}^{\text{c}} = V$. For linear sweep voltammetry (LSV) where we impose a linearly time-varying electric potential on the cathode, $\phi_{\text{e}}^{\text{c}} = \beta_{\text{LSV}} t$ where β_{LSV} is the sweep rate.

2.3.3.3 Initial conditions

Based on the discussion in Section 2.3.1 about the neutral salt bulk concentration, we specify the initial condition for c as $c(t = 0) = c_0$, therefore $c_-(t = 0) = \nu_- c_0 - \frac{\rho_{\text{s}} + |\rho_{\text{s}}|}{2 z_- e} \equiv \beta_1$.

2.4 Model implementation

For all results, we specialize the model to one spatial dimension x. To numerically solve the steady state equations in Section 2.5.2, we use MATLAB's `bvp4c` boundary value problem solver. The form of equations that is appropriate for use with the `bvp4c` solver is given in Appendix 2.8.2. We also provide all the necessary Jacobians to the `bvp4c` function to increase convergence rate; they are especially useful for the highly nonlinear Butler-Volmer boundary conditions. The expressions for these Jacobians are given in Appendix 2.8.3. For computing the semi-analytical steady state current-voltage relation for Butler-Volmer boundary conditions in Section 2.5.2.3, we use MATLAB's `fsolve` and `fzero` functions with default relative and absolute tolerances to invert the nonlinear algebraic Butler-Volmer equations.

In Section 2.5.3, to fit the experimental datasets with the steady state current-voltage relation for Butler-Volmer boundary conditions, we use MATLAB's `lsqnonlin` function to perform nonlinear least squares fitting. For the time-dependent linear sweep voltammetry (LSV) numerical simulations, we implement the model in COMSOL Multiphysics 5.3a, which uses the finite element method, by using the General

Form PDE interface. After the numerical data are generated, we use MATLAB R2017b to postprocess and plot them. We also use MATLAB's `polyfit` function to estimate the experimental overlimiting conductances.

2.5 Results

2.5.1 Limiting current density and limiting current

We derive the limiting current density, which is denoted by J_{lim}, and the limiting current, which is denoted by I_{lim}. To do so, we assume the following: 1) $\rho_{\text{s}} = 0$, 2) a 1D system at steady state $\left(\frac{\partial c_{\pm}}{\partial t} = 0\right)$ where the domain of the system is $x \in [0, L]$ and we arbitrarily choose the anode to be at $x = 0$ and the cathode to be at $x = L$, and 3) ignore Faradaic reactions at both the anode and cathode. We assume that the anions are inert and cannot leave the system, therefore the boundary conditions for the system are $F_{-}(x = 0) = F_{-}(x = L) = 0$. That the anions cannot leave the system also implies that the number of anions in the system is conserved, which is expressed by the integral constraint $\int_0^L c_{-}\,\mathrm{d}x = \nu_{-}c_0 L$ where c_0 is the neutral salt bulk concentration. Limiting current is attained when the concentrations of both the cations and anions vanish at the cathode. Therefore, using the boundary conditions and integral constraint and setting $c_{-} = 0$ at $x = L$, we obtain

$$J_{\text{lim}} = \frac{2z_{+}e\epsilon_{\text{p}}D_{+0}\left(1 - \frac{z_{-}}{z_{+}}\right)\nu_{-}c_0}{L} = \frac{2(\nu_{+} + \nu_{-})z_{+}e\epsilon_{\text{p}}D_{+0}c_0}{L}. \tag{2.23}$$

We note that $(\nu_{+} + \nu_{-})c_0$ is the sum of the concentrations of the cations and anions. Hence,

$$I_{\text{lim}} \equiv J_{\text{lim}}A = \frac{2z_{+}e\epsilon_{\text{p}}D_{+0}\left(1 - \frac{z_{-}}{z_{+}}\right)\nu_{-}c_0 A}{L} = \frac{2(\nu_{+} + \nu_{-})z_{+}e\epsilon_{\text{p}}D_{+0}c_0 A}{L} \tag{2.24}$$

where A is the total surface area of the anode or cathode.

2.5.2 Steady state current-voltage relations and overlimiting conductances

It is convenient to simplify the model at steady state in order to derive analytical or semi-analytical expressions for c_-, ϕ, steady state current-voltage relation and overlimiting conductance that can be easily used for fitting experimental data. Overlimiting conductance is only defined for $\rho_s < 0$ and not for $\rho_s \geq 0$ because the system can exceed the limiting current, i.e., become overlimiting, only when $\rho_s < 0$. We consider three types of boundary conditions that are commonly realized in experiments: 1) reservoir boundary condition at the anode, 2) no-anion-flux boundary condition at the anode, and 3) Butler-Volmer boundary conditions at the anode and cathode. To verify these analytical or semi-analytical expressions, we compare them with numerical solutions obtained from solving the equations using MATLAB's `bvp4c` boundary value problem solver.

All parameters used in this section are given in Table 2.1. In this section, copper electrodeposition and electrodissolution occurs in AAO membranes containing copper(II) sulfate ($CuSO_4$) as the electrolyte. For AAO membranes that have parallel straight cylindrical pores with the same length and a constant pore radius, the assumptions that ϵ_p, τ, a_p and h_p are uniform and constant are reasonable. Denoting the pore radius as r_p, we obtain $h_p = \frac{\epsilon_p}{a_p} = \frac{r_p}{2}$. The electrodes are circular with a radius r_e, therefore $A = \pi r_e^2$ where A is the total surface area of the anode or cathode.

2.5.2.1 Case 1: reservoir boundary condition at anode

We make the same assumptions used to derive J_{lim} and I_{lim} in Section 2.5.1 except that we assume $\rho_s \neq 0$. For the boundary conditions, we assume that there is a reservoir at $x = 0$ and an ideal cation-selective and anion-blocking surface at $x = L$. We also set ϕ at the anode at $x = 0$ to 0 and ϕ at the cathode at $x = L$ to $-V$ where $V \geq 0$ so that the current I flows from $x = 0$ to $x = L$. In summary, the boundary

Table 2.1: Parameters for copper electrodeposition and electrodissolution for AAO membranes at $T = 298\,\mathrm{K}$ and copper(II) sulfate ($CuSO_4$) electrolyte ($\nu_+ = 1, \nu_- = 1, z_+ = 2, z_- = -2$).

Parameter	Value	Notes and references
E^Θ	$0.3419\,\mathrm{V}$	Ref. [110]
D^m_{+0}	$7.14 \times 10^{-10}\,\mathrm{m^2/s}$	Ref. [110]
D^m_{-0}	$1.065 \times 10^{-9}\,\mathrm{m^2/s}$	Ref. [110]
J^ref_0	$2.9\,\mathrm{mA/cm^2}$	Mean of exchange current densities for E electrodes in Table 2 of [157]
$c^\mathrm{ref}_{\mathrm{Cu^{2+}}}$	$75\,\mathrm{mM}$	Ref. [157]
α_1	0.75	Compromise between 0.5 in [157] and 1.16 in [172]
M_m	$63.546\,\mathrm{g/mol}$	Ref. [110]
ρ_m	$8.96\,\mathrm{g/cm^3}$	Ref. [110]
r_p	$175\,\mathrm{nm}$	Mean of product specification of $150\,\mathrm{nm} - 200\,\mathrm{nm}$
L	$60\,\mu\mathrm{m}$	Product specification
ϵ_p	0.375	Mean of product specification of $0.25 - 0.50$
r_e	$6\,\mathrm{mm}$	Product specification
τ	1	Straight pores
$c^\Theta_{\mathrm{Cu^{2+}}}$	$1\,\mathrm{M} = 10^3\,\mathrm{mol/m^3}$	Standard concentration

conditions are given by

$$c_-(x=0) = \nu_- c_0 - \frac{\rho_\mathrm{s} + |\rho_\mathrm{s}|}{2 z_- e} \equiv \beta_1, \tag{2.25}$$

$$\phi(x=0) = 0, \tag{2.26}$$

$$F_-(x=L) = 0, \tag{2.27}$$

$$\phi(x=L) = -V, \quad V \geq 0. \tag{2.28}$$

Using these boundary conditions, we obtain

$$I = JA = \frac{1}{2} I_\mathrm{lim} \frac{\beta_1}{\nu_- c_0} \left[1 - \exp\left(\frac{z_- e V}{k_\mathrm{B} T} \right) \right] - \frac{z_+ e \epsilon_\mathrm{p} D_{+0} \rho_\mathrm{s} A}{L k_\mathrm{B} T} V. \tag{2.29}$$

Setting $\rho_\mathrm{s} = 0$, we define the limiting current $I^\mathrm{reservoir}_\mathrm{lim}$ as

$$I^\mathrm{reservoir}_\mathrm{lim} \equiv \lim_{V \to \infty} \lim_{\rho_\mathrm{s} \to 0} I = \frac{1}{2} I_\mathrm{lim}. \tag{2.30}$$

For $\rho_s < 0$, Equation 2.29 shows that $I > I_{lim}^{reservoir}$ for sufficiently large values of V, i.e., the current I becomes overlimiting. Therefore, for $\rho_s < 0$,

$$\lim_{V\to\infty} I(\rho_s < 0) = I_{lim}^{reservoir} + \sigma_{OLC} V \tag{2.31}$$

where we define the overlimiting conductance σ_{OLC} as

$$\sigma_{OLC} \equiv -\frac{z_+ e \epsilon_p D_{+0} \rho_s A}{L k_B T} = -\frac{z_+ e \epsilon_p D_{+0}^m \sigma_s A}{\tau L k_B T h_p}, \quad \rho_s < 0. \tag{2.32}$$

Equation 2.31 predicts that I varies linearly with V for a sufficiently large V and the overlimiting conductance σ_{OLC} is the gradient of this linear relationship. For $\rho_s \leq 0$, because c_- can reach 0, there are no restrictions on how large V can be. For $\rho_s > 0$, there is a finite maximum value of V, which is denoted by $V_{max}^{reservoir}$, for which the steady state I-V relation is valid. The current that corresponds to $V_{max}^{reservoir}$ is denoted as $I_{max}^{reservoir}$. $V_{max}^{reservoir}$ is determined by setting $c_+ = 0$, or equivalently, $c_- = -\frac{\rho_s}{z_- e}$, and $\phi = -V_{max}^{reservoir}$ at $x = L$:

$$V_{max}^{reservoir} = \frac{k_B T}{z_- e} \ln\left(\frac{\rho_s}{-z_- e \nu_- c_0 + \rho_s}\right), \quad \rho_s > 0. \tag{2.33}$$

Because $I_{max}^{reservoir} < I_{lim}^{reservoir}$, the presence of a positive background charge effectively reduces the diffusion-limited current, which is defined in Equation 2.30 for $\rho_s = 0$.

We define the following nondimensionalization to make the equations more compact: $\tilde{x} \equiv \frac{x}{L}$, $\tilde{c}_\pm \equiv \frac{c_\pm}{\nu_\pm c_0}$, $\tilde{\beta}_1 \equiv \frac{\beta_1}{\nu_- c_0} = 1 + \frac{\tilde{\rho}_s + |\tilde{\rho}_s|}{2}$, $\tilde{\phi} \equiv \frac{e\phi}{k_B T}$, $\tilde{D}_{\pm 0} \equiv \frac{D_{\pm 0}}{D_{amb0}}$, $\tilde{I} \equiv \frac{I}{I_{lim}}$ and $\tilde{\rho}_s \equiv \frac{\rho_s}{z_+ \nu_+ e c_0} = -\frac{\rho_s}{z_- \nu_- e c_0}$ where D_{amb0} is the ambipolar diffusivity of the neutral salt

in the dilute limit and is given by $D_{\text{amb0}} = \frac{(z_+ - z_-)D_{+0}D_{-0}}{z_+ D_{+0} - z_- D_{-0}}$ [172]. Therefore,

$$\tilde{I}_{\text{lim}}^{\text{reservoir}} = \frac{1}{2}, \tag{2.34}$$

$$\tilde{c}_- = \tilde{\beta}_1 \exp\Big(-z_- \tilde{\phi}\Big), \tag{2.35}$$

$$\tilde{I}\tilde{x} = \frac{1}{2}\left[\tilde{\beta}_1 - \tilde{c}_- + \frac{z_+ \tilde{\rho}_{\text{s}}}{z_+ - z_-} \ln\left(\frac{\tilde{c}_-}{\tilde{\beta}_1}\right)\right] = \frac{1}{2}\left\{\tilde{\beta}_1\Big[1 - \exp\Big(-z_- \tilde{\phi}\Big)\Big] - \frac{z_+ z_- \tilde{\rho}_{\text{s}}}{z_+ - z_-}\tilde{\phi}\right\}, \tag{2.36}$$

$$\tilde{I} = \frac{1}{2}\left\{\tilde{\beta}_1\Big[1 - \exp\Big(z_- \tilde{V}\Big)\Big] + \frac{z_+ z_- \tilde{\rho}_{\text{s}}}{z_+ - z_-}\tilde{V}\right\}. \tag{2.37}$$

It is possible to express $\tilde{c}_-$ and $\tilde{\phi}$ as explicit functions of $\tilde{x}$. We first define $\tilde{\alpha}_1 \equiv \frac{z_+ \tilde{\rho}_{\text{s}}}{z_+ - z_-}$ and $\tilde{\alpha}_2 \equiv z_- \tilde{\alpha}_1$. If $\tilde{\rho}_{\text{s}} = 0$, then

$$\tilde{c}_- = 1 - 2\tilde{I}\tilde{x}, \tag{2.38}$$

$$\tilde{\phi} = -\frac{1}{z_-} \ln \tilde{c}_- = -\frac{1}{z_-} \ln\Big(1 - 2\tilde{I}\tilde{x}\Big). \tag{2.39}$$

If $\tilde{\rho}_{\text{s}} \neq 0$, we use the Lambert W function [68], which is denoted as $W(\cdot)$. Given the form of Equation 2.37, for $\tilde{\rho}_{\text{s}} < 0$, we can interpret the bulk electrolyte as a diode that is connected in parallel to the electric double layers on the pore surfaces that act as a shunt resistor to conduct OLC via surface conduction in regions where the anions are depleted [77, 76]. It is therefore not surprising that the Lambert W function is applicable here as it is invoked in describing current flow through a diode with series resistance under an applied voltage [23], in describing current in solar cells with series and shunt resistances under an applied voltage [118], and in ion transport problems in ion-exchange membranes [166, 227, 177] and electrolysis cells [188]. For physically valid concentration and electric potential profiles, we restrict the Lambert W function and its argument to be real-valued. In this case, the function consists of two branches that are denoted by W_0 and W_{-1} [68]. Because we require $\tilde{c}_-$ to be nonnegative, we must use the W_0 branch for $\tilde{\rho}_{\text{s}} < 0$ and the W_{-1} branch for $\tilde{\rho}_{\text{s}} > 0$. We will leave out the subscript in $W(\cdot)$ and the appropriate branch to be used is implied by the sign of

$\tilde{\rho}_s$. Therefore,

$$\tilde{c}_- = -\tilde{\alpha}_1 W\left[-\frac{\tilde{\beta}_1}{\tilde{\alpha}_1}\exp\left(\frac{2\tilde{I}\tilde{x}-\tilde{\beta}_1}{\tilde{\alpha}_1}\right)\right], \tag{2.40}$$

$$\tilde{\phi} = -\frac{\tilde{\alpha}_1}{\tilde{\alpha}_2}\ln\left(\frac{\tilde{c}_-}{\tilde{\beta}_1}\right) = -\frac{\tilde{c}_- + 2\tilde{I}\tilde{x} - \tilde{\beta}_1}{\tilde{\alpha}_2}. \tag{2.41}$$

Noting that $\tilde{\phi}(\tilde{x}=1) = -\tilde{V}$, we can evaluate Equations 2.39 and 2.41 at $\tilde{x}=1$ to express $\tilde{V}$ as a function of $\tilde{I}$:

$$\tilde{V} = \begin{cases} \frac{1}{z_-}\ln\left(1-2\tilde{I}\right), & \tilde{\rho}_s = 0 \\ \frac{-\tilde{\alpha}_1 W\left[-\frac{\tilde{\beta}_1}{\tilde{\alpha}_1}\exp\left(\frac{2\tilde{I}-\tilde{\beta}_1}{\tilde{\alpha}_1}\right)\right]+2\tilde{I}-\tilde{\beta}_1}{\tilde{\alpha}_2}, & \tilde{\rho}_s \neq 0. \end{cases} \tag{2.42}$$

For both analytical expressions and numerical solutions, we plot $\tilde{c}_-$ and $\tilde{\phi}$ as functions of $\tilde{x}$ for $\tilde{\rho}_s = -0.01, -0.25$ in Figure 2-2 and $\tilde{\rho}_s = 0, 0.01, 0.25$ in Figure 2-3. For $\tilde{\rho}_s = 0$, we choose $\tilde{I} = 0.25, 0.495$ and avoid $\tilde{I} = \tilde{I}_{\text{lim}}^{\text{reservoir}} = 0.5$. This is because $\tilde{I} = \tilde{I}_{\text{lim}}^{\text{reservoir}} = 0.5$ implies $\tilde{V} \to \infty$, which cannot be displayed exactly in $\tilde{\phi}$-$\tilde{x}$ plots and also cannot be attained in numerical simulations. For $\tilde{\rho}_s = 0.01, 0.25$, we choose $\tilde{I} = 0.5\tilde{I}_{\text{max}}^{\text{reservoir}}, 0.99\tilde{I}_{\text{max}}^{\text{reservoir}}$ and for $\tilde{\rho}_s = -0.01, -0.25$, we choose $\tilde{I} = 0.25, 0.5, 0.75$. We first observe that the analytical expressions agree very well with the numerical solutions, thus verifying that the analytical expressions are correct. Regardless of $\tilde{\rho}_s$, when current is either underlimiting ($\tilde{I} = 0.25, 0.495, 0.5\tilde{I}_{\text{max}}^{\text{reservoir}}, 0.99\tilde{I}_{\text{max}}^{\text{reservoir}}$) or limiting ($\tilde{I} = \tilde{I}_{\text{lim}}^{\text{reservoir}} = 0.5$), $\tilde{c}_-$ is approximately linear in $\tilde{x}$, which is expected because the dominant physics at work is ambipolar diffusion. When current is overlimiting ($\tilde{I} = 0.75$), for small $|\tilde{\rho}_s|$ values such as $\tilde{\rho}_s = -0.01$, anions are depleted near and beyond the cathode and the depletion region extends for a finite distance from the cathode into the electrolyte. In the depletion region, $\tilde{\phi}$ is linear in $\tilde{x}$, which implies that electromigration under a constant electric field, i.e., surface conduction, is responsible for carrying current in this region. In contrast, because the concentration gradient is almost zero, diffusion only carries a negligible portion of the current. We also plot $\tilde{I}$ against $\tilde{V}$ for $\tilde{\rho}_s = 0, \pm 0.01, \pm 0.05, \pm 0.25$ and $\tilde{V} \in [0, 20]$ in Figure 2-4. For $\tilde{\rho}_s = 0$,

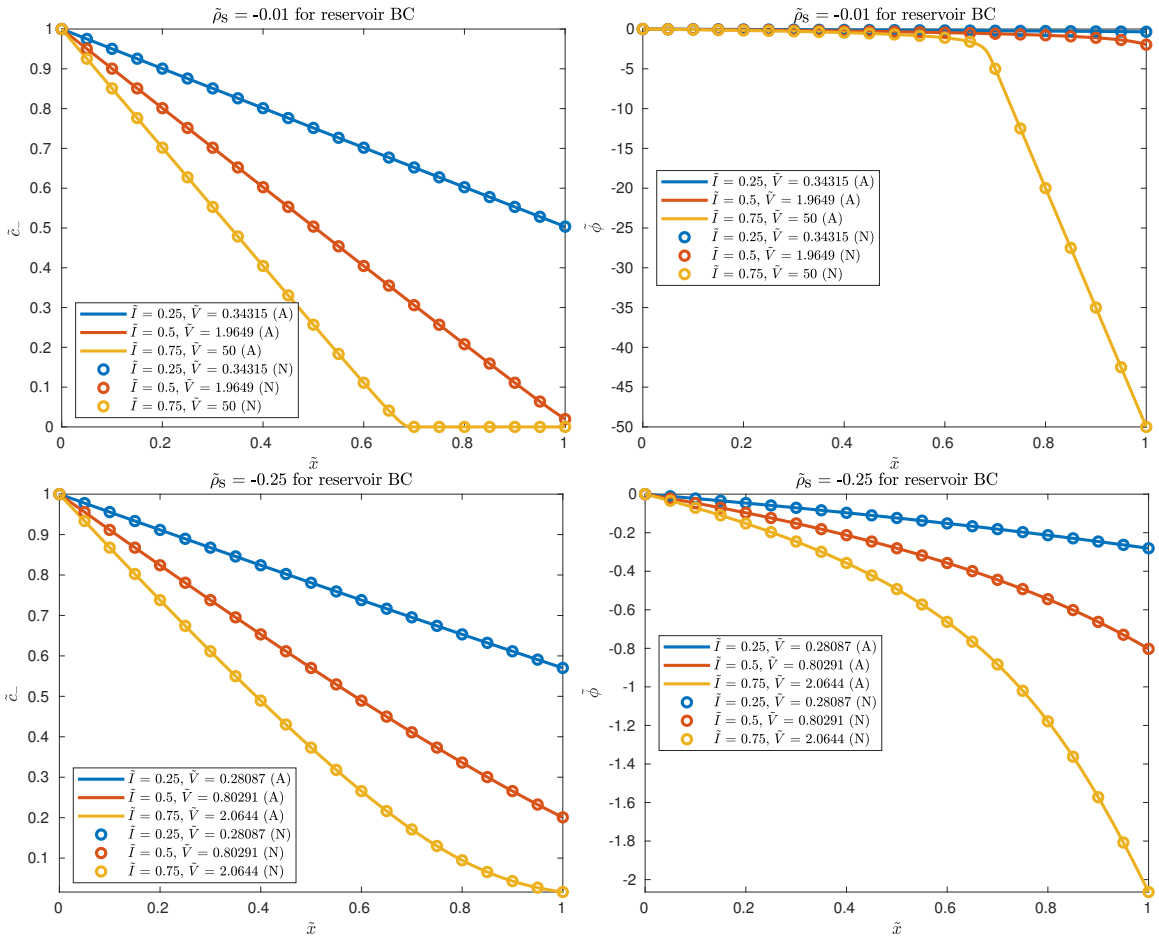

Figure 2-2: Plots of $\tilde{c}_-$ and $\tilde{\phi}$ against $\tilde{x}$ for $\tilde{\rho}_s = -0.01, -0.25$ and $\tilde{I} = 0.25, 0.5, 0.75$ for reservoir boundary condition at anode. (A) refers to analytical solutions and (N) refers to numerical solutions.

$\tilde{I}$ asymptotically approaches $\tilde{I}_{\text{lim}}^{\text{reservoir}}$ as expected. For $\tilde{\rho}_s = -0.01, -0.05, -0.25$, $\tilde{I}$ eventually becomes larger than $\tilde{I}_{\text{lim}}^{\text{reservoir}}$ at a sufficiently large $\tilde{V}$ and $\tilde{I}$ becomes a linear function of $\tilde{V}$ whose gradient gives the overlimiting conductance. On the other hand, for $\tilde{\rho}_s = 0.01, 0.05, 0.25$, the right plot in Figure 2-4 illustrates that having a positive background charge imposes a finite maximum voltage, which corresponds to a finite maximum current that is smaller than the limiting current $\tilde{I}_{\text{lim}}^{\text{reservoir}} = 0.5$.

2.5.2.2 Case 2: no-anion-flux boundary condition at anode

We repeat the analysis done in Section 2.5.2.1 except that we replace the boundary condition for c_- given by Equation 2.25 with $F_-(x = 0) = 0$ such that the anode is also

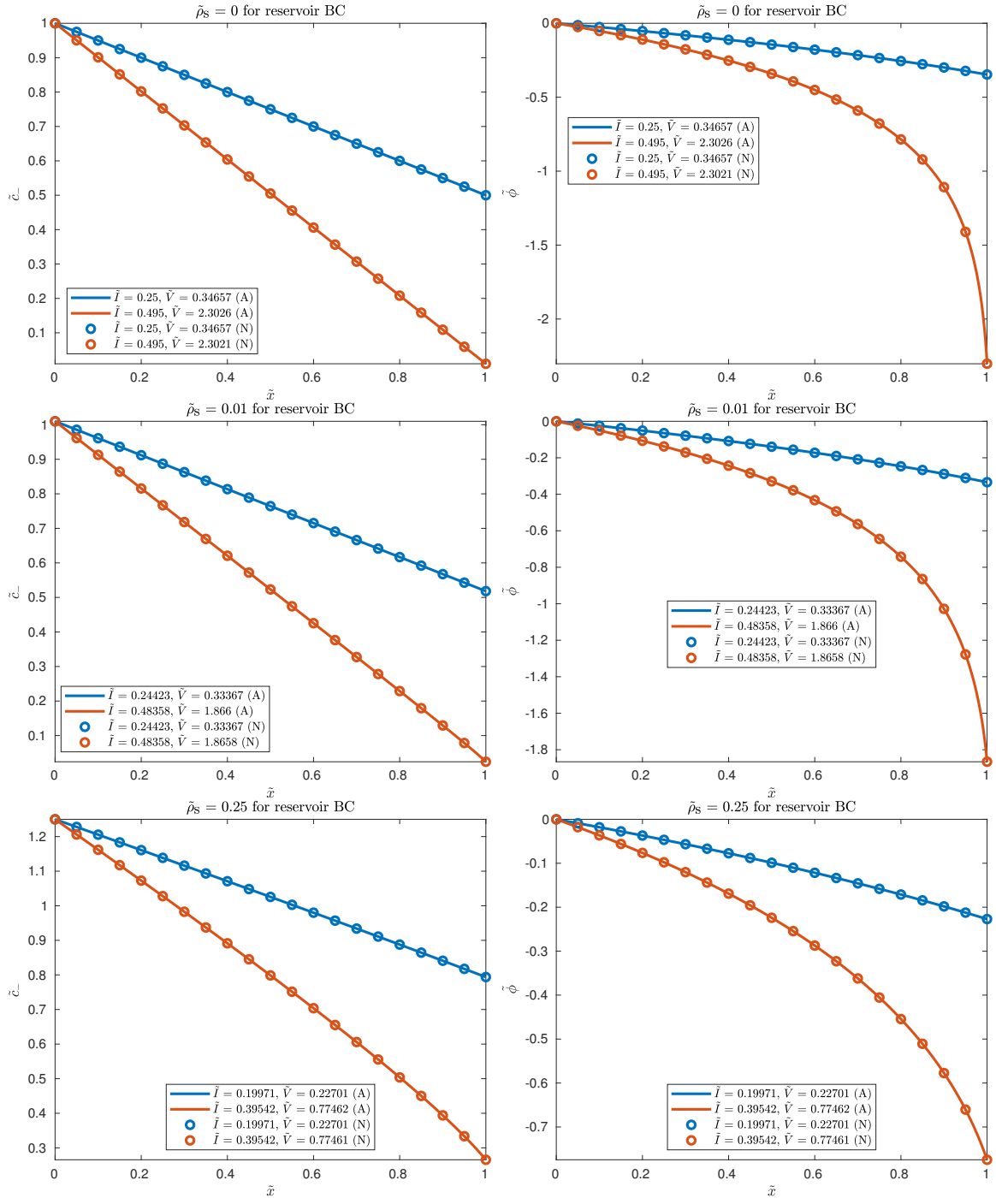

Figure 2-3: Plots of $\tilde{c}_-$ and $\tilde{\phi}$ against $\tilde{x}$ for 1) $\tilde{\rho}_s = 0$ and $\tilde{I} = 0.25, 0.495$ (top row) and 2) $\tilde{\rho}_s = 0.01, 0.25$ and $\tilde{I} = 0.5\tilde{I}_{\text{max}}^{\text{reservoir}}, 0.99\tilde{I}_{\text{max}}^{\text{reservoir}}$ (second and third rows) for reservoir boundary condition at anode. (A) refers to analytical solutions and (N) refers to numerical solutions.

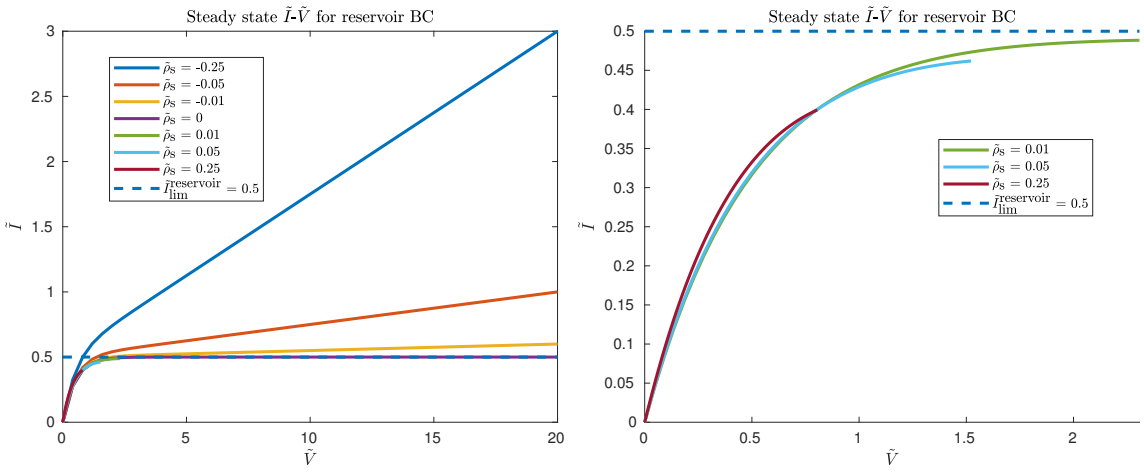

Figure 2-4: Left: steady state $\tilde{I}$-$\tilde{V}$ relations for $\tilde{\rho}_s = 0, \pm 0.01, \pm 0.05, \pm 0.25$ for reservoir boundary condition at anode. Right: zoom-in view of left plot for only $\tilde{\rho}_s = 0.01, 0.05, 0.25$. The dashed line denotes $\tilde{I}_{lim}^{reservoir} = 0.5$, which is the maximum $\tilde{I}$ that the system can reach when $\tilde{\rho}_s = 0$.

an ideal cation-selective and anion-blocking surface. Because the anions cannot leave the system, the number of anions in the system is conserved, which is expressed by the integral constraint $\int_0^L c_- \, \mathrm{d}x = \beta_1 L$. Using the boundary conditions and integral constraint, we obtain

$$I = JA = \frac{1}{2} I_{lim} \tilde{\alpha}_3 \left[1 - \exp\left(z_- \tilde{V}\right)\right] - \frac{z_+ e \epsilon_p D_{+0} \rho_s A}{L k_B T} V, \tag{2.43}$$

$$\tilde{\alpha}_3 = \frac{-\tilde{A}_2 + \sqrt{\tilde{A}_2^2 - 4\tilde{A}_1 \tilde{A}_3}}{2\tilde{A}_1}, \tag{2.44}$$

$$\tilde{A}_1 \equiv \frac{1}{2}\left(1 - \frac{z_-}{z_+}\right)\left[1 - \exp\left(2 z_- \tilde{V}\right)\right], \tag{2.45}$$

$$\tilde{A}_2 \equiv -\left[\tilde{\rho}_s + \left(1 - \frac{z_-}{z_+}\right)\tilde{\beta}_1\right]\left[1 - \exp\left(z_- \tilde{V}\right)\right], \tag{2.46}$$

$$\tilde{A}_3 \equiv -z_- \tilde{\beta}_1 \tilde{\rho}_s \tilde{V}. \tag{2.47}$$

$\tilde{\alpha}_3$ is obtained by solving the quadratic equation $\tilde{A}_1 \tilde{\alpha}_3^2 + \tilde{A}_2 \tilde{\alpha}_3 + \tilde{A}_3 = 0$ and keeping only the positive root because we require physically valid concentration and electric potential profiles. Setting $\rho_s = 0$, we define the limiting current I_{lim}^{NAF} as

$$I_{lim}^{NAF} \equiv \lim_{V \to \infty} \lim_{\rho_s \to 0} I = I_{lim} \tag{2.48}$$

where the "NAF" superscript denotes no anion flux. For $\rho_s < 0$, Equation 2.43 shows that $I > I_{lim}^{NAF}$ for sufficiently large values of V, i.e., the current I becomes overlimiting. Therefore, for $\rho_s < 0$,

$$\lim_{V\to\infty} I(\rho_s < 0) = \frac{1}{2} I_{lim}^{NAF} \frac{\left(\tilde{\rho}_s + 1 - \frac{z_-}{z_+}\right) + \sqrt{\left(\tilde{\rho}_s + 1 - \frac{z_-}{z_+}\right)^2 + 2\left(1 - \frac{z_-}{z_+}\right) z_- \tilde{\rho}_s \tilde{V}}}{1 - \frac{z_-}{z_+}} + \sigma_{OLC} V \tag{2.49}$$

where we define the overlimiting conductance σ_{OLC} as

$$\sigma_{OLC} \equiv -\frac{z_+ e \epsilon_p D_{+0} \rho_s A}{L k_B T} = -\frac{z_+ e \epsilon_p D_{+0}^m \sigma_s A}{\tau L k_B T h_p}, \quad \rho_s < 0. \tag{2.50}$$

Comparing Equations 2.50 and 2.32, even though the boundary conditions for cases 1 and 2 differ, both cases have the same expression for overlimiting conductance. Equation 2.49 predicts that for a sufficiently large V, the V term dominates the $\sqrt{V}$ term and I varies linearly with V and the overlimiting conductance σ_{OLC} is the gradient of this linear relationship. Like in case 1, there are no restrictions on how large V can be for $\rho_s \leq 0$ but there is a finite maximum value of V, which is denoted by V_{max}^{NAF}, for $\rho_s > 0$ for which the steady state I-V relation is valid. The current that corresponds to V_{max}^{NAF} is denoted as I_{max}^{NAF}. V_{max}^{NAF} is determined by setting $c_+ = 0$, or equivalently, $c_- = -\frac{\rho_s}{z_- e}$, and $\phi = -V_{max}^{NAF}$ at $x = L$, which results in the following nonlinear algebraic equation that is solved using MATLAB's `fsolve` or `fzero` function:

$$(1 + \tilde{\rho}_s) y^2 \ln y = (1 - y)\{\gamma_1 \tilde{\rho}_s (1 + y) - [\tilde{\rho}_s + 2\gamma_1 (1 + \tilde{\rho}_s)] y\}, \quad \tilde{\rho}_s > 0, \tag{2.51}$$

$$y = \exp\left(z_- \tilde{V}_{max}^{NAF}\right), \tag{2.52}$$

$$\gamma_1 = \frac{1}{2}\left(1 - \frac{z_-}{z_+}\right). \tag{2.53}$$

Using the nondimensionalization defined in Section 2.5.2.1, we obtain

$$\tilde{I}_{\text{lim}}^{\text{NAF}} = 1, \tag{2.54}$$

$$\tilde{c}_- = \tilde{\alpha}_3 \exp\Big(-z_-\tilde{\phi}\Big), \tag{2.55}$$

$$\tilde{I}\tilde{x} = \frac{1}{2}\left[\tilde{\alpha}_3 - \tilde{c}_- + \frac{z_+\tilde{\rho}_\text{s}}{z_+ - z_-}\ln\left(\frac{\tilde{c}_-}{\tilde{\alpha}_3}\right)\right] = \frac{1}{2}\left\{\tilde{\alpha}_3\Big[1 - \exp\Big(-z_-\tilde{\phi}\Big)\Big] - \frac{z_+z_-\tilde{\rho}_\text{s}}{z_+ - z_-}\tilde{\phi}\right\}, \tag{2.56}$$

$$\tilde{I} = \frac{1}{2}\left\{\tilde{\alpha}_3\Big[1 - \exp\Big(z_-\tilde{V}\Big)\Big] + \frac{z_+z_-\tilde{\rho}_\text{s}}{z_+ - z_-}\tilde{V}\right\}. \tag{2.57}$$

Like in case 1, it is possible to express $\tilde{c}_-$ and $\tilde{\phi}$ as explicit functions of $\tilde{x}$. We use the definitions for $\tilde{\alpha}_1$ and $\tilde{\alpha}_2$ in Section 2.5.2.1. If $\tilde{\rho}_\text{s} = 0$, then

$$\tilde{c}_- = \tilde{\alpha}_3 - 2\tilde{I}\tilde{x}, \tag{2.58}$$

$$\tilde{\phi} = -\frac{1}{z_-}\ln\left(\frac{\tilde{c}_-}{\tilde{\alpha}_3}\right) = -\frac{1}{z_-}\ln\left(1 - \frac{2\tilde{I}}{\tilde{\alpha}_3}\tilde{x}\right). \tag{2.59}$$

If $\tilde{\rho}_\text{s} \neq 0$, we obtain

$$\tilde{c}_- = -\tilde{\alpha}_1 W\left[-\frac{\tilde{\alpha}_3}{\tilde{\alpha}_1}\exp\left(\frac{2\tilde{I}\tilde{x} - \tilde{\alpha}_3}{\tilde{\alpha}_1}\right)\right], \tag{2.60}$$

$$\tilde{\phi} = -\frac{\tilde{\alpha}_1}{\tilde{\alpha}_2}\ln\left(\frac{\tilde{c}_-}{\tilde{\alpha}_3}\right) = -\frac{\tilde{c}_- + 2\tilde{I}\tilde{x} - \tilde{\alpha}_3}{\tilde{\alpha}_2}. \tag{2.61}$$

Noting that $\tilde{\phi}(\tilde{x} = 1) = -\tilde{V}$, we can evaluate Equations 2.59 and 2.61 at $\tilde{x} = 1$ to express $\tilde{V}$ as an implicit function of $\tilde{I}$:

$$\tilde{V} = \begin{cases} \frac{1}{z_-}\ln\Big(1 - \frac{2\tilde{I}}{\tilde{\alpha}_3}\Big), & \tilde{\rho}_\text{s} = 0 \\ \frac{-\tilde{\alpha}_1 W\Big[-\frac{\tilde{\alpha}_3}{\tilde{\alpha}_1}\exp\Big(\frac{2\tilde{I} - \tilde{\alpha}_3}{\tilde{\alpha}_1}\Big)\Big] + 2\tilde{I} - \tilde{\alpha}_3}{\tilde{\alpha}_2}, & \tilde{\rho}_\text{s} \neq 0 \end{cases} \tag{2.62}$$

where we recall that $\tilde{\alpha}_3$ is a function of $\tilde{V}$. We solve Equation 2.62 using MATLAB's `fsolve` or `fzero` function.

For both analytical expressions and numerical solutions, we plot $\tilde{c}_-$ and $\tilde{\phi}$ as

functions of $\tilde{x}$ for $\tilde{\rho}_s = -0.01, -0.25$ in Figure 2-5 and $\tilde{\rho}_s = 0, 0.01, 0.25$ in Figure 2-6. For $\tilde{\rho}_s = 0$, we choose $\tilde{I} = 0.5, 0.99$ and avoid $\tilde{I} = \tilde{I}_{lim}^{NAF} = 1$ for the same reason discussed for case 1. For $\tilde{\rho}_s = 0.01, 0.25$, we choose $\tilde{I} = 0.5\tilde{I}_{max}^{NAF}, 0.99\tilde{I}_{max}^{NAF}$ and for $\tilde{\rho}_s = -0.01, -0.25$, we choose $\tilde{I} = 0.5, 1, 1.5$. We observe that the analytical expressions agree very well with the numerical solutions. The qualitative features of the $\tilde{c}_-$-$\tilde{x}$ and $\tilde{\phi}$-$\tilde{x}$ plots are very similar to that for case 1. Regardless of $\tilde{\rho}_s$, when current is either underlimiting ($\tilde{I} = 0.5, 0.99, 0.5\tilde{I}_{max}^{NAF}, 0.99\tilde{I}_{max}^{NAF}$) or limiting ($\tilde{I} = \tilde{I}_{lim}^{NAF} = 1$), $\tilde{c}_-$ is approximately linear in $\tilde{x}$ because of predominant ambipolar diffusion. When current is overlimiting ($\tilde{I} = 1.5$), the depletion region extends for a finite distance from the cathode into the electrolyte. Because of the integral constraint on the anion concentration, anions can be exchanged across the anode to provide more conductivity to the electrolyte and it is possible for $\tilde{c}_-(\tilde{x} = 0) > \tilde{\beta}_1$, in contrast to $\tilde{c}_-(\tilde{x} = 0) = \tilde{\beta}_1$ for case 1. We also plot $\tilde{I}$ against $\tilde{V}$ for $\tilde{\rho}_s = 0, \pm 0.01, \pm 0.05, \pm 0.25$ and $\tilde{V} \in [0, 20]$ in Figure 2-7. For $\tilde{\rho}_s = -0.01, -0.05, -0.25$, $\tilde{I}$ eventually becomes larger than $\tilde{I}_{lim}^{NAF}$ at a sufficiently large $\tilde{V}$ and becomes linear in $\tilde{V}$ with a gradient that is equal to the overlimiting conductance. In contrast, like in case 1, the presence of a positive background charge results in a finite maximum voltage, which corresponds to a finite maximum current that is smaller than the limiting current $\tilde{I}_{lim}^{NAF} = 1$.

2.5.2.3 Case 3: Butler-Volmer boundary conditions at anode and cathode

We repeat the analysis done in Section 2.5.2.2 except that we replace the boundary conditions for ϕ given by Equations 2.26 and 2.28 with Butler-Volmer boundary conditions at the anode and cathode

$$-J(x = 0) = \epsilon_p J_F^a, \quad \phi_e^a = 0, \tag{2.63}$$

$$J(x = L) = \epsilon_p J_F^c, \quad \phi_e^c = -V, \quad V \geq 0, \tag{2.64}$$

where we use the expression for J_F given by Equation 2.19 in Section 2.3.2 for copper electrodeposition and electrodissolution.

We first compare the boundary conditions for ϕ given by the Butler-Volmer bound-

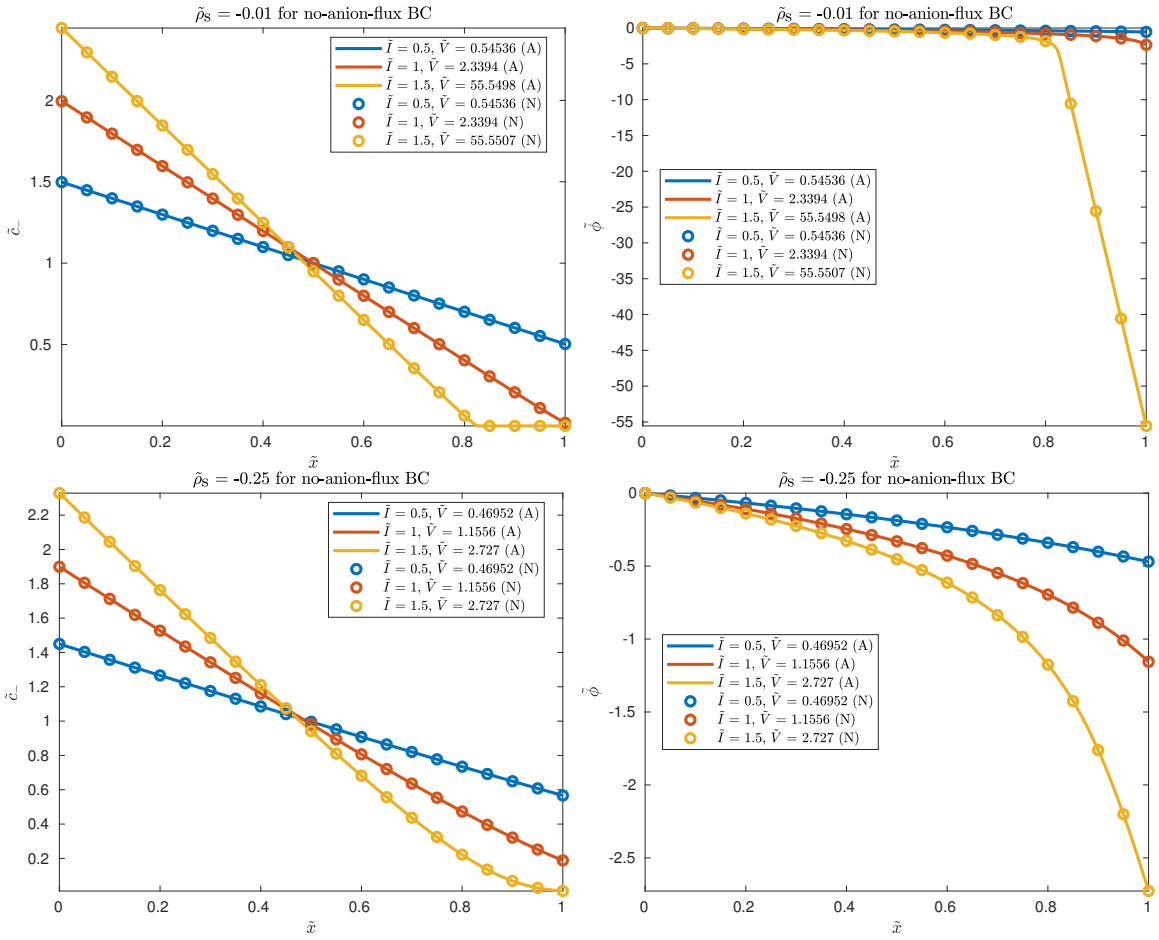

Figure 2-5: Plots of $\tilde{c}_-$ and $\tilde{\phi}$ against $\tilde{x}$ for $\tilde{\rho}_s = -0.01, -0.25$ and $\tilde{I} = 0.5, 1, 1.5$ for no-anion-flux boundary condition at anode. (A) refers to analytical solutions and (N) refers to numerical solutions.

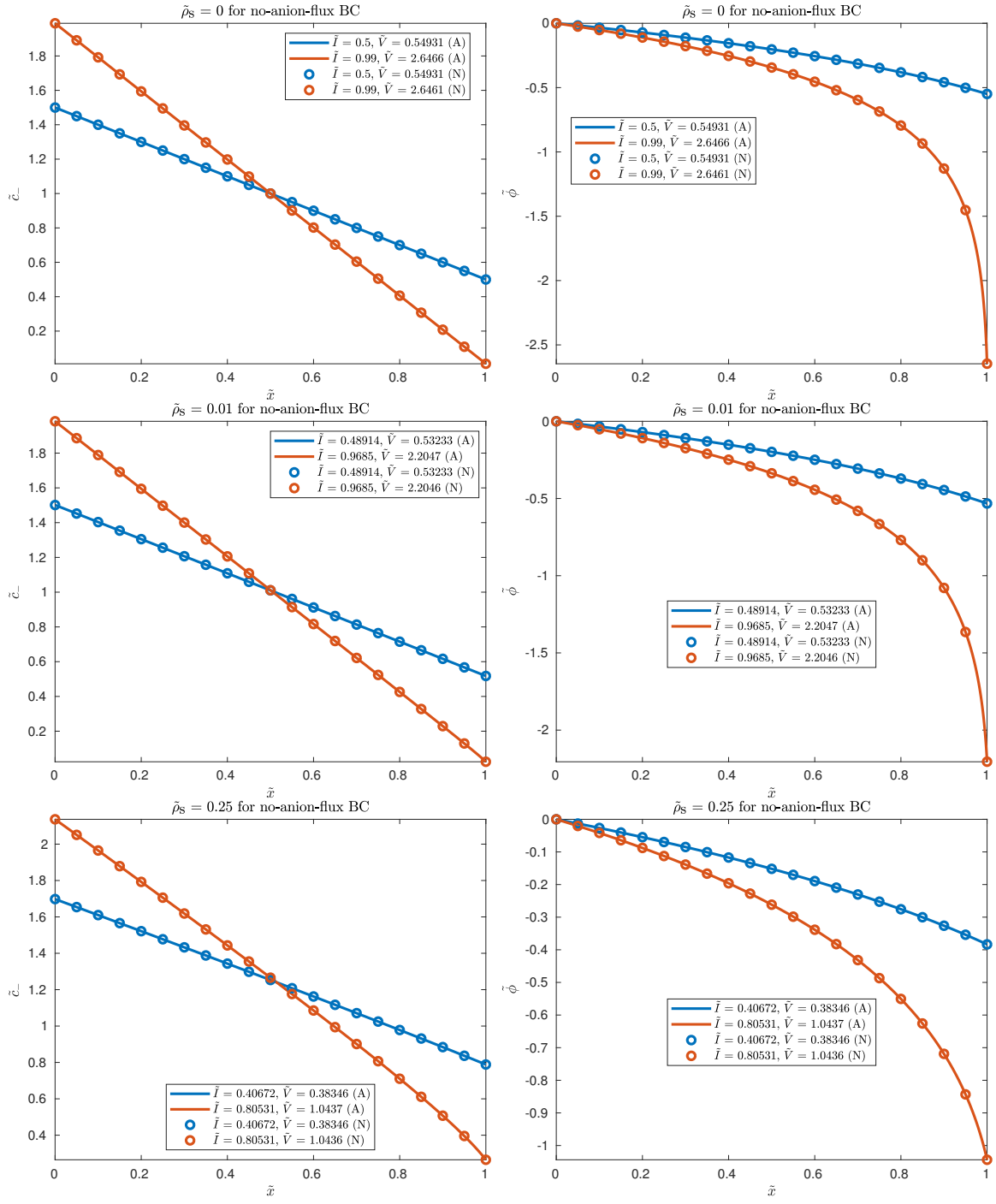

Figure 2-6: Plots of $\tilde{c}_-$ and $\tilde{\phi}$ against $\tilde{x}$ for 1) $\tilde{\rho}_s = 0$ and $\tilde{I} = 0.5, 0.99$ (top row) and 2) $\tilde{\rho}_s = 0.01, 0.25$ and $\tilde{I} = 0.5\tilde{I}_{\max}^{\text{NAF}}, 0.99\tilde{I}_{\max}^{\text{NAF}}$ (second and third rows) for no-anion-flux boundary condition at anode. (A) refers to analytical solutions and (N) refers to numerical solutions.

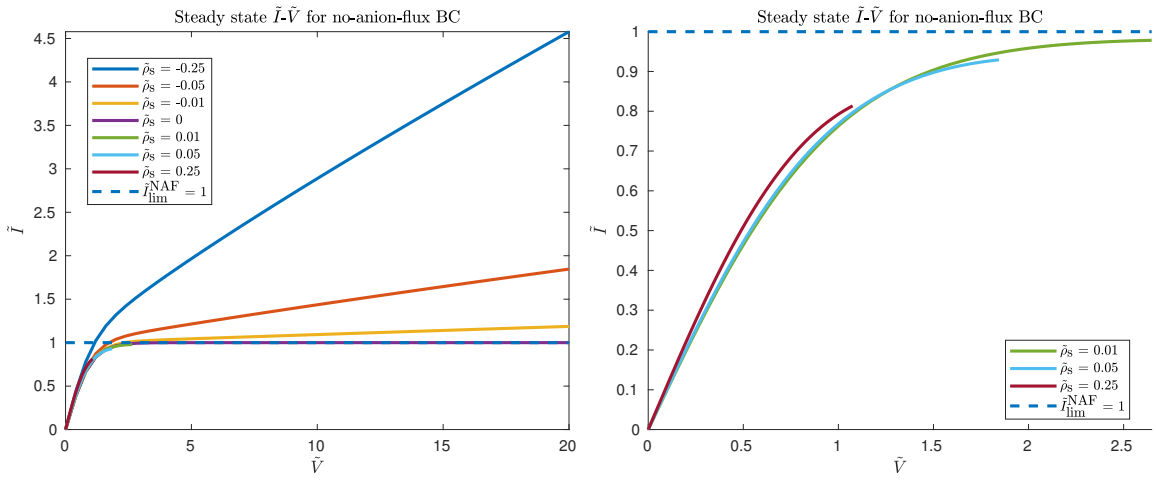

Figure 2-7: Left: steady state $\tilde{I}$-$\tilde{V}$ relations for $\tilde{\rho}_s = 0, \pm 0.01, \pm 0.05, \pm 0.25$ for no-anion-flux boundary condition at anode. Right: zoom-in view of left plot for only $\tilde{\rho}_s = 0.01, 0.05, 0.25$. The dashed line denotes $\tilde{I}_{lim}^{NAF} = 1$, which is the maximum $\tilde{I}$ that the system can reach when $\tilde{\rho}_s = 0$.

ary conditions with the boundary conditions given by Equations 2.26 and 2.28 that are used in cases 1 and 2. We define the electric potential difference across the electrolyte $\Delta\phi^{\text{electrolyte}} \equiv \phi(x = L) - \phi(x = 0)$ and the electric potential difference between the cathode and anode $\Delta\phi^{\text{electrode}} \equiv \phi_e^c - \phi_e^a = \Delta\phi^c + \Delta\phi^{\text{electrolyte}} - \Delta\phi^a = -V$ where the "a" and "c" superscripts denote the anode and cathode respectively. Experimentally, $\Delta\phi^{\text{electrode}}$, not $\Delta\phi^{\text{electrolyte}}$, is the quantity that we either impose under potentiostatic conditions or linear sweep voltammetry (LSV), or measure under galvanostatic conditions. The assumption we make in going from the Butler-Volmer boundary conditions to Equations 2.26 and 2.28 is $\Delta\phi^{\text{electrolyte}} \approx -V = \Delta\phi^{\text{electrode}}$. We expect this approximation to become better as $\left|\Delta\phi^{\text{electrode}}\right|$ increases. This is because a larger $\left|\Delta\phi^{\text{electrode}}\right|$ results in lower cation and anion concentrations at the cathode that in turn result in a larger electric field at the cathode to sustain the current. This larger electric field at the cathode implies a larger $\left|\Delta\phi^{\text{electrolyte}}\right|$, hence improving the approximation. Comparing cases 2 and 3, case 2 can be thought of as the limit of case 3 with $\text{Da} \to \infty$ or $\frac{J_F}{J_0} \to 0$, i.e., the reaction resistance tends to zero. Therefore, the expressions for limiting current, which is denoted as I_{lim}^{BV}, and overlimiting conductance are the same as that for case 2 given by Equations 2.48 and 2.50 respectively. The expression for overlimiting conductance is thus the same in all three cases regardless

of boundary conditions. The main advantage of using such an approximation is that we can replace the nonlinear Butler-Volmer boundary conditions with linear Dirichlet boundary conditions for ϕ, which have allowed us to derive an analytical expression for the steady state current-voltage relation in cases 1 and 2.

Unlike for cases 1 and 2, it is not possible to obtain an analytical expression for the steady state current-voltage relation for the nonlinear Butler-Volmer boundary conditions. However, at steady state, when compared to case 2, the governing ODEs (ordinary differential equations) in the domain remain unchanged. Moreover, the Butler-Volmer boundary conditions are functions of only concentrations and electric potentials but not functions of their higher order spatial derivatives. Therefore, when compared to case 2, for a given $\tilde{I}$ and $\tilde{\rho}_{\mathrm{s}}$, the $\tilde{c}_{-}$ profile remains unchanged while the $\tilde{\phi}$ profile is shifted downwards by a constant that allows the system to achieve the necessary overpotential for driving the appropriate amount of Faradaic current density at both electrodes. This constant is a function of $\tilde{I}$ and $\tilde{\rho}_{\mathrm{s}}$ and is computed using Equations 2.63 and 2.64 with MATLAB's `fsolve` or `fzero` function. Hence, we can obtain an analytical expression for $\tilde{c}_{-}$ and semi-analytical expressions for $\tilde{\phi}$ and steady state current-voltage relation. Regarding the steady state current-voltage relation, like in cases 1 and 2, there are no restrictions on how large V can be for $\rho_{\mathrm{s}} \leq 0$. For $\rho_{\mathrm{s}} > 0$, there are still no restrictions on the value of V. However, as $V \to \infty$, I tends to a finite maximum value, which is denoted as $I_{\mathrm{max}}^{\mathrm{BV}}$. For a given ρ_{s}, $I_{\mathrm{max}}^{\mathrm{BV}}$ is equal to $I_{\mathrm{max}}^{\mathrm{NAF}}$ at that ρ_{s} value because as $V \to \infty$, the overpotential diverges and the reaction resistance tends to zero.

We plot $\tilde{c}_{-}$ and $\tilde{\phi}$ as functions of $\tilde{x}$ for $\tilde{\rho}_{\mathrm{s}} = -0.01, -0.25$ in Figure 2-8 and $\tilde{\rho}_{\mathrm{s}} = 0.01, 0.25$ in Figure 2-9. For $\tilde{\rho}_{\mathrm{s}} = 0.01, 0.25$, we choose $\tilde{I} = 0.5\tilde{I}_{\mathrm{max}}^{\mathrm{BV}}, 0.99\tilde{I}_{\mathrm{max}}^{\mathrm{BV}}$ and for $\tilde{\rho}_{\mathrm{s}} = -0.01, -0.25$, we choose $\tilde{I} = 0.5, 1, 1.5$. As expected, the analytical and semi-analytical solutions agree very well with the numerical solutions. The features of the $\tilde{c}_{-}$-$\tilde{x}$ and $\tilde{\phi}$-$\tilde{x}$ plots are the same as that for case 2 except that for a particular $\tilde{I}$ and $\tilde{\rho}_{\mathrm{s}}$, $\tilde{V}$ is significantly larger than that for case 2 because additional electric potential differences and overpotentials are required to drive the Faradaic reactions at the electrodes. We also plot $\tilde{I}$ against $\tilde{V}$ for $\tilde{\rho}_{\mathrm{s}} = 0, \pm 0.01, \pm 0.05, \pm 0.25$ and $\tilde{V} \in [0, 20]$ in

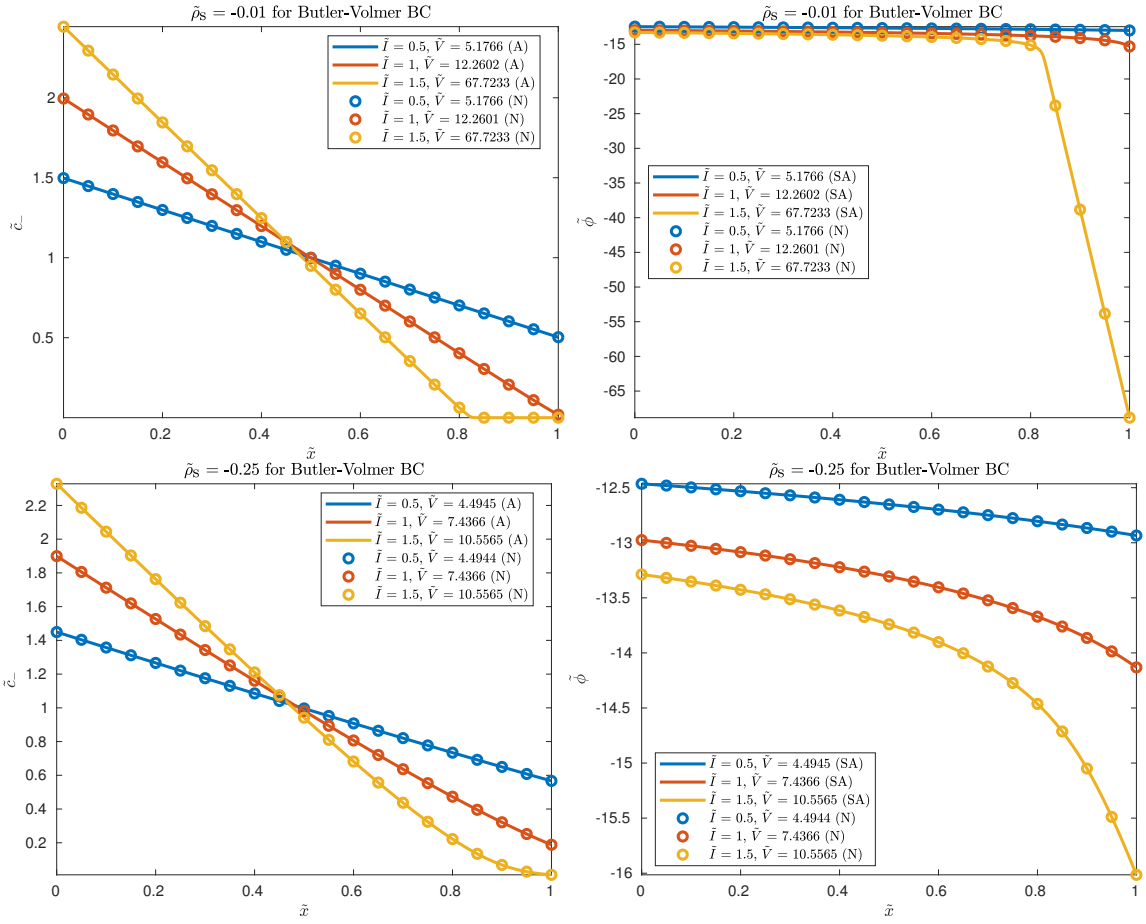

Figure 2-8: Plots of $\tilde{c}_-$ and $\tilde{\phi}$ against $\tilde{x}$ for $\tilde{\rho}_s = -0.01, -0.25$ and $\tilde{I} = 0.5, 1, 1.5$ for Butler-Volmer boundary conditions at anode and cathode. (A) refers to analytical solutions, (SA) refers to semi-analytical solutions and (N) refers to numerical solutions.

Figure 2-10. Regardless of $\tilde{\rho}_s$, we observe that the $\tilde{I}$-$\tilde{V}$ curve has a positive curvature at small $\tilde{V}$ because the system is reaction-limited and hence, Butler-Volmer reaction kinetics causes current to have an exponential dependence on voltage. At high $\tilde{V}$, the system becomes transport-limited in which surface conduction sustains OLC, therefore $\tilde{I}$ becomes linear in $\tilde{V}$ and the gradient of this linear relationship is equal to the overlimiting conductance.

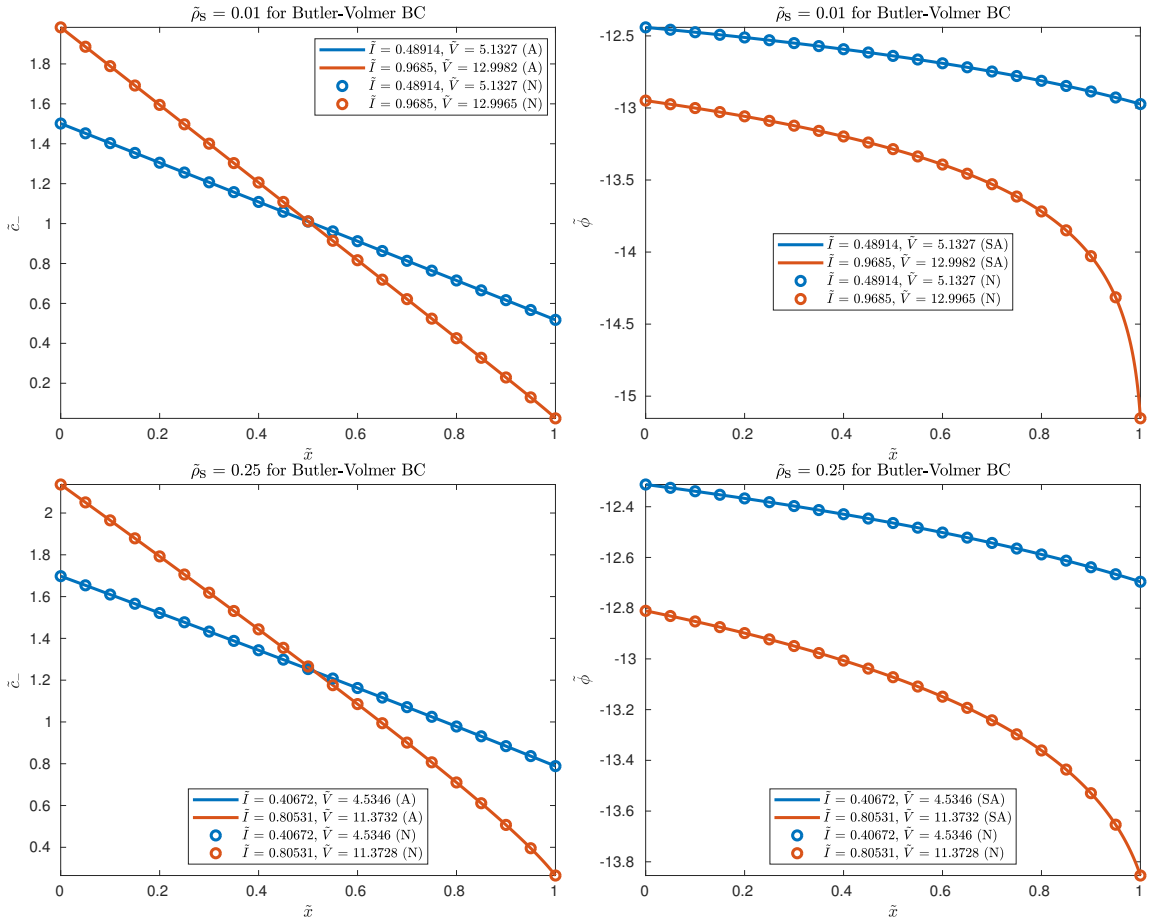

Figure 2-9: Plots of $\tilde{c}_-$ and $\tilde{\phi}$ against $\tilde{x}$ for $\tilde{\rho}_s = 0.01, 0.25$ and $\tilde{I} = 0.5\tilde{I}^{BV}_{max}, 0.99\tilde{I}^{BV}_{max}$ for Butler-Volmer boundary conditions at anode and cathode. (A) refers to analytical solutions, (SA) refers to semi-analytical solutions and (N) refers to numerical solutions.

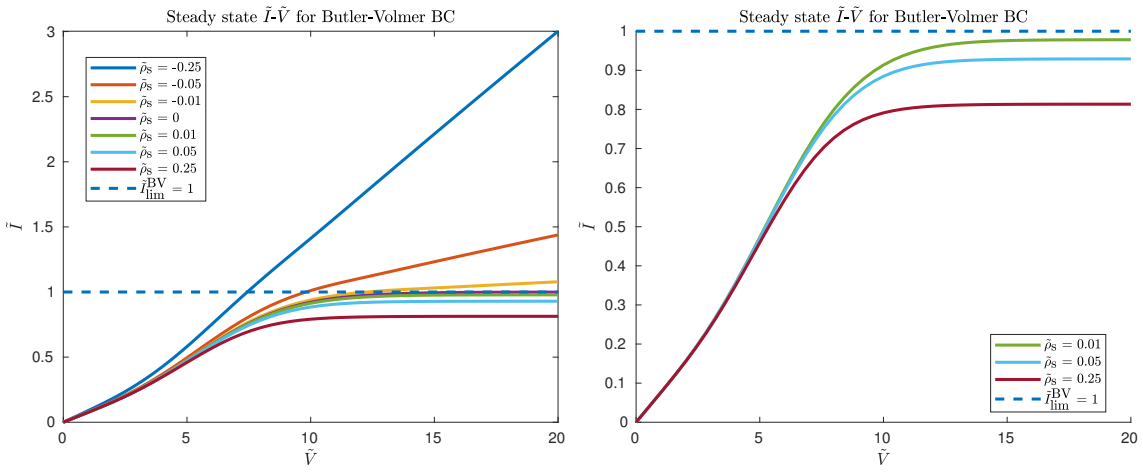

Figure 2-10: Left: steady state $\tilde{I}$-$\tilde{V}$ relations for $\tilde{\rho}_s = 0, \pm 0.01, \pm 0.05, \pm 0.25$ for Butler-Volmer boundary conditions at anode and cathode. Right: zoom-in view of left plot for only $\tilde{\rho}_s = 0.01, 0.05, 0.25$. The dashed line denotes $\tilde{I}_{lim}^{BV} = 1$, which is the maximum $\tilde{I}$ that the system can reach when $\tilde{\rho}_s = 0$.

2.5.3 Copper electrodeposition and electrodissolution in AAO, CN and PE membranes

Experimental steady state current-voltage relations are typically obtained using linear sweep voltammetry (LSV) with a sufficiently slow sweep rate. Using the steady state current-voltage relation for Butler-Volmer boundary conditions in Section 2.5.2.3, we perform nonlinear least squares fitting on the experimental datasets for copper electrodeposition and electrodissolution in charged nanoporous AAO [105], CN [106] and PE [106] membranes to demonstrate the usefulness of such a relation for extracting best-fit parameter values. We first use these best-fit parameter values to implement time-dependent LSV numerical simulations at various sweep rates to verify if the experimental sweep rate used is sufficiently slow for measuring quasisteady current-voltage relations. We then use these best-fit parameter values for computing steady state current-voltage relations and time-dependent LSV numerical simulations to see how well they compare with the experimental datasets. We also estimate the experimental overlimiting conductances for negatively charged membranes and compare them with the steady state overlimiting conductances that are computed using Equation 2.50.

Table 2.2: Geometrical parameters for AAO, CN and PE membranes. Values are based on product specifications.

Parameter	AAO membranes	CN membranes	PE membranes
r_p / nm	175 (mean of $150-200$)	125 (mean of $100-150$)	25
L / μm	60	130	20
r_e / mm	6	6.5	6.5

The AAO membranes used in [105] have parallel straight cylindrical pores with the same length and a constant pore radius, therefore the assumptions that ϵ_p, τ, a_p and h_p are uniform and constant are reasonable. Denoting the pore radius as r_p, we obtain $h_\mathrm{p} = \frac{\epsilon_\mathrm{p}}{a_\mathrm{p}} = \frac{r_\mathrm{p}}{2}$. In [105], boric acid ($H_3BO_3$) is added to reduce the rate of hydrogen evolution at high voltages by increasing the overpotential needed to do so [111]. We assume that boric acid is inert and does not dissociate at all, so the electrolyte consists of only Cu^{2+} and SO_4^{2-} ions. The CN and PE membranes used in [106] are random porous media with well connected pores, in contrast to the ordered AAO membranes that are a massively parallel network of non-intersecting straight cylindrical pores. In the absence of detailed geometrical information, we approximate $h_\mathrm{p} \approx \frac{r_\mathrm{p}}{2}$. In both [105] and [106], the electrolyte used is copper(II) sulfate ($CuSO_4$) and the electrodes used are circular with a radius r_e, therefore $A = \pi r_\mathrm{e}^2$ where A is the total surface area of the anode or cathode. The geometrical parameters r_p, L and r_e for AAO, CN and PE membranes are given in Table 2.2. In Table 2.3, we label all the experimental datasets in [105] and [106] based on the membrane identity (AAO, CN or PE), sign of membrane charge, sweep rate β_LSV and electrolyte concentration c_0.

The exchange current densities and charge transfer coefficients are generally sensitive to experimental conditions such as the method of electrode preparation and electrode surface roughness. There are also no estimates for the surface charge densities of the polyelectrolyte multilayers used in [105, 106]. Using tortuosities that deviate from the Bruggeman relation is not uncommon in porous membranes such as the porous separators used in batteries [240]. In our case, for the CN and PE membranes, which are polymeric porous separators commonly used in lithium-ion

Table 2.3: Dataset labels (first three columns) and fitted parameter values (last five columns) for AAO, CN and PE membranes.

Label	β_{LSV} / mV s^{-1}	c_0 / mM	σ_{s} / e nm^{-2}	τ	J_0^{ref} / mA cm^{-2}	α_1	ϵ_{p}
$\mathrm{AAO}_1(-)$	-1	10	-0.591	1.00 (fixed)	1.65	1.00	0.500
$\mathrm{AAO}_1(+)$	-1	10	1.63	1.00 (fixed)	2.76	0.750	0.375
$\mathrm{AAO}_2(-)$	-10	100	-0.517	1.00 (fixed)	4.90	1.00	0.443
$\mathrm{AAO}_2(+)$	-10	100	2.64	1.00 (fixed)	4.59	0.650	0.400
$\mathrm{CN}_1(-)$	-1	10	-0.0723	1.83	14.4	0.287	0.803
$\mathrm{CN}_1(+)$	-1	10	0.617	1.91	13.0	0.845	0.664
$\mathrm{CN}_2(-)$	-10	100	-0.0478	2.11	16.6	0.612	0.684
$\mathrm{CN}_2(+)$	-10	100	1.78	2.07	5.20	0.985	0.761
PE$(-)$	-2	10	-0.0549	5.44	6.15	0.995	0.409
PE$(+)$	-2	10	0.0752	7.84	0.500	0.918	0.470

batteries [277], tortuosity can be used as a fitting parameter. The membrane porosities are also typically specified as a range and may not be known with certainty. Therefore, when using the steady state current-voltage relation for Butler-Volmer boundary conditions to perform nonlinear least squares fitting on the experimental datasets, we pick $\tilde{\rho}_{\mathrm{s}}$, τ (only for CN and PE membranes; fixed at 1 for AAO membranes), $\tilde{J}_0^{\mathrm{ref}}$, α_1 and ϵ_{p} as fitting parameters. This nonlinear least squares fitting is carried out using MATLAB's `lsqnonlin` function and the initial guesses and lower and upper bounds for the fitting parameters are given in Table 2.6 in Appendix 2.8.4. All parameters that are not fitting parameters or given in Table 2.2 are taken from Table 2.1. The fitted parameter values that are obtained for all the experimental datasets are given in Table 2.3; for $\tilde{\rho}_{\mathrm{s}}$ and $\tilde{J}_0^{\mathrm{ref}}$, we report their dimensional values σ_{s} and J_0^{ref} respectively.

Experimentally, to generate the steady state current-voltage relations in a reasonable amount of time, linear sweep voltammetry (LSV) with a sufficiently slow sweep rate is used. Therefore, we would like to first use numerical simulations to determine if the sweep rate used in experiments is slow enough for the experimental current-voltage relations to accurately approximate the true steady state ones. For datasets $\mathrm{AAO}_1(+/-)$, a sweep rate of -1 mV/s is used. To determine if this sweep rate is sufficiently slow, in our numerical simulations, we pick $\beta_{\mathrm{LSV}} = -10^3$ mV/s, -10^2 mV/s, -1 mV/s. We also plot the semi-analytical steady state current-voltage relations for case 3 discussed in Section 2.5.2.3 and the experimental current-

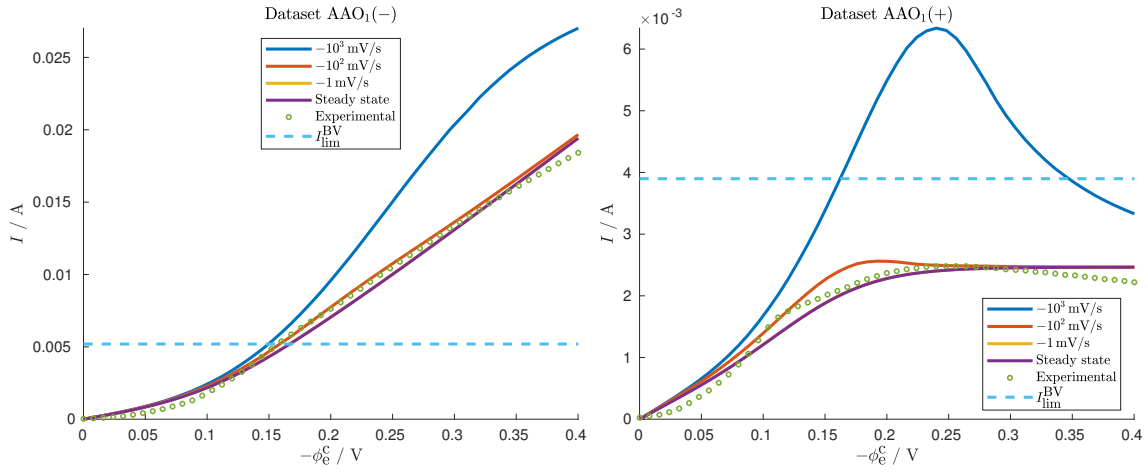

Figure 2-11: Numerical current-voltage relations obtained by linear sweep voltammetry with $\beta_{\text{LSV}} = -10^3\,\text{mV/s}, -10^2\,\text{mV/s}, -1\,\text{mV/s}$ for copper electrodeposition and electrodissolution from copper(II) sulfate ($CuSO_4$) for datasets $AAO_1(+/-)$. Steady state and experimental current-voltage relations are also plotted. $-\phi_{\text{e}}^{\text{c}}$ is the negative of the cathode electric potential while I is the current. Note that the lines for $\beta_{\text{LSV}} = -1\,\text{mV/s}$ and steady state overlap.

voltage relations in Figure 2-11. Figure 2-11 shows that the current-voltage relations for $\beta_{\text{LSV}} = -1\,\text{mV/s}$ are almost identical with the steady state current-voltage relations, and both agree reasonably well with the experimental current-voltage relations. Therefore, we conclude that the sweep rate of $-1\,\text{mV/s}$ used experimentally is sufficiently slow. On the other hand, the sweep rates of $-10^3\,\text{mV/s}$ and $-10^2\,\text{mV/s}$ are too fast because at every value of $-\phi_{\text{e}}^{\text{c}}$, they result in currents that are significantly larger than their corresponding steady state and experimental values. In particular, for dataset $AAO_1(+)$, the current significantly overshoots the limiting current $I_{\text{lim}}^{\text{BV}}$, which is caused by diffusion limitation as the time scale for the voltammetry is smaller than the diffusion time scale [167, 266].

Using the fitted parameter values in Table 2.3, we compute the steady state current-voltage relations for case 3 described in Section 2.5.2.3 and also perform time-dependent LSV numerical simulations. We plot and compare both sets of current-voltage relations with the experimental datasets in Figure 2-12. Note that although the nonlinear least squares fitting is performed on full experimental datasets, these datasets have too many data points to be plotted clearly. Therefore, we only plot 51

points per dataset in Figure 2-12. Generally, the steady state and numerical current-voltage relations agree well with the experimental ones, therefore demonstrating the usefulness of the steady state current-voltage relation for case 3 in Section 2.5.2.3 for extracting important best-fit parameters such as σ_s, which may be difficult to measure directly in experiments. In addition, the generally close agreement of the steady state current-voltage relations with the experimental and numerical ones indicates that the experimental sweep rates used are slow enough to generate quasi-steady current-voltage relations. For datasets PE(+/−), the current bumps at around $-\phi_e^c = 0.2\,\mathrm{V}$ cannot be captured by the steady state and numerical current-voltage relations. In the context of our model, these current bumps are not caused by an overly fast sweep rate because the steady state current-voltage relation agrees very well with the numerical one. Instead, they are probably caused by unaccounted side reactions that contribute a current peak at $-\phi_e^c = 0.2\,\mathrm{V}$ that can for example be described by the "modified" Randles-Sevcik equation given by Equation 33 of [266].

For negatively charged membranes, the experimental current-voltage relations become approximately linear above a cutoff potential and the gradient of this line is the overlimiting conductance. Therefore, using MATLAB's `polyfit` function, we can estimate the experimental overlimiting conductance σ_{OLC} by performing a linear fit of the linear portion of the experimental current-voltage relation. We also compute the steady state overlimiting conductance given by Equation 2.50. We tabulate all the cutoff potentials and experimental and steady state overlimiting conductances in Table 2.4. Generally, the experimental overlimiting conductances agree well with the steady state ones, showing that the nonlinear least squares fitting procedure accurately fits the linear portions of the experimental current-voltage relations.

2.6 Conclusion

We have coupled transport described by the leaky membrane model, which is capable of predicting OLC, with Butler-Volmer boundary conditions and studied the resulting model at steady state in order to derive analytical and semi-analytical expressions

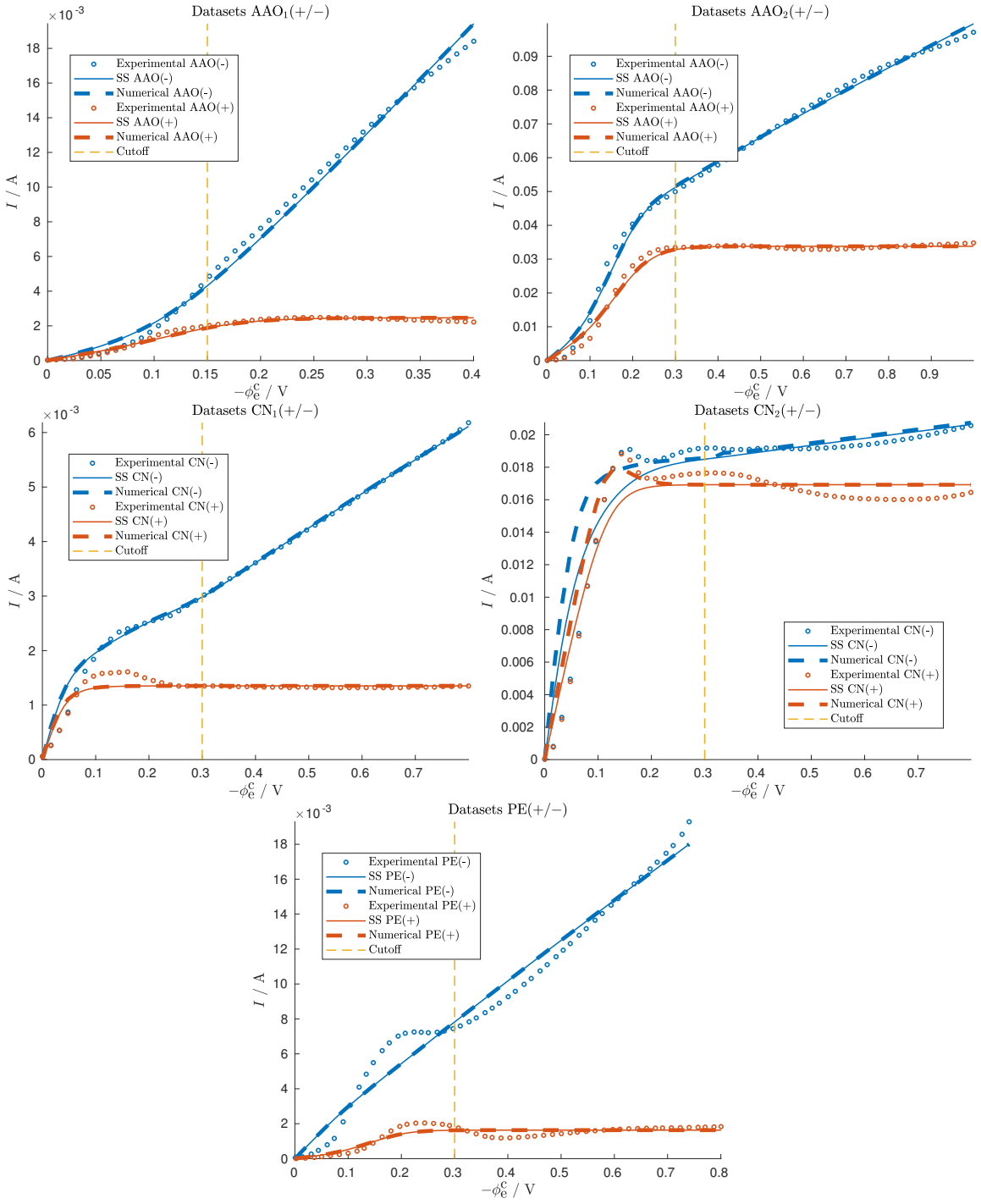

Figure 2-12: Current-voltage relations for copper electrodeposition and electrodissolution from copper(II) sulfate ($CuSO_4$) in different charged nanoporous media. $-\phi_e^c$ is the negative of the cathode electric potential while I is the current. (-) and (+) refer to negatively and positively charged membranes respectively. SS stands for steady state and the cutoff line indicates the cutoff potential for estimating overlimiting conductance.

Table 2.4: Cutoff potentials and overlimiting conductances for all negatively charged membranes.

Dataset	Cutoff potential / V	Experimental σ_{OLC} / Ω^{-1}	Steady state σ_{OLC} / Ω^{-1}
$\mathrm{AAO}_1(-)$	0.15	0.0553	0.0567
$\mathrm{AAO}_2(-)$	0.3	0.0685	0.0439
$\mathrm{CN}_1(-)$	0.3	0.00630	0.00461
$\mathrm{CN}_2(-)$	0.3	0.00261	0.00225
PE$(-)$	0.3	0.0268	0.0195

for quantities of interest, namely concentration profiles, electric potential profiles, current-voltage relations and overlimiting conductances. These results generalize the ones in [77, 76, 241] to a binary electrolyte that is asymmetric with unequal diffusivities and to Butler-Volmer boundary conditions. We have also analyzed linear sweep voltammetry with the model, building on the work of Yan et al [266], and validated its predictions against experimental data for copper electrodeposition in a variety of charged nanoporous media, with reasonable agreement for a simple, analytically tractable model.

Throughout the paper, we have assumed concentration-independent diffusivities, but this is generally not the case in concentrated solutions, where Stefan-Maxwell coupled fluxes and concentration-dependent activity coefficients contribute to the effective diffusion process [172]. Even the most basic concentration dependence of the Debye-Hückel theory for dilute-solution activity, or its generalization to concentrated solutions [220], can significantly affect the steady state concentration and electric potential profiles, as well as the current-voltage relation, in a leaky membrane [76]. It would be interesting in future work to analyze how such effects couple with the highly nonlinear Butler-Volmer boundary conditions. In addition, copper(II) sulfate and boric acid, which is commonly added to suppress hydrogen evolution at high voltages, are slightly acidic, thus it is possible that charge regulation and pH changes provide additional conductivity [6]. We have also used the simplest reaction model for copper electro-deposition/dissolution, but more sophisticated reaction models do not assume any rate-determining step and take into account additional phenomena such as the adsorption of copper(I) ions on the electrode surface [113, 133, 114]. Using these

models may help with achieving better predictions for the current-voltage relation, especially at low voltages when the system is reaction-limited. We have assumed that macroscopic electroneutrality holds when the coion concentration is depleted at a current higher than its diffusion-limited value. In a free solution, above the diffusion-limited current, macroscopic electroneutrality does not hold and the electric double layers are no longer at equilibrium [29, 66]. A more detailed analysis of the structure of the electric double layers above the diffusion-limited current in charged porous media would be useful for determining if the assumption of macroscopic electroneutrality is valid at such a current.

2.7 Acknowledgments

E. Khoo acknowledges support from the National Science Scholarship (PhD) funded by Agency for Science, Technology and Research, Singapore (A*STAR). We acknowledge J.-H. Han and M. Wang for providing the raw experimental datasets, H. Zhao and K. M. Conforti for useful suggestions regarding data visualization, J. Song for discussion regarding the Lambert W function and P. M. Biesheuvel for helpful comments on the manuscript.

2.8 Appendix

2.8.1 Symbols for variables, parameters and constants.

Table 2.5 lists the symbols for variables, parameters and constants used throughout the paper.

2.8.2 Construction of steady state equations for use in MATLAB

Throughout this section, we use dimensionless variables. To avoid cluttering the notation, we drop tildes on all dimensionless variables and the $-$ subscript on $\tilde{c}_-$.

Table 2.5: Symbols for variables, parameters and constants. ± subscript refers to cation and anion and TS stands for transition state.

Symbol	Variable / Parameter / Constant
$a_\pm$	Ion activity
a_p	Internal pore surface area/volume ratio
c	Neutral salt bulk concentration
$c_\pm$	Ion concentration
$c_\pm^\Theta$	Ion standard concentration
$\hat{c}_\pm$	Ion concentration normalized by standard concentration
$D_\pm^\mathrm{m}$	Ion molecular (free solution) tracer diffusivity
$D_{\pm 0}$	Ion macroscopic tracer diffusivity in dilute limit
$D_{\pm 0}^\mathrm{m}$	Ion molecular (free solution) tracer diffusivity in dilute limit
Da	Damköhler number
E^Θ	Standard electrode potential
$F_\pm$	Ion diffusional molar flux
h_p	Effective pore size
I	Current
J	Current density
J_0	Exchange current density
J_F	Faradaic current density
k_B	Boltzmann constant
M_m	Atomic mass of solid metal and electroactive cations
$\hat{n}$	Unit normal pointing outwards from electrolyte
r	Position vector
$r_\mathrm{m}^\mathrm{a,c}$	Position of anode/electrolyte or cathode/electrolyte interface
T	Temperature
$z_\pm$	Ion charge number
α	Charge transfer coefficient
$\gamma_\pm$	Ion activity coefficient
$\gamma_\ddagger^\mathrm{r}$	Activity coefficient of TS for Faradaic reaction
$\gamma_{\ddagger,\pm}^\mathrm{d}$	Activity coefficient of TS for activated diffusion of ion
ϵ_p	Porosity
η	Overpotential
$\mu_\pm$	Ion electrochemical potential
$\mu_\pm^\Theta$	Ion standard electrochemical potential
$\nu_\pm$	Subscript of ion in chemical formula of neutral salt
ρ_m	Mass density of solid metal
ρ_s	Volume-averaged background charge density
σ_s	Pore surface charge/area ratio
τ	Tortuosity
ϕ	Electrolyte electric potential
ϕ_e	Electrode electric potential
Ω_m	Atomic volume of solid metal

MATLAB's `bvp4c` function solves boundary value problems of the form

$$\frac{\mathrm{d}y}{\mathrm{d}x} = f(x, y, p), \quad y_{\mathrm{BC}} = 0, \tag{2.65}$$

where x is the scalar independent variable, y is the vector of dependent variables, p is the vector of parameters, f is the vector function relating $\frac{\mathrm{d}y}{\mathrm{d}x}$ to x, y and p, and y_{BC} is the vector of boundary conditions. Different boundary conditions result in different expressions for y, p, f and y_{BC}. Throughout this section, we use primes to denote derivatives taken with respect to x. We first provide the expression for J, which will be used throughout the section:

$$J = \beta_{\mathrm{D}}[(D_{-0} - D_{+0})c' - (z_+ D_{+0} - z_- D_{-0})c\phi' + z_+ D_{+0}\rho_{\mathrm{s}}\phi'], \tag{2.66}$$

$$\beta_{\mathrm{D}} = -\frac{z_- D_{-0}}{2(z_+ D_{+0} - z_- D_{-0})}. \tag{2.67}$$

2.8.2.1 Case 1: reservoir boundary condition at anode

p is not required and y and f are given by:

$$y = \begin{bmatrix} c \\ c' \\ \phi \\ \phi' \end{bmatrix}, \tag{2.68}$$

$$f = \begin{bmatrix} c' \\ c'' \\ \phi' \\ \phi'' \end{bmatrix} = \begin{bmatrix} c' \\ \frac{z_+ z_- \rho_{\mathrm{s}} c'\phi'}{(z_+ - z_-)c - z_+\rho_{\mathrm{s}}} \\ \phi' \\ -\frac{(z_+ - z_-)c'\phi'}{(z_+ - z_-)c - z_+\rho_{\mathrm{s}}} \end{bmatrix}. \tag{2.69}$$

For galvanostatic conditions where we impose $J(x=1) = I_{\text{applied}}$,

$$y_{\text{BC}} = \begin{bmatrix} c(x=0) - \beta_1 \\ \phi(x=0) \\ c' + z_- c\phi'|_{x=1} \\ I_{\text{applied}} - J(x=1) \end{bmatrix}, \tag{2.70}$$

while for potentiostatic conditions where we impose $\phi(x=1) = -V$,

$$y_{\text{BC}} = \begin{bmatrix} c(x=0) - \beta_1 \\ \phi(x=0) \\ c' + z_- c\phi'|_{x=1} \\ \phi(x=1) + V \end{bmatrix}. \tag{2.71}$$

2.8.2.2 Case 2: no-anion-flux boundary condition at anode

We need to add a new variable to y that enforces the integral constraint for the conservation of the number of anions. This variable is simply called y_5 as it is the 5th element of y. p is not required and y and f are given by:

$$y = \begin{bmatrix} c \\ c' \\ \phi \\ \phi' \\ y_5 \end{bmatrix}, \tag{2.72}$$

$$f = \begin{bmatrix} c' \\ c'' \\ \phi' \\ \phi'' \\ c \end{bmatrix} = \begin{bmatrix} c' \\ \frac{z_+ z_- \rho_{\text{s}} c'\phi'}{(z_+ - z_-)c - z_+ \rho_{\text{s}}} \\ \phi' \\ -\frac{(z_+ - z_-)c'\phi'}{(z_+ - z_-)c - z_+ \rho_{\text{s}}} \\ c \end{bmatrix}. \tag{2.73}$$

For galvanostatic conditions where we impose $J(x=1) = I_{\text{applied}}$,

$$y_{\text{BC}} = \begin{bmatrix} y_5(x=0) \\ \phi(x=0) \\ c' + z_- c\phi'|_{x=1} \\ I_{\text{applied}} - J(x=1) \\ y_5(x=1) - \beta_1 \end{bmatrix}, \tag{2.74}$$

while for potentiostatic conditions where we impose $\phi(x=1) = -V$,

$$y_{\text{BC}} = \begin{bmatrix} y_5(x=0) \\ \phi(x=0) \\ c' + z_- c\phi'|_{x=1} \\ \phi(x=1) + V \\ y_5(x=1) - \beta_1 \end{bmatrix}. \tag{2.75}$$

2.8.2.3 Case 3: Butler-Volmer boundary conditions at anode and cathode

Like in case 2, we need to add a new variable to y, which is called y_5, that enforces the integral constraint for the conservation of the number of anions. p is needed for galvanostatic conditions where we impose $J(x=1) = I_{\text{applied}}$ in order to find V (recall that $\phi_{\text{e}}^{\text{c}} = -V$) while p is not required for potentiostatic conditions where we impose

$\phi_{\mathrm{e}}^{\mathrm{c}} = -V$. y and f are given by:

$$y = \begin{bmatrix} c \\ c' \\ \phi \\ \phi' \\ y_5 \end{bmatrix}, \tag{2.76}$$

$$f = \begin{bmatrix} c' \\ c'' \\ \phi' \\ \phi'' \\ c \end{bmatrix} = \begin{bmatrix} c' \\ \frac{z_+ z_- \rho_{\mathrm{s}} c' \phi'}{(z_+ - z_-)c - z_+ \rho_{\mathrm{s}}} \\ \phi' \\ -\frac{(z_+ - z_-)c' \phi'}{(z_+ - z_-)c - z_+ \rho_{\mathrm{s}}} \\ c \end{bmatrix}. \tag{2.77}$$

For galvanostatic conditions where we impose $J(x = 1) = I_{\mathrm{applied}}$,

$$p = V, \tag{2.78}$$

$$y_{\mathrm{BC}} = \begin{bmatrix} y_5(x = 0) \\ J(x = 0) + J_{\mathrm{F}}^{\mathrm{a}} \\ c' + z_- c \phi' \big|_{x=1} \\ -J(x = 1) + J_{\mathrm{F}}^{\mathrm{c}} \\ y_5(x = 1) - \beta_1 \\ I_{\mathrm{applied}} - J(x = 1) \end{bmatrix}, \tag{2.79}$$

while for potentiostatic conditions where we impose $\phi_{\mathrm{e}}^{\mathrm{c}} = -V$,

$$y_{\mathrm{BC}} = \begin{bmatrix} y_5(x = 0) \\ J(x = 0) + J_{\mathrm{F}}^{\mathrm{a}} \\ c' + z_- c \phi' \big|_{x=1} \\ -J(x = 1) + J_{\mathrm{F}}^{\mathrm{c}} \\ y_5(x = 1) - \beta_1 \end{bmatrix}. \tag{2.80}$$

2.8.3 Jacobians for steady state equations

To increase convergence speed, we provide Jacobians to the `bvp4c` function. There are two types of Jacobians we can provide: 1) partial derivatives of f with respect to y and p ($\frac{\partial f}{\partial y}$ and $\frac{\partial f}{\partial p}$), and 2) partial derivatives of y_{BC} with respect to $y(x=0)$, $y(x=1)$ and p ($\frac{\partial y_{\mathrm{BC}}}{\partial y(x=0)}$, $\frac{\partial y_{\mathrm{BC}}}{\partial y(x=1)}$ and $\frac{\partial y_{\mathrm{BC}}}{\partial p}$). For simplicity, the elements of f, y, y_{BC},

$y(x=0)$ and $y(x=1)$ are written as:

$$f = \begin{bmatrix} f_1 \\ f_2 \\ f_3 \\ f_4 \end{bmatrix} \quad \text{or} \quad \begin{bmatrix} f_1 \\ f_2 \\ f_3 \\ f_4 \\ f_5 \end{bmatrix}, \tag{2.81}$$

$$y = \begin{bmatrix} y_1 \\ y_2 \\ y_3 \\ y_4 \end{bmatrix} \quad \text{or} \quad \begin{bmatrix} y_1 \\ y_2 \\ y_3 \\ y_4 \\ y_5 \end{bmatrix}, \tag{2.82}$$

$$y_{\text{BC}} = \begin{bmatrix} y_{\text{BC},1} \\ y_{\text{BC},2} \\ y_{\text{BC},3} \\ y_{\text{BC},4} \end{bmatrix} \quad \text{or} \quad \begin{bmatrix} y_{\text{BC},1} \\ y_{\text{BC},2} \\ y_{\text{BC},3} \\ y_{\text{BC},4} \\ y_{\text{BC},5} \end{bmatrix} \quad \text{or} \quad \begin{bmatrix} y_{\text{BC},1} \\ y_{\text{BC},2} \\ y_{\text{BC},3} \\ y_{\text{BC},4} \\ y_{\text{BC},5} \\ y_{\text{BC},6} \end{bmatrix}, \tag{2.83}$$

$$y(x=0) = \begin{bmatrix} y_{0,1} \\ y_{0,2} \\ y_{0,3} \\ y_{0,4} \end{bmatrix} \quad \text{or} \quad \begin{bmatrix} y_{0,1} \\ y_{0,2} \\ y_{0,3} \\ y_{0,4} \\ y_{0,5} \end{bmatrix}, \tag{2.84}$$

$$y(x=1) = \begin{bmatrix} y_{1,1} \\ y_{1,2} \\ y_{1,3} \\ y_{1,4} \end{bmatrix} \quad \text{or} \quad \begin{bmatrix} y_{1,1} \\ y_{1,2} \\ y_{1,3} \\ y_{1,4} \\ y_{1,5} \end{bmatrix}. \tag{2.85}$$

2.8.3.1 Case 1: reservoir boundary condition at anode

The nonzero elements of the $\frac{\partial f}{\partial y}$ Jacobian $\in \mathbb{R}^{4\times 4}$ are given by:

$$\frac{\partial f_1}{\partial y_2} = 1, \tag{2.86}$$

$$\frac{\partial f_2}{\partial y_1} = -\frac{(z_+ - z_-)z_+ z_- \rho_s c' \phi'}{\left[(z_+ - z_-)c - z_+\rho_s\right]^2}, \tag{2.87}$$

$$\frac{\partial f_2}{\partial y_2} = \frac{z_+ z_- \rho_s \phi'}{(z_+ - z_-)c - z_+\rho_s}, \tag{2.88}$$

$$\frac{\partial f_2}{\partial y_4} = \frac{z_+ z_- \rho_s c'}{(z_+ - z_-)c - z_+\rho_s}, \tag{2.89}$$

$$\frac{\partial f_3}{\partial y_4} = 1, \tag{2.90}$$

$$\frac{\partial f_4}{\partial y_1} = \frac{(z_+ - z_-)^2 c' \phi'}{\left[(z_+ - z_-)c - z_+\rho_s\right]^2}, \tag{2.91}$$

$$\frac{\partial f_4}{\partial y_2} = -\frac{(z_+ - z_-)\phi'}{(z_+ - z_-)c - z_+\rho_s}, \tag{2.92}$$

$$\frac{\partial f_4}{\partial y_4} = -\frac{(z_+ - z_-)c'}{(z_+ - z_-)c - z_+\rho_s}. \tag{2.93}$$

The nonzero elements of the $\frac{\partial y_{BC}}{\partial y(x=0)}$ Jacobian $\in \mathbb{R}^{4\times 4}$ are given by:

$$\frac{\partial y_{BC,1}}{\partial y_{0,1}} = 1, \tag{2.94}$$

$$\frac{\partial y_{BC,2}}{\partial y_{0,3}} = 1. \tag{2.95}$$

For galvanostatic conditions, the nonzero elements of the $\frac{\partial y_{\mathrm{BC}}}{\partial y(x=1)}$ Jacobian $\in \mathbb{R}^{4\times 4}$ are given by

$$\frac{\partial y_{\mathrm{BC},3}}{\partial y_{1,1}} = z_- \phi'(x=1), \tag{2.96}$$

$$\frac{\partial y_{\mathrm{BC},3}}{\partial y_{1,2}} = 1, \tag{2.97}$$

$$\frac{\partial y_{\mathrm{BC},3}}{\partial y_{1,4}} = z_- c(x=1), \tag{2.98}$$

$$\frac{\partial y_{\mathrm{BC},4}}{\partial y_{1,1}} = \beta_{\mathrm{D}}(z_+ D_{+0} - z_- D_{-0})\phi'(x=1), \tag{2.99}$$

$$\frac{\partial y_{\mathrm{BC},4}}{\partial y_{1,2}} = -\beta_{\mathrm{D}}(D_{-0} - D_{+0}), \tag{2.100}$$

$$\frac{\partial y_{\mathrm{BC},4}}{\partial y_{1,4}} = -\beta_{\mathrm{D}}[-(z_+ D_{+0} - z_- D_{-0})c(x=1) + z_+ D_{+0}\rho_{\mathrm{s}}], \tag{2.101}$$

while for potentiostatic conditions, the nonzero elements of the $\frac{\partial y_{\mathrm{BC}}}{\partial y(x=1)}$ Jacobian $\in \mathbb{R}^{4\times 4}$ are given by

$$\frac{\partial y_{\mathrm{BC},3}}{\partial y_{1,1}} = z_- \phi'(x=1), \tag{2.102}$$

$$\frac{\partial y_{\mathrm{BC},3}}{\partial y_{1,2}} = 1, \tag{2.103}$$

$$\frac{\partial y_{\mathrm{BC},3}}{\partial y_{1,4}} = z_- c(x=1), \tag{2.104}$$

$$\frac{\partial y_{\mathrm{BC},4}}{\partial y_{1,3}} = 1. \tag{2.105}$$

2.8.3.2 Case 2: no-anion-flux boundary condition at anode

The nonzero elements of the $\frac{\partial f}{\partial y}$ Jacobian $\in \mathbb{R}^{5\times 5}$ are given by:

$$\frac{\partial f_1}{\partial y_2} = 1, \tag{2.106}$$

$$\frac{\partial f_2}{\partial y_1} = -\frac{(z_+ - z_-)z_+ z_- \rho_s c' \phi'}{\left[(z_+ - z_-)c - z_+\rho_s\right]^2}, \tag{2.107}$$

$$\frac{\partial f_2}{\partial y_2} = \frac{z_+ z_- \rho_s \phi'}{(z_+ - z_-)c - z_+\rho_s}, \tag{2.108}$$

$$\frac{\partial f_2}{\partial y_4} = \frac{z_+ z_- \rho_s c'}{(z_+ - z_-)c - z_+\rho_s}, \tag{2.109}$$

$$\frac{\partial f_3}{\partial y_4} = 1, \tag{2.110}$$

$$\frac{\partial f_4}{\partial y_1} = \frac{(z_+ - z_-)^2 c' \phi'}{\left[(z_+ - z_-)c - z_+\rho_s\right]^2}, \tag{2.111}$$

$$\frac{\partial f_4}{\partial y_2} = -\frac{(z_+ - z_-)\phi'}{(z_+ - z_-)c - z_+\rho_s}, \tag{2.112}$$

$$\frac{\partial f_4}{\partial y_4} = -\frac{(z_+ - z_-)c'}{(z_+ - z_-)c - z_+\rho_s}, \tag{2.113}$$

$$\frac{\partial f_5}{\partial y_1} = 1. \tag{2.114}$$

The nonzero elements of the $\frac{\partial y_{BC}}{\partial y(x=0)}$ Jacobian $\in \mathbb{R}^{5\times 5}$ are given by:

$$\frac{\partial y_{BC,1}}{\partial y_{0,5}} = 1, \tag{2.115}$$

$$\frac{\partial y_{BC,2}}{\partial y_{0,3}} = 1. \tag{2.116}$$

For galvanostatic conditions, the nonzero elements of the $\frac{\partial y_{\mathrm{BC}}}{\partial y(x=1)}$ Jacobian $\in \mathbb{R}^{5\times 5}$ are given by

$$\frac{\partial y_{\mathrm{BC},3}}{\partial y_{1,1}} = z_- \phi'(x=1), \tag{2.117}$$

$$\frac{\partial y_{\mathrm{BC},3}}{\partial y_{1,2}} = 1, \tag{2.118}$$

$$\frac{\partial y_{\mathrm{BC},3}}{\partial y_{1,4}} = z_- c(x=1), \tag{2.119}$$

$$\frac{\partial y_{\mathrm{BC},4}}{\partial y_{1,1}} = \beta_{\mathrm{D}}(z_+ D_{+0} - z_- D_{-0})\phi'(x=1), \tag{2.120}$$

$$\frac{\partial y_{\mathrm{BC},4}}{\partial y_{1,2}} = -\beta_{\mathrm{D}}(D_{-0} - D_{+0}), \tag{2.121}$$

$$\frac{\partial y_{\mathrm{BC},4}}{\partial y_{1,4}} = -\beta_{\mathrm{D}}[-(z_+ D_{+0} - z_- D_{-0})c(x=1) + z_+ D_{+0}\rho_{\mathrm{s}}], \tag{2.122}$$

$$\frac{\partial y_{\mathrm{BC},5}}{\partial y_{1,5}} = 1, \tag{2.123}$$

while for potentiostatic conditions, the nonzero elements of the $\frac{\partial y_{\mathrm{BC}}}{\partial y(x=1)}$ Jacobian $\in \mathbb{R}^{5\times 5}$ are given by

$$\frac{\partial y_{\mathrm{BC},3}}{\partial y_{1,1}} = z_- \phi'(x=1), \tag{2.124}$$

$$\frac{\partial y_{\mathrm{BC},3}}{\partial y_{1,2}} = 1, \tag{2.125}$$

$$\frac{\partial y_{\mathrm{BC},3}}{\partial y_{1,4}} = z_- c(x=1), \tag{2.126}$$

$$\frac{\partial y_{\mathrm{BC},4}}{\partial y_{1,3}} = 1, \tag{2.127}$$

$$\frac{\partial y_{\mathrm{BC},5}}{\partial y_{1,5}} = 1. \tag{2.128}$$

2.8.3.3 Case 3: Butler-Volmer boundary conditions at anode and cathode

The nonzero elements of the $\frac{\partial f}{\partial y}$ Jacobian $\in \mathbb{R}^{5\times5}$ are given by:

$$\frac{\partial f_1}{\partial y_2} = 1, \tag{2.129}$$

$$\frac{\partial f_2}{\partial y_1} = -\frac{(z_+ - z_-)z_+z_-\rho_{\mathrm{s}}c'\phi'}{\left[(z_+ - z_-)c - z_+\rho_{\mathrm{s}}\right]^2}, \tag{2.130}$$

$$\frac{\partial f_2}{\partial y_2} = \frac{z_+z_-\rho_{\mathrm{s}}\phi'}{(z_+ - z_-)c - z_+\rho_{\mathrm{s}}}, \tag{2.131}$$

$$\frac{\partial f_2}{\partial y_4} = \frac{z_+z_-\rho_{\mathrm{s}}c'}{(z_+ - z_-)c - z_+\rho_{\mathrm{s}}}, \tag{2.132}$$

$$\frac{\partial f_3}{\partial y_4} = 1, \tag{2.133}$$

$$\frac{\partial f_4}{\partial y_1} = \frac{(z_+ - z_-)^2c'\phi'}{\left[(z_+ - z_-)c - z_+\rho_{\mathrm{s}}\right]^2}, \tag{2.134}$$

$$\frac{\partial f_4}{\partial y_2} = -\frac{(z_+ - z_-)\phi'}{(z_+ - z_-)c - z_+\rho_{\mathrm{s}}}, \tag{2.135}$$

$$\frac{\partial f_4}{\partial y_4} = -\frac{(z_+ - z_-)c'}{(z_+ - z_-)c - z_+\rho_{\mathrm{s}}}, \tag{2.136}$$

$$\frac{\partial f_5}{\partial y_1} = 1. \tag{2.137}$$

For galvanostatic conditions, the $\frac{\partial f}{\partial p}$ Jacobian $\in \mathbb{R}^{5\times1}$ is a zero vector. The nonzero elements of the $\frac{\partial y_{\mathrm{BC}}}{\partial y(x=0)}$ Jacobian ($\in \mathbb{R}^{6\times5}$ for galvanostatic conditions or $\in \mathbb{R}^{5\times5}$ for

potentiostatic conditions) are given by:

$$\frac{\partial y_{\mathrm{BC},1}}{\partial y_{0,5}} = 1, \tag{2.138}$$

$$\frac{\partial y_{\mathrm{BC},2}}{\partial y_{0,1}} = -\beta_{\mathrm{D}}(z_+ D_{+0} - z_- D_{-0})\phi'(x=0) + J_0^{\mathrm{ref}}\left(\frac{\xi_+}{\hat{c}_+^{\mathrm{ref}}}\right)^{1-\frac{\alpha_1}{2}}(c-\rho_{\mathrm{s}})^{-\frac{\alpha_1}{2}}\exp(-\alpha_1\eta)\Big|_{x=0}, \tag{2.139}$$

$$\frac{\partial y_{\mathrm{BC},2}}{\partial y_{0,2}} = \beta_{\mathrm{D}}(D_{-0} - D_{+0}), \tag{2.140}$$

$$\frac{\partial y_{\mathrm{BC},2}}{\partial y_{0,3}} = J_0^{\mathrm{ref}}\left[\frac{\xi_+(c-\rho_{\mathrm{s}})}{\hat{c}_+^{\mathrm{ref}}}\right]^{1-\frac{\alpha_1}{2}}\{\alpha_1\exp(-\alpha_1\eta) + (2-\alpha_1)\exp[(2-\alpha_1)\eta]\}\Big|_{x=0}, \tag{2.141}$$

$$\frac{\partial y_{\mathrm{BC},2}}{\partial y_{0,4}} = \beta_{\mathrm{D}}[-(z_+ D_{+0} - z_- D_{-0})c(x=0) + z_+ D_{+0}\rho_{\mathrm{s}}]. \tag{2.142}$$

For galvanostatic conditions, the nonzero elements of the $\frac{\partial y_{\mathrm{BC}}}{\partial y(x=1)}$ Jacobian $\in \mathbb{R}^{6\times 5}$ are given by

$$\frac{\partial y_{\mathrm{BC},3}}{\partial y_{1,1}} = z_- \phi'(x=1), \tag{2.143}$$

$$\frac{\partial y_{\mathrm{BC},3}}{\partial y_{1,2}} = 1, \tag{2.144}$$

$$\frac{\partial y_{\mathrm{BC},3}}{\partial y_{1,4}} = z_- c(x=1), \tag{2.145}$$

$$\begin{aligned}\frac{\partial y_{\mathrm{BC},4}}{\partial y_{1,1}} = {} & \beta_{\mathrm{D}}(z_+ D_{+0} - z_- D_{-0})\phi'(x=1) \\ & + J_0^{\mathrm{ref}} \left(\frac{\xi_+}{\hat{c}_+^{\mathrm{ref}}}\right)^{1-\frac{\alpha_1}{2}} (c-\rho_{\mathrm{s}})^{-\frac{\alpha_1}{2}} \exp(-\alpha_1 \eta)\Bigg|_{x=1},\end{aligned} \tag{2.146}$$

$$\frac{\partial y_{\mathrm{BC},4}}{\partial y_{1,2}} = -\beta_{\mathrm{D}}(D_{-0} - D_{+0}), \tag{2.147}$$

$$\frac{\partial y_{\mathrm{BC},4}}{\partial y_{1,3}} = J_0^{\mathrm{ref}} \left[\frac{\xi_+(c-\rho_{\mathrm{s}})}{\hat{c}_+^{\mathrm{ref}}}\right]^{1-\frac{\alpha_1}{2}} \{\alpha_1 \exp(-\alpha_1\eta) + (2-\alpha_1)\exp[(2-\alpha_1)\eta]\}\Bigg|_{x=1}, \tag{2.148}$$

$$\frac{\partial y_{\mathrm{BC},4}}{\partial y_{1,4}} = -\beta_{\mathrm{D}}[-(z_+ D_{+0} - z_- D_{-0})c(x=1) + z_+ D_{+0}\rho_{\mathrm{s}}], \tag{2.149}$$

$$\frac{\partial y_{\mathrm{BC},5}}{\partial y_{1,5}} = 1, \tag{2.150}$$

$$\frac{\partial y_{\mathrm{BC},6}}{\partial y_{1,1}} = \beta_{\mathrm{D}}(z_+ D_{+0} - z_- D_{-0})\phi'(x=1), \tag{2.151}$$

$$\frac{\partial y_{\mathrm{BC},6}}{\partial y_{1,2}} = -\beta_{\mathrm{D}}(D_{-0} - D_{+0}), \tag{2.152}$$

$$\frac{\partial y_{\mathrm{BC},6}}{\partial y_{1,4}} = -\beta_{\mathrm{D}}[-(z_+ D_{+0} - z_- D_{-0})c(x=1) + z_+ D_{+0}\rho_{\mathrm{s}}], \tag{2.153}$$

and the nonzero element of the $\frac{\partial y_{\mathrm{BC}}}{\partial p}$ Jacobian $\in \mathbb{R}^{6\times 1}$ is given by

$$\frac{\partial y_{\mathrm{BC},4}}{\partial p} = J_0^{\mathrm{ref}} \left[\frac{\xi_+(c-\rho_{\mathrm{s}})}{\hat{c}_+^{\mathrm{ref}}}\right]^{1-\frac{\alpha_1}{2}} \{\alpha_1 \exp(-\alpha_1\eta) + (2-\alpha_1)\exp[(2-\alpha_1)\eta]\}\Bigg|_{x=1}, \tag{2.154}$$

while for potentiostatic conditions, the nonzero elements of the $\frac{\partial y_{\mathrm{BC}}}{\partial y(x=1)}$ Jacobian $\in \mathbb{R}^{5\times5}$ are given by

$$\frac{\partial y_{\mathrm{BC},3}}{\partial y_{1,1}} = z_- \phi'(x=1), \tag{2.155}$$

$$\frac{\partial y_{\mathrm{BC},3}}{\partial y_{1,2}} = 1, \tag{2.156}$$

$$\frac{\partial y_{\mathrm{BC},3}}{\partial y_{1,4}} = z_- c(x=1), \tag{2.157}$$

$$\begin{aligned}\frac{\partial y_{\mathrm{BC},4}}{\partial y_{1,1}} = {} & \beta_{\mathrm{D}}(z_+ D_{+0} - z_- D_{-0})\phi'(x=1) \\ & + J_0^{\mathrm{ref}} \left(\frac{\xi_+}{\hat{c}_+^{\mathrm{ref}}}\right)^{1-\frac{\alpha_1}{2}} (c-\rho_{\mathrm{s}})^{-\frac{\alpha_1}{2}} \exp(-\alpha_1 \eta)\Bigg|_{x=1},\end{aligned} \tag{2.158}$$

$$\frac{\partial y_{\mathrm{BC},4}}{\partial y_{1,2}} = -\beta_{\mathrm{D}}(D_{-0} - D_{+0}), \tag{2.159}$$

$$\frac{\partial y_{\mathrm{BC},4}}{\partial y_{1,3}} = J_0^{\mathrm{ref}} \left[\frac{\xi_+(c-\rho_{\mathrm{s}})}{\hat{c}_+^{\mathrm{ref}}}\right]^{1-\frac{\alpha_1}{2}} \{\alpha_1 \exp(-\alpha_1\eta) + (2-\alpha_1)\exp[(2-\alpha_1)\eta]\}\Bigg|_{x=1}, \tag{2.160}$$

$$\frac{\partial y_{\mathrm{BC},4}}{\partial y_{1,4}} = -\beta_{\mathrm{D}}[-(z_+ D_{+0} - z_- D_{-0})c(x=1) + z_+ D_{+0}\rho_{\mathrm{s}}], \tag{2.161}$$

$$\frac{\partial y_{\mathrm{BC},5}}{\partial y_{1,5}} = 1. \tag{2.162}$$

2.8.4 Initial guesses and lower and upper bounds for fitting parameters

Table 2.6 lists the initial guesses and lower and upper bounds for the fitting parameters $\tilde{\rho}_{\mathrm{s}}$, τ (only for CN and PE membranes; fixed at 1 for AAO membranes), $\tilde{J}_0^{\mathrm{ref}}$, α_1 and ϵ_{p}.

Table 2.6: Initial guesses and lower and upper bounds for fitting parameters. Initial guess is the first value, and lower and upper bounds are provided as an interval. Lower and upper bounds for ϵ_{p} for datasets $\mathrm{AAO}_1(+/-)$, $\mathrm{AAO}_2(+/-)$, $\mathrm{CN}_1(+/-)$ and $\mathrm{CN}_2(+/-)$ are based on product specifications.

Dataset	$\tilde{\rho}_{\mathrm{s}}$	τ	$\tilde{J}_0^{\mathrm{ref}}$	α_1	ϵ_{p}
$\mathrm{AAO}_1(-)$	$-0.5, (-\infty, 0]$	1 (fixed)	$0.5, [0, \infty)$	$0.5, [0, 1]$	$0.375, [0.25, 0.5]$
$\mathrm{AAO}_1(+)$	$1.55, [0, \infty)$	1 (fixed)	$0.3, [0, \infty)$	$0.75, [0, 1]$	$0.375, [0.25, 0.5]$
$\mathrm{AAO}_2(-)$	$-0.05, (-\infty, 0]$	1 (fixed)	$0.05, [0, \infty)$	$0.5, [0, 1]$	$0.375, [0.25, 0.5]$
$\mathrm{AAO}_2(+)$	$0.25, [0, \infty)$	1 (fixed)	$0.05, [0, \infty)$	$0.65, [0, 1]$	$0.4, [0.25, 0.5]$
$\mathrm{CN}_1(-)$	$-0.1, (-\infty, 0]$	$2, [1, \infty)$	$6, [0, \infty)$	$0.5, [0, 1]$	$0.77, [0.66, 0.88]$
$\mathrm{CN}_1(+)$	$0.75, [0, \infty)$	$1.25, [1, \infty)$	$6, [0, \infty)$	$1, [0, 1]$	$0.77, [0.66, 0.88]$
$\mathrm{CN}_2(-)$	$-0.0125, (-\infty, -0.00625]$	$1, [1, \infty)$	$0.7, [0, \infty)$	$0.75, [0, 1]$	$0.77, [0.66, 0.88]$
$\mathrm{CN}_2(+)$	$0.1, [0, \infty)$	$2, [1, \infty)$	$0.4, [0, \infty)$	$0.65, [0, 1]$	$0.77, [0.66, 0.88]$
$\mathrm{PE}(-)$	$-0.25, (-\infty, 0]$	$5, [1, \infty)$	$0.5, [0, \infty)$	$0.75, [0, 1]$	$0.47, [0, 1]$
$\mathrm{PE}(+)$	$0.5, [0, \infty)$	$7, [1, \infty)$	$0.25, [0, \infty)$	$0.75, [0, 1]$	$0.47, [0, 1]$

Chapter 3

Linear stability analysis of time-dependent electrodeposition in charged porous media

The contents of this chapter will be submitted for publication in the near future.

3.1 Abstract

We study the linear stability analysis of time-dependent electrodeposition in a charged random porous medium, whose pore surface charges can be of any sign, flanked by a pair of planar metal electrodes. Discretization of the linear stability problem results in a generalized eigenvalue problem for the dispersion relation that is solved numerically, which agrees well with the analytical approximation obtained from a boundary layer analysis valid at high wavenumbers. Under galvanostatic conditions in which an overlimiting current is applied, in the classical case of zero surface charges, the electric field at the cathode diverges at Sand's time due to electrolyte depletion. The same phenomenon happens for positive charges but earlier than Sand's time. In contrast, negative charges allow the system to sustain an overlimiting current via surface conduction past Sand's time, keeping the electric field bounded. Therefore, at Sand's time, negative charges greatly reduce surface instabilities while zero and

positive charges magnify them. We compare theoretical predictions for overall surface stabilization with published experimental data for copper electrodeposition in cellulose nitrate membranes and demonstrate good agreement between theory and experiment. We also apply the stability analysis to pulse electroplating to analyze how the crystal grain size varies with duty cycle.

3.2 Introduction

Linear stability analysis is routinely applied to nonlinear systems to study how the onset of linear instabilities is related to system parameters of interest and to provide physical insights on understanding, controlling and exploiting such instabilities and the concomitant pattern formation [132, 121, 70]. Some examples in hydrodynamics include the Orr-Sommerfeld equation that predicts the dependence on Reynolds number of the transition from laminar flow to turbulent flow [179, 180, 230, 181] and the electroconvective instability that causes the transition of a quasiequilibrium electric double layer to an nonequilibrium one that contains an additional extended space charge region [270]. Here, we focus on morphological stability analysis in which linear stability analysis is used to analyze morphological instabilities of interfaces formed between different phases observed in various diverse phenomena such as electrodeposition [121, 41, 141, 148, 214, 201, 223, 199], solidification [132, 121, 41, 70] and morphogenesis [247, 70]. Some particular examples of morphological stability analysis include the Saffman-Taylor instability (viscous fingering) [213, 212, 42, 112], viscous fingering coupled with electrokinetic effects [161], the Mullins-Sekerka instability of a spherical particle during diffusion-controlled or thermally controlled growth [168] and of a planar interface during solidification of a dilute binary alloy [169, 225], and control of phase separation using electro-autocatalysis or electro-autoinhibition in driven open electrochemical systems [31, 32].

We now focus on electrodeposition as a specific example of an electrochemical system for which morphological stability analysis has been widely researched theoretically and experimentally. The study of electrodeposition has both funda-

mental and practical aspects: the fundamental aspect is about the inherent instability of the physics governing electrodeposition and how to control it while the practical aspect is about applications such as electroplating of metals and charging of metal batteries. To elucidate the fundamental physics behind electrodeposition, the morphologies of electrodeposits formed and their transitions during electrodeposition of metals such as copper, zinc and silver in liquid electrolytes are particularly well studied [41, 141, 148, 214, 201, 199, 222]. Depending on conditions such as applied current, applied voltage and electrolyte concentration, a variety of morphological patterns such as diffusion-limited aggregation (DLA) patterns [261, 262, 160, 254, 48, 156, 37, 217, 99, 245, 81], dense branching morphologies (DBM) [37, 217, 99, 34, 35, 100, 36, 93, 245, 90, 81, 79, 146] and dendritic structures [39, 40, 38, 37, 217, 99, 35, 36, 245] have been observed. Ion concentration fields [16, 143, 144, 145, 147, 195], electroconvection [85, 86, 88, 197, 117], gravity-induced convection (buoyancy) [197, 117, 61] and the presence of impurities [89, 90, 128, 130, 129] have also been examined to determine their significant effects on morphology. While the range of possible morphologies of electrodeposits is diverse, for electroplating of metals, it is desirable to electrodeposit layers that are as uniform and homogeneous as possible.

Electrodeposition is also a critical process in the development of rechargeable/secondary lithium metal batteries (LMBs) that use lithium metal for the negative electrode. For negative electrodes that use lithium chemistry, because lithium metal has the lowest standard electrochemical potential ($-3.04\,\mathrm{V}$ vs. the standard hydrogen electrode), highest theoretical specific ($3860\,\mathrm{mAh/g}$) and volumetric ($2061\,\mathrm{mAh/cm^3}$) capacities, and lowest mass density ($0.53\,\mathrm{g/cm^3}$) out of all possible candidates, it is the most promising choice for achieving high energy densities in LMBs [49, 238, 19, 263, 17, 57, 224, 82, 264, 138, 246, 243, 65, 44, 139, 64, 140, 5, 142]. However, the charging of LMBs is equivalent to lithium electrodeposition at the negative electrode, which is an inherently unstable process that can cause the formation of dendrites that penetrate the separator and result in internal short circuits and thermal runaway during charging [49, 238, 19, 263, 17, 57, 224, 82, 264, 138, 246, 243, 65, 44,

139, 64, 140, 5, 142]. This process has been especially well investigated in lithium polymer batteries that use a polymer electrolyte [50, 51, 52, 53, 198, 239, 200, 234]. Detailed studies of various growth modes of lithium in liquid electrolytes during charging have been recently performed [22, 131, 21], which will aid in the development of better models for lithium electrodeposition. Modern lithium-ion batteries (LIBs) [49, 238, 19, 259, 263, 17, 55, 57, 224, 96, 82, 97, 138, 44, 142] partially mitigate this problem of dendrite formation and propagation by employing lithium intercalating materials such as graphite for the negative electrode where only lithium ions and not reduced lithium atoms are involved in the intercalation reactions, which is also known as the "rocking chair technology" [238]. Nonetheless, lithium plating still occurs in LIBs when they are charged at high rates or low temperatures [253, 96, 97, 138, 183]. Although the root causes of the widely publicized LIB failures in two Boeing 787 Dreamliners in January 2013 were not conclusively identified [260], there is no doubt that safety is of paramount importance in both LMBs and LIBs, which requires a thorough understanding of dendrite formation.

For both electroplating of metals and charging of high energy density LMBs, it would be advantageous to perform them at as large a current or voltage as possible without causing dendrite formation. It is therefore important to understand the possible mechanisms for the electrochemical system to sustain a high current or voltage and how these mechanisms interact with the metal electrodeposition and LMB charging processes. In a neutral channel or porous medium containing an electrolyte, when ion transport is governed by diffusion and electromigration, which is collectively termed electrodiffusion, the maximum current that can be attained by the electrochemical system is called the diffusion-limited current [172, 24]. In practice, overlimiting current (OLC) beyond the electrodiffusion limit has been observed experimentally in ion-exchange membranes [207, 211, 126, 125, 203, 208, 72, 221, 219, 176, 175, 235] and microchannels and nanochannels [123, 269, 271, 273, 272, 170, 218, 229]. Depending on the length scale of the pores or channel, some possible physical mechanisms for OLC [77] are surface conduction [271, 273, 272, 155, 154, 76], electroosmotic flow [268, 206] and electroosmotic instability [205, 270]. Some chemical mech-

anisms for OLC include water splitting [176, 175] and current-induced membrane discharge [6]. In this paper, we focus on porous media consisting of pores with a nanometer length scale, therefore the dominant OLC mechanism is expected to be surface conduction [77]. When a sufficiently large current or voltage is applied across a porous medium whose pore surfaces are charged, the bulk electrolyte eventually gets depleted at an ion-selective interface such as an electrode. In order to sustain the current beyond the electrodiffusion limit, the counterions in the electric double layers (EDLs) next to the charged pore surfaces migrate under the large electric field generated in the depletion region. This phenomenon is termed surface conduction and results in the formation and propagation of deionization shocks away from the ion-selective interface in porous media [154, 76, 267] and microchannels and nanochannels [271, 273, 272, 77, 155, 173]. The deionization shock separates the "front" electrolyte-rich region, in which bulk electrodiffusion dominates, from the "back" electrolyte-poor region, in which electromigration in the EDLs dominates.

Morphological stability analysis of electrodeposition is typically performed in the style of the pioneering Mullins-Sekerka stability analysis [168, 169]. The destabilizing effect arises from the amplification of surface protrusions by diffusive fluxes while the main stabilizing effect arises from the surface energy penalty incurred in creating additional surface area. The balance between these two effects, which is influenced by system parameters, sets a characteristic length scale or wavenumber for the surface instability. In 1963, by applying an infinitesimally small spherical harmonic perturbation to the surface of a spherical particle undergoing growth by solute diffusion or heat diffusion, Mullins and Sekerka derived a dispersion relation that related growth rates of the eigenmodes to particle radius and degree of supersaturation [168]. Similarly, in 1964, Mullins and Sekerka imposed a infinitesimally small sinusoidal perturbation on a planar liquid-solid interface during the solidification of a dilute binary alloy and obtained a dispersion relation relating the surface perturbation growth rate to system parameters such as temperature and concentration gradients [169]. In the spirit of the Mullins-Sekerka stability analysis, about 16 years later in 1980, Aogaki, Kitazawa, Kose and Fueki applied linear stability analysis

to study electrodeposition with a steady-state base state in the presence of a supporting electrolyte, i.e., electromigration of the minor species can be ignored, and without explicitly accounting for electrochemical reaction kinetics [9]. Following up on this work, from 1981 to 1982, Aogaki and Makino changed the steady-state base state to a time-dependent base state under galvanostatic conditions while keeping other assumptions intact [10, 7, 8]. In 1984, Aogaki and Makino extended their previous work to account for surface diffusion of adsorbed metal atoms under galvanostatic [11, 12] and potentiostatic conditions [13, 14]. In the same year, Makino, Aogaki and Niki also used such a linear stability analysis to extract surface parameters of metals under galvanostatic and potentiostatic conditions [153] and applied it to study how hydrogen adsorption affects these extracted parameters under galvanostatic conditions [152]. Later work by Barkey, Muller and Tobias in 1989 [25, 26], and Chen and Jorne in 1991 [62] additionally assumed the presence of a diffusion boundary layer next to the electrode.

Subsequent developments in linear stability analysis of electrodeposition relaxed some assumptions made in the past literature and added more physics and electrochemistry. Butler-Volmer reaction kinetics was first explicitly considered by Pritzker and Fahidy in 1992 for a steady-state base state with a diffusion boundary layer next to the electrode [189]. Also considering Butler-Volmer reaction kinetics with a steady-state base state, in 1995, Sundström and Bark used the Nernst-Planck equations for ion transport without assuming the existence of a diffusion boundary layer, numerically solved for the dispersion relation and performed extensive parameter sweeps over key parameters of interest such as surface energy and exchange current density [236]. Extending these two papers in 1998, Elezgaray, Léger and Argoul used a time-dependent base state under galvanostatic conditions, numerically solved for both the time-dependent base state and perturbed state to obtain the dispersion relation and demonstrated good agreement between their theory and experiments on copper electrodeposition in a thin gap cell [78]. The role of electrolyte additives in stabilizing electrodeposition was examined in the linear stability analysis performed by Haataja, Srolovitz and Bocarsly in 2002 and 2003 [101, 102, 103], and McFadden

et al. in 2003 [159]. By demonstrating that the effects of the anode can be ignored under certain conditions when deriving the dispersion relation, BuAli, Johns and Narayanan in 2006 simplified Sundström and Bark's analysis to obtain an analytical expression for the dispersion relation [56]. In 2004 and 2005, Monroe and Newman included additional mechanical effects such as pressure, viscous stress and deformational stress to the linear stability analysis of electrodeposition, which provided more stabilization beyond that provided by surface energy [164, 165]. For a steady-state base state, in 2014, Tikekar, Archer and Koch studied how tethered immobilized anions provide additional stabilization to electrodeposition by reducing the electric field at the cathode and, after making some approximations, derived analytical expressions for the dispersion relation for small and large current densities [241]. Tikekar, Archer and Koch then extended this work in 2016 by accounting for elastic deformations that provide further stabilization [242]. Building on Monroe and Newman's 2004 and 2005 work on interfacial deformation effects [164, 165], Ahmad and Viswanathan identified a new mechanism for stabilization driven by the difference of the metal density in the metal electrode and solid electrolyte in 2017 [2], and further generalized this work in the same year to account for anisotropy [1]. Natsiavas, Weinberg, Rosato and Ortiz in 2016 also investigated the stabilizing effect of prestress and showed good agreement between theory and experiment [171]. Relaxing the usual assumption of electroneutrality, in 2015, Nielsen and Bruus performed linear stability analysis for a steady-state base state that accounts for the extended space charge region that is formed when the electric double layer becomes nonequilibrium at an overlimiting current [174].

Without performing a linear stability analysis, some models focus on describing the initiation and subsequent propagation of dendrites. The classic work in this class of models is by Chazalviel in 1990 in which they used the Poisson's equation for electrostatics, i.e., electroneutrality is not assumed, and showed that the initiation of ramified electrodeposits is caused by the creation of a space charge layer upon anion depletion at the cathode, the induction time for initiation is the time needed for building up this space charge layer, and the velocity of the ramified growth is equal to

the electromigration velocity of the anions [60]; some experimental results were also obtained by Fleury, Chazalviel, Rosso and Sapoval in support of this model [87], and some of the numerical results of the original analysis were subsequently improved by Rosso, Chazalviel and Chassaing [196]. Via an asymptotic analysis of the Poisson-Nernst-Planck equations for ion transport, Bazant also showed that the velocity of the ramified growth is approximately equal to the anion electromigration velocity and estimated the induction time for the onset of ramified growth [30]. Building on past theoretical and experimental work done on silver electrodeposition by Barton and Bockris [28], and zinc electrodeposition by Despic, Diggle and Bockris [73, 75], Monroe and Newman investigated the propagation velocity and length of a dendrite tip that grows via Butler-Volmer kinetics [163]. By examining the thermodynamics and kinetics of heterogeneous nucleation and growth, which is assumed to proceed via the linearized Butler-Volmer equation valid for small overpotentials, Ely and García identified five different regimes of nucleus behavior [80]. Assuming a concentration-dependent electrolyte diffusivity and the existence of a hemispherical dendrite "precursor" that grows with Tafel kinetics, Akolkar studied the subsequent propagation velocity and length of the dendrite [3] and how they are affected by temperature [4].

In this paper, we perform linear stability analysis of electrodeposition inside a charged random porous medium, whose pore surface charges can generally be of any sign, that is filled with a liquid electrolyte and flanked on its sides by a pair of planar metal electrodes. The linear stability analysis is carried out with respect to a time-dependent base state and focuses on overlimiting current carried by surface conduction. By doing so, we combine and generalize previous work done in [236, 78, 241]. For simplicity, we ignore bulk convection, electroosmotic flow, surface adsorption, surface diffusion of adsorbed species [11, 12, 13, 14] and additional mechanical effects such as pressure, viscous stress and deformational stress [164, 165, 242, 2, 1, 171]. We expect surface diffusion of adsorbed species, which alleviates electrodiffusion limitations, and interfacial deformation effects to stabilize electrodeposition, hence our work here can be considered a worst-case analysis. The only electrochemical reaction considered here is metal electrodeposition, therefore in the context of LMBs and

LIBs, electrochemical and chemical reactions between lithium and the electrolyte that cause the formation of the solid electrolyte interphase (SEI) layer [252, 63, 184, 256] are not included. We first derive governing equations for the full model that consists of coupling ion transport with electrochemical reaction kinetics, followed by applying linear stability analysis on the full model via the imposition of sinusoidal spatial perturbations around the time-dependent base state. For the dispersion relation, we perform a boundary layer analysis on the perturbed state to derive an accurate approximation for it and a convergence analysis of its full numerical solution. To better understand the physics of the dispersion relation, we carry out parameter sweeps over the pore surface charge density, Damköhler number and applied current density under galvanostatic conditions. We also compare the numerical and approximate solutions of the maximum wavenumber, maximum growth rate and critical wavenumber in order to verify the accuracy of these approximations. Subsequently, we apply the linear stability analysis to compare theoretical predictions and experimental data for copper electrodeposition in cellulose nitrate membranes [106], and also use the stability analysis as a tool for investigating the dependence of crystal grain size on duty cycle during pulse electroplating.

3.3 Full model

3.3.1 Transport

The starting point for modeling ion transport is the leaky membrane model that is able to predict overlimiting current carried by surface conduction, which we have previously coupled with Butler-Volmer reaction kinetics for analyzing steady state current-voltage relations and linear sweep voltammetry [122]. The system under consideration is a binary asymmetric liquid electrolyte in a finite 3D charged random nanoporous medium where $x \in [0, L_x]$, $y \in [0, L_y]$ and $z \in [0, L_z]$, whose 2D projection is illustrated in Figure 3-1. We assume that the nanoporous medium is random with well connected pores such as cellulose nitrate membranes so that we can inves-

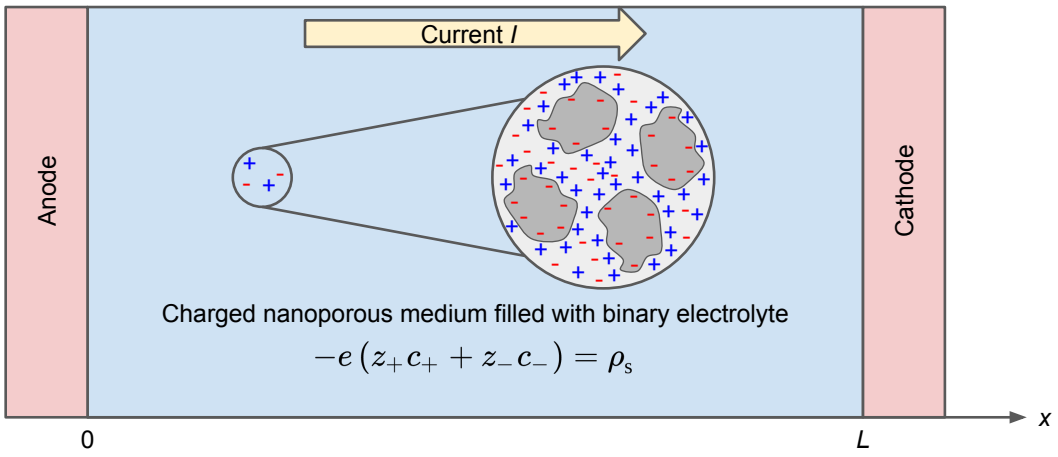

Figure 3-1: 2D projection of 3D system considered: charged random nanoporous medium filled with binary asymmetric liquid electrolyte where anode is on the left at $x = 0$ and cathode is on the right at $x = L_x$ along the x axis, which is the direction of the inter-electrode spacing, and y axis is the direction of the sinusoidal perturbation. $\lambda = \frac{2\pi}{k_y}$ is the perturbation wavelength where k_y is the wavenumber in the y direction. The linear stability analysis is actually performed in 3D in which the sinusoidal perturbation is applied in the y and z directions, and the extension of this 2D projection to the 3D case is straightforward. The current in the electrolyte flows from left to right. The equation shown on the left describes macroscopic electroneutrality given by Equation 3.3 where ρ_s is the volume-averaged background charge density.

tigate macroscopic electrode-scale morphological instabilities [106]. The cations are electroactive and the anions are inert. Initially, at $t = 0$, the anode surface is located at $x = 0$ while the cathode surface is located at $x = L_x$. As is typical for linear stability analysis of electrodeposition [236, 78, 174], we pick a moving reference frame with a velocity $u(t) = u_x(t)e_x$ that is equal to the velocity of the electrode/electrolyte interface so that the average positions of the dissolving anode and growing cathode remain stationary. For the porous medium, we denote its porosity, tortuosity, internal pore surface area per unit volume and pore surface charge per unit area as ϵ_p, τ, a_p and σ_s respectively. We assume that there are no homogeneous reactions and all material properties such as ϵ_p, τ, a_p and σ_s are constant and uniform. We also assume that dilute solution theory holds true, hence all activity coefficients are 1 and the cation and anion macroscopic diffusivities $D_{\pm 0}$, where the 0 subscript indicates dilute limit, are constant, uniform and independent of concentrations. Accounting for corrections due to the tortuosity of the porous medium, the macroscopic diffusivity $D_{\pm 0}$ is related to the molecular (free solution) diffusivity $D^\mathrm{m}_{\pm 0}$ by $D_{\pm 0} = \frac{D^\mathrm{m}_{\pm 0}}{\tau}$ [84]. The assumption of dilute solution theory further implies that the convective flux in the moving reference frame is negligible and the effect of the moving reference frame velocity $u(t) = u_x(t)e_x$ is only significant in the equation describing electrode surface growth or dissolution [236, 78, 174], which we will discuss in Section 3.3.3. Under these assumptions, for ion transport, the Nernst-Planck equations describing species conservation, charge conservation equation and macroscopic electroneutrality constraint are given by

$$\epsilon_\mathrm{p}\frac{\partial c_\pm}{\partial t} + \nabla \cdot F_\pm = 0, \quad F_\pm = -\epsilon_\mathrm{p} D_{\pm 0}\left(\nabla c_\pm + \frac{z_\pm e c_\pm}{k_\mathrm{B}T}\nabla\phi\right), \tag{3.1}$$

$$\nabla \cdot J = 0, \quad J = e(z_+F_+ + z_-F_-), \tag{3.2}$$

$$\rho_\mathrm{s} = \frac{\sigma_\mathrm{s}}{h_\mathrm{p}} = \frac{a_\mathrm{p}\sigma_\mathrm{s}}{\epsilon_\mathrm{p}} = -e(z_+c_+ + z_-c_-), \tag{3.3}$$

where $c_\pm$, $F_\pm$, $z_\pm$, are the cation and anion concentrations, fluxes and charge numbers respectively, ϕ is the electrolyte electric potential, J is the electrolyte current density, $h_\mathrm{p} = \frac{\epsilon_\mathrm{p}}{a_\mathrm{p}}$ is the effective pore size and ρ_s is the volume-averaged background

charge density. Denoting the numbers of cations and anions that are formed from complete dissociation of 1 molecule of neutral salt as $\nu_\pm$, electroneutrality requires that $z_+\nu_+ + z_-\nu_- = 0$. We will use the macroscopic electroneutrality constraint given by Equation 3.3 to eliminate c_+ as a dependent variable, therefore leaving c_- and ϕ as the remaining dependent variables.

For a classical system with an uncharged nanoporous medium, i.e., $\rho_\mathrm{s} = 0$, the maximum current density that the system can possibly attain under electrodiffusion is called the diffusion-limited or limiting current density J_lim, which is given by [122]

$$J_\mathrm{lim} = \frac{2(z_+ - z_-)e\epsilon_\mathrm{p} D_{+0}\nu_- c_0}{L_x} \tag{3.4}$$

where c_0 is the neutral salt bulk concentration. The limiting current I_lim is then given by $I_\mathrm{lim} = J_\mathrm{lim}A$ where $A = L_y L_z$ is the surface area of the electrode. Under galvanostatic conditions, when a current density J_a larger than J_lim is applied, the cation and anion concentrations at the cathode reach 0 and the electrolyte electric potential and electric field there diverge in finite time, which is called Sand's time [215] denoted as t_s; see [249] for a discussion of some subtlety associated with this transition time when J_a is exactly equal to J_lim. Defining the dimensionless Sand's time $\tilde{t}_\mathrm{s} = \frac{D_\mathrm{amb0} t_\mathrm{s}}{L_x^2}$ and dimensionless applied current density $\tilde{J}_\mathrm{a} = \frac{J_\mathrm{a}}{J_\mathrm{lim}}$ where $D_\mathrm{amb0} = \frac{(z_+ - z_-)D_{+0}D_{-0}}{z_+ D_{+0} - z_- D_{-0}}$ [172, 122] is the ambipolar diffusivity of the neutral salt in the dilute limit and $\frac{L_x^2}{D_\mathrm{amb0}}$ is the diffusion time scale, $\tilde{t}_\mathrm{s}$ is given by [249]

$$\tilde{t}_\mathrm{s} = \frac{\pi}{16\tilde{J}_\mathrm{a}^2}, \quad \tilde{J}_\mathrm{a} > 1. \tag{3.5}$$

For galvanostatic conditions, t_s is a critically important time scale because the formation of dendrites often occurs near or at t_s, therefore it will be central to the linear stability analysis results discussed in Section 3.5.

Unlike the classical case of $\rho_\mathrm{s} = 0$, for $\rho_\mathrm{s} < 0$, the system can sustain an overlimiting current $\tilde{J}_\mathrm{a} > 1$ via surface conduction that is the electromigration of the counterions in the electric double layers (EDLs), which are formed next to the charged pore surfaces, under a large electric field generated in the depletion region next to the

cathode. This additional surface conductivity thus enables the system to go beyond t_s and eventually reach a steady state, in stark contrast to the finite time divergence of the classical case at t_s. On the other hand, for $\rho_s > 0$, the counterions in the EDLs are the inert anions instead of the electroactive cations, which contribute a surface current that flows in the opposite direction from that of the bulk current. Because of this "negative" surface conductivity conferred by $\rho_s > 0$ relative to $\rho_s = 0$, at the cathode, the bulk electrolyte concentration vanishes and the electric field diverges earlier than t_s; in other words, $\rho_s > 0$ effectively reduces t_s. A more quantitative way of explaining this is that the "negative" surface conductivity causes the maximum current density that can be achieved, which is denoted as J_{max}, to be smaller than J_{lim}, and J_{max} decreases as ρ_s increases. In effect, a more positive ρ_s decreases J_{lim}, which thus leads to a smaller t_s for a given J_a according to Equation 3.5. Details of how to numerically compute J_{max} are found in [122]; note that J_{max} here corresponds to I_{max}^{BV} in [122].

3.3.2 Electrochemical reaction kinetics

In order to analyze how spatial perturbations of an electrode surface affect its linear stability, we need to account for the effects of surface curvature and surface energy in the electrochemical reaction kinetics model. The mean curvature of the electrode/electrolyte interface $\mathscr{H}$ is given by $\mathscr{H} = -\frac{1}{2}\nabla_s \cdot \hat{n}$ where ∇_s is the surface gradient operator and $\hat{n}$ is the unit normal that points outwards from the electrolyte [71]. In this paper, we consider a charge transfer reaction that involves only the cations and electrons while the anions are inert. More concretely, we suppose the following charge transfer reaction consuming n electrons $O^{z_O} + ne^- \rightleftharpoons R^{z_R}$ where O^{z_O} is the oxidized species O with charge z_O, e^- is the electron e with charge -1, R^{z_R} is the reduced species R with charge z_R, and $z_O - n = z_R$ because of charge conservation. If the reduced species is solid metal, i.e., $z_R = 0$, as is the case in metal electrodeposition, the creation of additional electrode/electrolyte interfacial area results in a surface energy penalty that appears in the electrochemical potential of the reduced species. Therefore, the electrochemical potentials μ_i of the oxidized species

O, electron e and reduced species R for $i \in \{\mathrm{O}, \mathrm{e}, \mathrm{R}\}$ are given by

$$\mu_{\mathrm{O}} = k_{\mathrm{B}}T \ln a_{\mathrm{O}} + z_{\mathrm{O}} e\phi + \mu_{\mathrm{O}}^{\Theta}, \tag{3.6}$$

$$\mu_{\mathrm{e}} = k_{\mathrm{B}}T \ln a_{\mathrm{e}} - e\phi_{\mathrm{e}} + \mu_{\mathrm{e}}^{\Theta}, \tag{3.7}$$

$$\mu_{\mathrm{R}} = k_{\mathrm{B}}T \ln a_{\mathrm{R}} + z_{\mathrm{R}} e\phi + \mu_{\mathrm{R}}^{\Theta} + 2\Omega\gamma\mathscr{H}, \tag{3.8}$$

where the surface energy term $2\Omega\gamma\mathscr{H}$ [236, 78, 163, 164, 165, 71, 241, 174] is included in μ_{R} when the reduced species is solid metal ($z_{\mathrm{R}} = 0$) and the Θ superscript indicates standard state. The activity of species i is given by $a_i = \gamma_i \hat{c}_i$ where γ_i is the activity coefficient of species i and $\hat{c}_i = \frac{c_i}{c_i^{\Theta}}$ is the concentration of species i normalized by its standard concentration c_i^{Θ}. μ_i^{Θ} is the standard electrochemical potential of species i, ϕ_{e} is the electrode electric potential, $\Omega = \frac{M_{\mathrm{m}}}{\rho_{\mathrm{m}}}$ is the atomic volume of the solid metal where M_{m} and ρ_{m} are the atomic mass and mass density of the metal respectively, and γ is the isotropic surface energy of the metal/electrolyte interface. The quantity $\frac{\Omega\gamma}{k_{\mathrm{B}}T}$ is the capillary constant that has units of length [168, 169, 225]. The interfacial electric potential difference $\Delta\phi$ is defined as $\Delta\phi = \phi_{\mathrm{e}} - \phi$. At equilibrium when $\mu_{\mathrm{O}} + n\mu_{\mathrm{e}} = \mu_{\mathrm{R}}$, we obtain the Nernst equation

$$\Delta\phi^{\mathrm{eq}} = \frac{k_{\mathrm{B}}T}{ne} \ln \frac{a_{\mathrm{O}} a_{\mathrm{e}}^n}{a_{\mathrm{R}}} + E^{\Theta} - \frac{2\Omega\gamma\mathscr{H}}{ne}, \quad E^{\Theta} = \frac{\mu_{\mathrm{O}}^{\Theta} + n\mu_{\mathrm{e}}^{\Theta} - \mu_{\mathrm{R}}^{\Theta}}{ne}, \tag{3.9}$$

where the "eq" superscript denotes equilibrium and E^{Θ} is the standard electrode potential. When the system is driven out of equilibrium so that $\mu_{\mathrm{O}} + n\mu_{\mathrm{e}} \neq \mu_{\mathrm{R}}$, it generates a Faradaic current density J_{F} that is given by [31, 32, 84]

$$J_{\mathrm{F}} = nek_0 \left[\exp\left(-\frac{\mu_{\ddagger}^{\mathrm{r,ex}} - \mu_{\mathrm{O}} - n\mu_{\mathrm{e}}}{k_{\mathrm{B}}T} \right) - \exp\left(-\frac{\mu_{\ddagger}^{\mathrm{r,ex}} - \mu_{\mathrm{R}}}{k_{\mathrm{B}}T} \right) \right] \tag{3.10}$$

where k_0 is the overall reaction rate constant and $\mu_{\ddagger}^{\mathrm{r,ex}}$ is the excess electrochemical potential of the transition state for the Faradaic reaction. Using the Butler-Volmer hypothesis, $\mu_{\ddagger}^{\mathrm{r,ex}}$ consists of a chemical contribution $k_{\mathrm{B}}T \ln \gamma_{\ddagger}^{\mathrm{r}}$, where $\gamma_{\ddagger}^{\mathrm{r}}$ is the activity coefficient of the transition state for the Faradaic reaction, and a convex combination of the electrostatic energies, surface energies (only for the reduced species) and stan-

dard electrochemical potentials weighted by α, which is the charge transfer coefficient. Therefore, $\mu_{\ddagger}^{\mathrm{r,ex}}$ is given by

$$\mu_{\ddagger}^{\mathrm{r,ex}} = k_{\mathrm{B}}T\ln\gamma_{\ddagger}^{\mathrm{r}} + (1-\alpha)\big(z_{\mathrm{O}}e\phi - ne\phi_{\mathrm{e}} + \mu_{\mathrm{O}}^{\Theta} + n\mu_{\mathrm{e}}^{\Theta}\big) + \alpha\big(z_{\mathrm{R}}e\phi + \mu_{\mathrm{R}}^{\Theta} + 2\Omega\gamma\mathscr{H}\big). \tag{3.11}$$

Defining the overpotential η as $\eta = \frac{\mu_{\mathrm{R}} - \mu_{\mathrm{O}} - n\mu_{\mathrm{e}}}{ne} = \Delta\phi - \Delta\phi^{\mathrm{eq}}$, we rewrite J_{F} as

$$J_{\mathrm{F}} = j_0\left\{\exp\left(-\frac{\alpha ne\eta}{k_{\mathrm{B}}T}\right) - \exp\left[\frac{(1-\alpha)ne\eta}{k_{\mathrm{B}}T}\right]\right\}, \quad j_0 = \frac{k_0 ne(a_{\mathrm{O}}a_{\mathrm{e}}^{n})^{1-\alpha}a_{\mathrm{R}}^{\alpha}}{\gamma_{\ddagger}^{\mathrm{r}}}, \tag{3.12}$$

where j_0 is the exchange current density. In this form, we can identify the cathodic and anodic charge transfer coefficients, which are denoted as α_{c} and α_{a} respectively, as $\alpha_{\mathrm{c}} = \alpha$ and $\alpha_{\mathrm{a}} = 1-\alpha$ such that $\alpha_{\mathrm{c}} + \alpha_{\mathrm{a}} = 1$. We note that our particular choice of $\mu_{\ddagger}^{\mathrm{r,ex}}$ in Equation 3.11 corresponds to choosing the "mechanical transfer coefficient" α_{m} defined in [164] to be equal to α_{a}, causing j_0 to not depend explicitly on $\mathscr{H}$.

In this paper, we assume that the only charge transfer reaction occurring is metal electrodeposition that happens via the electrochemical reduction of cations in the electrolyte to solid metal on the electrode. The activity of solid metal is 1 while we assume that the activity of electrons is 1. In addition, like in Section 3.3.1, we assume that dilute solution theory is applicable, therefore the activity coefficients of the cation, anion and transition state for the Faradaic reaction are 1 and we replace activities of the cation and anion with their normalized concentrations $\hat{c}_{\pm}$. Therefore, $\Delta\phi^{\mathrm{eq}}$ and j_0 simplify to

$$\Delta\phi^{\mathrm{eq}} = \frac{k_{\mathrm{B}}T}{ne}\ln\hat{c}_{+} + E^{\Theta} - \frac{2\Omega\gamma\mathscr{H}}{ne}, \quad j_0 = k_0 ne\hat{c}_{+}^{1-\alpha}. \tag{3.13}$$

To compare the reaction and diffusion rates, we define the Damköhler number Da as the ratio of the Faradaic current density scale $e\epsilon_{\mathrm{p}}k_0$ and limiting current density J_{lim} given by

$$\mathrm{Da} = \frac{e\epsilon_{\mathrm{p}}k_0}{J_{\mathrm{lim}}}. \tag{3.14}$$

When Da is large, i.e., $\mathrm{Da} \gg 1$, the system is diffusion-limited but when Da is small,

i.e., Da $\ll 1$, the system is reaction-limited.

3.3.3 Boundary conditions, constraints and initial conditions

We use "a" and "c" superscripts to denote the anode and cathode respectively, $r = [x, y, z]^{\mathrm{T}}$ to denote the position vector, and $r_{\mathrm{m}}^{\mathrm{a,c}} = [x_{\mathrm{m}}^{\mathrm{a,c}}, y_{\mathrm{m}}^{\mathrm{a,c}}, z_{\mathrm{m}}^{\mathrm{a,c}}]^{\mathrm{T}}$ to denote the positions of the anode and cathode. We ground the anode at all times, i.e., $\phi_{\mathrm{e}}^{\mathrm{a}} = 0$. Because the cations are electroactive, we impose no-flux boundary conditions for the cation flux on all boundaries except the anode and cathode where Faradaic reactions involving the cations occur. On the other hand, because the anions are inert, we impose no-flux boundary conditions for the anion flux on all boundaries. At the anode and cathode, we require the conservation of charges across the electrode/electrolyte interfaces. In summary, the boundary conditions are given by $\hat{n} \cdot F_{-}(r = r_{\mathrm{m}}^{\mathrm{a,c}}) = 0$, $\hat{n} \cdot J(r = r_{\mathrm{m}}^{\mathrm{a,c}}) = \epsilon_{\mathrm{p}} J_{\mathrm{F}}^{\mathrm{a,c}}$, $\hat{n} \cdot F_{-}(r = r_{\mathrm{other}}) = 0$ and $\hat{n} \cdot J(r = r_{\mathrm{other}}) = 0$ where r_{other} refers to all boundaries except the anode and cathode.

The velocity of the electrode/electrolyte interface $v_{\mathrm{I}}^{\mathrm{a,c}}$ is defined as $v_{\mathrm{I}}^{\mathrm{a,c}} = \epsilon_{\mathrm{p}} \frac{\mathrm{d}r_{\mathrm{m}}^{\mathrm{a,c}}}{\mathrm{d}t}$ and its normal component $v_{\mathrm{In}}^{\mathrm{a,c}}$ is given by $v_{\mathrm{In}}^{\mathrm{a,c}} = \hat{n} \cdot v_{\mathrm{I}}^{\mathrm{a,c}} = \epsilon_{\mathrm{p}} \hat{n} \cdot \frac{\mathrm{d}r_{\mathrm{m}}^{\mathrm{a,c}}}{\mathrm{d}t}$. Because the growth (dissolution) of the electrode surface is caused by metal electrodeposition (electrodissolution), taking into account the moving reference frame velocity $u(t) = u_x(t) e_x$, the normal interfacial velocity is related to the normal current density by $v_{\mathrm{In}}^{\mathrm{a,c}} = -\frac{\Omega \hat{n} \cdot J(r = r_{\mathrm{m}}^{\mathrm{a,c}})}{z_+ e} - \hat{n} \cdot u(r = r_{\mathrm{m}}^{\mathrm{a,c}})$ and therefore, $\epsilon_{\mathrm{p}} \hat{n} \cdot \frac{\mathrm{d}r_{\mathrm{m}}^{\mathrm{a,c}}}{\mathrm{d}t} = -\frac{\Omega \hat{n} \cdot J(r = r_{\mathrm{m}}^{\mathrm{a,c}})}{z_+ e} - \hat{n} \cdot u(r = r_{\mathrm{m}}^{\mathrm{a,c}})$.

For galvanostatic conditions in which we apply a current I_{a} on the system, we require $\int \hat{n} \cdot J(r = r_{\mathrm{m}}^{\mathrm{c}}) \, \mathrm{d}S^{\mathrm{c}} = \int -\hat{n} \cdot J(r = r_{\mathrm{m}}^{\mathrm{a}}) \, \mathrm{d}S^{\mathrm{a}} = I_{\mathrm{a}}$ to satisfy charge conservation whereas for potentiostatic conditions in which we apply an electric potential V on the cathode, we set $\phi_{\mathrm{e}}^{\mathrm{c}} = V$. For initial conditions, we set $c_{-}(t = 0) = \nu_{-} c_0 - \frac{\rho_{\mathrm{s}} + |\rho_{\mathrm{s}}|}{2 z_{-} e} \equiv \beta_1$ where c_0 is the initial neutral salt bulk concentration [122], and $x_{\mathrm{m}}^{\mathrm{a}}(t = 0) = 0$ and $x_{\mathrm{m}}^{\mathrm{c}}(t = 0) = L_x$, i.e., the anode and cathode are initially planar.

3.4 Linear stability analysis

3.4.1 Perturbations and linearization

Linear stability analysis generally involves imposing a spatial perturbation around a base state, keeping constant and linear terms of the perturbed state, and determining the dispersion relation that relates the growth rate of the perturbation to its wavenumber or wavelength. For electrodeposition specifically, the objective is to impose a spatial perturbation on a planar electrode surface and determine the effects of key system parameters on the linear stability of the surface in response to this perturbation. In this paper, we will choose a time-dependent base state, therefore the dispersion relation is also time-dependent. In 3D, the electrode/electrolyte interface can be written explicitly as $x = h(y, z, t)$ where h is the electrode surface height. Given h, we can derive explicit expressions for surface variables such as the curvature $\mathscr{H}$ and normal interfacial velocity v_{In} in terms of h and its spatial and temporal derivatives [71, 69], which are provided in Appendix 3.8.1. For brevity, we let $k = [k_y, k_z]^{\text{T}}$ and $\xi = [y, z]^{\text{T}}$ where k is the wavevector, and k_y and k_z are the wavenumbers in the y and z directions respectively. Therefore, $k \cdot \xi = k_y y + k_z z$, $k^2 = \|k\|_2^2 = k_y^2 + k_z^2$ where $\|\cdot\|_2$ is the L^2-norm and $\|k\|_2$ is the overall wavenumber, and the wavelength λ is given by $\lambda = \frac{2\pi}{\|k\|_2}$. For brevity again, we write the overall wavenumber as k and it is obvious from context whether k refers to the wavevector or overall wavenumber. The perturbation that will be imposed is sinusoidal in the y and z directions given by

$$h(\xi, t) = h^{(0)}(t) + \epsilon \Re\big[h^{(1)} \exp(ik \cdot \xi + \omega t)\big] + \mathcal{O}\big(\epsilon^2\big) \tag{3.15}$$

where $\epsilon \ll 1$ is a dimensionless small parameter, the (0) and (1) superscripts denote the base and perturbed states respectively, $\Re(\cdot)$ gives the real part of a complex number, $h^{(1)}$ is the complex-valued perturbation amplitude of the electrode surface height, and ω is the complex-valued growth rate of the perturbation. In response to such an electrode surface perturbation, we assume that the perturbations to c_- and

ϕ are similarly given by

$$c_-(x,\xi,t) = c_-^{(0)}(x,t) + \epsilon\Re\Big[c_-^{(1)}(x)\exp(ik\cdot\xi+\omega t)\Big] + \mathcal{O}\big(\epsilon^2\big), \tag{3.16}$$

$$\phi(x,\xi,t) = \phi^{(0)}(x,t) + \epsilon\Re\big[\phi^{(1)}(x)\exp(ik\cdot\xi+\omega t)\big] + \mathcal{O}\big(\epsilon^2\big), \tag{3.17}$$

where $c_-^{(1)}$ and $\phi^{(1)}$ are the complex-valued perturbation amplitudes of anion concentration and electrolyte electric potential respectively.

To evaluate c_- and ϕ and their gradients ∇c_- and $\nabla\phi$ at the interface at $x = h$, we require their Taylor series expansions around the base state interface at $x = h^{(0)}$. Letting $\hat{\epsilon} = \epsilon\exp(ik\cdot\xi+\omega t)$ and $\theta \in \{c_-, \phi\}$, these expansions are given by [236, 78, 174]

$$\theta(x=h) = \theta^{(0)}\big(x=h^{(0)}\big) + \hat{\epsilon}\left(h^{(1)}\frac{\partial\theta^{(0)}}{\partial x} + \theta^{(1)}\right)\bigg|_{x=h^{(0)}} + \mathcal{O}\big(\epsilon^2\big), \tag{3.18}$$

$$\frac{\partial\theta}{\partial x}(x=h) = \frac{\partial\theta^{(0)}}{\partial x}\big(x=h^{(0)}\big) + \hat{\epsilon}\left(h^{(1)}\frac{\partial^2\theta^{(0)}}{\partial x^2} + \frac{\mathrm{d}\theta^{(1)}}{\mathrm{d}x}\right)\bigg|_{x=h^{(0)}} + \mathcal{O}\big(\epsilon^2\big), \tag{3.19}$$

$$\frac{\partial\theta}{\partial y}(x=h) = \hat{\epsilon}ik_y\theta^{(1)}\big(x=h^{(0)}\big) + \mathcal{O}\big(\epsilon^2\big), \quad \frac{\partial\theta}{\partial z}(x=h) = \hat{\epsilon}ik_z\theta^{(1)}\big(x=h^{(0)}\big) + \mathcal{O}\big(\epsilon^2\big), \tag{3.20}$$

$$\nabla\theta(x=h) = \frac{\partial\theta}{\partial x}(x=h)e_x + \frac{\partial\theta}{\partial y}(x=h)e_y + \frac{\partial\theta}{\partial z}(x=h)e_z + \mathcal{O}\big(\epsilon^2\big). \tag{3.21}$$

After substituting these perturbation expressions into the full model in Section 3.3, we obtain the base and perturbed states by matching the $\mathcal{O}(1)$ and $\mathcal{O}(\epsilon)$ terms respectively. The dispersion relation $\omega(k)$ is subsequently computed by solving these $\mathcal{O}(1)$ and $\mathcal{O}(\epsilon)$ equations. The growth rate ω is generally complex-valued and for a particular k value, there is an infinite discrete spectrum of ω values. However, for linear stability analysis, we are primarily interested in the maximum of the real parts of the ω values, which is denoted as $\max\{\Re(\omega)\}$, that corresponds to the most unstable eigenmode. If $\max\{\Re(\omega)\} < 0$, the perturbation decays exponentially in time and the base state is linearly stable. On the other hand, if $\max\{\Re(\omega)\} > 0$, the perturbation grows exponentially in time and the base state is linearly unstable. Lastly, if $\max\{\Re(\omega)\} = 0$, the perturbation does not decay nor grow and the base

state is marginally stable.

3.4.2 Nondimensionalization

To make the equations more compact and derive key dimensionless parameters, in Table 3.1, we define the scales that are used for nondimensionalizing the full model in Section 3.3 and the perturbation expressions in Section 3.4.1. $\tilde{L}_y$ and $\tilde{L}_z$ are the aspect ratios in the y and z directions respectively. For convenience, we also define $\beta_{\mathrm{D}} = -\frac{z_- D_{-0}}{2(z_+ D_{+0} - z_- D_{-0})}$, $\beta_{\mathrm{m}} = \nu_+ c_0 \Omega$, $\beta_{\mathrm{v}} = \frac{\beta_{\mathrm{m}}}{\beta_{\mathrm{D}}}$ and $\xi_+ = \frac{\nu_+ c_0}{c_+^{\ominus}}$, and note that $\hat{c}_+ = \xi_+(\tilde{c}_- - \tilde{\rho}_{\mathrm{s}})$. Two important dimensionless parameters emerge from this nondimensionalization process, namely the Damköhler number $\mathrm{Da} = \tilde{k}_0$ that is described earlier in Equation 3.14 and the capillary number Ca that is given by

$$\mathrm{Ca} = \tilde{\gamma} = \frac{\Omega \gamma}{L_x k_{\mathrm{B}} T}, \tag{3.22}$$

which is the ratio of the capillary constant $\frac{\Omega\gamma}{k_{\mathrm{B}}T}$ [168, 169, 225] to the inter-electrode distance L_x, and $\tilde{\gamma}$ is the dimensionless isotropic surface energy of the metal/electrolyte interface.

To avoid cluttering the notation, we drop tildes for all dimensionless variables and parameters, and all variables and parameters are dimensionless in the following sections unless otherwise stated. We also rewrite the (0) and (1) superscripts, which denote the base and perturbed states respectively, as 0 and 1 subscripts respectively. Similarly, we drop the 0 subscript for diffusivities and the $-$ subscript for anion-related variables and parameters. As shorthand, we use subscripts to denote partial derivatives with respect to x, y, z and t, primes to denote total derivatives with respect to x, and an overhead dot to denote the total derivative with respect to t. All equations for the dimensionless full model are provided in Appendix 3.8.2. Details for deriving the dimensionless equations for the base and perturbed states are provided in Appendix 3.8.3, and we summarize them in Sections 3.4.3 and 3.4.4 below.

Table 3.1: Scales used for nondimensionalization.

Variables and parameters	Scale
x, y, z, L_y, L_z, r, r_m, h, λ, ξ	L_x
t	$\frac{L_x^2}{D_\mathrm{amb0}}$ (diffusion time)
$c_\pm$	$\nu_\pm c_0$
ϕ, ϕ_e, $\Delta\phi^\mathrm{eq}$, E^Θ, $\Delta\phi$, η	$\frac{k_\mathrm{B}T}{e}$ (thermal voltage)
$D_{\pm0}$	D_amb0
ρ_s	$z_+\nu_+ec_0 = -z_-\nu_-ec_0$
$F_\pm$	$\frac{\epsilon_\mathrm{p}D_\mathrm{amb0}\nu_\pm c_0}{L_x}$
u, u_x, v_I, v_In	$\frac{\epsilon_\mathrm{p}D_\mathrm{amb0}}{L_x}$
J	J_lim
I	I_lim
j_0, J_F	$\frac{J_\mathrm{lim}}{\epsilon_\mathrm{p}}$
k_0	$\frac{J_\mathrm{lim}}{e\epsilon_p}$
γ	$\frac{L_xk_\mathrm{B}T}{\Omega}$
$\mathscr{H}$, k_y, k_z, k	$\frac{1}{L_x}$
ω	$\frac{D_\mathrm{amb0}}{L_x^2}$ (reciprocal diffusion time)

3.4.3 Base state

The equations for the base state are obtained by substituting the perturbation expressions in Section 3.4.1 into the full model in Section 3.3 and matching terms at $\mathcal{O}(1)$. Equivalently, the base state is simply the full model specialized to 1D in the x direction with the curvature-related terms dropped, which only appear at $\mathcal{O}(\epsilon)$. Therefore, at $\mathcal{O}(1)$, the governing PDEs (partial differential equations) are given by

$$c_{0,t} - D\big[c_{0,xx} + z(c_0\phi_{0,x})_x\big] = 0, \tag{3.23}$$

$$\beta_\mathrm{D}\big[(D-D_+)c_{0,xx} + z_+D_+\rho_\mathrm{s}\phi_{0,xx} - (z_+D_+ - zD)(c_0\phi_{0,x})_x\big] = 0, \tag{3.24}$$

where the first PDE is the Nernst-Planck equation describing species conservation of anions and the second PDE is the charge conservation equation. The boundary

conditions at the anode at $x = h_0^{\mathrm{a}}$ are given by

$$\phi_{\mathrm{e}}^{\mathrm{a}} = 0, \tag{3.25}$$

$$-D(-c_{0,x} - zc_0\phi_{0,x}) = 0, \tag{3.26}$$

$$\beta_{\mathrm{D}}[-(D - D_+)c_{0,x} - z_+D_+\rho_{\mathrm{s}}\phi_{0,x} + (z_+D_+ - zD)c_0\phi_{0,x}] = j_{0,0}\{\exp(-\alpha n\eta_0) - \exp[(1-\alpha)n\eta_0]\}, \tag{3.27}$$

$$-\dot{h}_0 = -\beta_{\mathrm{v}}\hat{n}\cdot J_0 + u_x, \tag{3.28}$$

where $\eta_0 = \phi_{\mathrm{e}} - \phi_0 - \frac{1}{n}\ln[\xi_+(c_0 - \rho_{\mathrm{s}})] - E^{\Theta}$, $j_{0,0} = \mathrm{Da}n[\xi_+(c_0 - \rho_{\mathrm{s}})]^{1-\alpha}$ and $\hat{n}\cdot J_0 = \beta_{\mathrm{D}}[-(D - D_+)c_{0,x} - z_+D_+\rho_{\mathrm{s}}\phi_{0,x} + (z_+D_+ - zD)c_0\phi_{0,x}]$. Since the unit normal at the cathode points in the opposite direction from that at the anode, the signs of the expressions involving $\hat{n}$ at the cathode are opposite to that at the anode. Therefore, the boundary conditions at the cathode at $x = h_0^{\mathrm{c}}$ are given by

$$-D(c_{0,x} + zc_0\phi_{0,x}) = 0, \tag{3.29}$$

$$\beta_{\mathrm{D}}[(D - D_+)c_{0,x} + z_+D_+\rho_{\mathrm{s}}\phi_{0,x} - (z_+D_+ - zD)c_0\phi_{0,x}] = j_{0,0}\{\exp(-\alpha n\eta_0) - \exp[(1-\alpha)n\eta_0]\}, \tag{3.30}$$

$$\dot{h}_0 = -\beta_{\mathrm{v}}\hat{n}\cdot J_0 - u_x, \tag{3.31}$$

where $\eta_0 = \phi_{\mathrm{e}} - \phi_0 - \frac{1}{n}\ln[\xi_+(c_0 - \rho_{\mathrm{s}})] - E^{\Theta}$, $j_{0,0} = \mathrm{Da}n[\xi_+(c_0 - \rho_{\mathrm{s}})]^{1-\alpha}$ and $\hat{n}\cdot J_0 = \beta_{\mathrm{D}}[(D - D_+)c_{0,x} + z_+D_+\rho_{\mathrm{s}}\phi_{0,x} - (z_+D_+ - zD)c_0\phi_{0,x}]$.

We pick $u_x(x = h_0^{\mathrm{a}})$ and $u_x(x = h_0^{\mathrm{c}})$ such that the positions of the anode and cathode in the base state remain stationary, i.e., $\dot{h}_0^{\mathrm{a}} = \dot{h}_0^{\mathrm{c}} = 0$. Therefore, $u_x = \beta_{\mathrm{v}}\hat{n}\cdot J_0(x = h_0^{\mathrm{a}}) = -\beta_{\mathrm{v}}\hat{n}\cdot J_0(x = h_0^{\mathrm{c}})$ where the second equality automatically holds true because of charge conservation in the 1D $\mathcal{O}(1)$ base state. Physically, u_x is equal to the velocity of the growing planar cathode/electrolyte interface or the dissolving planar anode/electrolyte interface in the base state. The initial conditions are given by

$$c_0(t = 0) = \beta_1, \quad h_0^{\mathrm{a}}(t = 0) = 0, \quad h_0^{\mathrm{c}}(t = 0) = 1. \tag{3.32}$$

Since $\dot{h}_0^{\mathrm{a}} = \dot{h}_0^{\mathrm{c}} = 0$, $h_0^{\mathrm{a}}(t) = 0$ and $h_0^{\mathrm{c}}(t) = 1$ at all t. For galvanostatic conditions in which we apply a current density J_{a} on the system, we impose

$$J_{\mathrm{a}} = \beta_{\mathrm{D}}[(D - D_+)c_{0,x} + z_+ D_+ \rho_{\mathrm{s}} \phi_{0,x} - (z_+ D_+ - zD)c_0 \phi_{0,x}]\big|_{x=h_0^{\mathrm{c}}} \tag{3.33}$$

$$= \beta_{\mathrm{D}}[(D - D_+)c_{0,x} + z_+ D_+ \rho_{\mathrm{s}} \phi_{0,x} - (z_+ D_+ - zD)c_0 \phi_{0,x}]\big|_{x=h_0^{\mathrm{a}}}. \tag{3.34}$$

For potentiostatic conditions in which we apply an electric potential V on the cathode, we impose $\phi_{\mathrm{e}}^{\mathrm{c}} = V$.

The equations for the time-dependent base state cannot generally be solved analytically, therefore we would have to solve them numerically. However, at steady state, the base state admits semi-analytical solutions for any ρ_{s} [122]. Specifically, c_0, $\phi_{0,x}$ and their spatial derivatives can be analytically expressed in terms of the Lambert W function [68]. On the other hand, ϕ_0 is known semi-analytically because it can be analytically expressed in terms of the Lambert W function up to an additive constant, which is a function of J_{a} and ρ_{s} and is found by numerically solving the algebraic Butler-Volmer equations given by Equations 3.27 and 3.30 with MATLAB's `fsolve` or `fzero` function.

3.4.4 Perturbed state

To derive the equations for the perturbed state at $\mathcal{O}(\epsilon)$, we substitute the perturbation expressions in Section 3.4.1 into the full model in Section 3.3 and match terms at $\mathcal{O}(\epsilon)$. One important outcome is that the curvature-related terms appear as functions of k^2 because they are associated with second-order spatial partial derivatives in the y and z directions. At $\mathcal{O}(\epsilon)$, the governing ODEs (ordinary differential equations) are given by

$$D\big\{c_1'' - k^2 c_1 + z\big[(c_0\phi_1' + \phi_{0,x}c_1)_x - k^2 c_0 \phi_1\big]\big\} = \omega c_1, \tag{3.35}$$

$$(D - D_+)\big(c_1'' - k^2 c_1\big) + z_+ D_+ \rho_{\mathrm{s}}\big(\phi_1'' - k^2\phi_1\big) - (z_+ D_+ - zD)\big[(c_0\phi_1' + \phi_{0,x}c_1)_x - k^2 c_0\phi_1\big] = 0, \tag{3.36}$$

where the first ODE describes the perturbation in species conservation of anions and the second ODE describes the perturbation in charge conservation. For brevity, we define $\alpha_3 = -\alpha \exp(-\alpha n \eta_0) - (1-\alpha)\exp[(1-\alpha)n\eta_0]$. The boundary conditions at the anode at $x = h_0^{\mathrm{a}}$ are given by

$$c_{0,t} h_1 - D[-c_1' - z(c_0 \phi_1' + \phi_{0,x} c_1)] = 0, \tag{3.37}$$

$$\beta_{\mathrm{v}} j_{0,0} \Big(\hat{D}_1 h_1 + \hat{D}_2 c_1 + \hat{D}_3 \phi_1 \Big) = \omega h_1, \tag{3.38}$$

$$\beta_{\mathrm{m}}[-(D - D_+)c_1' - z_+ D_+ \rho_{\mathrm{s}} \phi_1' + (z_+ D_+ - zD)(c_0 \phi_1' + \phi_{0,x} c_1)] = \omega h_1, \tag{3.39}$$

where the $\hat{D}_1$, $\hat{D}_2$ and $\hat{D}_3$ parameters are

$$\hat{D}_1 = \alpha_3 n \left(-\phi_{0,x} + \frac{\gamma k^2}{n} \right) + \frac{\exp(-\alpha n \eta_0) c_{0,x}}{c_0 - \rho_{\mathrm{s}}}, \quad \hat{D}_2 = \frac{\exp(-\alpha n \eta_0)}{c_0 - \rho_{\mathrm{s}}}, \quad \hat{D}_3 = -\alpha_3 n. \tag{3.40}$$

Because the unit normal at the cathode is in the opposite direction from that at the anode, the signs of the expressions involving $\hat{n}$ at the cathode are opposite to that at the anode. Hence, the boundary conditions at the cathode at $x = h_0^{\mathrm{c}}$ are given by

$$-c_{0,t} h_1 - D[c_1' + z(c_0 \phi_1' + \phi_{0,x} c_1)] = 0, \tag{3.41}$$

$$\beta_{\mathrm{v}} j_{0,0} \Big(\hat{G}_1 h_1 + \hat{G}_2 c_1 + \hat{G}_3 \phi_1 \Big) = -\omega h_1, \tag{3.42}$$

$$\beta_{\mathrm{m}}[(D - D_+)c_1' + z_+ D_+ \rho_{\mathrm{s}} \phi_1' - (z_+ D_+ - zD)(c_0 \phi_1' + \phi_{0,x} c_1)] = -\omega h_1, \tag{3.43}$$

where the $\hat{G}_1$, $\hat{G}_2$ and $\hat{G}_3$ parameters are

$$\hat{G}_1 = \alpha_3 n \left(-\phi_{0,x} - \frac{\gamma k^2}{n} \right) + \frac{\exp(-\alpha n \eta_0) c_{0,x}}{c_0 - \rho_{\mathrm{s}}}, \quad \hat{G}_2 = \frac{\exp(-\alpha n \eta_0)}{c_0 - \rho_{\mathrm{s}}}, \quad \hat{G}_3 = -\alpha_3 n. \tag{3.44}$$

The capillary number $\mathrm{Ca} = \gamma$ appears in the $\hat{D}_1$ and $\hat{G}_1$ parameters in the form of γk^2, which is the source of the surface stabilizing effect that arises from the surface energy penalty incurred in creating additional surface area. The competition between

this surface stabilizing effect and the surface destabilizing effect arising from the c_0, $c_{0,x}$ and $\phi_{0,x}$ fields sets the scale for the critical wavenumber k_c, which is the wavenumber at which the perturbation growth rate ω is 0 and the electrode surface is marginally stable.

3.4.5 Discretization of perturbed state

Without making further approximations, the equations for the perturbed state do not admit analytical solutions, thus we have to resort to numerical methods to solve them. To do so, the equations for the perturbed state are spatially discretized over a uniform grid with N grid points and a grid spacing $\Delta x = \frac{1}{N-1}$ using second-order accurate finite differences [135]. Details of this discretization process are provided in Appendix 3.8.4. In summary, the discretized equations can be written as a generalized eigenvalue problem given by

$$Yv = \omega Zv, \quad v = \begin{bmatrix} h_1^{\mathrm{a}} & c_{1,1} & \phi_{1,1} & c_{1,2} & \phi_{1,2} & \cdots & c_{1,N-1} & \phi_{1,N-1} & c_{1,N} & \phi_{1,N} & h_1^{\mathrm{c}} \end{bmatrix}^{\mathrm{T}}, \tag{3.45}$$

where $Y, Z \in \mathbb{R}^{(2N+2)\times(2N+2)}$, $v \in \mathbb{C}^{2N+2}$, $\omega \in \mathbb{C}$ and the second subscript in $c_{1,i}$ and $\phi_{1,i}$ for $i = 1, 2, \ldots, N$ denotes the grid point index. In the context of a generalized eigenvalue problem, the eigenvector v consists of the complex-valued amplitudes c_1, ϕ_1, h_1^{a} and h_1^{c} evaluated at the grid points, and the eigenvalue is the complex-valued growth rate ω. Although Y is non-singular, the time-independent terms in the equations for the perturbed state introduce rows of zeros in Z, therefore Z is singular and the generalized eigenvalue problem cannot be reduced to a standard eigenvalue problem. Specifically, Y is non-singular with rank $2N + 2$ while Z is singular with rank N, and the total number of eigenvalues is $2N + 2$.

Because Z is singular with rank N, there are N finite eigenvalues and $N + 2$ infinite eigenvalues. This mathematical property is not always consistently noted in past literature on linear stability analysis of electrodeposition, although Sundström and Bark did mention that N different eigenvalues are obtained with N grid points

that give rise to $2N + 2$ equations without explicitly stating that the other $N + 2$ eigenvalues are infinite [236]. The infinite eigenvalues are physically irrelevant to the linear stability analysis [248, 120], therefore we would want to focus on solving for the finite eigenvalues. This can be achieved by mapping the infinite eigenvalues to other arbitrarily chosen points in the complex plane via simple matrix transformations [98]. Details of how these transformations are performed are given in Appendix 3.8.4. There are methods for directly removing the infinite eigenvalues such as the "reduced" method [94, 185, 248] but they are more intrusive and require more extensive matrix manipulations as compared to the mapping technique [98] that we use.

The modified generalized eigenvalue problem that results from these transformations can then be solved using any eigenvalue solver. For linear stability analysis, we only need to find the eigenvalue with the largest real part instead of all the finite eigenvalues. Since the time complexity of finding all the eigenvalues typically scales as $\mathcal{O}(N^3)$ while that for finding $k \leq N$ of them, where $k = 1$ in our case, scales as $\mathcal{O}(kN^2)$, the computational cost is dramatically reduced by a factor of $\mathcal{O}(N)$ if we use an eigenvalue solver that can find subsets of eigenvalues and eigenvectors such as MATLAB's `eigs` solver.

3.4.6 Numerical implementation

The equations for the time-dependent base state in Section 3.4.3 are numerically solved using the finite element method in COMSOL Multiphysics 5.3a. The eigenvalue with the largest real part and its corresponding eigenvector from the generalized eigenvalue problem for the perturbed state in Section 3.4.5 are then solved for using the `eigs` function in MATLAB R2018a. When the `eigs` function occasionally fails to converge for small values of the wavenumber k, we use Rostami and Xue's eigenvalue solver based on the matrix exponential [202, 265], which is more robust than the `eigs` function. The colormaps used for some of the plots in Section 3.5 are obtained from BrewerMap [67], which is a MATLAB program available in the MATLAB File Exchange that implements the ColorBrewer colormaps [108].

3.5 Results

Because of the large number of dimensionless parameters present, the parameter space is too immense to be explored thoroughly in this paper. Instead, the key dimensionless parameters that we focus on and vary are ρ_s, Da and J_a under galvanostatic conditions. $\rho_s = 0$ corresponds to the classical case of an uncharged nanoporous medium while $\rho_s \neq 0$ allows us to depart from this classical case and study its effects on the linear stability of the electrode surface. Experimentally, ρ_s can be tuned via layer-by-layer deposition of polyelectrolytes [105, 106, 104] or tethered immobilized anions [246]. Da is very sensitive to the specific reactions considered and varies significantly in practice. We focus on galvanostatic conditions instead of potentiostatic conditions because when an overlimiting current $J_a > 1$ is applied on a classical system with $\rho_s = 0$, as discussed in Section 3.3.1, the Sand's time t_s provides a time scale at which the electric field at the cathode diverges that causes the perturbation growth rate to diverge too. This allows us to focus the linear stability analysis on times immediately before, at and immediately after t_s.

For the results discussed in Sections 3.5.2, 3.5.3, 3.5.4 and 3.5.6 below, we assume the following dimensional quantities for a typical electrolyte in a typical nanoporous medium: $T = 298\,\mathrm{K}$, $M_m = 6.941\,\mathrm{g/mol}$ (arbitrarily pick lithium metal) [210], $\rho_m = 0.534\,\mathrm{g/cm^3}$ (arbitrarily pick lithium metal) [210], $L_x = 60\,\mu\mathrm{m}$, $L_y = L_z = 100L_x = 6\,\mathrm{mm}$, $c_0 = 10\,\mathrm{mM}$ (initial neutral salt bulk concentration), $c_+^\ominus = 1\,\mathrm{M} = 10^3\,\mathrm{mol/m^3}$ (standard concentration) and $\gamma = 1\,\mathrm{J/m^2}$ (typical surface energy of metal/electrolyte interface) [236]. Corresponding to these dimensional quantities, all dimensionless parameters that are kept constant for the results in Sections 3.5.2, 3.5.3, 3.5.4 and 3.5.6 are given in Table 3.2.

3.5.1 Approximations

At the heart of the linear stability analysis is the competition between the destabilizing effect that arises from the amplification of surface protrusions by diffusive fluxes in a positive feedback loop and the stabilizing effect that arises from the sur-

Table 3.2: Dimensionless parameters that are kept constant for results in Sections 3.5.2, 3.5.3, 3.5.4 and 3.5.6 for a typical electrolyte in a typical nanoporous medium.

Dimensionless parameter	Value
ν_+	1
ν	1
z_+	1
z	-1
D_+	1
D	1
n	1
α	0.5
$\mathrm{Ca} = \gamma$	8.74×10^{-5}
β_{m}	1.30×10^{-4}
β_{D}	0.25
β_{v}	5.20×10^{-4}
ξ_+	0.01
E^{Θ}	0
L_y	100
L_z	100

face energy penalty incurred in the creation of additional surface area. Therefore, in the dispersion relation $\omega(k)$, we expect to see some local maxima or possibly just a single global maximum, which we denote as $\{k_{\max}, \omega_{\max}\}$, where the electrode surface is maximally unstable. We also expect to see a critical wavenumber k_{c} corresponding to $\omega = 0$ where the electrode surface is marginally stable. When k is larger than k_{c}, ω is always negative because the surface energy stabilizing effect always dominates when the wavenumber is sufficiently large. We note that k_{c} is always greater than $k_{\max}$. Corresponding to $k_{\max}$ and k_{c} are the maximum wavelength $\lambda_{\max} = \frac{2\pi}{k_{\max}}$ and critical wavelength $\lambda_{\mathrm{c}} = \frac{2\pi}{k_{\mathrm{c}}}$ respectively. In a porous medium, the characteristic pore size $h_{\mathrm{c}} = 2d_{\mathrm{p}}$, where d_{p} is the pore diameter, sets a threshold or cutoff for overall electrode surface stabilization: we should observe stabilization if h_{c} is smaller than λ_{c} [241]. If h_{c} is larger than λ_{c}, then the most unstable eigenmode dominates the electrode surface growth with a growth rate of $\omega_{\max}$ and the characteristic length scale of this instability is $\lambda_{\max}$. Therefore, $\{k_{\max}, \omega_{\max}\}$ and k_{c} are the most physically informative points of the dispersion relation. We now derive an approximation

for the dispersion relation $\omega(k)$ that is valid at high values of k and will be useful for computing $\{k_{\max}, \omega_{\max}\}$ and k_{c} quickly and accurately because $k_{\max}$ and k_{c} tend to be large. The approximation is also useful for verifying the full numerical solution at high k, which will be discussed in Section 3.5.2.

When k is sufficiently large, at the cathode at $x = h_0^{\mathrm{c}} = 1$, we expect $k^2 c_1$ to balance c_1'', and $k^2\phi_1$ to balance ϕ_1'' in Equations 3.35 and 3.36 respectively. Therefore, k^{-2} is a small parameter multiplying the highest order spatial derivative terms c_1'' and ϕ_1'', and the spatial profiles for c_1 and ϕ_1 form a boundary layer with characteristic thickness k^{-1}. Hence, as an ansatz for the boundary layer analysis, we assume

$$c_1 = A\exp[k(x-1)], \quad \phi_1 = B\exp[k(x-1)], \tag{3.46}$$

where A and B are arbitrary constants that are determined from the boundary conditions at $x = h_0^{\mathrm{c}} = 1$. By assuming such an ansatz, the cathode is effectively decoupled from the anode and the perturbation growth rate is entirely dependent on the boundary conditions at the cathode. Imposing the boundary conditions at $x = h_0^{\mathrm{c}} = 1$, we obtain

$$\xi_1(k) = \frac{c_{0,t}}{zc_0Dk}, \quad \xi_2(k) = -\frac{z\phi_{0,x} + k}{zc_0k}, \quad B(k) = -\xi_1 h_1 + \xi_2 A, \tag{3.47}$$

$$A(k) = -\frac{\beta_{\mathrm{v}} j_{0,0}\left(\hat{G}_1 - \xi_1\hat{G}_3\right) - \beta_{\mathrm{m}}\alpha_5\xi_1 k}{\beta_{\mathrm{v}} j_{0,0}\left(\hat{G}_2 + \xi_2\hat{G}_3\right) - \beta_{\mathrm{m}}[(\alpha_1 - \alpha_5\xi_2)k - \alpha_2\phi_{0,x}]} h_1, \tag{3.48}$$

$$\omega(k) = \beta_{\mathrm{m}}\left\{\frac{[(\alpha_1 - \alpha_5\xi_2)k - \alpha_2\phi_{0,x}]\left[\beta_{\mathrm{v}} j_{0,0}\left(\hat{G}_1 - \xi_1\hat{G}_3\right) - \beta_{\mathrm{m}}\alpha_5\xi_1 k\right]}{\beta_{\mathrm{v}} j_{0,0}\left(\hat{G}_2 + \xi_2\hat{G}_3\right) - \beta_{\mathrm{m}}[(\alpha_1 - \alpha_5\xi_2)k - \alpha_2\phi_{0,x}]} - \alpha_5\xi_1 k\right\}, \tag{3.49}$$

where we define $\alpha_1 = D - D_+$, $\alpha_2 = z_+D_+ - zD$ and $\alpha_5 = \alpha_2 c_0 - z_+D_+\rho_{\mathrm{s}}$ for brevity.

Approximate values of $\{k_{\max}, \omega_{\max}\}$ can be obtained by solving $\omega'(k) = 0$ and requiring $\omega''(k) < 0$ where the primes indicate total derivatives with respect to k. In addition, by solving $\omega(k) = 0$, we can obtain approximate values of k_{c}. However, this process is tedious because the first term inside the braces in Equation 3.49 is a rational

function that consists of polynomials in k of relatively high degrees. Specifically, after multiplying the numerator and denominator of this term by k, it becomes a rational function with a numerator that is a polynomial in k of degree 4 and a denominator that is a polynomial in k of degree 2. Therefore, for the purpose of quickly approximating $\{k_{\max}, \omega_{\max}\}$ and k_{c}, we first find a simpler and yet still accurate analytical approximation for k_{c}, which can then used as an initial guess for numerically solving for $\{k_{\max}, \omega_{\max}\}$ using Equation 3.49 with MATLAB's `fminbnd` optimizer. Such an approximation can be obtained by assuming k_{c} is large enough that $\hat{G}_2 c_1 \ll \hat{G}_1 h_1$ and $\hat{G}_3 \phi_1 \ll \hat{G}_1 h_1$ and then setting $\omega = 0$ in Equation 3.42, thus resulting in

$$k_{\mathrm{c}} = \left\{ \frac{1}{\alpha_3 \gamma} \left[-\alpha_3 n \phi_{0,x} + \frac{\exp(-\alpha n \eta_0) c_{0,x}}{c_0 - \rho_{\mathrm{s}}} \right] \right\}^{\frac{1}{2}}. \tag{3.50}$$

We observe that k_{c} scales as $\mathrm{Ca}^{-\frac{1}{2}} = \gamma^{-\frac{1}{2}}$, which is expected because the surface energy stabilizing effect appears in the form of γk^2 in $\hat{G}_1$ in Equation 3.42, and this scaling agrees with that obtained in previous work done on linear stability analysis of electrodeposition [236, 78, 124, 241, 174].

3.5.2 Convergence analysis

Before analyzing the physical significance of the linear stability analysis results, we would want to first establish the accuracy and convergence of the full numerical solution of the dispersion relation $\omega(k)$. To this end, we perform a numerical convergence analysis in which we examine the convergence of the numerical solution as the number of grid points N increases. At the same time, we also compute the approximate $\omega(k)$ given by Equation 3.49 because we expect the numerical and approximate solutions to agree well at high values of k; this therefore provides another way of checking the accuracies of both the numerical and approximate solutions.

To demonstrate how the numerical dispersion relation $\omega(k)$ changes with N, we fix $\mathrm{Da} = 1$ and $J_{\mathrm{a}} = 1.5$ (overlimiting current) and plot numerically computed $\Re(\omega)$ against $\log_{10} k$ for $\rho_{\mathrm{s}} \in \{-0.05, 0, 0.05\}$ and $N \in \{251, 501, 1001, 2001, 4001\}$ at specific $\frac{t}{t_{\mathrm{s}}}$ values in Figure 3-2. As expected, the numerical solutions converge quickly

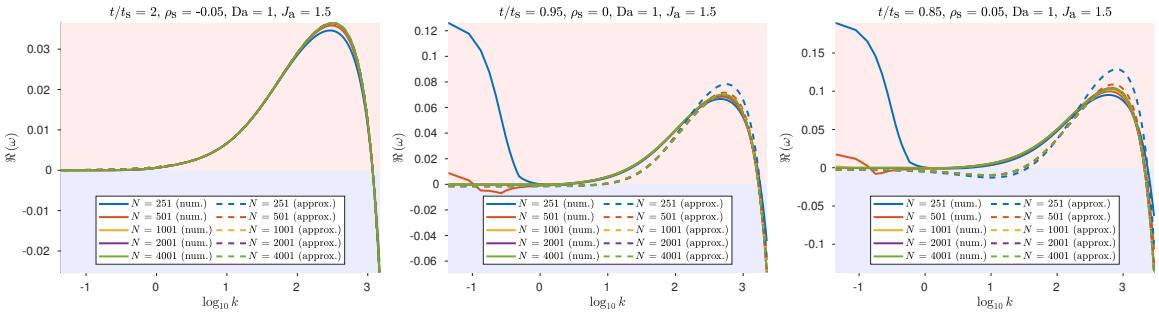

Figure 3-2: Convergence plots of $\Re(\omega)$ against $\log_{10} k$ with Da $= 1$ and $J_a = 1.5$ (overlimiting current) for $\rho_s \in \{-0.05, 0, 0.05\}$ and $N \in \{251, 501, 1001, 2001, 4001\}$ used in convergence analysis. The $\frac{t}{t_s}$ values to which the curves correspond are indicated in the figure titles. In the legends, "num." refers to numerical solutions while "approx." refers to approximate solutions.

as N increases from 251 to 4001. For $\rho_s = 0$ and $\rho_s = 0.05$ at small values of k, when the value of N is small at 251 or 501, we observe that there are anomalously large values of $\Re(\omega)$ that vanish at larger values of N. This is because when N is too small, the grid is not sufficiently fine to accurately resolve the base state variables, in particular the rapidly increasing electric field at the cathode near t_s, thus leading to an overestimation of the destabilizing effect caused by electrodiffusion and an underestimation of the stabilizing effect caused by surface energy. The numerical and approximate solutions also expectedly agree well with each other at large values of k and this agreement improves as N increases, thus confirming that the approximations are accurate at high k.

Because we are mostly interested in the k_{max}, ω_{max} and k_c points on the $\omega(k)$ curve, we plot them against N in Figure 3-3. We observe that the numerically computed k_{max}, ω_{max} and k_c curves rapidly level off and converge to constant values as N increases. The numerical and approximate solutions also agree very well as N increases, which is expected because k_{max} and k_c are large and the approximations are accurate at high k. As a compromise between numerical accuracy and computational time, we pick $N = 1001$ for all numerical and approximate solutions computed in the following sections.

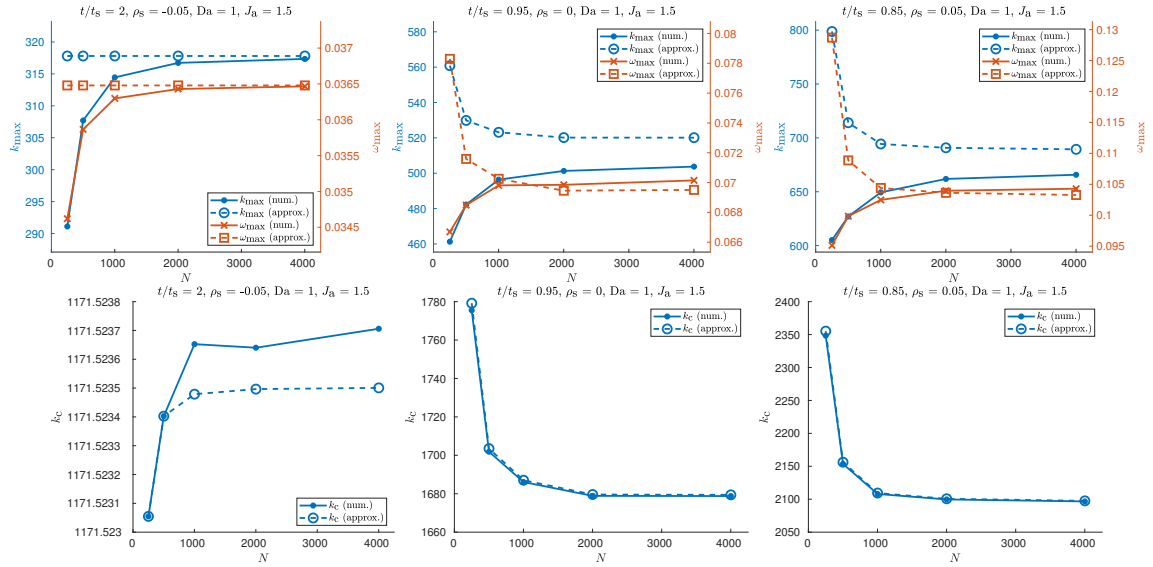

Figure 3-3: Convergence plots of $k_{\max}$, $\omega_{\max}$ and k_c against N with Da $= 1$ and $J_a = 1.5$ (overlimiting current) for $\rho_s \in \{-0.05, 0, 0.05\}$ used in convergence analysis. Top row: Convergence plots of $k_{\max}$ and $\omega_{\max}$. Bottom row: Convergence plots of k_c. The $\frac{t}{t_s}$ values to which the curves correspond are indicated in the figure titles. In the legends, "num." refers to numerical solutions while "approx." refers to approximate solutions.

3.5.3 Parameter sweeps

The base state anion concentration field c_0, electrolyte electric potential field ϕ_0 and electric field $E_0 = -\phi_{0,x}$ possess salient features that are useful for understanding the linear stability analysis results. We focus on galvanostatic conditions under an overlimiting current $J_a > 1$ because as explained in Section 3.3.1, doing so provides us with Sand's time t_s as a time scale at which the bulk electrolyte is depleted at the cathode. Depending on the sign of ρ_s, the c_0, ϕ_0 and E_0 fields behave differently at $t = t_s$ and beyond. Fixing Da $= 1$ and $J_a = 1.5$ (overlimiting current), we plot c_0, ϕ_0 and E_0 against x for various $\frac{t}{t_s}$ values for $\rho_s \in \{-0.05, 0, 0.05\}$ in Figure 3-4. For $\rho_s = -0.05$, because the system can go beyond t_s and eventually reach a steady state, we show plots up to $t = 2t_s$. For $\rho_s = 0$, since ϕ_0 and E_0 at the cathode diverge at t_s, which cause the numerical solver to stop converging, we can only show plots up to $t = 0.95t_s$. For $\rho_s = 0.05$, because $\rho_s > 0$ effectively reduces t_s as discussed in Section 3.3.1, we show plots up to $t = 0.85t_s$.

For $\rho_s = -0.05 < 0$, the distinguishing features of running the system at an overlimiting current carried by surface conduction are the anion depletion region at the cathode and the bounded and constant electric field E_0 in this depletion region after $t = t_s$. Because the anion concentration gradient almost vanishes in the depletion region, the current in this region is predominantly not carried by electrodiffusion but by electromigration of the counterions in the electric double layers (EDLs) under the aforementioned bounded and constant electric field E_0, i.e., surface conduction. Moreover, because of this additional surface conductivity, when compared to $\rho_s = 0$ and $\rho_s = 0.05$, E_0 is always smaller at all x for a given t. On the other hand, for the classical case of $\rho_s = 0$, E_0 at the cathode quickly increases near t_s and eventually diverges at t_s. Relative to this classical case, for $\rho_s = 0.05 > 0$, E_0 is always greater at all x for a given t and eventually diverges at the cathode earlier than t_s because of the "negative" surface conductivity conferred by the positive background charge as discussed in Section 3.3.1.

We now examine the dispersion relation $\omega(k)$ by plotting numerically computed $\Re(\omega)$ against k for various $\frac{t}{t_s}$ values for $\rho_s \in \{-0.05, 0, 0.05\}$, Da $\in \{0.1, 1, 10\}$ and $J_a = 1.5$ (overlimiting current) in Figure 3-5. In Figure 3-5, ρ_s increases from left to right and Da increases from bottom to top. Generally for all the parameters considered, the ω curve, in particular the k_{max}, ω_{max} and k_c points, increases and "moves in the northeast direction" as t increases; qualitatively, the "total amount of instability" increases with t. For $\rho_s = -0.05 < 0$, when compared to $\rho_s = 0$ and $\rho_s = 0.05$, the ω curve is the smallest at a given t because of a smaller base state electric field E_0. The ω curve also remains bounded at all t and eventually reaches a steady state that is almost attained near $t = 2t_s$ because E_0 at the cathode behaves in the same fashion. In sharp contrast, for the classical case of $\rho_s = 0$ near t_s, the ω curve grows dramatically because of the rapidly increasing E_0 at the cathode, which eventually diverges at t_s and in turn causes the ω curve to diverge at t_s too. Compared to this classical case, for $\rho_s = 0.05 > 0$, because E_0 at the cathode is larger at a given t and diverges earlier than t_s, the ω curve accordingly grows even more rapidly at earlier times and diverges earlier than t_s. Therefore, by

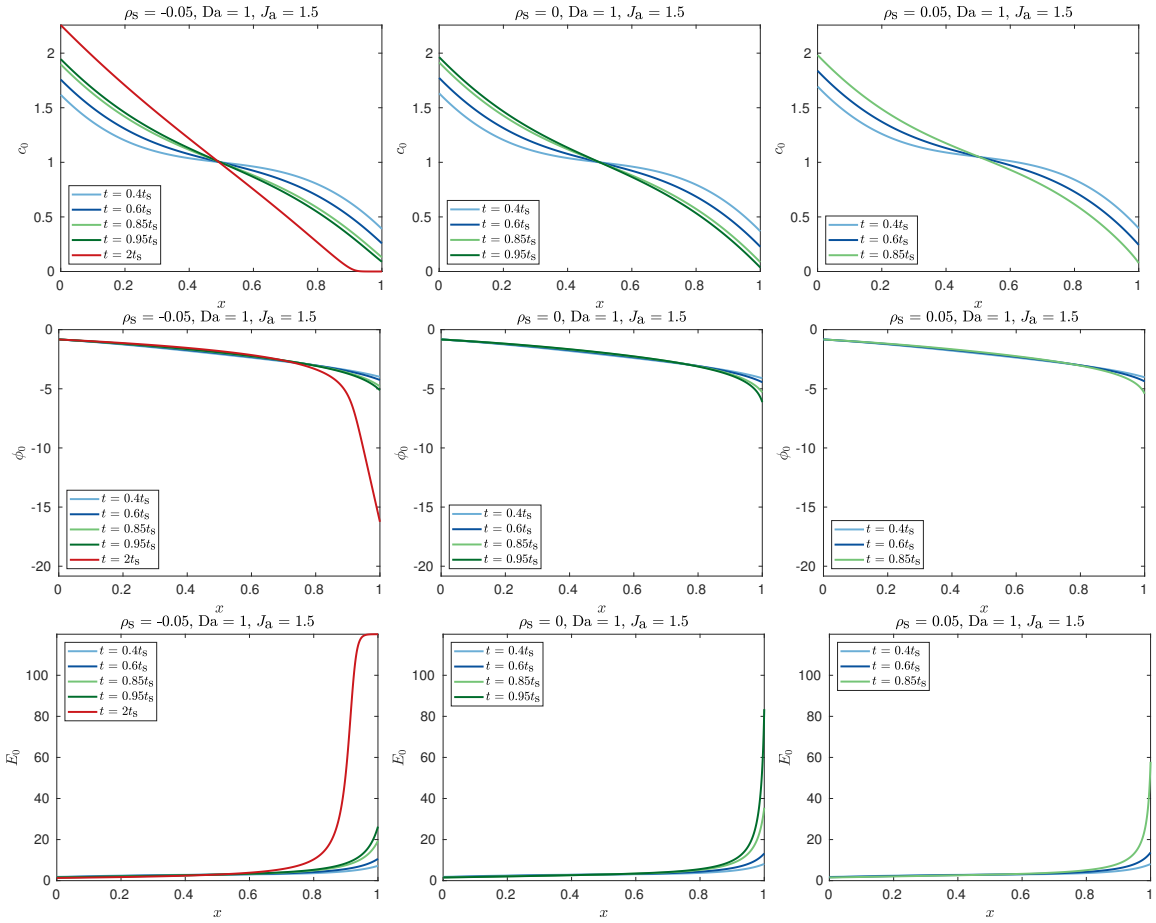

Figure 3-4: Plots of base state c_0, ϕ_0 and E_0 against x for various $\frac{t}{t_s}$ values with $\mathrm{Da} = 1$ and $J_a = 1.5$ (overlimiting current) for $\rho_s \in \{-0.05, 0, 0.05\}$. First row: Plots of c_0 against x. Second row: Plots of ϕ_0 against x. Third row: Plots of E_0 against x. Blue lines correspond to early times $t = 0.4t_s$ and $t = 0.6t_s$, green lines correspond to times near Sand's time $t = 0.85t_s$ and $t = 0.95t_s$, and red line corresponds to time beyond Sand's time $t = 2t_s$. For each color, intensity increases in the direction of increasing t.

bounding the electric field at the cathode, the presence of a negative background charge confers additional stabilization to the system beyond what is provided by surface energy effects, although it does not completely stabilize the system as there are still regions of positive growth rate in the dispersion relation. On the other hand, for the classical case of zero background charge, the system rapidly destabilizes near Sand's time and ultimately diverges at Sand's time because of the diverging electric field at the cathode, which is also demonstrated in [78]. Relative to this classical case, the presence of a positive background charge destabilizes the system even further by generating an electric field at the cathode that is larger at a given time and diverges earlier than Sand's time, resulting in higher growth rates at earlier times and in finite time divergence earlier than Sand's time.

We observe that increasing Da generally increases ω but this effect is very insignificant because the application of an overlimiting current implies that the system is always diffusion-limited regardless of what Da is. Hence, in this regime of diffusion-limited electrodeposition under an overlimiting current, specific details of the electrochemical reaction kinetics model are not important in influencing the dispersion relation as long as the model includes the surface energy stabilizing effect, which typically occurs in the functional form of γk^2.

In the interest of space, plots of numerically computed $\Re(\omega)$ against k for $J_\mathrm{a} = 1$ (limiting current) and $J_\mathrm{a} = 0.5$ (underlimiting current) are not shown here but are given in Figures 3-13 and 3-14 in Appendix 3.8.5 respectively. Since the system is still always diffusion-limited for $J_\mathrm{a} = 1$, the trends observed for $J_\mathrm{a} = 1$ are qualitatively similar to our previous discussion for $J_\mathrm{a} = 1.5$, except that the ω values are smaller because a smaller applied current density results in a smaller electric field at the cathode. For $J_\mathrm{a} = 0.5$, because the applied current density is underlimiting, Sand's time is not defined and at the cathode, the bulk electrolyte concentration does not vanish and the electric field does not diverge at any t. Therefore, the ω curve remains bounded at all t and reaches a steady state eventually. Moreover, ω generally increases with Da, and this increase is especially pronounced when Da increases from 1 to 10. This is because as discussed in Section 3.3.2, the system becomes diffusion-limited

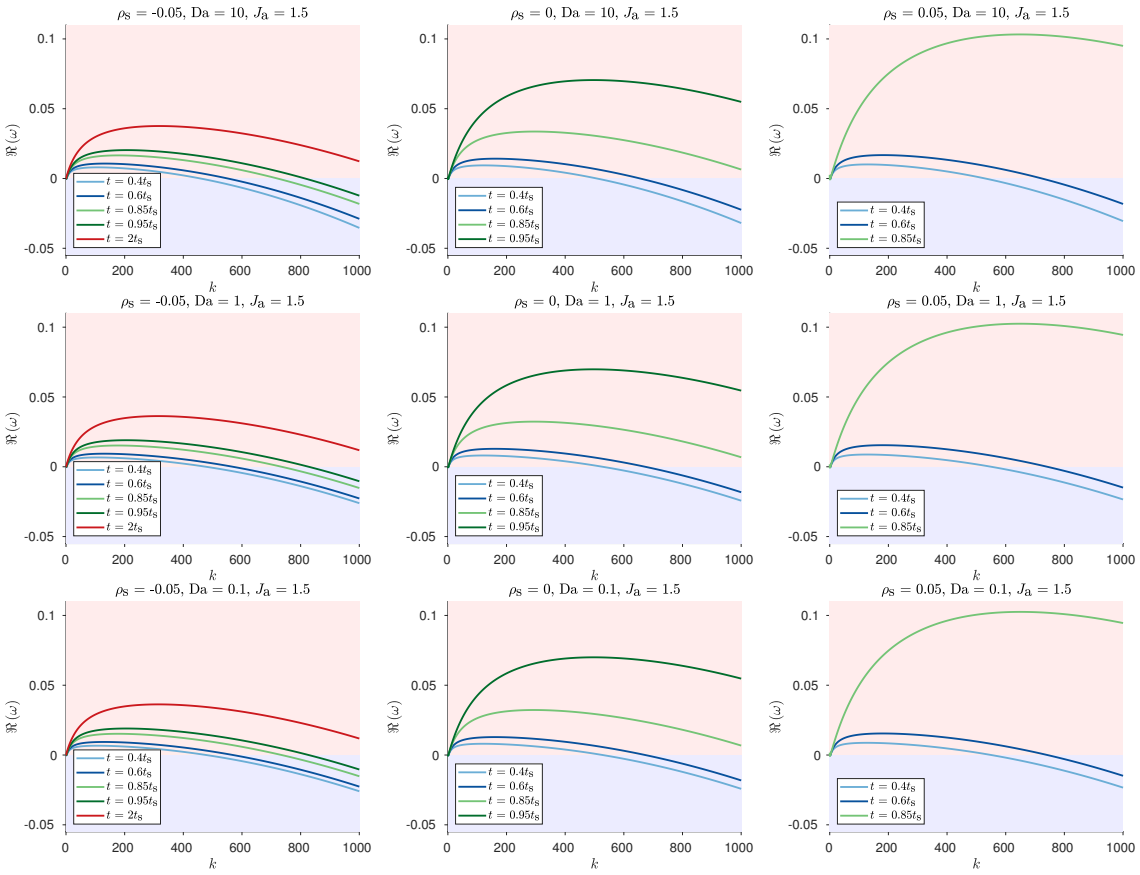

Figure 3-5: Plots of numerical $\Re(\omega)$ against k for various $\frac{t}{t_s}$ values for $\rho_s \in \{-0.05, 0, 0.05\}$, Da $\in \{0.1, 1, 10\}$ and $J_a = 1.5$ (overlimiting current). ρ_s increases from left to right and Da increases from bottom to top. Blue lines correspond to early times $t = 0.4t_s$ and $t = 0.6t_s$, green lines correspond to times near Sand's time $t = 0.85t_s$ and $t = 0.95t_s$, and red line corresponds to time beyond Sand's time $t = 2t_s$. For each color, intensity increases in the direction of increasing t.

when Da $\gg 1$, thus increasing the ion concentration gradients and electric field at the cathode and resulting in a larger growth rate.

As discussed in Section 3.5.1, at each t point, each ω curve exhibits a global maximum $\{k_{max}, \omega_{max}\}$ and a critical wavenumber k_c, which is where the curve crosses the horizontal axis $\omega = 0$. The $\{k_{max}, \omega_{max}\}$ and k_c points provide a succinct way to summarize the most physically significant features of the $\omega(k)$ curve for all the parameter ranges we have explored thus far. Therefore, for $\rho_s \in \{-0.05, 0, 0.05\}$, Da $\in \{0.1, 1, 10\}$ and $J_a \in \{0.5, 1, 1.5\}$, we plot numerically computed k_{max} and ω_{max} against $\frac{t}{t_s}$ in Figure 3-6 and numerically computed k_c against $\frac{t}{t_s}$ in Figure 3-7. For

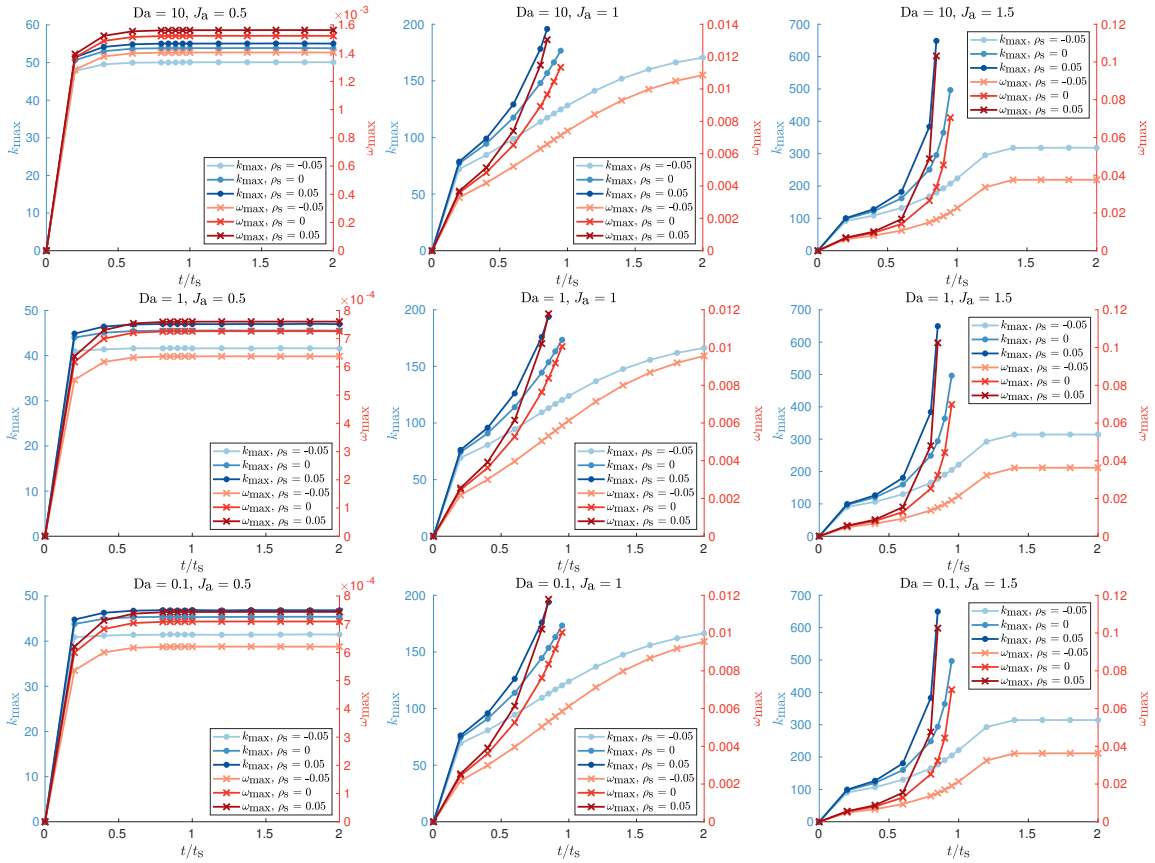

Figure 3-6: Plots of numerical k_{max} and ω_{max} against $\frac{t}{t_s}$ for $\rho_s \in \{-0.05, 0, 0.05\}$, Da $\in \{0.1, 1, 10\}$ and $J_a \in \{0.5, 1, 1.5\}$. ρ_s increases from left to right and Da increases from bottom to top.

$J_a \geq 1$, we observe that the k_{max} and ω_{max} curves diverge near t_s for $\rho_s \geq 0$ but level off to constant values past t_s for $\rho_s < 0$, therefore these curves appear as if they are "fanning out". In contrast, for $J_a < 1$, the k_{max} and ω_{max} curves level off past t_s for all values of ρ_s as the system eventually reaches a steady state when an underlimiting current is applied. The k_c curves have the same qualitative shape as the k_{max} curves except that they are larger, as expected. The effects of Da and J_a on the k_{max}, ω_{max} and k_c values, which are previously discussed in the context of the dispersion relation, are also clearly reflected in Figures 3-6 and 3-7.

In an effort to make the electrode surface less unstable at overlimiting current, we focus on $\rho_s < 0$ to determine how much additional stabilization a negative ρ_s confers to the surface as it gets increasingly more negative. Subsequently, we plot numerically computed k_{max}, ω_{max} and k_c against $\frac{t}{t_s}$ for $\rho_s \in \{-1, -0.75, -0.5, -0.25, -0.05\}$,

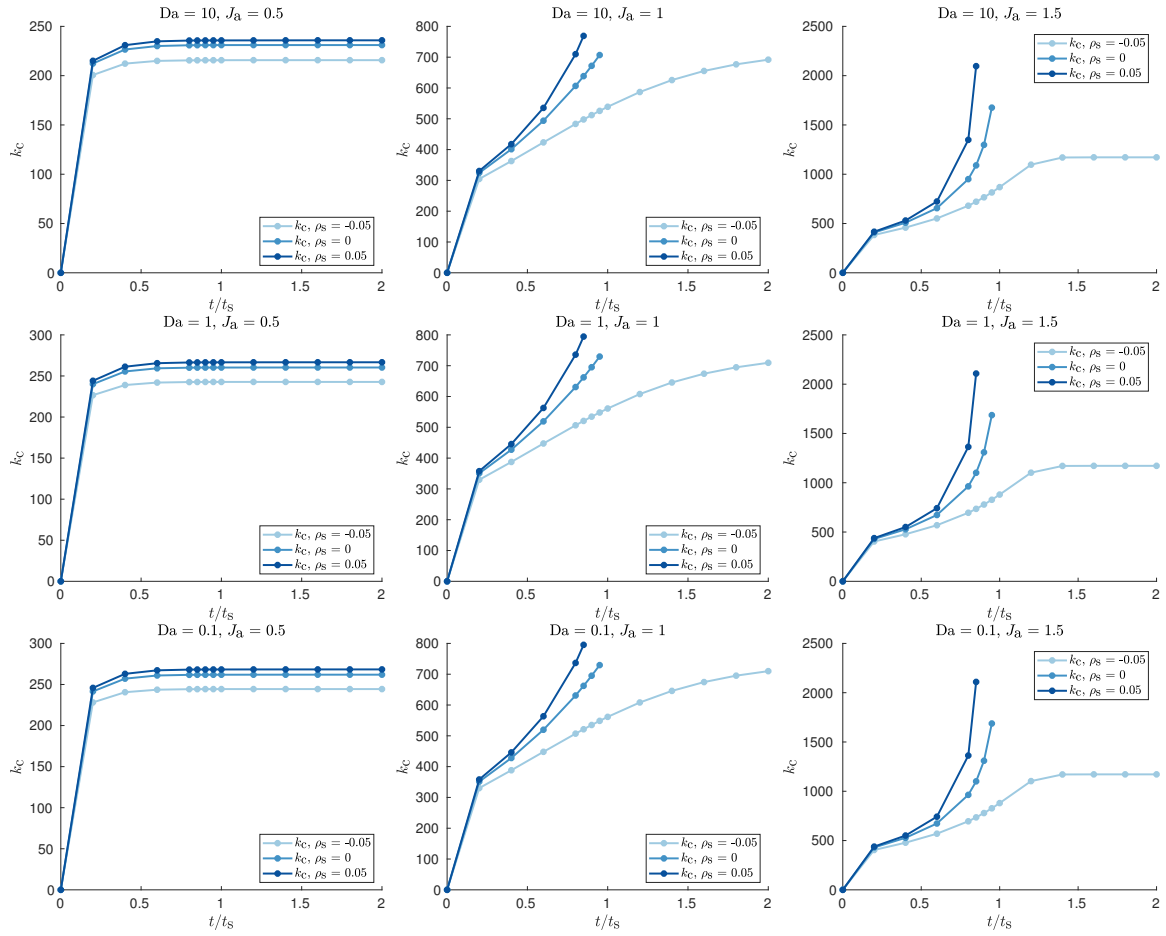

Figure 3-7: Plots of numerical k_c against $\frac{t}{t_s}$ for $\rho_s \in \{-0.05, 0, 0.05\}$, Da $\in \{0.1, 1, 10\}$ and $J_a \in \{0.5, 1, 1.5\}$. ρ_s increases from left to right and Da increases from bottom to top.

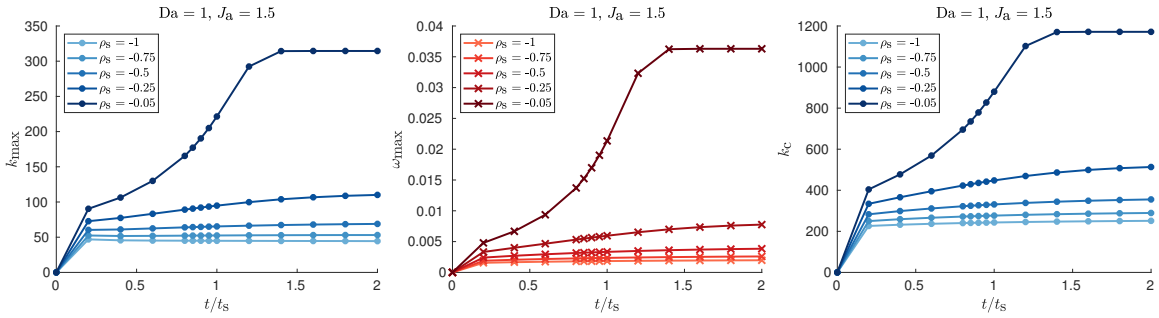

Figure 3-8: Plots of numerical $k_{\max}$, $\omega_{\max}$ and k_c against $\frac{t}{t_s}$ for $\rho_s \in \{-1, -0.75, -0.5, -0.25, -0.05\}$, Da $= 1$ and $J_a = 1.5$ (overlimiting current) for investigating additional stabilization of electrode surface conferred by increasingly negative ρ_s values.

Da $= 1$ and $J_a = 1.5$ in Figure 3-8. While a more negative ρ_s generally decreases $k_{\max}$, $\omega_{\max}$ and k_c, it is clear that there are diminishing returns to the amount of additional stabilization achieved. It also appears that complete stabilization is not possible as $\omega_{\max}$ remains positive even for $\rho_s = -1$, albeit at a small value. In practice, it is probable that a sufficiently small and positive $\omega_{\max}$ value can be deemed to be small enough for considering an electrode surface "practically stable".

3.5.4 Comparison between numerical and approximate solutions

To illustrate how well the approximations given by Equations 3.49 and 3.50 work for the parameter ranges considered, we plot numerical and approximate values of $k_{\max}$, $\omega_{\max}$ and k_c against $\frac{t}{t_s}$ for $\rho_s \in \{-0.05, 0, 0.05\}$, Da $= 1$ and $J_a = 1.5$ in Figure 3-9. In the interest of space, these plots for other values of Da and J_a are provided in Figures 3-15 to 3-20 of Appendix 3.8.6. For all parameter ranges considered, the agreement between numerical and approximate values of $k_{\max}$, $\omega_{\max}$ and k_c is excellent, giving us confidence that the approximations are useful for rapidly and accurately computing $k_{\max}$, $\omega_{\max}$ and k_c. This confirms that $k_{\max}$ and k_c are large enough that Equations 3.49 and 3.50, which have assumed that k is sufficiently large, are accurate for approximating them. We will therefore use Equations 3.49 and 3.50 extensively in Sections 3.5.5 and 3.5.6 that follow.

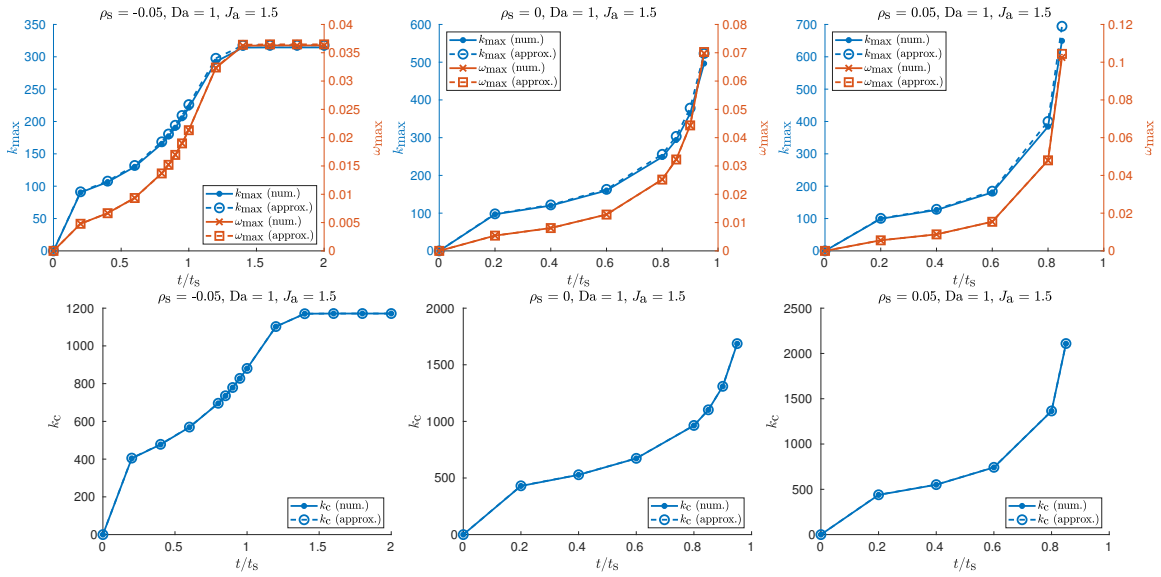

Figure 3-9: Plots of numerical and approximate values of $k_{\max}$, $\omega_{\max}$ and k_c against $\frac{t}{t_s}$ for $\rho_s \in \{-0.05, 0, 0.05\}$, Da $= 1$ and $J_a = 1.5$ (overlimiting current). Top row: Plots of $k_{\max}$ and $\omega_{\max}$. Bottom row: Plots of k_c. In the legends, "num." refers to numerical solutions while "approx." refers to approximate solutions.

3.5.5 Application to copper electrodeposition

We now apply linear stability analysis to the specific case of copper electrodeposition and electrodissolution and compare it with experimental data [106] to determine how well theory agrees with experiment. Because copper electrodeposition involves the overall transfer of two electrons that are transferred one at a time in a serial manner, we need to first derive the overall expression for the Faradaic current density J_F.

Assuming that the activity of electrons is 1 and dilute solution theory is applicable, for a n-electron transfer reaction, the dimensionless forms of Equations 3.12 and 3.9 are given by

$$J_F = j_0\{\exp(-\alpha n\eta) - \exp[(1-\alpha)n\eta]\}, \quad j_0 = k_0 n \hat{c}_O^{1-\alpha}\hat{c}_R^{\alpha} = \mathrm{Da} n \hat{c}_O^{1-\alpha}\hat{c}_R^{\alpha}, \tag{3.51}$$

$$\Delta\phi^{eq} = \frac{1}{n}\ln\frac{\hat{c}_O}{\hat{c}_R} + E^{\ominus} - \frac{2\gamma\mathscr{H}}{n}. \tag{3.52}$$

For multistep electron transfer reactions, it is more convenient to work with $\Delta\phi$

instead of η. Therefore, we rewrite J_{F} in terms of $\Delta\phi$ as

$$J_{\mathrm{F}} = n\left\{k_{\mathrm{c}}\hat{c}_{\mathrm{O}}\exp\left[-\alpha n\left(\Delta\phi + \frac{2\gamma\mathscr{H}}{n}\right)\right] - k_{\mathrm{a}}\hat{c}_{\mathrm{R}}\exp\left[(1-\alpha)n\left(\Delta\phi + \frac{2\gamma\mathscr{H}}{n}\right)\right]\right\}, \tag{3.53}$$

$$E^{\Theta} = \frac{1}{n}\ln\frac{k_{\mathrm{c}}}{k_{\mathrm{a}}}, \quad k_0 = k_{\mathrm{a}}^{\alpha}k_{\mathrm{c}}^{1-\alpha}, \tag{3.54}$$

where k_{c} and k_{a} are the cathodic and anodic rate constants respectively.

The reaction mechanism for copper electrodeposition and electrodissolution is given by [172, 157, 45, 54]

$$\mathrm{Cu}^{2+}(\mathrm{aq}) + \mathrm{e}^{-} \rightleftharpoons \mathrm{Cu}^{+}(\mathrm{ads}), \tag{3.55}$$

$$\mathrm{Cu}^{+}(\mathrm{ads}) + \mathrm{e}^{-} \rightleftharpoons \mathrm{Cu}(\mathrm{s}), \tag{3.56}$$

where (aq), (ads) and (s) indicate aqueous, adsorbed and solid respectively. The first step is assumed to be the rate-determining step while the second step is assumed to be at equilibrium. Applying Equation 3.53 to each step, noting that the activity of solid metal is 1 and rewriting J_{F} in terms of η, we obtain

$$J_{\mathrm{F}} = j_0\{\exp(-\alpha_1\eta) - \exp[(2-\alpha_1)\eta]\}, \quad j_0 = 2k_0\hat{c}_{+}^{1-\frac{\alpha_1}{2}} = 2\mathrm{Da}\hat{c}_{+}^{1-\frac{\alpha_1}{2}}, \tag{3.57}$$

$$\Delta\phi^{\mathrm{eq}} = \frac{1}{2}\ln\hat{c}_{+} + E^{\Theta} - 2\gamma\mathscr{H}, \tag{3.58}$$

where α_1 is the charge transfer coefficient of the first step.

Previously in Section 3.3.2, for a 1-step n-electron transfer metal electrodeposition reaction, the dimensionless forms of Equations 3.12 and 3.13 are given by

$$J_{\mathrm{F}} = j_0\{\exp(-\alpha n\eta) - \exp[(1-\alpha)n\eta]\}, \quad j_0 = k_0 n\hat{c}_{+}^{1-\alpha} = \mathrm{Da}n\hat{c}_{+}^{1-\alpha}, \tag{3.59}$$

$$\Delta\phi^{\mathrm{eq}} = \frac{1}{n}\ln\hat{c}_{+} + E^{\Theta} - \frac{2\gamma\mathscr{H}}{n}. \tag{3.60}$$

By comparing Equations 3.57 and 3.58 with Equations 3.59 and 3.60, we set $n = 2$ and $\alpha = \frac{\alpha_1}{2}$ and replace γ with 2γ in the original set of equations in order to adapt

the linear stability analysis for copper electrodeposition.

By carrying out nonlinear least squares fitting on experimental steady state current-voltage relations, we have previously performed parameter estimation [122] for copper electrodeposition in a copper(II) sulfate ($CuSO_4$) electrolyte in cellulose nitrate (CN) membranes [106], which are a random nanoporous medium with well connected pores. The parameters that are estimated are ρ_s, τ, Da, α_1 and ϵ_p and their fitted values are provided in Table III in [122]. Other parameters specific to the copper electrodeposition reaction, $CuSO_4$ electrolyte and CN membranes used are also provided in Tables I and II in [122]. For the surface energy of the copper/electrolyte interface, we use dimensional $\gamma = 1.85\,\mathrm{J/m^2}$ given in Table I in [174].

For our analysis here, the specific experimental datasets that we focus on are labeled $CN_2(-)$ and $CN_2(+)$ in [122], which correspond to negatively and positively charged CN membranes respectively with a dimensional electrolyte concentration c_0 of 100 mM. We will drop the 2 subscript for brevity. The morphologies of the electrodeposited copper films, which are visualized by EDS (energy dispersive X-ray spectroscopy) maps, for these CN(−) and CN(+) membranes at 2000 s for dimensional applied currents I_a of 15 mA, 20 mA and 25 mA are given in Figure 3-10(a) that consists of magnifications of EDS maps taken from Figures 6(a) to 6(f) of [106]. At 15 mA, the copper films for both CN(+) and CN(−) membranes appear to be uniform and stable. However, at 20 mA and 25 mA, the film for CN(+) becomes very unstable and roughens more as the applied current increases. It is difficult to determine quantitatively the instability wavelength using the relatively low resolution EDS maps but it is probably much smaller than 5 μm. In contrast, for CN(−), the film still remains uniform and stable at 20 mA but slightly destabilizes and roughens at 25 mA with an instability wavelength probably on the order of 5 μm. In summary, the onset of overall electrode surface destabilization occurs at 20 mA for CN(+) with an instability wavelength of much smaller than 5 μm and at 25 mA for CN(−) with an instability wavelength of about 5 μm.

Because the EDS maps are taken at 2000 s, which is much longer than the diffusion times for CN(−) and CN(+) of 41.8 s and 40.9 s respectively, we assume that

the system is at steady state. This assumption allows us to use the semi-analytical expressions for the base state variables in [122], which we have previously discussed in Section 3.4.3, to compute approximate values of $\{k_{\max}, \omega_{\max}\}$ and k_c using Equations 3.49 and 3.50. The CN(−) dataset has a dimensional limiting current of 18.2 mA while the CN(+) dataset has a dimensional maximum current, which we have discussed in Section 3.3.1, of 16.9 mA. Therefore, for CN(−), the three applied currents of 15 mA, 20 mA and 25 mA correspond to underlimiting, slightly overlimiting and overlimiting currents respectively. On the other hand, for CN(+), the model eventually diverges and does not admit a steady state when the applied current I_a is above the maximum current $I_{\max}$, therefore we can only obtain finite values of $\{k_{\max}, \omega_{\max}\}$ and k_c for the applied current of 15 mA while the model predicts infinite values of $\{k_{\max}, \omega_{\max}\}$ and k_c for the applied currents of 20 mA and 25 mA due to finite time divergence of the system. Other fitted key dimensionless parameters include $\rho_s \approx -0.01$ and $\mathrm{Da} \approx 2.50$ for CN(−) and $\rho_s \approx 0.236$ and $\mathrm{Da} \approx 0.473$ for CN(+).

To summarize the model predictions, we plot approximate dimensional values of λ_c and $\lambda_{\max}$ against the dimensional applied current I_a in Figure 3-10. In the λ_c plot in Figure 3-10(a), we also indicate the characteristic pore size h_c of $0.5 \pm 0.1\,\mu$m, which is given by twice the pore diameter d_p of 250 ± 50 nm [106], in order to determine if the model predicts overall electrode surface stabilization. As discussed in Section 3.5.1, we expect overall electrode surface stabilization if $h_c < \lambda_c$, which corresponds to the blue shaded region in the λ_c plot. On the contrary, we expect overall electrode surface destabilization if $h_c > \lambda_c$, which corresponds to the red shaded region in the λ_c plot, and the characteristic instability wavelength is $\lambda_{\max}$. Comparing the λ_c plot with our previous discussion of the onset of overall electrode surface destabilization suggested by the copper film morphologies observed experimentally, we see that the model generally agrees well with experiment; the only disagreement is at $I_a = 20$ mA where the model predicts destabilization for CN(−), which has $\lambda_c = 0.352\,\mu$m, while the EDS map of the copper film at this applied current shows that the film appears to be stable. Nonetheless, this disagreement in theory and experiment is relatively minor since $\lambda_c = 0.352\,\mu$m for CN(−) at $I_a = 20$ mA is only slightly smaller than

the mean of h_c of $0.5\,\mu$m and is almost equal to the lower bound of h_c of $0.4\,\mu$m. In addition, the model predicts $\lambda_{max} = 0$ (because $k_{max} \to \infty$ when $I_a > I_{max}$) at $I_a = 20\,$mA and $I_a = 25\,$mA for CN(+) while it predicts $\lambda_{max} = 1.09\,\mu$m at $I_a = 25\,$mA for CN(−). These model predictions of λ_{max} qualitatively agree well with the experimentally observed instability wavelengths at these applied currents that we have previously discussed. Therefore, in conclusion, the theory agrees reasonably well with experimental data, especially given that many assumptions and simplifications are made in the model.

3.5.6 Pulse electroplating and pulse charging

For many electrochemical applications such as electroplating and charging of metal batteries, which is equivalent to electrodeposition at the metal negative electrode, it is desirable to operate them as quickly as possible at a high current without causing the formation of dendrites that short-circuit the system. To delay or prevent the formation of dendrites, it is common to perform pulse electroplating of metals [74, 58] or pulse charging of lithium metal batteries (LMBs) and lithium-ion batteries (LIBs) [137, 191, 190, 276, 116, 226, 216, 158, 18] so that there is sufficient time between pulses for the concentration gradients and electric field in the system to relax. For pulse electroplating of metals, it has been empirically observed that the crystal grain size generally decreases with applied current [74, 58]. Using an applied direct current to perform silver electrodeposition under galvanostatic conditions, Aogaki experimentally observed that the crystal grain size decreases with time [7, 8], which agrees well with theoretical predictions from linear stability analysis previously done by Aogaki and Makino [10]. With all these considerations in mind, we apply our linear stability analysis with a time-dependent base state as a tool to investigate how pulse electroplating protocols with high average applied currents, which are inherently time-dependent, affect the linear stability of the electrode surface and the crystal grain size for both zero and negative pore surface charges.

Based on the results in Section 3.5.5, we generally expect the characteristic pore size h_c to be larger than the critical wavelength λ_c at high applied currents, therefore

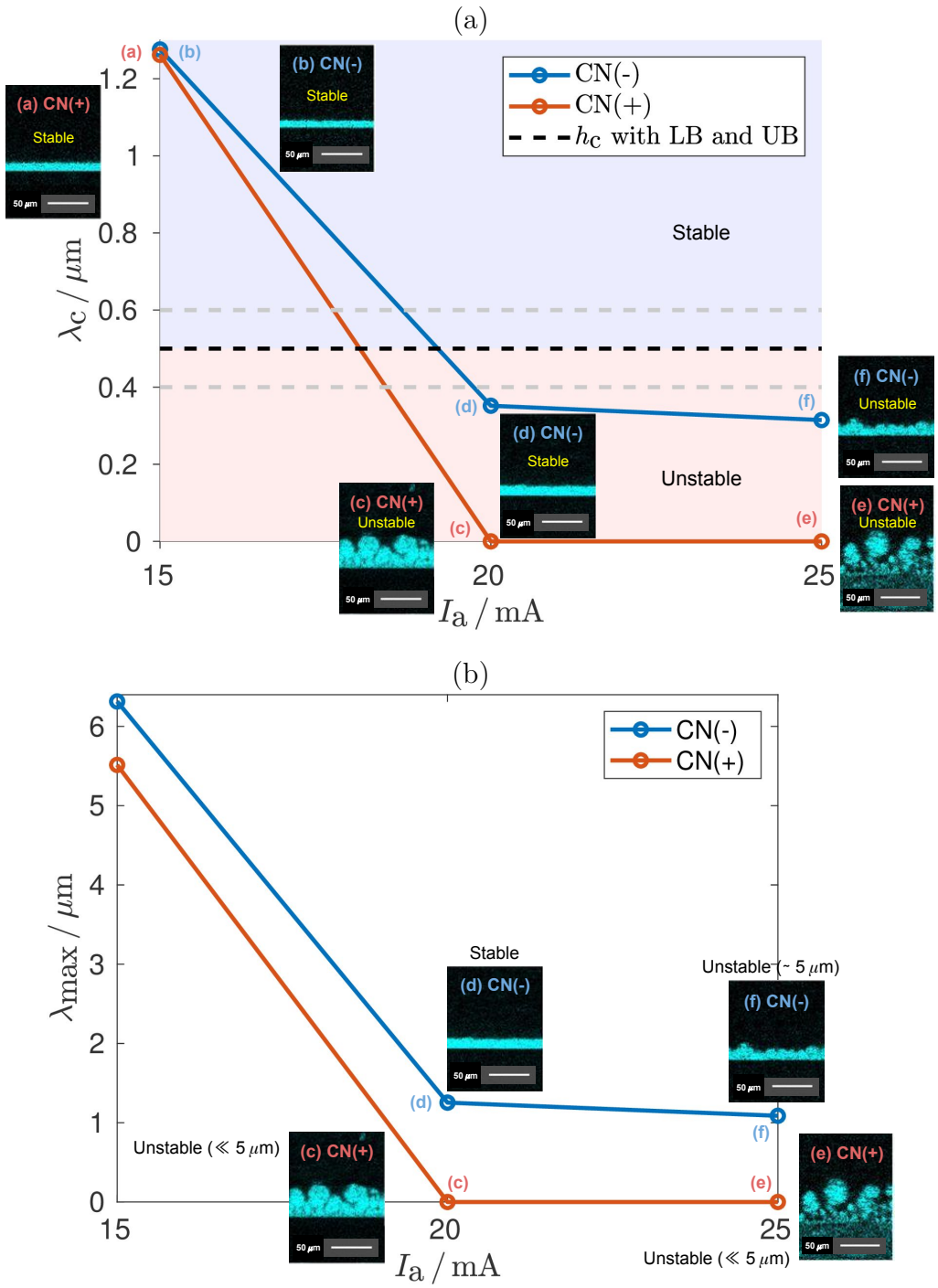

Figure 3-10: Plots of EDS (energy dispersive X-ray spectroscopy) maps at 2000 s, and approximate dimensional λ_c (a) and λ_{max} (b) at steady state against dimensional applied current I_a for copper electrodeposition in 100 mM copper(II) sulfate ($CuSO_4$) electrolyte in cellulose nitrate (CN) membranes. EDS maps in (a) and (b) are magnifications of EDS maps in Figures 6(a) to 6(f) of [106] where the scale bars indicate 50 μm. $h_c = 0.5 \pm 0.1\,\mu$m in the λ_c plot in (a) is the characteristic pore size where the mean is indicated by the black dashed line while the lower (LB) and upper (UB) bounds are indicated by gray dashed lines.

the electrode surface is unstable with a characteristic instability wavelength $\lambda_{\max}$. Because a pulse current is applied, $\lambda_{\max}$ varies in time and hence, it would be useful to define an average $\lambda_{\max}$ that averages out the effect of time. In this spirit, we define the average maximum wavenumber $\bar{k}_{\max}$ and the corresponding average maximum wavelength $\bar{\lambda}_{\max}$ as

$$\bar{k}_{\max} = \frac{\int_0^{t_f} k_{\max}\omega_{\max}\,\mathrm{d}t}{\int_0^{t_f} \omega_{\max}\,\mathrm{d}t}, \quad \bar{\lambda}_{\max} = \frac{2\pi}{\bar{k}_{\max}}, \tag{3.61}$$

where t_f is the final time of the pulse and each maximum wavenumber $k_{\max}$ is weighted by its corresponding maximum growth rate $\omega_{\max}$. We expect $\bar{\lambda}_{\max}$ to be on the same order of magnitude as the the crystal grain size that is observed experimentally. As a simple example, we suppose that the pulse electroplating protocol is a periodic pulse wave J_a with an "on" (charging) time of Δt_{on}, a "off" (relaxation) time of Δt_{off}, and a period T given by $T = \Delta t_{on} + \Delta t_{off}$. The duty cycle γ_{dc} is given by $\gamma_{dc} = \frac{\Delta t_{on}}{T}$ and the average applied current density $\bar{J}_a$ over one period is given by $\bar{J}_a = J_{a,p}\gamma_{dc}$ where $J_{a,p}$ is the peak applied current density. Hence, for a particular $\bar{J}_a$, a smaller γ_{dc} implies a larger $J_{a,p}$.

For the classical case of $\rho_s = 0$, we pick $\bar{J}_a = 1$ and $\Delta t_{on} = 0.0125 t_s$ and vary γ_{dc} from 0.2 to 1 (direct current) where the Sand's time t_s is calculated based on $\bar{J}_a$. $\bar{J}_a$, Δt_{on} and γ_{dc} should be carefully chosen such that $J_{a,p}$ is not too high to deplete the bulk electrolyte at the cathode during the "on" cycle so that the system does not diverge at any point in time; this explains why $\gamma_{dc} < 0.2$ for our choice of $\bar{J}_a = 1$ and $\Delta t_{on} = 0.0125 t_s$ cannot be numerically simulated. For $\rho_s = -0.05$, we pick $\bar{J}_a = 1.5$ and $\Delta t_{on} = t_s$ and vary γ_{dc} from 0.1 to 1 (direct current) to drive the system at an overlimiting average applied current density. We also fix Da = 1 for both cases and use Equations 3.49 and 3.50 to compute approximate values of $k_{\max}$ and $\omega_{\max}$. For these choices of parameters, as an illustrative example, we plot J_a, approximate $k_{\max}$ and approximate $\omega_{\max}$ against t for $\gamma_{dc} = 0.5$ in Figure 3-11. We note that the large overshoot in $k_{\max}$ at the beginning of each "on" cycle for $\rho_s = 0$ is caused by the sharp rate of increase of the concentration gradients and electric field as J_a

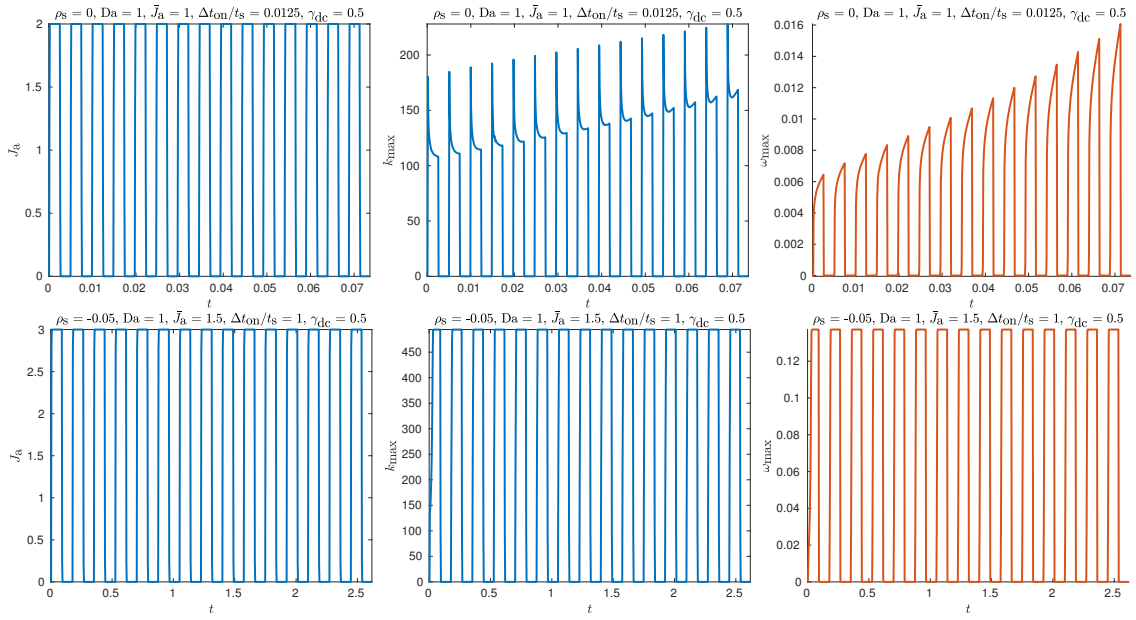

Figure 3-11: Plots of J_a, approximate k_{max} and approximate ω_{max} against t with Da $= 1$ and $\gamma_{dc} = 0.5$ for pulse electroplating. Top row: $\rho_s = 0$, $\bar{J}_a = 1$ and $\Delta t_{on} = 0.0125 t_s$. Bottom row: $\rho_s = -0.05$, $\bar{J}_a = 1.5$ and $\Delta t_{on} = t_s$.

rapidly increases from 0 in the "off" cycle to $J_{a,p}$ in the "on" cycle. Corresponding to these pulse waves, we plot $\bar{\lambda}_{max}$ against γ_{dc} in Figure 3-12. For both $\rho_s = 0$ and $\rho_s = -0.05$, $\bar{\lambda}_{max}$ increases with γ_{dc}, which agrees with the empirical observation that the crystal grain size generally decreases with applied current [74, 58]. The ability to experimentally impart a negative pore surface charge to the nanoporous medium therefore enables pulse electroplating at overlimiting currents for electrodepositing a large amount of charge at a high rate and tuning the desired crystal grain size.

3.6 Conclusion

We have derived the full model that couples the leaky membrane model for ion transport, which is capable of predicting overlimiting current due to surface conduction, with Butler-Volmer reaction kinetics, which describes the metal electrodeposition reaction, and performed linear stability analysis on it with respect to a time-dependent base state. The volume-averaged background charge density can generally be of any sign. As a result, we have generalized previous work on linear stability analysis of

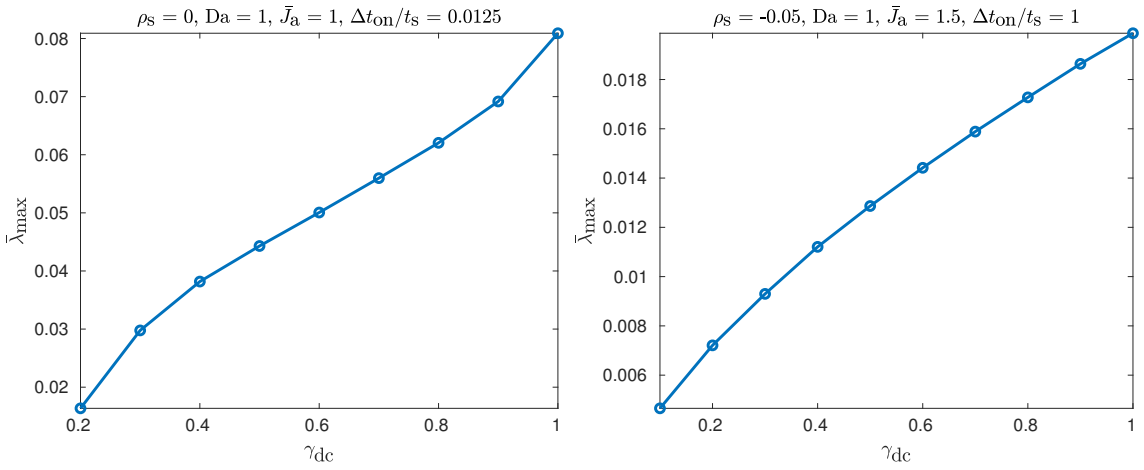

Figure 3-12: Plots of $\bar{\lambda}_{max}$ against γ_{dc} with Da $= 1$. Left: $\rho_s = 0$, $\bar{J}_a = 1$ and $\Delta t_{on} = 0.0125 t_s$. Right: $\rho_s = -0.05$, $\bar{J}_a = 1.5$ and $\Delta t_{on} = t_s$.

electrodeposition carried out in [236, 78, 241]. We then performed a boundary layer analysis on the perturbed state in order to derive an accurate approximation for the dispersion relation and a convergence analysis to verify the accuracy and convergence of the full numerical solution of the dispersion relation. By performing parameter sweeps over the volume-averaged background charge density, Damköhler number and applied current density under galvanostatic conditions, we have concluded that a negative background charge significantly stabilizes the electrode surface instability, although it does not completely stabilize it, while a positive background charge further destabilizes this instability. We have also verified that the approximations for the maximum wavenumber, maximum growth rate and and critical wavenumber are very accurate, and applied them to demonstrate good agreement between theory and experimental data for copper electrodeposition in cellulose nitrate membranes [106]. Lastly, we have employed the linear stability analysis as a tool to analyze the dependence of the crystal grain size on duty cycle in pulse electroplating. These results demonstrate the predictive power and robustness of the theory despite its simplicity. Although detailed analysis of the Poisson-Nernst-Planck-Stokes equations for transport in a microchannel by Nielsen and Bruus [173] reveals that the leaky membrane model for surface conduction is at best a rough approximation of the real system, the good agreement between theory and experiment that we have demonstrated sug-

gests that the model is applicable in similar electrochemical systems using charged membranes such as shock electrodialysis [72, 221, 219].

We have made many assumptions and simplifications in the model presented, and relaxing some of them offers opportunities for extending it in useful ways. First, we have ignored surface adsorption, surface diffusion of adsorbed species [11, 12, 13, 14] and additional mechanical effects such as pressure, viscous stress and deformational stress [164, 165, 242, 2, 1, 171], which confer additional stabilization to the electrode surface. Adding these physics and chemistry to the model are likely to result in finite values of the maximum wavenumber, maximum growth rate and critical wavenumber near and at Sand's time under an overlimiting current for zero and positive background charges respectively, as opposed to diverging in our current model. The inclusion of these additional mechanical effects will also extend the applicability of the model to solid electrolytes that are used in solid state batteries. Second, in order to apply the linear stability analysis to lithium metal batteries (LMBs), we would also need to model the solid electrolyte interphase (SEI) layer [252, 63, 184, 256], which will certainly increase the complexity of the model but also make it more predictive. Third, other chemical mechanisms for overlimiting current such as water splitting [176, 175] and current-induced membrane discharge [6] may be present. These effects are typically highly nonlinear and therefore, we expect them to significantly influence the transient base state and linear stability analysis. Fourth, we should consider the effects of coupling nucleation, which is fundamentally a nonlinear instability unlike spinodal decomposition that is a linear instability, to the current model. Specifically, nucleation may affect the transient base state during initial and early reaction-limited surface growth and create surface roughness on the scale of the characteristic nucleus size, which may in turn influence overall electrode surface stabilization or destabilization when the system reaches transport limitation near or at Sand's time. Fifth, an interesting and useful generalization of the reaction model would be to use the symmetric Marcus-Hush-Chidsey kinetics [20, 275] or asymmetric Marcus-Hush kinetics [274] instead of Butler-Volmer kinetics for modeling electron transfer reactions, which would afford us the reorganization energy as a key system

parameter whose influence on the linear stability of the electrode surface can be investigated.

3.7 Acknowledgments

E. Khoo acknowledges support from the National Science Scholarship (PhD) funded by Agency for Science, Technology and Research, Singapore (A*STAR).

3.8 Appendix

Throughout the appendix, to avoid cluttering the notation, we rewrite the (0) and (1) superscripts, which denote the base and perturbed states respectively in the main text, as 0 and 1 subscripts respectively. The "a" and "c" superscripts denote the anode and cathode respectively. We use subscripts to denote partial derivatives with respect to x, y, z and t, primes to denote total derivatives with respect to x, and an overhead dot to denote the total derivative with respect to t.

3.8.1 Electrode/electrolyte interfaces

An illustration of the system under consideration is given in Figure 1 of the main text. In general, the electrode/electrolyte interfaces in 3D can be represented by $g^{\mathrm{a,c}}(x,y,z,t)=0$ where $x\in[0,L_x]$, $y\in[0,L_y]$ and $z\in[0,L_z]$. If the electrode/electrolyte interfaces can be represented explicitly by $x=h^{\mathrm{a,c}}(y,z,t)$ where $h^{\mathrm{a,c}}$ is the electrode surface height, we express $g^{\mathrm{a,c}}(x,y,z,t)$ as $g^{\mathrm{a,c}}(x,y,z,t)=x-h^{\mathrm{a,c}}(y,z,t)=0$. Thus [71, 69],

$$H=\big(1+h_y^2+h_z^2\big)^{\frac{1}{2}}, \tag{3.62}$$

$$\begin{aligned}\nabla_{\mathrm{s}}=\frac{1}{H^2}\big\{&\big[\big(h_y^2+h_z^2\big)e_x+h_ye_y+h_ze_z\big]\partial_x\\&+\big[h_ye_x+\big(h_z^2+1\big)e_y-h_yh_ze_z\big]\partial_y\\&+\big[h_ze_x-h_yh_ze_y+\big(h_y^2+1\big)e_z\big]\partial_z\big\},\end{aligned} \tag{3.63}$$

$$\hat{n}(r = r_{\mathrm{m}}^{\mathrm{a}}) = -\frac{\nabla g^{\mathrm{a}}}{|\nabla g^{\mathrm{a}}|} = -\frac{e_x - h_y^{\mathrm{a}} e_y - h_z^{\mathrm{a}} e_z}{H^{\mathrm{a}}}, \tag{3.64}$$

$$\hat{n}(r = r_{\mathrm{m}}^{\mathrm{c}}) = \frac{\nabla g^{\mathrm{c}}}{|\nabla g^{\mathrm{c}}|} = \frac{e_x - h_y^{\mathrm{c}} e_y - h_z^{\mathrm{c}} e_z}{H^{\mathrm{c}}}, \tag{3.65}$$

$$\hat{n}(y = 0) = -e_y, \tag{3.66}$$

$$\hat{n}(y = L_y) = e_y, \tag{3.67}$$

$$\hat{n}(z = 0) = -e_z, \tag{3.68}$$

$$\hat{n}(z = L_z) = e_z, \tag{3.69}$$

$$2\mathscr{H}^{\mathrm{a}} = -\nabla_{\mathrm{s}} \cdot \hat{n}(r = r_{\mathrm{m}}^{\mathrm{a}}) = -\frac{1}{(H^{\mathrm{a}})^3}\Big\{\big[(h_z^{\mathrm{a}})^2 + 1\big]h_{yy}^{\mathrm{a}} - 2h_y^{\mathrm{a}} h_z^{\mathrm{a}} h_{yz}^{\mathrm{a}} + \Big[\big(h_y^{\mathrm{a}}\big)^2 + 1\Big]h_{zz}^{\mathrm{a}}\Big\}, \tag{3.70}$$

$$2\mathscr{H}^{\mathrm{c}} = -\nabla_{\mathrm{s}} \cdot \hat{n}(r = r_{\mathrm{m}}^{\mathrm{c}}) = \frac{1}{(H^{\mathrm{c}})^3}\Big\{\big[(h_z^{\mathrm{c}})^2 + 1\big]h_{yy}^{\mathrm{c}} - 2h_y^{\mathrm{c}} h_z^{\mathrm{c}} h_{yz}^{\mathrm{c}} + \Big[\big(h_y^{\mathrm{c}}\big)^2 + 1\Big]h_{zz}^{\mathrm{c}}\Big\}, \tag{3.71}$$

$$v_{\mathrm{I}} = \epsilon_{\mathrm{p}} \dot{r}_{\mathrm{m}} = \epsilon_{\mathrm{p}}[(h_t + h_y \dot{y} + h_z \dot{z})e_x + \dot{y} e_y + \dot{z} e_z], \tag{3.72}$$

$$v_{\mathrm{In}}^{\mathrm{a}} = \hat{n} \cdot v_{\mathrm{I}}(r = r_{\mathrm{m}}^{\mathrm{a}}) = -\frac{\epsilon_{\mathrm{p}}}{H^{\mathrm{a}}} h_t^{\mathrm{a}}, \tag{3.73}$$

$$v_{\mathrm{In}}^{\mathrm{c}} = \hat{n} \cdot v_{\mathrm{I}}(r = r_{\mathrm{m}}^{\mathrm{c}}) = \frac{\epsilon_{\mathrm{p}}}{H^{\mathrm{c}}} h_t^{\mathrm{c}}, \tag{3.74}$$

where $r = [x, y, z]^{\mathrm{T}}$ is the position vector, $r_{\mathrm{m}}^{\mathrm{a,c}} = [x_{\mathrm{m}}^{\mathrm{a,c}}, y_{\mathrm{m}}^{\mathrm{a,c}}, z_{\mathrm{m}}^{\mathrm{a,c}}]^{\mathrm{T}}$, $\mathscr{H}^{\mathrm{a,c}}$, $v_{\mathrm{I}}^{\mathrm{a,c}}$ and $v_{\mathrm{In}}^{\mathrm{a,c}}$ are the position, mean curvature, velocity and normal velocity of the electrode/electrolyte interface respectively, ∇_{s} is the surface gradient operator and $\hat{n}(r = r_{\mathrm{m}}^{\mathrm{a,c}})$ is the unit normal that points outwards from the electrolyte. We let $k = [k_y, k_z]^{\mathrm{T}}$ and $\xi = [y, z]^{\mathrm{T}}$ where k is the wavevector, and k_y and k_z are the wavenumbers in the y and z directions respectively. Therefore, $k \cdot \xi = k_y y + k_z z$, $k^2 = \|k\|_2^2 = k_y^2 + k_z^2$ where $\|\cdot\|_2$ is the L^2-norm and $\|k\|_2$ is the overall wavenumber, and the wavelength λ is given by $\lambda = \frac{2\pi}{\|k\|_2}$. For brevity, we write the overall wavenumber as k and it is obvious from context whether k refers to the wavevector or overall wavenumber. We assume that the perturbations to the electrode/electrolyte interfaces are sinusoidal in the y and z directions given by

$$h(\xi, t) = h_0(t) + \epsilon \Re[h_1 \exp(ik \cdot \xi + \omega t)] + \mathcal{O}\big(\epsilon^2\big) \tag{3.75}$$

where $\epsilon \ll 1$ is a dimensionless small parameter, the 0 and 1 subscripts denote the base and perturbed states respectively, $\Re(\cdot)$ gives the real part of a complex number, h_1 is the complex-valued perturbation amplitude of the electrode surface height, and ω is the complex-valued growth rate of the perturbation.

For nondimensionalization, we define $\tilde{x} \equiv \frac{x}{L_x}$, $\tilde{y} \equiv \frac{y}{L_x}$, $\tilde{z} \equiv \frac{z}{L_x}$, $\tilde{t} \equiv \frac{D_{\mathrm{amb0}} t}{L_x^2}$, $\tilde{L}_y \equiv \frac{L_y}{L_x}$, $\tilde{L}_z \equiv \frac{L_z}{L_x}$, $\tilde{r} \equiv \frac{r}{L_x}$, $\tilde{r}_{\mathrm{m}}^{\mathrm{a,c}} \equiv \frac{r_{\mathrm{m}}^{\mathrm{a,c}}}{L_x}$, $\tilde{\nabla} \equiv L_x \nabla$, $\tilde{\mathscr{H}}^{\mathrm{a,c}} \equiv L_x \mathscr{H}^{\mathrm{a,c}}$, $\tilde{v}_{\mathrm{I}}^{\mathrm{a,c}} \equiv \frac{L_x v_{\mathrm{I}}^{\mathrm{a,c}}}{\epsilon_{\mathrm{p}} D_{\mathrm{amb0}}}$, $\tilde{v}_{\mathrm{In}}^{\mathrm{a,c}} \equiv \frac{L_x v_{\mathrm{In}}^{\mathrm{a,c}}}{\epsilon_{\mathrm{p}} D_{\mathrm{amb0}}}$, $\tilde{h}^{\mathrm{a,c}} \equiv \frac{h^{\mathrm{a,c}}}{L_x}$, $\tilde{h}_0 \equiv \frac{h_0}{L_x}$, $\tilde{h}_1 \equiv \frac{h_1}{L_x}$, $\tilde{k}_y \equiv L_x k_y$, $\tilde{k}_z \equiv L_x k_z$, $\tilde{k} \equiv L_x k$, $\tilde{\lambda} \equiv \frac{\lambda}{L_x}$, $\tilde{\xi} \equiv \frac{\xi}{L_x}$ and $\tilde{\omega} \equiv \frac{L_x^2 \omega}{D_{\mathrm{amb0}}}$. Therefore, dropping tildes on dimensionless variables and parameters to avoid cluttering the notation,

$$H = \left(1 + h_y^2 + h_z^2\right)^{\frac{1}{2}}, \tag{3.76}$$

$$\hat{n}(r = r_{\mathrm{m}}^{\mathrm{a}}) = -\frac{e_x - h_y^{\mathrm{a}} e_y - h_z^{\mathrm{a}} e_z}{H^{\mathrm{a}}}, \tag{3.77}$$

$$\hat{n}(r = r_{\mathrm{m}}^{\mathrm{c}}) = \frac{e_x - h_y^{\mathrm{c}} e_y - h_z^{\mathrm{c}} e_z}{H^{\mathrm{c}}}, \tag{3.78}$$

$$\hat{n}(y = 0) = -e_y, \tag{3.79}$$

$$\hat{n}(y = L_y) = e_y, \tag{3.80}$$

$$\hat{n}(z = 0) = -e_z, \tag{3.81}$$

$$\hat{n}(z = L_z) = e_z, \tag{3.82}$$

$$2\mathscr{H}^{\mathrm{a}} = -\frac{1}{\left(H^{\mathrm{a}}\right)^3}\left\{\left[\left(h_z^{\mathrm{a}}\right)^2 + 1\right] h_{yy}^{\mathrm{a}} - 2h_y^{\mathrm{a}} h_z^{\mathrm{a}} h_{yz}^{\mathrm{a}} + \left[\left(h_y^{\mathrm{a}}\right)^2 + 1\right] h_{zz}^{\mathrm{a}}\right\}, \tag{3.83}$$

$$2\mathscr{H}^{\mathrm{c}} = \frac{1}{\left(H^{\mathrm{c}}\right)^3}\left\{\left[\left(h_z^{\mathrm{c}}\right)^2 + 1\right] h_{yy}^{\mathrm{c}} - 2h_y^{\mathrm{c}} h_z^{\mathrm{c}} h_{yz}^{\mathrm{c}} + \left[\left(h_y^{\mathrm{c}}\right)^2 + 1\right] h_{zz}^{\mathrm{c}}\right\}, \tag{3.84}$$

$$v_{\mathrm{In}}^{\mathrm{a}} = -\frac{1}{H^{\mathrm{a}}} h_t^{\mathrm{a}}, \tag{3.85}$$

$$v_{\mathrm{In}}^{\mathrm{c}} = \frac{1}{H^{\mathrm{c}}} h_t^{\mathrm{c}}, \tag{3.86}$$

$$h(\xi, t) = h_0(t) + \epsilon \Re[h_1 \exp(ik \cdot \xi + \omega t)] + \mathcal{O}\left(\epsilon^2\right). \tag{3.87}$$

3.8.2 Dimensionless full model

We define more dimensionless variables and parameters in order to nondimensionalize the full model: $\tilde{c}_{\pm} \equiv \frac{c_{\pm}}{\nu_{\pm} c_0}$, $\tilde{\beta}_1 \equiv \frac{\beta_1}{\nu_- c_0} = 1 + \frac{\tilde{\rho}_{\mathrm{s}} + |\tilde{\rho}_{\mathrm{s}}|}{2}$, $\tilde{\phi} \equiv \frac{e\phi}{k_{\mathrm{B}} T}$, $\tilde{F}_{\pm} \equiv \frac{L_x F_{\pm}}{\epsilon_{\mathrm{p}} D_{\mathrm{amb0}} \nu_{\pm} c_0}$, $\tilde{D}_{\pm 0} \equiv \frac{D_{\pm 0}}{D_{\mathrm{amb0}}}$, $\tilde{J} \equiv \frac{J}{J_{\mathrm{lim}}}$, $\tilde{I} \equiv \frac{I}{I_{\mathrm{lim}}}$, $\tilde{\rho}_{\mathrm{s}} \equiv \frac{\rho_{\mathrm{s}}}{z_+ \nu_+ e c_0} = -\frac{\rho_{\mathrm{s}}}{z_- \nu_- e c_0}$, $\tilde{j}_0 \equiv \frac{\epsilon_{\mathrm{p}} j_0}{J_{\mathrm{lim}}}$, $\tilde{J}_{\mathrm{F}} \equiv \frac{\epsilon_{\mathrm{p}} J_{\mathrm{F}}}{J_{\mathrm{lim}}}$,

$\tilde{k}_0 \equiv \frac{e\epsilon_\mathrm{p} k_0}{J_\mathrm{lim}}$, $\tilde{\gamma} \equiv \frac{\Omega\gamma}{L_x k_\mathrm{B} T}$, $\tilde{u} \equiv \frac{L_x u}{\epsilon_\mathrm{p} D_\mathrm{amb0}}$, $\tilde{u}_x \equiv \frac{L_x u_x}{\epsilon_\mathrm{p} D_\mathrm{amb0}}$, $\beta_\mathrm{D} = -\frac{z_- D_{-0}}{2(z_+ D_{+0} - z_- D_{-0})}$, $\beta_\mathrm{m} = \nu_+ c_0 \Omega$, $\beta_\mathrm{v} = \frac{\beta_\mathrm{m}}{\beta_\mathrm{D}}$, $\xi_+ = \frac{\nu_+ c_0}{c_+^\Theta}$, $\mathrm{Da} = \tilde{k}_0 = \frac{e\epsilon_\mathrm{p} k_0}{J_\mathrm{lim}}$ and $\mathrm{Ca} = \tilde{\gamma} = \frac{\Omega\gamma}{L_x k_\mathrm{B} T}$ where we note that $I_\mathrm{lim} = J_\mathrm{lim} A$ and $A = L_y L_z$. To avoid cluttering the notation, we drop tildes on all dimensionless variables and parameters, the 0 subscript for diffusivities and the $-$ subscript for anion-related variables and parameters in all following sections unless otherwise stated. Recall that we have picked a moving reference frame with a velocity $u(t) = u_x(t) e_x$ such that the average positions of the dissolving anode and growing cathode remain stationary. The dimensionless governing PDEs (partial differential equations) are

$$\frac{\partial c}{\partial t} + \nabla \cdot F = 0, \quad F = -D(\nabla c + zc\nabla\phi), \tag{3.88}$$

$$\nabla \cdot J = 0, \quad J = \beta_\mathrm{D}\{(D - D_+)\nabla c + [z_+ D_+ \rho_\mathrm{s} - (z_+ D_+ - zD)c]\nabla\phi\}, \tag{3.89}$$

$$\rho_\mathrm{s} = c - c_+. \tag{3.90}$$

The dimensionless Faradaic current density J_F is

$$J_\mathrm{F} = j_0\{\exp(-\alpha n\eta) - \exp[(1-\alpha)n\eta]\}, \tag{3.91}$$

$$j_0 = \mathrm{Da} n[\xi_+(c - \rho_\mathrm{s})]^{1-\alpha}, \tag{3.92}$$

$$\eta = \Delta\phi - \Delta\phi^\mathrm{eq}, \tag{3.93}$$

$$\Delta\phi = \phi_\mathrm{e} - \phi, \tag{3.94}$$

$$\Delta\phi^\mathrm{eq} = \frac{1}{n}\ln[\xi_+(c - \rho_\mathrm{s})] + E^\Theta - \frac{2\gamma\mathscr{H}}{n}. \tag{3.95}$$

The dimensionless boundary conditions are

$$\phi_\mathrm{e}^\mathrm{a} = 0, \tag{3.96}$$

$$\hat{n} \cdot F(r = r_\mathrm{m}^\mathrm{a,c}) = 0, \tag{3.97}$$

$$\hat{n} \cdot J(r = r_\mathrm{m}^\mathrm{a,c}) = J_\mathrm{F}^\mathrm{a,c}, \tag{3.98}$$

$$\hat{n} \cdot F(r = r_\mathrm{other}) = 0, \tag{3.99}$$

$$\hat{n} \cdot J(r = r_\mathrm{other}) = 0, \tag{3.100}$$

$$v_{\mathrm{In}}^{\mathrm{a,c}} = -\beta_{\mathrm{v}} \hat{n} \cdot J(r = r_{\mathrm{m}}^{\mathrm{a,c}}) - \hat{n} \cdot u(r = r_{\mathrm{m}}^{\mathrm{a,c}}). \tag{3.101}$$

For galvanostatic conditions,

$$\int \hat{n} \cdot J(r = r_{\mathrm{m}}^{\mathrm{c}}) \, \mathrm{d}S^{\mathrm{c}} = \int -\hat{n} \cdot J(r = r_{\mathrm{m}}^{\mathrm{a}}) \, \mathrm{d}S^{\mathrm{a}} = I_{\mathrm{a}}. \tag{3.102}$$

For potentiostatic conditions,

$$\phi_{\mathrm{e}}^{\mathrm{c}} = V. \tag{3.103}$$

The dimensionless initial conditions are

$$c(t = 0) = \beta_1, \tag{3.104}$$

$$x_{\mathrm{m}}^{\mathrm{a}}(t = 0) = 0, \tag{3.105}$$

$$x_{\mathrm{m}}^{\mathrm{c}}(t = 0) = 1. \tag{3.106}$$

3.8.3 Equations for base and perturbed states

We derive the perturbation expressions in Sections 3.8.3.1, 3.8.3.2, 3.8.3.3 and 3.8.3.4. We then substitute these expressions into the full model in Section 3.8.2 and match the $\mathcal{O}(1)$ (base state) and $\mathcal{O}(\epsilon)$ (perturbed state) terms. The equations for the base state are given in Section 3.8.3.5 and that for the perturbed state are given in Section 3.8.3.6. The goal of the linear stability analysis is to solve the equations at $\mathcal{O}(1)$ and $\mathcal{O}(\epsilon)$ and compute the dimensionless dispersion relation $\omega(k)$. In general, ω is complex-valued. If $\max\{\Re(\omega)\} < 0$, we conclude that the base state is linearly stable and if $\max\{\Re(\omega)\} > 0$, we conclude that the base state is linearly unstable. However, if $\max\{\Re(\omega)\} = 0$, the base state is marginally stable.

3.8.3.1 Perturbations and linearization

In response to the perturbations to the electrode/electrolyte interfaces, we assume that the perturbations to the field variables c and ϕ are similarly given by

$$c(x,\xi,t) = c_0(x,t) + \epsilon\Re[c_1(x)\exp(ik\cdot\xi+\omega t)] + \mathcal{O}\big(\epsilon^2\big), \tag{3.107}$$

$$\phi(x,\xi,t) = \phi_0(x,t) + \epsilon\Re[\phi_1(x)\exp(ik\cdot\xi+\omega t)] + \mathcal{O}\big(\epsilon^2\big), \tag{3.108}$$

where c_1 and ϕ_1 are the complex-valued perturbation amplitudes of anion concentration and electrolyte electric potential respectively. For brevity, we let $\hat{\epsilon} = \epsilon\exp(ik\cdot\xi+\omega t)$ and $\theta \in \{c,\phi\}$. We also drop $\Re(\cdot)$ with the understanding that we are only interested in the real parts of complex-valued variables. Therefore,

$$h(\xi,t) = h_0(t) + \hat{\epsilon}h_1 + \mathcal{O}\big(\epsilon^2\big), \tag{3.109}$$

$$\theta(x,\xi,t) = \theta_0(x,t) + \hat{\epsilon}\theta_1(x) + \mathcal{O}\big(\epsilon^2\big). \tag{3.110}$$

The required temporal and spatial derivatives are given by

$$h_t = \dot{h}_0 + \hat{\epsilon}\omega h_1 + \mathcal{O}\big(\epsilon^2\big), \tag{3.111}$$

$$h_y = \hat{\epsilon}ik_y h_1 + \mathcal{O}\big(\epsilon^2\big), \quad h_z = \hat{\epsilon}ik_z h_1 + \mathcal{O}\big(\epsilon^2\big), \tag{3.112}$$

$$h_{yy} = -\hat{\epsilon}k_y^2 h_1 + \mathcal{O}\big(\epsilon^2\big), \quad h_{zz} = -\hat{\epsilon}k_z^2 h_1 + \mathcal{O}\big(\epsilon^2\big), \quad h_{yz} = -\hat{\epsilon}k_y k_z h_1 + \mathcal{O}\big(\epsilon^2\big), \tag{3.113}$$

$$\theta_t = \theta_{0,t} + \hat{\epsilon}\omega\theta_1 + \mathcal{O}\big(\epsilon^2\big), \tag{3.114}$$

$$\theta_x = \theta_{0,x} + \hat{\epsilon}\theta_1' + \mathcal{O}\big(\epsilon^2\big), \tag{3.115}$$

$$\theta_{xx} = \theta_{0,xx} + \hat{\epsilon}\theta_1'' + \mathcal{O}\big(\epsilon^2\big), \tag{3.116}$$

$$\theta_y = \hat{\epsilon}ik_y\theta_1 + \mathcal{O}\big(\epsilon^2\big), \quad \theta_z = \hat{\epsilon}ik_z\theta_1 + \mathcal{O}\big(\epsilon^2\big), \tag{3.117}$$

$$\theta_{yy} = -\hat{\epsilon}k_y^2\theta_1 + \mathcal{O}\big(\epsilon^2\big), \quad \theta_{zz} = -\hat{\epsilon}k_z^2\theta_1 + \mathcal{O}\big(\epsilon^2\big), \tag{3.118}$$

$$c\phi_x = c_0\phi_{0,x} + \hat{\epsilon}(c_0\phi_1' + \phi_{0,x}c_1) + \mathcal{O}\big(\epsilon^2\big), \tag{3.119}$$

$$(c\phi_x)_x = (c_0\phi_{0,x})_x + \hat{\epsilon}(c_0\phi_1' + \phi_{0,x}c_1)_x + \mathcal{O}\big(\epsilon^2\big), \tag{3.120}$$

$$c\phi_y = \hat{\epsilon}ik_y c_0\phi_1 + \mathcal{O}\big(\epsilon^2\big), \quad c\phi_z = \hat{\epsilon}ik_z c_0\phi_1 + \mathcal{O}\big(\epsilon^2\big), \tag{3.121}$$

$$(c\phi_y)_y = -\hat{\epsilon}k_y^2 c_0\phi_1 + \mathcal{O}\big(\epsilon^2\big), \quad (c\phi_z)_z = -\hat{\epsilon}k_z^2 c_0\phi_1 + \mathcal{O}\big(\epsilon^2\big), \tag{3.122}$$

$$H^{-1} = 1 + \mathcal{O}\big(\epsilon^2\big), \tag{3.123}$$

$$H^{-3} = 1 + \mathcal{O}\big(\epsilon^2\big), \tag{3.124}$$

$$\hat{n}(r = r_{\mathrm{m}}^{\mathrm{a}}) = -\big\{\big[1 + \mathcal{O}\big(\epsilon^2\big)\big]e_x - \big[\hat{\epsilon}ik_y h_1^{\mathrm{a}} + \mathcal{O}\big(\epsilon^2\big)\big]e_y - \big[\hat{\epsilon}ik_z h_1^{\mathrm{a}} + \mathcal{O}\big(\epsilon^2\big)\big]e_z\big\}, \tag{3.125}$$

$$\hat{n}(r = r_{\mathrm{m}}^{\mathrm{c}}) = \big[1 + \mathcal{O}\big(\epsilon^2\big)\big]e_x - \big[\hat{\epsilon}ik_y h_1^{\mathrm{c}} + \mathcal{O}\big(\epsilon^2\big)\big]e_y - \big[\hat{\epsilon}ik_z h_1^{\mathrm{c}} + \mathcal{O}\big(\epsilon^2\big)\big]e_z, \tag{3.126}$$

$$2\mathscr{H}^{\mathrm{a}} = \hat{\epsilon}k^2 h_1^{\mathrm{a}} + \mathcal{O}\big(\epsilon^2\big), \tag{3.127}$$

$$2\mathscr{H}^{\mathrm{c}} = -\hat{\epsilon}k^2 h_1^{\mathrm{c}} + \mathcal{O}\big(\epsilon^2\big), \tag{3.128}$$

$$v_{\mathrm{In}}^{\mathrm{a}} = -\Big(\dot{h}_0^{\mathrm{a}} + \hat{\epsilon}\omega h_1^{\mathrm{a}}\Big) + \mathcal{O}\big(\epsilon^2\big), \tag{3.129}$$

$$v_{\mathrm{In}}^{\mathrm{c}} = \dot{h}_0^{\mathrm{c}} + \hat{\epsilon}\omega h_1^{\mathrm{c}} + \mathcal{O}\big(\epsilon^2\big). \tag{3.130}$$

3.8.3.2 Expressions in domain

For brevity, we stop writing $\mathcal{O}(\epsilon^2)$. In the domain,

$$\nabla^2\theta = \theta_{xx} + \theta_{yy} + \theta_{zz} = \theta_{0,xx} + \hat{\epsilon}\big(\theta_1'' - k^2\theta_1\big), \tag{3.131}$$

$$\nabla\cdot(c\nabla\phi) = (c\phi_x)_x + (c\phi_y)_y + (c\phi_z)_z = (c_0\phi_{0,x})_x + \hat{\epsilon}\big[(c_0\phi_1' + \phi_{0,x}c_1)_x - k^2 c_0\phi_1\big], \tag{3.132}$$

$$\nabla\cdot F = -D\big[\nabla^2 c + z\nabla\cdot(c\nabla\phi)\big] = \nabla\cdot F_0 + \hat{\epsilon}\nabla\cdot F_1, \tag{3.133}$$

$$\nabla\cdot F_0 = -D\big[c_{0,xx} + z(c_0\phi_{0,x})_x\big], \tag{3.134}$$

$$\nabla\cdot F_1 = -D\big\{c_1'' - k^2 c_1 + z\big[(c_0\phi_1' + \phi_{0,x}c_1)_x - k^2 c_0\phi_1\big]\big\}, \tag{3.135}$$

$$\nabla\cdot J = \beta_{\mathrm{D}}\big[(D - D_+)\nabla^2 c + z_+ D_+\rho_{\mathrm{s}}\nabla^2\phi - (z_+ D_+ - zD)\nabla\cdot(c\nabla\phi)\big] = \nabla\cdot J_0 + \hat{\epsilon}\nabla\cdot J_1, \tag{3.136}$$

$$\nabla\cdot J_0 = \beta_{\mathrm{D}}\big[(D - D_+)c_{0,xx} + z_+ D_+\rho_{\mathrm{s}}\phi_{0,xx} - (z_+ D_+ - zD)(c_0\phi_{0,x})_x\big], \tag{3.137}$$

$$\nabla\cdot J_1 = \beta_{\mathrm{D}}\big\{(D - D_+)\big(c_1'' - k^2 c_1\big) + z_+ D_+\rho_{\mathrm{s}}\big(\phi_1'' - k^2\phi_1\big) - (z_+ D_+ - zD)\big[(c_0\phi_1' + \phi_{0,x}c_1)_x - k^2 c_0\phi_1\big]\big\}. \tag{3.138}$$

3.8.3.3 Expressions at boundaries

To evaluate θ, $\nabla\theta$ and $\hat{n}\cdot\theta$ at the electrode/electrolyte interface at $x = h$, we require their Taylor series expansions around the base electrode/electrolyte interface at $x = h_0$. We first note that

$$h - h_0 = \hat{\epsilon}h_1 + \mathcal{O}\big(\epsilon^2\big), \tag{3.139}$$

$$|h - h_0| = \big|\hat{\epsilon}h_1 + \mathcal{O}\big(\epsilon^2\big)\big| = \mathcal{O}(\epsilon), \tag{3.140}$$

$$|h - h_0|^2 = \big|\hat{\epsilon}h_1 + \mathcal{O}\big(\epsilon^2\big)\big|^2 = \mathcal{O}\big(\epsilon^2\big). \tag{3.141}$$

For brevity, we stop writing $\mathcal{O}(\epsilon^2)$. Therefore, performing the Taylor series expansion of θ around $x = h_0$,

$$\begin{aligned}\theta(x = h) &= \theta_0(x = h) + \hat{\epsilon}\theta_1(x = h)\\ &= \theta_0(x = h_0) + \theta_{0,x}(x = h_0)(h - h_0) + \hat{\epsilon}\theta_1(x = h_0)\\ &= \theta_0(x = h_0) + \hat{\epsilon}[h_1\theta_{0,x}(x = h_0) + \theta_1(x = h_0)].\end{aligned} \tag{3.142}$$

To avoid cluttering the notation, we stop writing $x = h$ and $x = h_0$ since it is obvious from context where the evaluations should be performed. Therefore, at both the anode and cathode,

$$\theta = \theta_0 + \hat{\epsilon}(h_1\theta_{0,x} + \theta_1), \tag{3.143}$$

$$\theta_x = \theta_{0,x} + \hat{\epsilon}(h_1\theta_{0,xx} + \theta_1'), \tag{3.144}$$

$$\theta_y = \hat{\epsilon}ik_y\theta_1, \quad \theta_z = \hat{\epsilon}ik_z\theta_1, \tag{3.145}$$

$$c\phi_x = c_0\phi_{0,x} + \hat{\epsilon}\big[h_1(c_0\phi_{0,x})_x + c_0\phi_1' + \phi_{0,x}c_1\big], \tag{3.146}$$

$$c\phi_y = \hat{\epsilon}ik_yc_0\phi_1, \quad c\phi_z = \hat{\epsilon}ik_zc_0\phi_1, \tag{3.147}$$

$$\nabla\theta = \theta_xe_x + \theta_ye_y + \theta_ze_z, \tag{3.148}$$

$$c\nabla\phi = c\phi_xe_x + c\phi_ye_y + c\phi_ze_z. \tag{3.149}$$

At the anode,

$$\hat{n}\cdot\nabla\theta = -\theta_x = -[\theta_{0,x} + \hat{\epsilon}(h_1\theta_{0,xx} + \theta_1')], \tag{3.150}$$

$$\hat{n}\cdot(c\nabla\phi) = -c\phi_x = -\big\{c_0\phi_{0,x} + \hat{\epsilon}\big[h_1(c_0\phi_{0,x})_x + c_0\phi_1' + \phi_{0,x}c_1\big]\big\}, \tag{3.151}$$

$$\hat{n}\cdot F = -D\hat{n}\cdot(\nabla c + zc\nabla\phi) = \hat{n}\cdot F_0 + \hat{\epsilon}\hat{n}\cdot F_1, \tag{3.152}$$

$$\hat{n}\cdot F_0 = -D(-c_{0,x} - zc_0\phi_{0,x}), \tag{3.153}$$

$$\hat{n}\cdot F_1 = -D\big\{-h_1c_{0,xx} - c_1' - z\big[h_1(c_0\phi_{0,x})_x + c_0\phi_1' + \phi_{0,x}c_1\big]\big\}, \tag{3.154}$$

$$\hat{n}\cdot J = \beta_{\mathrm{D}}\hat{n}\cdot[(D-D_+)\nabla c + z_+D_+\rho_{\mathrm{s}}\nabla\phi - (z_+D_+ - zD)c\nabla\phi] = \hat{n}\cdot J_0 + \hat{\epsilon}\hat{n}\cdot J_1, \tag{3.155}$$

$$\hat{n}\cdot J_0 = \beta_{\mathrm{D}}[-(D-D_+)c_{0,x} - z_+D_+\rho_{\mathrm{s}}\phi_{0,x} + (z_+D_+ - zD)c_0\phi_{0,x}], \tag{3.156}$$

$$\begin{aligned}\hat{n}\cdot J_1 = \beta_{\mathrm{D}}\{&-(D-D_+)(h_1c_{0,xx} + c_1') - z_+D_+\rho_{\mathrm{s}}(h_1\phi_{0,xx} + \phi_1')\\ &+ (z_+D_+ - zD)\big[h_1(c_0\phi_{0,x})_x + c_0\phi_1' + \phi_{0,x}c_1\big]\big\},\end{aligned} \tag{3.157}$$

$$\hat{n}\cdot u = -u_x. \tag{3.158}$$

For the electrochemical reaction kinetics,

$$\Delta\phi = \phi_{\mathrm{e}} - \phi_0 - \hat{\epsilon}(h_1\phi_{0,x} + \phi_1), \tag{3.159}$$

$$\Delta\phi^{\mathrm{eq}} = \frac{1}{n}\ln[\xi_+(c_0-\rho_{\mathrm{s}})] + E^{\Theta} + \hat{\epsilon}\left[\frac{1}{n}\left(\frac{h_1c_{0,x}+c_1}{c_0-\rho_{\mathrm{s}}} - \gamma k^2h_1\right)\right], \tag{3.160}$$

$$\eta = \eta_0 + \hat{\epsilon}\eta_1, \tag{3.161}$$

$$\eta_0 = \phi_{\mathrm{e}} - \phi_0 - \frac{1}{n}\ln[\xi_+(c_0-\rho_{\mathrm{s}})] - E^{\Theta}, \tag{3.162}$$

$$\eta_1 = -(h_1\phi_{0,x} + \phi_1) - \frac{1}{n}\left(\frac{h_1c_{0,x}+c_1}{c_0-\rho_{\mathrm{s}}} - \gamma k^2h_1\right), \tag{3.163}$$

$$j_0 = j_{0,0} + \hat{\epsilon}j_{0,1}, \tag{3.164}$$

$$j_{0,0} = \mathrm{Da}n[\xi_+(c_0-\rho_{\mathrm{s}})]^{1-\alpha}, \tag{3.165}$$

$$j_{0,1} = j_{0,0}\frac{(1-\alpha)(h_1c_{0,x}+c_1)}{c_0-\rho_{\mathrm{s}}}, \tag{3.166}$$

$$J_{\mathrm{F}} = J_{\mathrm{F},0} + \hat{\epsilon}J_{\mathrm{F},1}, \tag{3.167}$$

$$J_{\mathrm{F},0} = j_{0,0}\{\exp(-\alpha n\eta_0) - \exp[(1-\alpha)n\eta_0]\}, \tag{3.168}$$

$$J_{\mathrm{F},1} = j_{0,0}\{[-\alpha\exp(-\alpha n\eta_0) - (1-\alpha)\exp[(1-\alpha)n\eta_0]]n\eta_1 + [\exp(-\alpha n\eta_0) - \exp[(1-\alpha)n\eta_0]]\frac{(1-\alpha)(h_1 c_{0,x} + c_1)}{c_0 - \rho_{\mathrm{s}}}\Big\}. \tag{3.169}$$

The signs of the expressions involving $\hat{n}$, including $\mathscr{H}$ and v_{In}, at the cathode are opposite to that at the anode. Therefore, at the cathode,

$$\hat{n}\cdot\nabla\theta = \theta_x = \theta_{0,x} + \hat{\epsilon}(h_1\theta_{0,xx} + \theta_1'), \tag{3.170}$$

$$\hat{n}\cdot(c\nabla\phi) = c\phi_x = c_0\phi_{0,x} + \hat{\epsilon}\big[h_1(c_0\phi_{0,x})_x + c_0\phi_1' + \phi_{0,x}c_1\big], \tag{3.171}$$

$$\hat{n}\cdot F = -D\hat{n}\cdot(\nabla c + zc\nabla\phi) = \hat{n}\cdot F_0 + \hat{\epsilon}\hat{n}\cdot F_1, \tag{3.172}$$

$$\hat{n}\cdot F_0 = -D(c_{0,x} + zc_0\phi_{0,x}), \tag{3.173}$$

$$\hat{n}\cdot F_1 = -D\big\{h_1 c_{0,xx} + c_1' + z\big[h_1(c_0\phi_{0,x})_x + c_0\phi_1' + \phi_{0,x}c_1\big]\big\}, \tag{3.174}$$

$$\hat{n}\cdot J = \beta_{\mathrm{D}}\hat{n}\cdot[(D-D_+)\nabla c + z_+D_+\rho_{\mathrm{s}}\nabla\phi - (z_+D_+ - zD)c\nabla\phi] = \hat{n}\cdot J_0 + \hat{\epsilon}\hat{n}\cdot J_1, \tag{3.175}$$

$$\hat{n}\cdot J_0 = \beta_{\mathrm{D}}[(D-D_+)c_{0,x} + z_+D_+\rho_{\mathrm{s}}\phi_{0,x} - (z_+D_+ - zD)c_0\phi_{0,x}], \tag{3.176}$$

$$\hat{n}\cdot J_1 = \beta_{\mathrm{D}}\big\{(D-D_+)(h_1c_{0,xx} + c_1') + z_+D_+\rho_{\mathrm{s}}(h_1\phi_{0,xx} + \phi_1') - (z_+D_+ - zD)\big[h_1(c_0\phi_{0,x})_x + c_0\phi_1' + \phi_{0,x}c_1\big]\big\}, \tag{3.177}$$

$$\hat{n}\cdot u = u_x. \tag{3.178}$$

For the electrochemical reaction kinetics,

$$\Delta\phi = \phi_{\mathrm{e}} - \phi_0 - \hat{\epsilon}(h_1\phi_{0,x} + \phi_1), \tag{3.179}$$

$$\Delta\phi^{\mathrm{eq}} = \frac{1}{n}\ln[\xi_+(c_0 - \rho_{\mathrm{s}})] + E^{\Theta} + \hat{\epsilon}\left[\frac{1}{n}\left(\frac{h_1c_{0,x} + c_1}{c_0 - \rho_{\mathrm{s}}} + \gamma k^2 h_1\right)\right], \tag{3.180}$$

$$\eta = \eta_0 + \hat{\epsilon}\eta_1, \tag{3.181}$$

$$\eta_0 = \phi_{\mathrm{e}} - \phi_0 - \frac{1}{n}\ln[\xi_+(c_0 - \rho_{\mathrm{s}})] - E^{\Theta}, \tag{3.182}$$

$$\eta_1 = -(h_1\phi_{0,x} + \phi_1) - \frac{1}{n}\left(\frac{h_1c_{0,x} + c_1}{c_0 - \rho_{\mathrm{s}}} + \gamma k^2 h_1\right), \tag{3.183}$$

$$j_0 = j_{0,0} + \hat{\epsilon}j_{0,1}, \tag{3.184}$$

$$j_{0,0} = \mathrm{Da}n[\xi_+(c_0 - \rho_{\mathrm{s}})]^{1-\alpha}, \tag{3.185}$$

$$j_{0,1} = j_{0,0}\frac{(1-\alpha)(h_1 c_{0,x} + c_1)}{c_0 - \rho_s}, \tag{3.186}$$

$$J_F = J_{F,0} + \hat{\epsilon} J_{F,1}, \tag{3.187}$$

$$J_{F,0} = j_{0,0}\{\exp(-\alpha n \eta_0) - \exp[(1-\alpha) n \eta_0]\}, \tag{3.188}$$

$$\begin{aligned} J_{F,1} = j_{0,0}\{&[-\alpha \exp(-\alpha n \eta_0) - (1-\alpha)\exp[(1-\alpha) n \eta_0]] n \eta_1 \\ &+ [\exp(-\alpha n \eta_0) - \exp[(1-\alpha) n \eta_0]] \frac{(1-\alpha)(h_1 c_{0,x} + c_1)}{c_0 - \rho_s} \Bigg\}. \end{aligned} \tag{3.189}$$

We can rewrite $J_{F,1}$ in a more physically interpretable fashion by first defining the following dimensionless variables

$$\alpha_3 = -\alpha \exp(-\alpha n \eta_0) - (1-\alpha)\exp[(1-\alpha) n \eta_0] = \frac{1}{n}\frac{\partial \alpha_4}{\partial \eta_0}, \tag{3.190}$$

$$\alpha_4 = \exp(-\alpha n \eta_0) - \exp[(1-\alpha) n \eta_0]. \tag{3.191}$$

Therefore, at the anode,

$$J_{F,1} = j_{0,0}\Big(\hat{D}_1 h_1 + \hat{D}_2 c_1 + \hat{D}_3 \phi_1\Big), \tag{3.192}$$

$$\hat{D}_1 = \alpha_3 n\left(-\phi_{0,x} + \frac{\gamma k^2}{n}\right) + \frac{\exp(-\alpha n \eta_0) c_{0,x}}{c_0 - \rho_s}, \tag{3.193}$$

$$\hat{D}_2 = \frac{\exp(-\alpha n \eta_0)}{c_0 - \rho_s}, \tag{3.194}$$

$$\hat{D}_3 = -\alpha_3 n, \tag{3.195}$$

and at the cathode,

$$J_{F,1} = j_{0,0}\Big(\hat{G}_1 h_1 + \hat{G}_2 c_1 + \hat{G}_3 \phi_1\Big), \tag{3.196}$$

$$\hat{G}_1 = \alpha_3 n\left(-\phi_{0,x} - \frac{\gamma k^2}{n}\right) + \frac{\exp(-\alpha n \eta_0) c_{0,x}}{c_0 - \rho_s}, \tag{3.197}$$

$$\hat{G}_2 = \frac{\exp(-\alpha n \eta_0)}{c_0 - \rho_s}, \tag{3.198}$$

$$\hat{G}_3 = -\alpha_3 n. \tag{3.199}$$

At the boundaries at $r = r_{\text{other}}$, because of the $\hat{n} \cdot F(r = r_{\text{other}}) = 0$ and $\hat{n} \cdot$

$J(r = r_{\text{other}}) = 0$ boundary conditions, we require $\theta_y(y = 0) = \theta_y(y = L_y) = 0$ and $\theta_z(z = 0) = \theta_z(z = L_z) = 0$, which imply that $\sin(k_y L_y) = 0$ and $\sin(k_z L_z) = 0$. Therefore, $k_y = \frac{n_y \pi}{L_y}$ and $k_z = \frac{n_z \pi}{L_z}$ for $n_y, n_z \in \mathbb{Z}$. Without loss of generality, we restrict n_y and n_z to nonnegative integers. In addition, because L_y and L_z are finite, the minimum values of k_y and k_z are nonzero and are equal to $\frac{\pi}{L_y}$ and $\frac{\pi}{L_z}$ respectively. In summary, we conclude that $n_y, n_z \in \mathbb{Z}^+$, which is the set of positive integers.

3.8.3.4 Constraints

For galvanostatic conditions,

$$\begin{aligned} I_{\text{a}} &= L_y L_z \hat{n} \cdot J_0(x = h_0^{\text{c}}) + \hat{n} \cdot J_1(x = h_0^{\text{c}}) \int_0^{L_y} \int_0^{L_z} \hat{\epsilon}^{\text{c}} \, \mathrm{d}y \, \mathrm{d}z \\ &= -L_y L_z \hat{n} \cdot J_0(x = h_0^{\text{a}}) - \hat{n} \cdot J_1(x = h_0^{\text{a}}) \int_0^{L_y} \int_0^{L_z} \hat{\epsilon}^{\text{a}} \, \mathrm{d}y \, \mathrm{d}z \end{aligned} \tag{3.200}$$

where the "a" and "c" superscripts on $\hat{\epsilon}$ denote that the surface integrals involving $\hat{\epsilon}$ are performed over the anode and cathode respectively. Because $k_y = \frac{n_y \pi}{L_y}$ and $k_z = \frac{n_z \pi}{L_z}$ for $n_y, n_z \in \mathbb{Z}^+$, the surface integrals involving $\hat{\epsilon}$ are 0 and the constraint is automatically satisfied at $\mathcal{O}(\epsilon)$. At $\mathcal{O}(1)$, defining the dimensionless limiting current density J_{a} as $J_{\text{a}} \equiv \frac{I_{\text{a}}}{A} = \frac{I_{\text{a}}}{L_y L_z}$,

$$\hat{n} \cdot J_0(x = h_0^{\text{c}}) = -\hat{n} \cdot J_0(x = h_0^{\text{a}}) = J_{\text{a}}. \tag{3.201}$$

For potentiostatic conditions, $\phi_{\text{e}}^{\text{c}} = V$.

3.8.3.5 Base state

At $\mathcal{O}(1)$, the governing PDEs are given by

$$c_{0,t} - D\big[c_{0,xx} + z(c_0 \phi_{0,x})_x\big] = 0, \tag{3.202}$$

$$\beta_{\text{D}}\big[(D - D_+)c_{0,xx} + z_+ D_+ \rho_{\text{s}} \phi_{0,xx} - (z_+ D_+ - zD)(c_0 \phi_{0,x})_x\big] = 0. \tag{3.203}$$

The boundary conditions at $x = h_0^{\mathrm{a}}$ are given by

$$\phi_{\mathrm{e}}^{\mathrm{a}} = 0, \tag{3.204}$$

$$-D(-c_{0,x} - zc_0\phi_{0,x}) = 0, \tag{3.205}$$

$$\beta_{\mathrm{D}}[-(D - D_+)c_{0,x} - z_+D_+\rho_{\mathrm{s}}\phi_{0,x} + (z_+D_+ - zD)c_0\phi_{0,x}] = j_{0,0}\{\exp(-\alpha n\eta_0) - \exp[(1-\alpha)n\eta_0]\}, \tag{3.206}$$

$$-\dot{h}_0 = -\beta_{\mathrm{v}}\hat{n} \cdot J_0 + u_x. \tag{3.207}$$

The boundary conditions at $x = h_0^{\mathrm{c}}$ are given by

$$-D(c_{0,x} + zc_0\phi_{0,x}) = 0, \tag{3.208}$$

$$\beta_{\mathrm{D}}[(D - D_+)c_{0,x} + z_+D_+\rho_{\mathrm{s}}\phi_{0,x} - (z_+D_+ - zD)c_0\phi_{0,x}] = j_{0,0}\{\exp(-\alpha n\eta_0) - \exp[(1-\alpha)n\eta_0]\}, \tag{3.209}$$

$$\dot{h}_0 = -\beta_{\mathrm{v}}\hat{n} \cdot J_0 - u_x. \tag{3.210}$$

We pick $u_x(x = h_0^{\mathrm{a}})$ and $u_x(x = h_0^{\mathrm{c}})$ such that the positions of the anode and cathode in the base state remain stationary, i.e., $\dot{h}_0^{\mathrm{a}} = \dot{h}_0^{\mathrm{c}} = 0$. Therefore, $u_x = \beta_{\mathrm{v}}\hat{n} \cdot J_0(x = h_0^{\mathrm{a}}) = -\beta_{\mathrm{v}}\hat{n} \cdot J_0(x = h_0^{\mathrm{c}})$ where the second equality automatically holds true because of charge conservation in the 1D $\mathcal{O}(1)$ base state. Physically, u_x is equal to the velocity of the growing planar cathode/electrolyte interface or the dissolving planar anode/electrolyte interface in the base state. The initial conditions are given by

$$c_0(t = 0) = \beta_1, \tag{3.211}$$

$$h_0^{\mathrm{a}}(t = 0) = 0, \tag{3.212}$$

$$h_0^{\mathrm{c}}(t = 0) = 1. \tag{3.213}$$

Since $\dot{h}_0^{\mathrm{a}} = \dot{h}_0^{\mathrm{c}} = 0$, $h_0^{\mathrm{a}}(t) = 0$ and $h_0^{\mathrm{c}}(t) = 1$ for all t. For galvanostatic conditions,

$$J_{\mathrm{a}} = \beta_{\mathrm{D}}[(D - D_+)c_{0,x} + z_+D_+\rho_{\mathrm{s}}\phi_{0,x} - (z_+D_+ - zD)c_0\phi_{0,x}]\big|_{x=h_0^{\mathrm{c}}} \tag{3.214}$$

$$= \beta_{\mathrm{D}}[(D - D_+)c_{0,x} + z_+ D_+ \rho_{\mathrm{s}} \phi_{0,x} - (z_+ D_+ - zD) c_0 \phi_{0,x}]\big|_{x=h_0^{\mathrm{a}}}. \tag{3.215}$$

For potentiostatic conditions, $\phi_{\mathrm{e}}^{\mathrm{c}} = V$.

3.8.3.6 Perturbed state

We first note that the PDEs given by Equations 3.202 and 3.203 apply at the $x = h_0^{\mathrm{a,c}}$ boundaries too. Therefore, at the anode,

$$\hat{n} \cdot F_1 = c_{0,t} h_1 - D[-c_1' - z(c_0 \phi_1' + \phi_{0,x} c_1)], \tag{3.216}$$

$$\hat{n} \cdot J_1 = \beta_{\mathrm{D}}[-(D - D_+)c_1' - z_+ D_+ \rho_{\mathrm{s}} \phi_1' + (z_+ D_+ - zD)(c_0 \phi_1' + \phi_{0,x} c_1)], \tag{3.217}$$

and at the cathode,

$$\hat{n} \cdot F_1 = -c_{0,t} h_1 - D[c_1' + z(c_0 \phi_1' + \phi_{0,x} c_1)], \tag{3.218}$$

$$\hat{n} \cdot J_1 = \beta_{\mathrm{D}}[(D - D_+)c_1' + z_+ D_+ \rho_{\mathrm{s}} \phi_1' - (z_+ D_+ - zD)(c_0 \phi_1' + \phi_{0,x} c_1)]. \tag{3.219}$$

At $\mathcal{O}(\epsilon)$, the governing ODEs (ordinary differential equations) are given by

$$D\big\{c_1'' - k^2 c_1 + z\big[(c_0 \phi_1' + \phi_{0,x} c_1)_x - k^2 c_0 \phi_1\big]\big\} = \omega c_1, \tag{3.220}$$

$$(D - D_+)\big(c_1'' - k^2 c_1\big) + z_+ D_+ \rho_{\mathrm{s}}\big(\phi_1'' - k^2 \phi_1\big) - (z_+ D_+ - zD)\big[(c_0 \phi_1' + \phi_{0,x} c_1)_x - k^2 c_0 \phi_1\big] = 0. \tag{3.221}$$

The boundary conditions at $x = h_0^{\mathrm{a}}$ are given by

$$c_{0,t} h_1 - D[-c_1' - z(c_0 \phi_1' + \phi_{0,x} c_1)] = 0, \tag{3.222}$$

$$\beta_{\mathrm{v}} j_{0,0}\Big(\hat{D}_1 h_1 + \hat{D}_2 c_1 + \hat{D}_3 \phi_1\Big) = \omega h_1, \tag{3.223}$$

$$\beta_{\mathrm{m}}[-(D - D_+)c_1' - z_+ D_+ \rho_{\mathrm{s}} \phi_1' + (z_+ D_+ - zD)(c_0 \phi_1' + \phi_{0,x} c_1)] = \omega h_1. \tag{3.224}$$

The boundary conditions at $x = h_0^{\mathrm{c}}$ are given by

$$-c_{0,t} h_1 - D[c_1' + z(c_0 \phi_1' + \phi_{0,x} c_1)] = 0, \tag{3.225}$$

$$\beta_{\mathrm{v}} j_{0,0}\Big(\hat{G}_1 h_1 + \hat{G}_2 c_1 + \hat{G}_3 \phi_1\Big) = -\omega h_1, \tag{3.226}$$

$$\beta_{\mathrm{m}}[(D - D_+)c_1' + z_+ D_+ \rho_{\mathrm{s}} \phi_1' - (z_+ D_+ - zD)(c_0 \phi_1' + \phi_{0,x} c_1)] = -\omega h_1. \tag{3.227}$$

3.8.4 Discretization of perturbed state

The 1D second-order accurate finite difference approximations for a uniform grid with a grid spacing Δx are given by [135]

$$f_i' = \frac{f_{i+1} - f_{i-1}}{2\Delta x} + \mathcal{O}\big(\Delta x^2\big), \tag{3.228}$$

$$f_i' = \frac{-3f_i + 4f_{i+1} - f_{i+2}}{2\Delta x} + \mathcal{O}\big(\Delta x^2\big), \tag{3.229}$$

$$f_i' = \frac{f_{i-2} - 4f_{i-1} + 3f_i}{2\Delta x} + \mathcal{O}\big(\Delta x^2\big), \tag{3.230}$$

$$f_i'' = \frac{f_{i+1} - 2f_i + f_{i-1}}{\Delta x^2} + \mathcal{O}\big(\Delta x^2\big). \tag{3.231}$$

We pick a uniform grid and let N be the number of grid points, therefore $\Delta x = \frac{1}{N-1}$. For brevity, we define the following dimensionless variables

$$\alpha_1 = D - D_+, \tag{3.232}$$

$$\alpha_2 = z_+ D_+ - zD. \tag{3.233}$$

We note that

$$\left(c_0 \phi_1' + \phi_{0,x} c_1\right)_x - k^2 c_0 \phi_1 = c_{0,x} \phi_1' + c_0 \phi_1'' + \phi_{0,xx} c_1 + \phi_{0,x} c_1' - k^2 c_0 \phi_1 \tag{3.234}$$

with the finite difference discretization

$$\begin{aligned}\left(c_0 \phi_1' + \phi_{0,x} c_1\right)_{x,i} - k^2 c_{0,i} \phi_{1,i} = {} & \left(-\frac{\phi_{0,x,i}}{2\Delta x}\right) c_{1,i-1} + (\phi_{0,xx,i}) c_{1,i} + \left(\frac{\phi_{0,x,i}}{2\Delta x}\right) c_{1,i+1} \\ & + \left(-\frac{c_{0,x,i}}{2\Delta x} + \frac{c_{0,i}}{\Delta x^2}\right) \phi_{1,i-1} + \left(-\frac{2c_{0,i}}{\Delta x^2} - k^2 c_{0,i}\right) \phi_{1,i} \\ & + \left(\frac{c_{0,x,i}}{2\Delta x} + \frac{c_{0,i}}{\Delta x^2}\right) \phi_{1,i+1}.\end{aligned} \tag{3.235}$$

In addition,

$$\left(\theta_1'' - k^2\theta_1\right)_i = \left(\frac{1}{\Delta x^2}\right)\theta_{1,i-1} + \left(-\frac{2}{\Delta x^2} - k^2\right)\theta_{1,i} + \left(\frac{1}{\Delta x^2}\right)\theta_{1,i+1}. \tag{3.236}$$

The finite difference discretization of the $\mathcal{O}(\epsilon)$ equations in the domain results in

$$M_{1,i}c_{1,i-1} + M_{2,i}c_{1,i} + M_{3,i}c_{1,i+1} + M_{4,i}\phi_{1,i-1} + M_{5,i}\phi_{1,i} + M_{6,i}\phi_{1,i+1} = \omega c_{1,i}, \quad i = 2, \ldots, N-1, \tag{3.237}$$

$$M_{1,i} = D\left(\frac{1}{\Delta x^2} - z\frac{\phi_{0,x,i}}{2\Delta x}\right), \tag{3.238}$$

$$M_{2,i} = D\left(-\frac{2}{\Delta x^2} - k^2 + z\phi_{0,xx,i}\right), \tag{3.239}$$

$$M_{3,i} = D\left(\frac{1}{\Delta x^2} + z\frac{\phi_{0,x,i}}{2\Delta x}\right), \tag{3.240}$$

$$M_{4,i} = zD\left(-\frac{c_{0,x,i}}{2\Delta x} + \frac{c_{0,i}}{\Delta x^2}\right), \tag{3.241}$$

$$M_{5,i} = zD\left(-\frac{2c_{0,i}}{\Delta x^2} - k^2 c_{0,i}\right), \tag{3.242}$$

$$M_{6,i} = zD\left(\frac{c_{0,x,i}}{2\Delta x} + \frac{c_{0,i}}{\Delta x^2}\right), \tag{3.243}$$

$$A_{1,i}c_{1,i-1} + A_{2,i}c_{1,i} + A_{3,i}c_{1,i+1} + A_{4,i}\phi_{1,i-1} + A_{5,i}\phi_{1,i} + A_{6,i}\phi_{1,i+1} = 0, \quad i = 2, \ldots, N-1, \tag{3.244}$$

$$A_{1,i} = \alpha_1\frac{1}{\Delta x^2} + \alpha_2\frac{\phi_{0,x,i}}{2\Delta x}, \tag{3.245}$$

$$A_{2,i} = \alpha_1\left(-\frac{2}{\Delta x^2} - k^2\right) - \alpha_2\phi_{0,xx,i}, \tag{3.246}$$

$$A_{3,i} = \alpha_1\frac{1}{\Delta x^2} - \alpha_2\frac{\phi_{0,x,i}}{2\Delta x}, \tag{3.247}$$

$$A_{4,i} = z_+D_+\rho_{\mathrm{s}}\frac{1}{\Delta x^2} - \alpha_2\left(-\frac{c_{0,x,i}}{2\Delta x} + \frac{c_{0,i}}{\Delta x^2}\right), \tag{3.248}$$

$$A_{5,i} = z_+D_+\rho_{\mathrm{s}}\left(-\frac{2}{\Delta x^2} - k^2\right) - \alpha_2\left(-\frac{2c_{0,i}}{\Delta x^2} - k^2 c_{0,i}\right), \tag{3.249}$$

$$A_{6,i} = z_+D_+\rho_{\mathrm{s}}\frac{1}{\Delta x^2} - \alpha_2\left(\frac{c_{0,x,i}}{2\Delta x} + \frac{c_{0,i}}{\Delta x^2}\right). \tag{3.250}$$

At the anode,

$$B_1c_{1,1} + B_2c_{1,2} + B_3c_{1,3} + B_4\phi_{1,1} + B_5\phi_{1,2} + B_6\phi_{1,3} = \omega h_1^{\mathrm{a}}, \tag{3.251}$$

$$B_1 = \beta_{\mathrm{m}}\left(\alpha_1\frac{3}{2\Delta x} + \alpha_2\phi_{0,x,1}\right), \tag{3.252}$$

$$B_2 = \beta_{\mathrm{m}}\left(-\alpha_1\frac{2}{\Delta x}\right), \tag{3.253}$$

$$B_3 = \beta_{\mathrm{m}}\left(\alpha_1\frac{1}{2\Delta x}\right), \tag{3.254}$$

$$B_4 = \beta_{\mathrm{m}}(\alpha_2 c_{0,1} - z_+ D_+\rho_{\mathrm{s}})\left(-\frac{3}{2\Delta x}\right), \tag{3.255}$$

$$B_5 = \beta_{\mathrm{m}}(\alpha_2 c_{0,1} - z_+ D_+\rho_{\mathrm{s}})\left(\frac{2}{\Delta x}\right), \tag{3.256}$$

$$B_6 = \beta_{\mathrm{m}}(\alpha_2 c_{0,1} - z_+ D_+\rho_{\mathrm{s}})\left(-\frac{1}{2\Delta x}\right), \tag{3.257}$$

$$C_1 h_1^{\mathrm{a}} + C_2 c_{1,1} + C_3 c_{1,2} + C_4 c_{1,3} + C_5\phi_{1,1} + C_6\phi_{1,2} + C_7\phi_{1,3} = 0, \tag{3.258}$$

$$C_1 = c_{0,t,1}, \tag{3.259}$$

$$C_2 = -D\left(\frac{3}{2\Delta x} - z\phi_{0,x,1}\right), \tag{3.260}$$

$$C_3 = -D\left(-\frac{2}{\Delta x}\right), \tag{3.261}$$

$$C_4 = -D\left(\frac{1}{2\Delta x}\right), \tag{3.262}$$

$$C_5 = zDc_{0,1}\left(-\frac{3}{2\Delta x}\right), \tag{3.263}$$

$$C_6 = zDc_{0,1}\left(\frac{2}{\Delta x}\right), \tag{3.264}$$

$$C_7 = zDc_{0,1}\left(-\frac{1}{2\Delta x}\right), \tag{3.265}$$

$$D_1 h_1^{\mathrm{a}} + D_2 c_{1,1} + D_3\phi_{1,1} = \omega h_1^{\mathrm{a}}, \tag{3.266}$$

$$D_1 = \beta_{\mathrm{v}} j_{0,0,1}\hat{D}_1 = \beta_{\mathrm{v}} j_{0,0,1}\left[\alpha_{3,1} n\left(-\phi_{0,x,1} + \frac{\gamma k^2}{n}\right) + \frac{\exp(-\alpha n\eta_{0,1})c_{0,x,1}}{c_{0,1} - \rho_{\mathrm{s}}}\right], \tag{3.267}$$

$$D_2 = \beta_{\mathrm{v}} j_{0,0,1}\hat{D}_2 = \beta_{\mathrm{v}} j_{0,0,1}\left[\frac{\exp(-\alpha n\eta_{0,1})}{c_{0,1} - \rho_{\mathrm{s}}}\right], \tag{3.268}$$

$$D_3 = \beta_{\mathrm{v}} j_{0,0,1}\hat{D}_3 = \beta_{\mathrm{v}} j_{0,0,1}(-\alpha_{3,1} n). \tag{3.269}$$

At the cathode,

$$E_1 c_{1,N-2} + E_2 c_{1,N-1} + E_3 c_{1,N} + E_4\phi_{1,N-2} + E_5\phi_{1,N-1} + E_6\phi_{1,N} = -\omega h_1^{\mathrm{c}}, \tag{3.270}$$

$$E_1 = \beta_{\mathrm{m}}\left(\alpha_1 \frac{1}{2\Delta x}\right), \tag{3.271}$$

$$E_2 = \beta_{\mathrm{m}}\left(-\alpha_1 \frac{2}{\Delta x}\right), \tag{3.272}$$

$$E_3 = \beta_{\mathrm{m}}\left(\alpha_1 \frac{3}{2\Delta x} - \alpha_2 \phi_{0,x,N}\right), \tag{3.273}$$

$$E_4 = \beta_{\mathrm{m}}(\alpha_2 c_{0,N} - z_+ D_+ \rho_{\mathrm{s}})\left(-\frac{1}{2\Delta x}\right), \tag{3.274}$$

$$E_5 = \beta_{\mathrm{m}}(\alpha_2 c_{0,N} - z_+ D_+ \rho_{\mathrm{s}})\left(\frac{2}{\Delta x}\right), \tag{3.275}$$

$$E_6 = \beta_{\mathrm{m}}(\alpha_2 c_{0,N} - z_+ D_+ \rho_{\mathrm{s}})\left(-\frac{3}{2\Delta x}\right), \tag{3.276}$$

$$F_1 h_1^{\mathrm{c}} + F_2 c_{1,N-2} + F_3 c_{1,N-1} + F_4 c_{1,N} + F_5 \phi_{1,N-2} + F_6 \phi_{1,N-1} + F_7 \phi_{1,N} = 0, \tag{3.277}$$

$$F_1 = -c_{0,t,N}, \tag{3.278}$$

$$F_2 = -D\left(\frac{1}{2\Delta x}\right), \tag{3.279}$$

$$F_3 = -D\left(-\frac{2}{\Delta x}\right), \tag{3.280}$$

$$F_4 = -D\left(\frac{3}{2\Delta x} + z\phi_{0,x,N}\right), \tag{3.281}$$

$$F_5 = zDc_{0,N}\left(-\frac{1}{2\Delta x}\right), \tag{3.282}$$

$$F_6 = zDc_{0,N}\left(\frac{2}{\Delta x}\right), \tag{3.283}$$

$$F_7 = zDc_{0,N}\left(-\frac{3}{2\Delta x}\right), \tag{3.284}$$

$$G_1 h_1^{\mathrm{c}} + G_2 c_{1,N} + G_3 \phi_{1,N} = -\omega h_1^{\mathrm{c}}, \tag{3.285}$$

$$G_1 = \beta_{\mathrm{v}} j_{0,0,N} \hat{G}_1 = \beta_{\mathrm{v}} j_{0,0,N}\left[\alpha_{3,N} n\left(-\phi_{0,x,N} - \frac{\gamma k^2}{n}\right) + \frac{\exp(-\alpha n \eta_{0,N}) c_{0,x,N}}{c_{0,N} - \rho_{\mathrm{s}}}\right], \tag{3.286}$$

$$G_2 = \beta_{\mathrm{v}} j_{0,0,N} \hat{G}_2 = \beta_{\mathrm{v}} j_{0,0,N}\left[\frac{\exp(-\alpha n \eta_{0,N})}{c_{0,N} - \rho_{\mathrm{s}}}\right], \tag{3.287}$$

$$G_3 = \beta_{\mathrm{v}} j_{0,0,N} \hat{G}_3 = \beta_{\mathrm{v}} j_{0,0,N}(-\alpha_{3,N} n). \tag{3.288}$$

We can write all equations as the following generalized eigenvalue problem

$$Yv = \omega Z v, \tag{3.289}$$

$$v = \begin{bmatrix} h_1^{\mathrm{a}} \\ c_{1,1} \\ \phi_{1,1} \\ c_{1,2} \\ \phi_{1,2} \\ \vdots \\ c_{1,N-1} \\ \phi_{1,N-1} \\ c_{1,N} \\ \phi_{1,N} \\ h_1^{\mathrm{c}} \end{bmatrix} \in \mathbb{C}^{2N+2}, \tag{3.290}$$

$$Y = \begin{bmatrix}
D_1 & D_2 & D_3 & & & & & & & & & & & & & & & & & & & & \\
C_1 & C_2 & C_5 & C_3 & C_6 & C_4 & C_7 & & & & & & & & & & & & & & & & \\
 & B_1 & B_4 & B_2 & B_5 & B_3 & B_6 & & & & & & & & & & & & & & & & \\
 & M_{1,2} & M_{4,2} & M_{2,2} & M_{5,2} & M_{3,2} & M_{6,2} & & & & & & & & & & & & & & & & \\
 & A_{1,2} & A_{4,2} & A_{2,2} & A_{5,2} & A_{3,2} & A_{6,2} & & & & & & & & & & & & & & & & \\
 & & & M_{1,3} & M_{4,3} & M_{2,3} & M_{5,3} & M_{3,3} & M_{6,3} & & & & & & & & & & & & & & \\
 & & & A_{1,3} & A_{4,3} & A_{2,3} & A_{5,3} & A_{3,3} & A_{6,3} & & & & & & & & & & & & & & \\
 & & & & & \ddots & \ddots & \ddots & \ddots & \ddots & \ddots & & & & & & & & & & & & \\
 & & & & & \ddots & \ddots & \ddots & \ddots & \ddots & \ddots & & & & & & & & & & & & \\
 & & & & & & & \ddots & \ddots & \ddots & \ddots & \ddots & \ddots & & & & & & & & & \\
 & & & & & & & \ddots & \ddots & \ddots & \ddots & \ddots & \ddots & & & & & & & & & \\
 & & & & & & & & & \ddots & \ddots & \ddots & \ddots & \ddots & \ddots & & & & & & & \\
 & & & & & & & & & \ddots & \ddots & \ddots & \ddots & \ddots & \ddots & & & & & & & \\
 & & & & & & & & & & & M_{1,N-2} & M_{4,N-2} & M_{2,N-2} & M_{5,N-2} & M_{3,N-2} & M_{6,N-2} & & & & & \\
 & & & & & & & & & & & A_{1,N-2} & A_{4,N-2} & A_{2,N-2} & A_{5,N-2} & A_{3,N-2} & A_{6,N-2} & & & & & \\
 & & & & & & & & & & & & & M_{1,N-1} & M_{4,N-1} & M_{2,N-1} & M_{5,N-1} & M_{3,N-1} & M_{6,N-1} & & \\
 & & & & & & & & & & & & & A_{1,N-1} & A_{4,N-1} & A_{2,N-1} & A_{5,N-1} & A_{3,N-1} & A_{6,N-1} & & \\
 & & & & & & & & & & & & & E_1 & E_4 & E_2 & E_5 & E_3 & E_6 & & \\
 & & & & & & & & & & & & & F_2 & F_5 & F_3 & F_6 & F_4 & F_7 & F_1 & \\
 & & & & & & & & & & & & & & & & & G_2 & G_3 & G_1
\end{bmatrix}$$

$$\in \mathbb{R}^{(2N+2)\times(2N+2)}, \tag{3.291}$$

$$Z = \begin{bmatrix}
1 & 0 & 0 & & & & & & & & & & \\
0 & 0 & 0 & & & & & & & & & & \\
1 & 0 & 0 & & & & & & & & & & \\
 & & & 1 & & & & & & & & & \\
 & & & & 0 & & & & & & & & \\
 & & & & & 1 & & & & & & & \\
 & & & & & & 0 & & & & & & \\
 & & & & & & & \ddots & & & & & \\
 & & & & & & & & 1 & & & & \\
 & & & & & & & & & 0 & & & \\
 & & & & & & & & & & 1 & & \\
 & & & & & & & & & & & 0 & \\
 & & & & & & & & & & & & 0 & 0 & -1 \\
 & & & & & & & & & & & & 0 & 0 & 0 \\
 & & & & & & & & & & & & 0 & 0 & -1
\end{bmatrix} \in \mathbb{R}^{(2N+2)\times(2N+2)}, \quad (3.292)$$

where $Y, Z \in \mathbb{R}^{(2N+2)\times(2N+2)}$, $v \in \mathbb{C}^{2N+2}$ and $\omega \in \mathbb{C}$. Y is non-singular with rank $2N+2$ and Z is singular with rank N, therefore some of the eigenvalues are infinite. Since $v \in \mathbb{C}^{2N+2}$, the total number of eigenvalues is $2N+2$. N eigenvalues are finite that correspond to the number of linearly independent rows/columns in Z, i.e., rank of Z, and $N+2$ eigenvalues are infinite that correspond to the number of linearly dependent rows/columns in Z. The linearly dependent rows/columns in Z arise from the time-independent terms in the equations for the perturbed state.

While the ordering of the equations in Y and Z and variables in v is natural and minimizes the bandwidths of Y and Z, we would want to map the infinite eigenvalues to other arbitrarily chosen points in the complex plane [98] because we are only interested in the finite eigenvalues. To do so, we first subtract row 1 with row 3 and row $2N+2$ with row $2N$ so that rows 1 and $2N+2$ of Z become zero rows:

$$D_1' h_1^{\mathrm{a}} + D_2' c_{1,1} + D_3' c_{1,2} + D_4' c_{1,3} + D_5' \phi_{1,1} + D_6' \phi_{1,2} + D_7' \phi_{1,3} = 0, \quad (3.293)$$

$$D_1' = D_1, \tag{3.294}$$

$$D_2' = D_2 - B_1, \tag{3.295}$$

$$D_3' = -B_2, \tag{3.296}$$

$$D_4' = -B_3, \tag{3.297}$$

$$D_5' = D_3 - B_4, \tag{3.298}$$

$$D_6' = -B_5, \tag{3.299}$$

$$D_7' = -B_6, \tag{3.300}$$

$$G_1' h_1^{\mathrm{c}} + G_2' c_{1,N-2} + G_3' c_{1,N-1} + G_4' c_{1,N} + G_5' \phi_{1,N-2} + G_6' \phi_{1,N-1} + G_7' \phi_{1,N} = 0, \tag{3.301}$$

$$G_1' = G_1, \tag{3.302}$$

$$G_2' = -E_1, \tag{3.303}$$

$$G_3' = -E_2, \tag{3.304}$$

$$G_4' = G_2 - E_3, \tag{3.305}$$

$$G_5' = -E_4, \tag{3.306}$$

$$G_6' = -E_5, \tag{3.307}$$

$$G_7' = G_3 - E_6. \tag{3.308}$$

Therefore, row 1 of Y becomes

$$\begin{bmatrix} D_1' & D_2' & D_5' & D_3' & D_6' & D_4' & D_7' & 0 & \cdots & 0 \end{bmatrix}, \tag{3.309}$$

while row $2N+2$ of Y becomes

$$\begin{bmatrix} 0 & \cdots & 0 & G_2' & G_5' & G_3' & G_6' & G_4' & G_7' & G_1' \end{bmatrix}. \tag{3.310}$$

By premultiplying Z with a permutation matrix $P_\pi \in \mathbb{R}^{(2N+2)\times(2N+2)}$, we then permute Z and accordingly Y so that the $N+2$ zero rows in Z are at the bottom. We denote the permuted Y and Z as $Y' \in \mathbb{R}^{(2N+2)\times(2N+2)}$ and $Z' \in \mathbb{R}^{(2N+2)\times(2N+2)}$ respectively and therefore, $Y' = P_\pi Y$ and $Z' = P_\pi Z$. The permutation matrix P_π

can be written as

$$P_\pi = \begin{bmatrix} e_{\pi(1)} \\ e_{\pi(2)} \\ \vdots \\ e_{\pi(2N+1)} \\ e_{\pi(2N+2)} \end{bmatrix} \tag{3.311}$$

where e_i is the standard basis row vector of length $2N+2$ with 1 at its i-th entry and 0 everywhere else, and $\pi(\cdot)$ is the function that determines the order of permutation. In our case, $\pi(\cdot)$ is given by

$$\pi(1) = 3, \tag{3.312}$$

$$\pi(i) = 2i, \quad i = 2, \ldots, N-1, \tag{3.313}$$

$$\pi(N) = 2N, \tag{3.314}$$

$$\pi(N+1) = 1, \tag{3.315}$$

$$\pi(N+2) = 2, \tag{3.316}$$

$$\pi(i) = 2[i-(N+3)] + 5, \quad i = N+3, \ldots, 2N, \tag{3.317}$$

$$\pi(2N+1) = 2N+1, \tag{3.318}$$

$$\pi(2N+2) = 2N+2. \tag{3.319}$$

Following [98], we write Y' and Z' as

$$Y' = \begin{bmatrix} H \\ P \end{bmatrix}, \tag{3.320}$$

$$Z' = \begin{bmatrix} \hat{Z} \\ O \end{bmatrix}, \tag{3.321}$$

where $H \in \mathbb{R}^{N\times(2N+2)}$, $P \in \mathbb{R}^{(N+2)\times(2N+2)}$, $\hat{Z} \in \mathbb{R}^{N\times(2N+2)}$ is a matrix consisting of the nonzero rows of Z', and $O \in \mathbb{R}^{(N+2)\times(2N+2)}$ is a zero matrix consisting of the zero rows of Z'. We define $E \in \mathbb{C}^{(N+2)\times(N+2)}$ as a diagonal matrix with entries $E_{ii} = -\sigma_i$ for $i = 1, \ldots, N+2$ where $\sigma_i \in \mathbb{C}$ is arbitrary and is the value that the i-th infinite

eigenvalue is mapped to. The modified generalized eigenvalue problem then becomes

$$\bar{Y}v = \omega \bar{Z}v, \tag{3.322}$$

$$\bar{Y} = \begin{bmatrix} H \\ EP \end{bmatrix} \in \mathbb{R}^{(2N+2)\times(2N+2)}, \tag{3.323}$$

$$\bar{Z} = \begin{bmatrix} \hat{Z} \\ -P \end{bmatrix} \in \mathbb{R}^{(2N+2)\times(2N+2)}. \tag{3.324}$$

3.8.5 Parameter sweeps

For various $\frac{t}{t_s}$ values for $\rho_s \in \{-0.05, 0, 0.05\}$ and Da $\in \{0.1, 1, 10\}$, we plot numerically computed $\Re(\omega)$ against k for $J_a = 1$ (limiting current) in Figure 3-13 and $J_a = 0.5$ (underlimiting current) in Figure 3-14.

3.8.6 Comparison between numerical and approximate solutions

To illustrate how well the approximations given by Equations 49 and 50 in the main text work, for $\rho_s \in \{-0.05, 0, 0.05\}$ and Da $\in \{0.1, 1, 10\}$, we plot numerical and approximate values of k_{max} and ω_{max} for $J_a = 1.5$ in Figure 3-15, $J_a = 1$ in Figure 3-16 and $J_a = 0.5$ in Figure 3-17. For the same ρ_s and Da ranges, we also plot numerical and approximate values of k_c for $J_a = 1.5$ in Figure 3-18, $J_a = 1$ in Figure 3-19 and $J_a = 0.5$ in Figure 3-20.

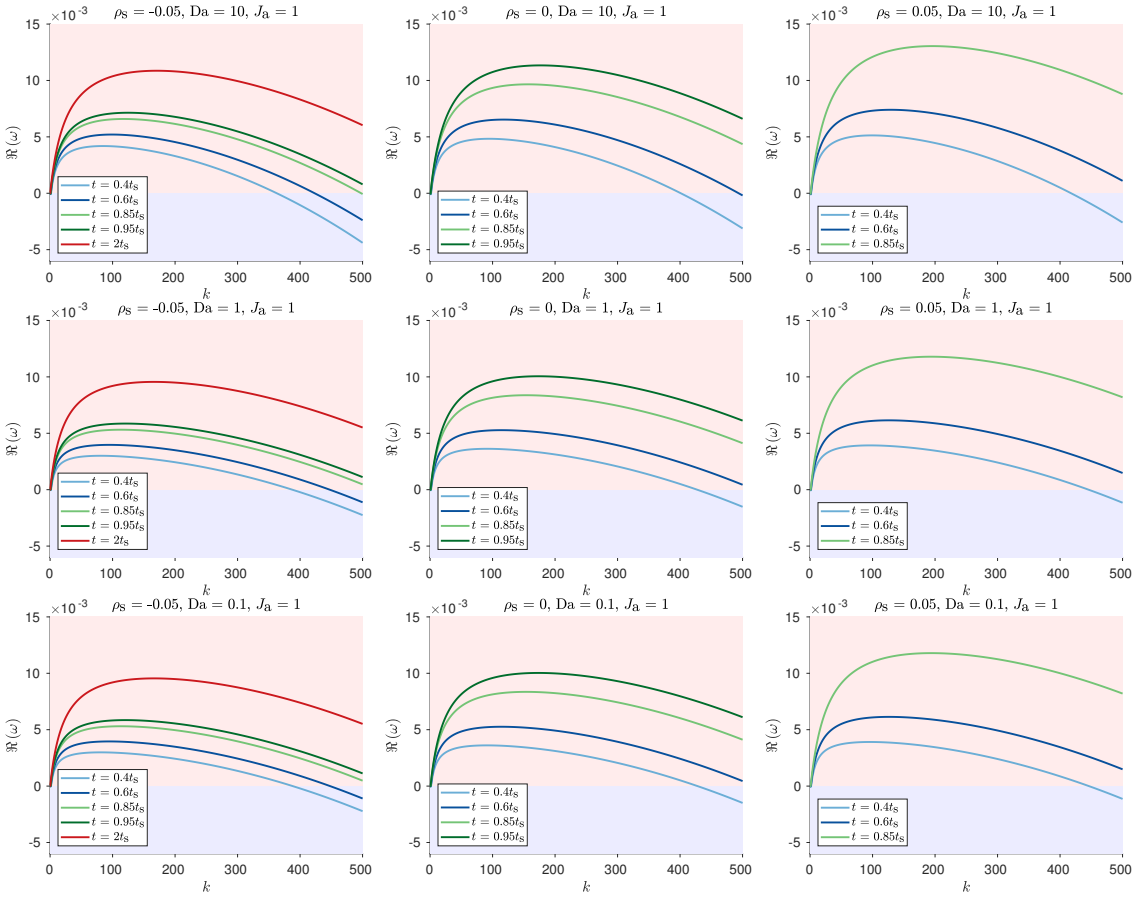

Figure 3-13: Plots of numerical $\Re(\omega)$ against k for various $\frac{t}{t_s}$ values for $\rho_s \in \{-0.05, 0, 0.05\}$, Da $\in \{0.1, 1, 10\}$ and $J_a = 1$ (limiting current). ρ_s increases from left to right and Da increases from bottom to top. Blue lines correspond to early times $t = 0.4t_s$ and $t = 0.6t_s$, green lines correspond to times near Sand's time $t = 0.85t_s$ and $t = 0.95t_s$, and red line corresponds to time beyond Sand's time $t = 2t_s$. For each color, intensity increases in the direction of increasing t.

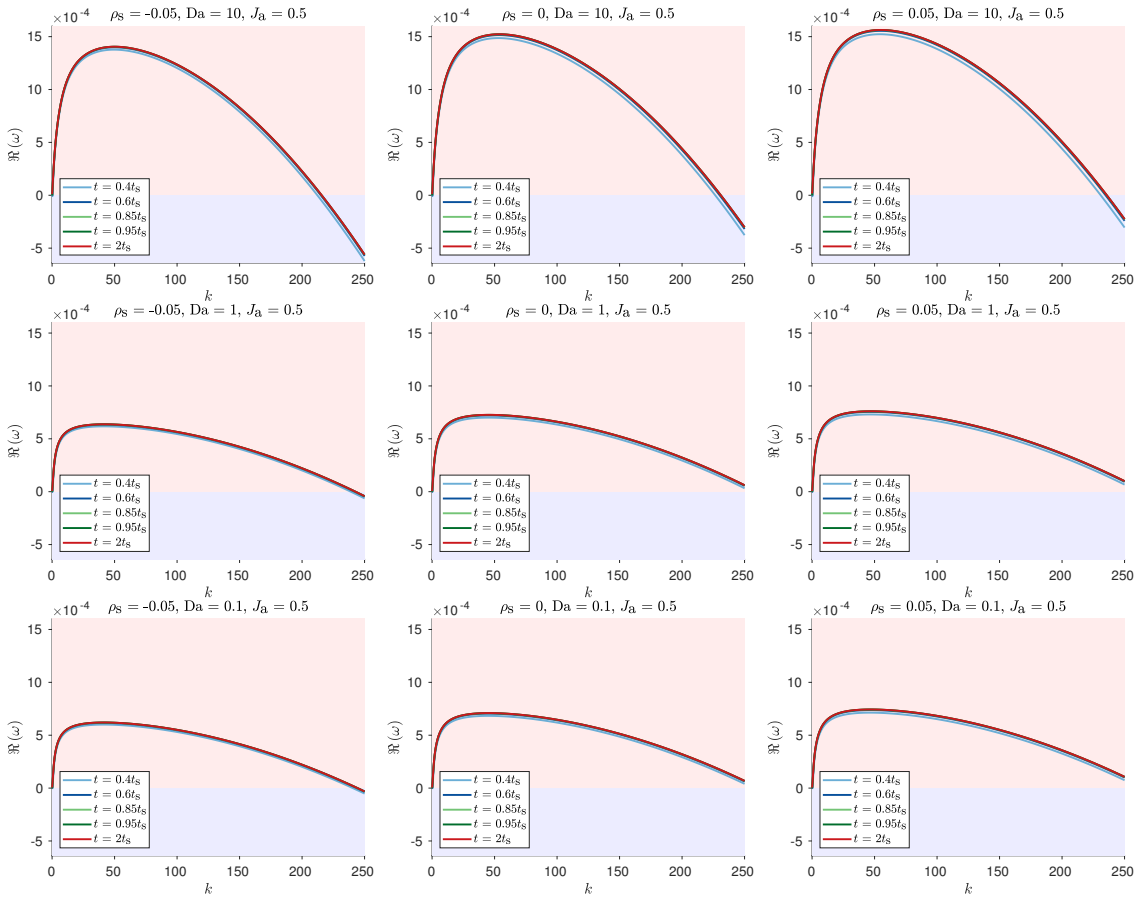

Figure 3-14: Plots of numerical $\Re(\omega)$ against k for various $\frac{t}{t_s}$ values for $\rho_s \in \{-0.05, 0, 0.05\}$, Da $\in \{0.1, 1, 10\}$ and $J_a = 0.5$ (underlimiting current). ρ_s increases from left to right and Da increases from bottom to top. Blue lines correspond to early times $t = 0.4t_s$ and $t = 0.6t_s$, green lines correspond to times near Sand's time $t = 0.85t_s$ and $t = 0.95t_s$, and red line corresponds to time beyond Sand's time $t = 2t_s$. For each color, intensity increases in the direction of increasing t.

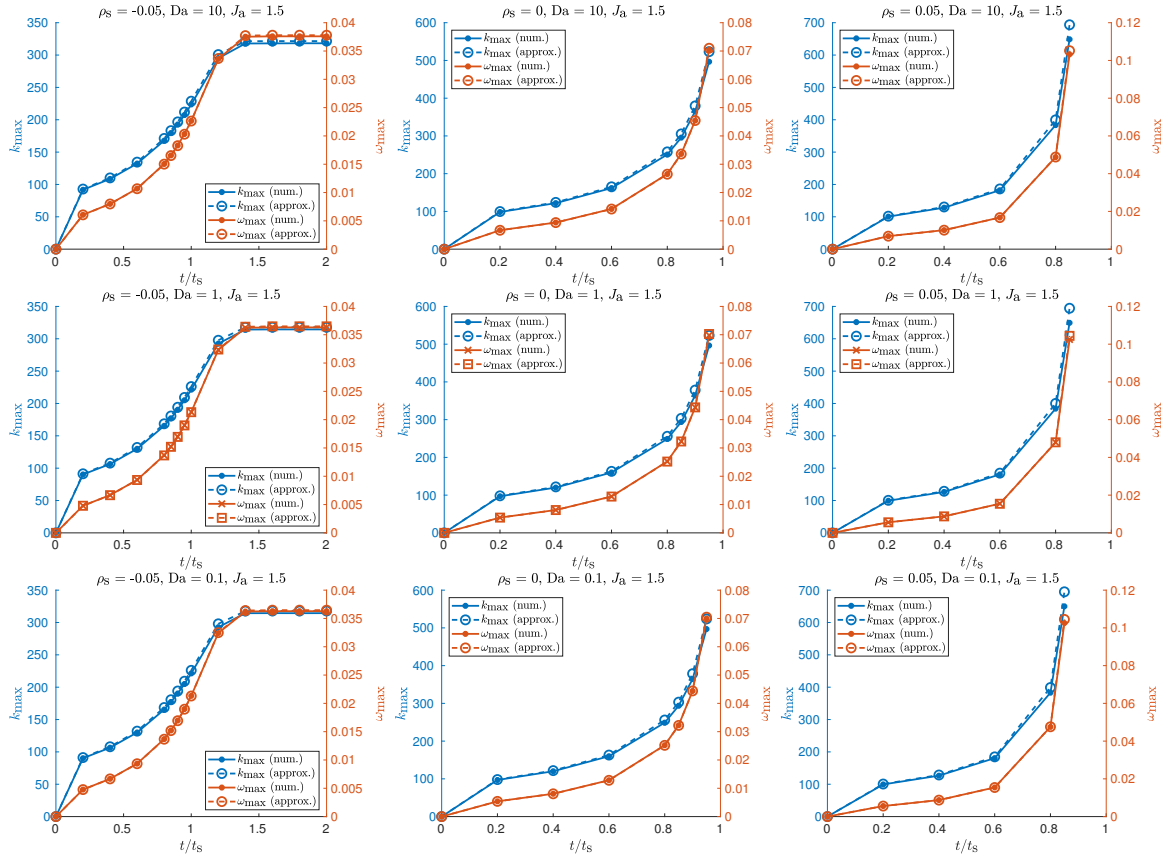

Figure 3-15: Plots of numerical and approximate values of $k_{\max}$ and $\omega_{\max}$ against $\frac{t}{t_s}$ for $\rho_s \in \{-0.05, 0, 0.05\}$, Da $\in \{0.1, 1, 10\}$ and $J_a = 1.5$ (overlimiting current). In the legends, "num." refers to numerical solutions while "approx." refers to approximate solutions.

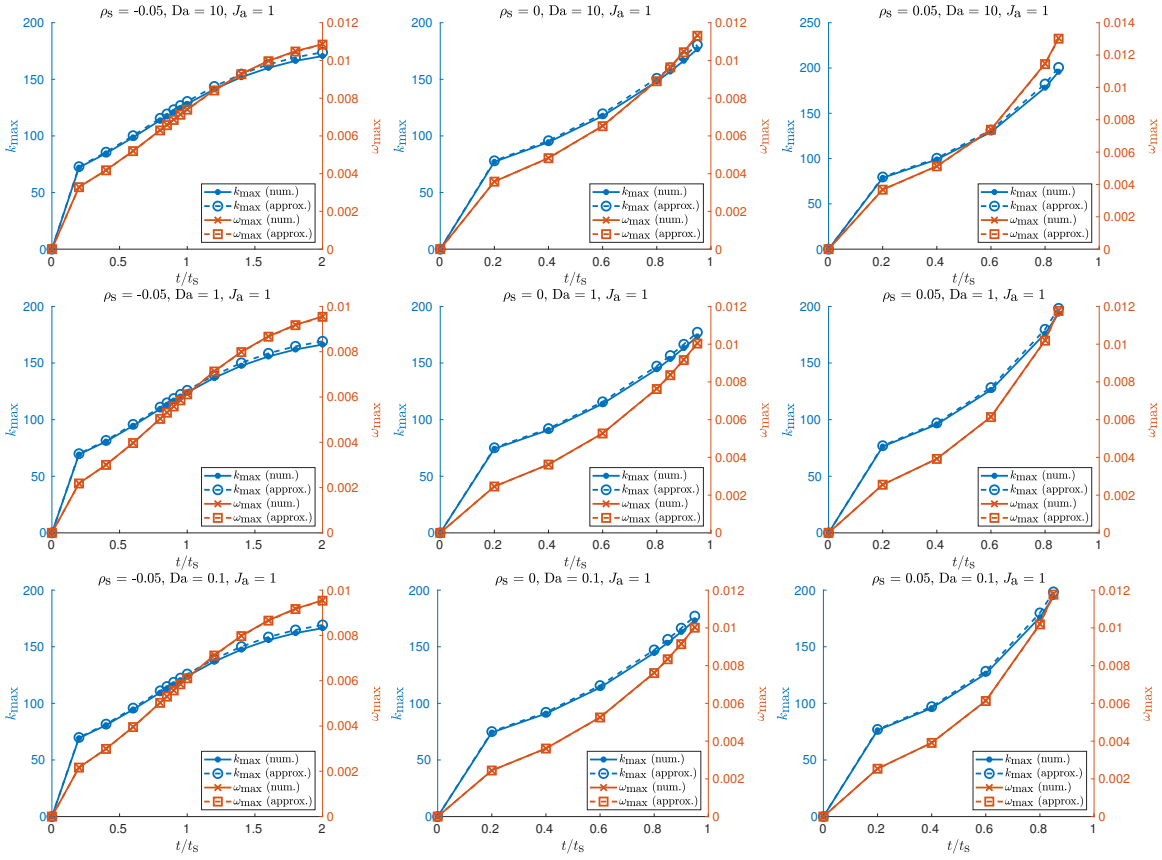

Figure 3-16: Plots of numerical and approximate values of $k_{\max}$ and $\omega_{\max}$ against $\frac{t}{t_s}$ for $\rho_s \in \{-0.05, 0, 0.05\}$, Da $\in \{0.1, 1, 10\}$ and $J_a = 1$ (limiting current). In the legends, "num." refers to numerical solutions while "approx." refers to approximate solutions.

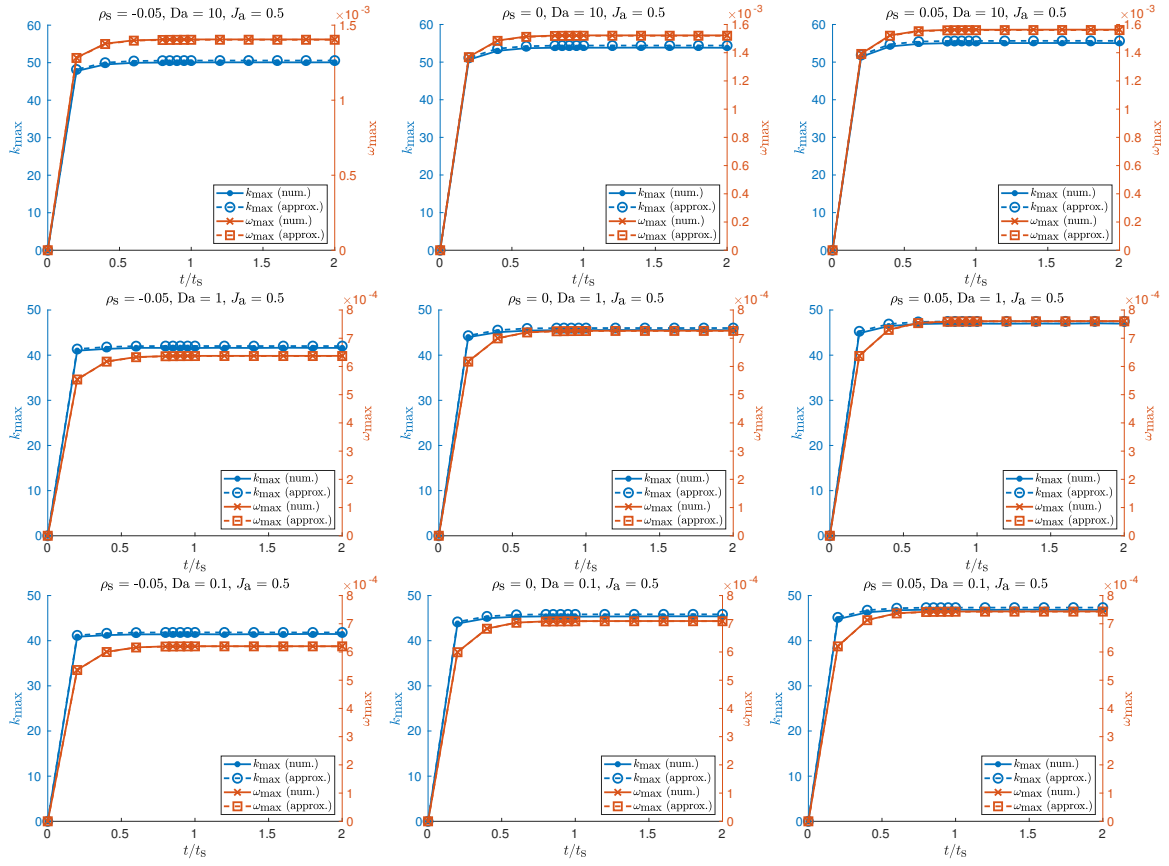

Figure 3-17: Plots of numerical and approximate values of $k_{\max}$ and $\omega_{\max}$ against $\frac{t}{t_s}$ for $\rho_s \in \{-0.05, 0, 0.05\}$, Da $\in \{0.1, 1, 10\}$ and $J_a = 0.5$ (underlimiting current). In the legends, "num." refers to numerical solutions while "approx." refers to approximate solutions.

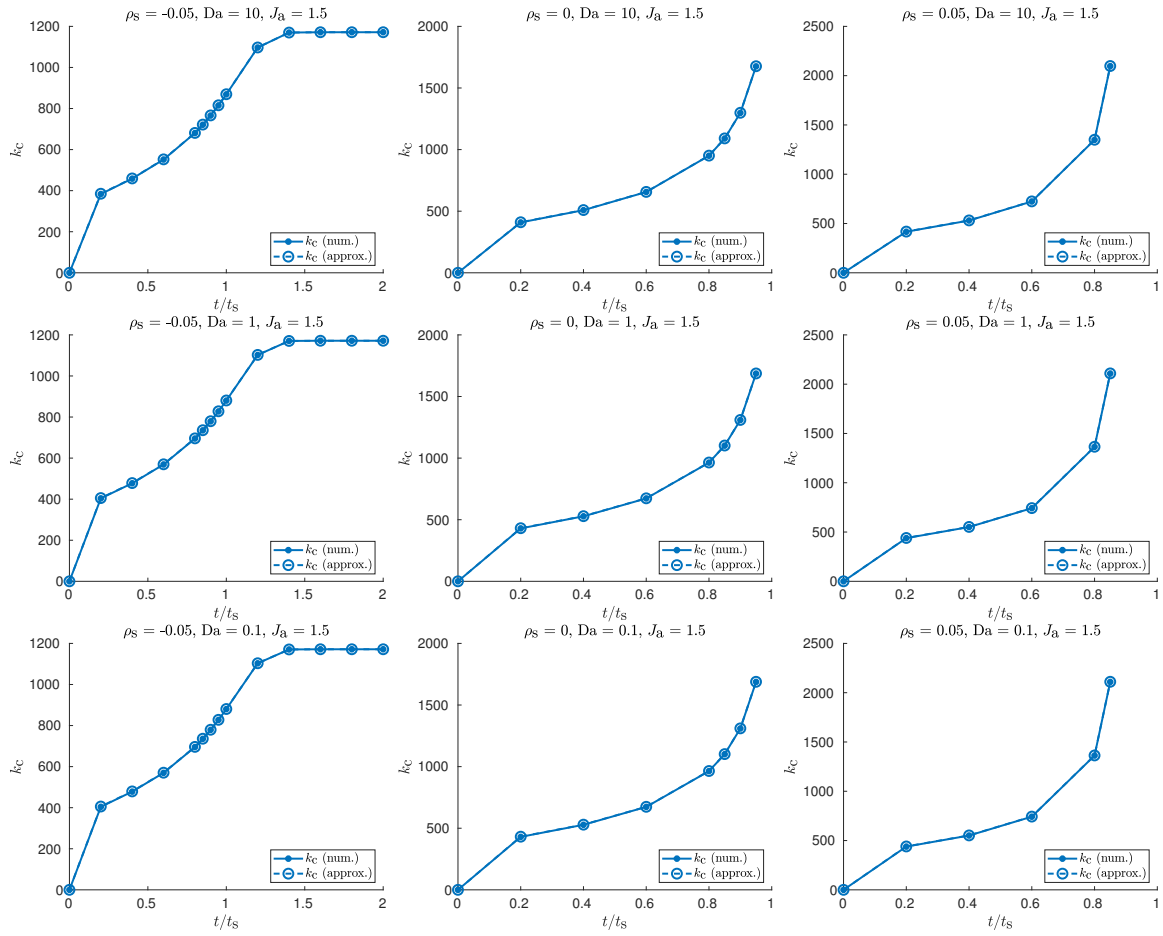

Figure 3-18: Plots of numerical and approximate values of k_c against $\frac{t}{t_s}$ for $\rho_s \in \{-0.05, 0, 0.05\}$, Da $\in \{0.1, 1, 10\}$ and $J_a = 1.5$ (overlimiting current). In the legends, "num." refers to numerical solutions while "approx." refers to approximate solutions.

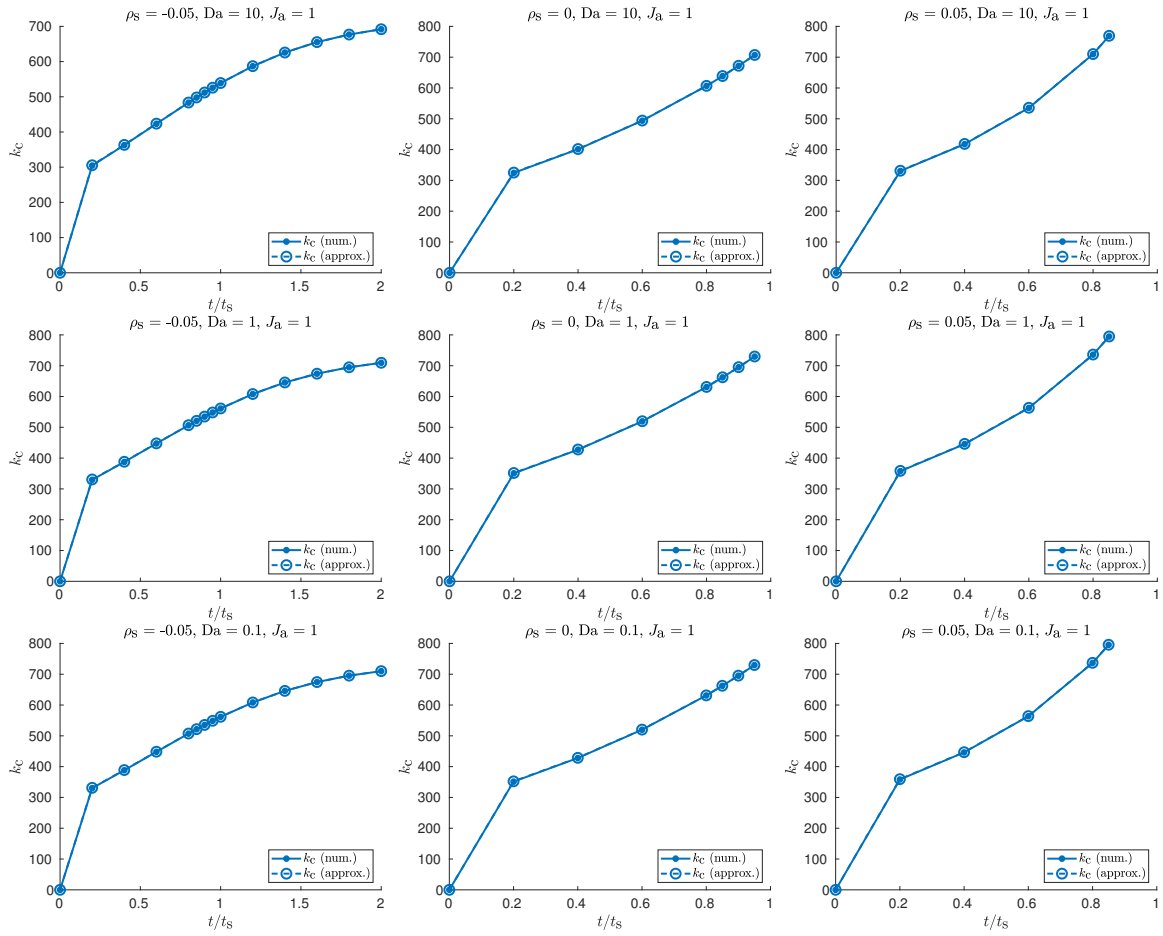

Figure 3-19: Plots of numerical and approximate values of k_c against $\frac{t}{t_s}$ for $\rho_s \in \{-0.05, 0, 0.05\}$, Da $\in \{0.1, 1, 10\}$ and $J_a = 1$ (limiting current). In the legends, "num." refers to numerical solutions while "approx." refers to approximate solutions.

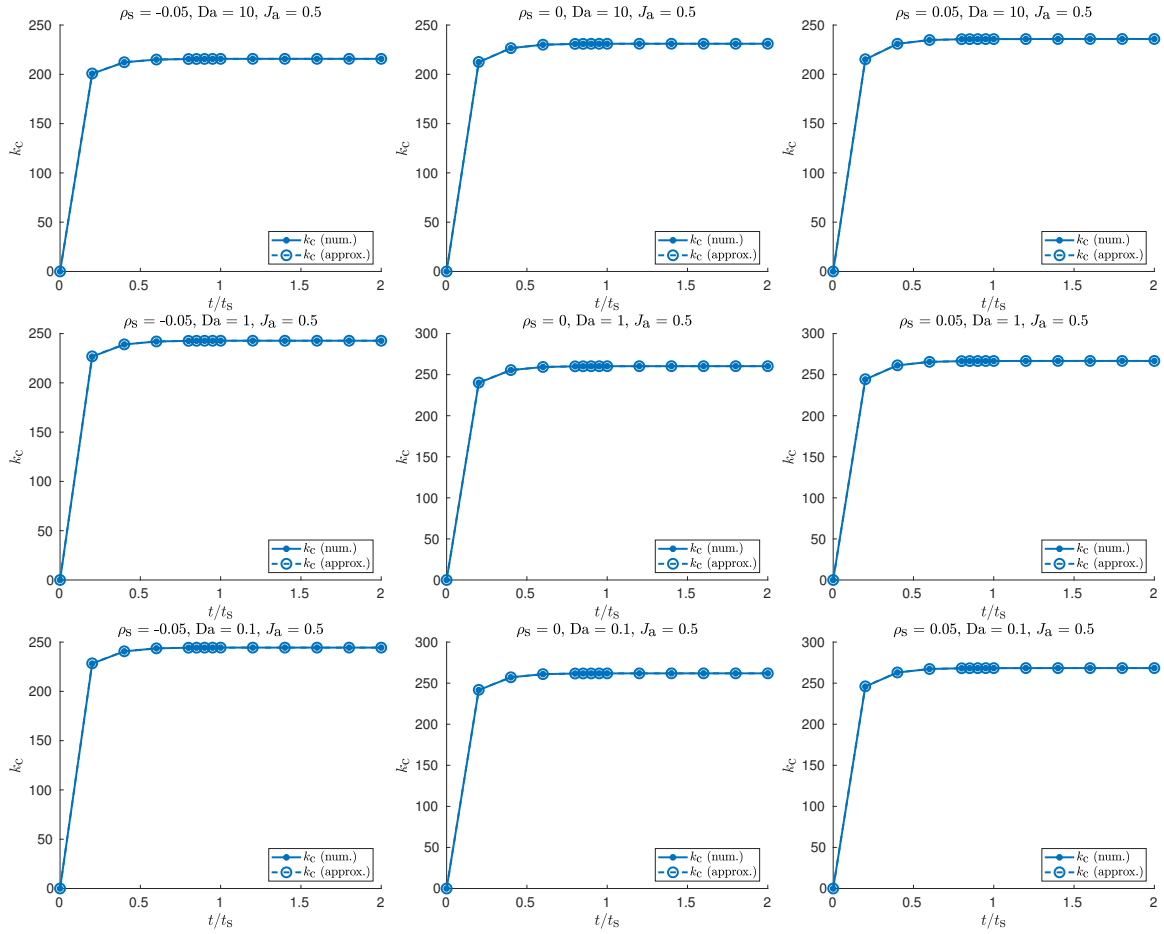

Figure 3-20: Plots of numerical and approximate values of k_c against $\frac{t}{t_s}$ for $\rho_s \in \{-0.05, 0, 0.05\}$, Da $\in \{0.1, 1, 10\}$ and $J_a = 0.5$ (underlimiting current). In the legends, "num." refers to numerical solutions while "approx." refers to approximate solutions.

Chapter 4

Electrochemical impedance spectroscopy of electrodiffusion and electrochemical reactions in charged porous media

The contents of this chapter will be submitted for publication in the near future.

4.1 Abstract

We study the impedance spectra for the leaky membrane model, which governs ion diffusion and electromigration in a porous medium with a fixed volume-averaged background charge density, coupled with Butler-Volmer kinetics for describing electrochemical reactions that occur at the electrodes flanking the porous medium. Copper electrodeposition and electrodissolution is used as a prototypical example of Butler-Volmer reaction kinetics. For a negatively charged porous medium, because the leaky membrane model predicts overlimiting current that is carried by surface conduction, we focus on analyzing impedance spectra generated at overlimiting currents and high overpotentials. We show that when the porous medium is sufficiently negatively charged such that the charge transfer resistance is larger than or comparable

with the bulk electrolyte impedance, the impedance spectrum in the Nyquist plot shifts leftwards as the applied steady state current increases. On the other hand, if the porous medium is neutral, positively charged or weakly negatively charged, the impedance spectrum shifts rightwards. Next, we perform nonlinear least squares fitting on experimental data to demonstrate that model predictions agree well with the data, thus providing a physical interpretation of the experimental impedance spectra and removing the need to fit them to ad hoc equivalent circuits.

4.2 Introduction

Through measuring the system response to a sinusoidal time-varying small-amplitude perturbation in current or voltage, impedance spectroscopy [27, 134, 24, 178, 150, 59] is commonly applied to decouple and analyze complex and coupled phenomena such as mass transport, charge transport and chemical reactions in liquid [151] and solid [47, 151, 46, 200] electrochemical systems in a non-invasive manner. Some common applications include measuring diffusion coefficients of ions [228, 15, 119, 127] and neutral species [136, 107, 209], double layer capacitances [228, 113, 133, 114, 127, 193, 83] and Faradaic reaction rate constants and charge transfer coefficients [192, 228, 113, 133, 114, 127, 193, 83], and elucidating reaction mechanisms and their associated rate constants [149]. For batteries that employ porous nanoparticle electrodes consisting of active particles, impedance spectroscopy can be used to identify the particle geometry and curvature and particle size distribution [231], and anisotropies in physical parameters such as diffusion coefficients, exchange current densities, rate constants, interfacial capacitances and length distributions [232]. For solid oxide fuel cells (SOFCs), impedance spectroscopy is used to extract parameters for heterogeneous electrocatalysis such as the forward and backward rate constants for oxygen adsorption and surface diffusion coefficient of oxygen adatoms [91], and geometrical parameters of the porous electrodes such as porosity and tortuosity [92]. Impedance spectroscopy is also used in inversion problems where the spectra are inverted with appropriate regularization to obtain distributions of relaxation times (DRT) [255] and

diffusion times (DDT) [233].

In a neutral channel or porous medium in which ion transport is governed by diffusion and electromigration, which is also collectively called electrodiffusion, there exists a diffusion-limited current that the electrochemical system cannot exceed [24, 172]. However, in practice, it has been demonstrated experimentally that overlimiting current (OLC) beyond the diffusion-limited current can be achieved in ion-exchange membranes [207, 211, 126, 125, 203, 208, 72, 221, 176, 175, 235], and microchannels and nanochannels [123, 269, 271, 273, 272, 170, 218, 229]. There are three physical mechanisms for OLC in a confined channel or porous medium [77]: surface conduction [271, 273, 272, 155, 154, 76], electroosmotic flow [268, 206] and electroosmotic instability [205, 270]. OLC can also be achieved via chemical mechanisms such as water splitting [176, 175] and current-induced membrane discharge [6]. In this paper, we focus on surface conduction because the pore size of interest is in the nanometer scale where surface conduction is expected to dominate [77]. When a sufficiently large current or voltage is applied across a porous medium with charged surface pores or a nanochannel with charged sidewalls such that the coions are depleted at an ion-selective interface such as an electrode, in order to sustain the current, a large electric field develops in the depletion region to transport the counterions in the electric double layers via electromigration. This phenomenon is known as as surface conduction that results in the formation and propagation of a deionization shock in porous media [154, 76, 267] and microchannels and nanochannels [271, 273, 272, 77, 155, 173] that moves away from the ion-selective interface where ions are depleted behind the deionization shock.

In this paper, we use the leaky membrane model [77, 154, 76] for modeling ion transport to describe OLC due to surface conduction and couple it with Butler-Volmer kinetics [172, 24, 31, 84] for describing electrochemical reaction kinetics. Copper electrodeposition and electrodissolution is used as a prototypical example of Butler-Volmer reaction kinetics because its reaction mechanism and parameters have been studied extensively [172, 157, 45, 54]. The full model here is based on the model explored in our previous work whose steady state current-voltage relations and linear

sweep voltammetry have been analyzed and applied to experimental data for copper electrodeposition in various porous media [122]. We study the impedance of this coupled model in a finite domain that contains a charged porous medium filled with a binary asymmetric liquid electrolyte. Because the domain under consideration is finite, some contributions to the total impedance response can be interpreted as finite length Warburg elements instead of the classical Warburg element for semi-infinite diffusion [258]. Because the leaky membrane model predicts OLC that is carried by surface conduction, we focus on predicting and interpreting impedance spectra at overlimiting currents and high overpotentials.

4.3 Model

The model whose impedance spectra we analyze in this paper is the leaky membrane model for ion transport, which is capable of predicting overlimiting current (OLC) carried by surface conduction, coupled with Butler-Volmer reaction kinetics. We summarize the governing equations and boundary conditions for this model in Sections 4.3.1 and 4.3.2 respectively and more details of the model can be found at [122]. In Section 4.3.3, we discuss how we perform nondimensionalization, which reveals useful scales and makes the equations more compact, while in Sections 4.3.4, 4.3.5, 4.3.6 and 4.3.7, we go through in detail the process of solving for the impedance spectra. Section 4.3.5 only discusses aspects of the steady state equations that are directly relevant to impedance analysis and a more in-depth discussion is given in [122].

4.3.1 Transport

As shown in Figure 4-1, we consider a binary asymmetric liquid electrolyte in a charged porous medium in 1D where $x \in [0, L]$ and the anode is located at $x = 0$ while the cathode is located at $x = L$. The cations are electroactive while the anions are inert. We denote the cation and anion concentrations as $c_{\pm}$, cation and anion fluxes as $F_{\pm}$, electrolyte electric potential as ϕ, cation and anion charge numbers as $z_{\pm}$, and numbers of cations and anions formed from complete dissociation of 1

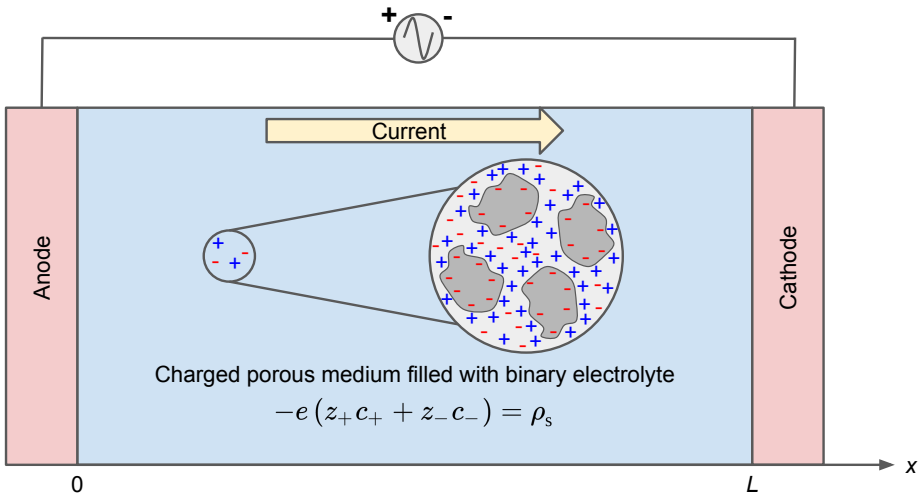

Figure 4-1: Diagram of system considered: charged porous medium filled with binary asymmetric liquid electrolyte where anode is on the left at $x = 0$ and cathode is on the right at $x = L$. An alternating current or voltage source is connected to the electrodes so that the impedance spectrum can be measured, and current in the system flows from left to right. The displayed equation describes macroscopic electroneutrality given by Equation 4.2 where ρ_s is the volume-averaged background charge density.

molecule of neutral salt as $\nu_\pm$. For the electroneutrality of 1 molecule of neutral salt, we require $z_+\nu_+ + z_-\nu_- = 0$. The porous medium considered has porosity ϵ_p, tortuosity τ, internal pore surface area per unit volume a_p and pore surface charge per unit area σ_s. We assume that there are no fluid flow and homogeneous reactions and all material properties such as ϵ_p, τ, a_p and σ_s are uniform and constant. We also assume that dilute solution theory is applicable, therefore all activity coefficients are 1 and the cation and anion macroscopic diffusivities $D_{\pm 0}$ are uniform, constant and concentration-independent where the 0 subscript indicates that the diffusivities are taken in the dilute limit. To account for corrections due to the tortuosity of the porous medium, the macroscopic diffusivities $D_{\pm 0}$ are related to their corresponding molecular (free solution) diffusivities $D^m_{\pm 0}$ via $D_{\pm 0} = \frac{D^m_{\pm 0}}{\tau}$ [84]. The PDEs (partial differential equations) governing ion transport are given by the Nernst-Planck equations, which are constrained by the macroscopic electroneutrality condition. Taking these assumptions into consideration, the PDEs and electroneutrality constraint are

given by

$$\epsilon_{\mathrm{p}} \frac{\partial c_{\pm}}{\partial t} + \frac{\partial F_{\pm}}{\partial x} = 0, \quad F_{\pm} = -\epsilon_{\mathrm{p}} D_{\pm 0} \left(\frac{\partial c_{\pm}}{\partial x} + \frac{z_{\pm} e c_{\pm}}{k_{\mathrm{B}} T} \frac{\partial \phi}{\partial x} \right), \tag{4.1}$$

$$\rho_{\mathrm{s}} \equiv \frac{\sigma_{\mathrm{s}}}{h_{\mathrm{p}}} = \frac{a_{\mathrm{p}} \sigma_{\mathrm{s}}}{\epsilon_{\mathrm{p}}} = -e(z_+ c_+ + z_- c_-), \tag{4.2}$$

where the effective pore size h_{p} is defined as $h_{\mathrm{p}} \equiv \frac{\epsilon_{\mathrm{p}}}{a_{\mathrm{p}}}$ while ρ_{s} is the volume-averaged background charge density. The current density J is given by the sum of the cation and anion fluxes and obeys the charge conservation equation given by

$$\frac{\partial J}{\partial x} = 0, \quad J = e(z_+ F_+ + z_- F_-). \tag{4.3}$$

In 1D, because of charge conservation, we require $J(x = 0) = J(x = L)$. Therefore, the current I is given by $I = J(x = 0)A = J(x = L)A$ where A is the surface area of either the anode or cathode.

4.3.2 Boundary conditions

While the steady state analysis in Section 4.2 of [122] discusses three different cases for boundary conditions, in this paper, we consider only Butler-Volmer reaction kinetics [172, 24, 31, 84] at the anode and cathode, which corresponds to case 3 in Section 4.2 of [122].

We denote the electrode electric potential as ϕ_{e}. We set $\phi_{\mathrm{e}}^{\mathrm{a}} = 0$, i.e., ground the anode, and $\phi_{\mathrm{e}}^{\mathrm{c}} = -V$ where $V \geq 0$ and the "a" and "c" superscripts refer to the anode and cathode respectively. We assume that the anode at $x = 0$ and the cathode at $x = L$ are ideal cation-selective and anion-blocking surfaces, therefore there is no anion flux at $x = 0$ and $x = L$

$$F_-(x = 0) = F_-(x = L) = 0. \tag{4.4}$$

At steady state, since the anions cannot leave the system, the number of anions is

conserved, which is described by the following integral constraint

$$\int_0^L c_- \, \mathrm{d}x = \beta_1 L, \quad \beta_1 \equiv \nu_- c_0 - \frac{\rho_\mathrm{s} + |\rho_\mathrm{s}|}{2 z_- e}, \tag{4.5}$$

where c_0 is the neutral salt bulk concentration [122].

We consider copper electrodeposition and electrodissolution as a prototypical example of electrochemical reaction kinetics, and its reaction mechanism is given by [172, 157, 45, 54]

$$\mathrm{Cu^{2+}(aq) + e^- \rightleftharpoons Cu^+(ads)}, \tag{4.6}$$

$$\mathrm{Cu^+(ads) + e^- \rightleftharpoons Cu(s)}, \tag{4.7}$$

where (aq), (ads) and (s) indicate aqueous, adsorbed and solid respectively. Assuming that the first step is the rate-determining step and the second step is at equilibrium, the Faradaic current density J_F is given by

$$J_\mathrm{F} = j_0 \left\{ \exp\left(-\frac{\alpha_1 e \eta}{k_\mathrm{B} T} \right) - \exp\left[\frac{(2-\alpha_1) e \eta}{k_\mathrm{B} T} \right] \right\}, \tag{4.8}$$

$$j_0 = j_0^\mathrm{ref} \left(\frac{\hat{c}_+}{\hat{c}_+^\mathrm{ref}} \right)^{1-\frac{\alpha_1}{2}} = 2 e k_0 \hat{c}_+^{\,1-\frac{\alpha_1}{2}}, \quad k_0 = \frac{j_0^\mathrm{ref}}{2e \left(\hat{c}_+^\mathrm{ref} \right)^{1-\frac{\alpha_1}{2}}}, \tag{4.9}$$

$$\Delta\phi^\mathrm{eq} = \frac{k_\mathrm{B} T}{2e} \ln \hat{c}_+ + E^\Theta, \tag{4.10}$$

where $\hat{c}_+ \equiv \frac{c_+}{c_+^\Theta}$ where the Θ superscript indicates standard state, j_0 is the exchange current density, j_0^ref is the exchange current density at a given reference $\hat{c}_+^\mathrm{ref}$, α_1 is the charge transfer coefficient of the first step, η is the overpotential given by $\eta = \Delta\phi - \Delta\phi^\mathrm{eq}$, $\Delta\phi$ is the interfacial electric potential difference given by $\Delta\phi = \phi_\mathrm{e} - \phi$, $\Delta\phi^\mathrm{eq}$ is the Nernst potential where the "eq" superscript denotes equilibrium, k_0 is the overall reaction rate constant and E^Θ is the standard electrode potential. For Butler-Volmer reaction kinetics at the anode and cathode, the boundary conditions describing conservation of charges across the electrode/electrolyte interfaces are given

by

$$-J(x=0) = \epsilon_{\mathrm{p}} J_{\mathrm{F}}^{\mathrm{a}}, \quad \phi_{\mathrm{e}}^{\mathrm{a}} = 0, \tag{4.11}$$

$$J(x=L) = \epsilon_{\mathrm{p}} J_{\mathrm{F}}^{\mathrm{c}}, \quad \phi_{\mathrm{e}}^{\mathrm{c}} = -V, \quad V \geq 0, \tag{4.12}$$

where the "a" and "c" superscripts refer to the anode and cathode respectively.

In this model, for simplicity, we do not account for the double layer charging current density that arises from the accumulation of excess counterions in the electric double layers. However, if we were to include it, a simple way to do so is to assume the electric double layer is an ideal capacitor and the double layer charging current density J_{DL} is given by $J_{\mathrm{DL}} = C_{\mathrm{DL}} \frac{\mathrm{d}\Delta\phi}{\mathrm{d}t}$ where C_{DL} is the double layer capacitance [231, 232]. The total current J is then given by the sum of the Faradaic and double layer charging current densities and we would modify the boundary conditions in Equations 4.11 and 4.12 to $-J(x=0) = \epsilon_{\mathrm{p}}(J_{\mathrm{F}}^{\mathrm{a}} + J_{\mathrm{DL}}^{\mathrm{a}})$ and $J(x=L) = \epsilon_{\mathrm{p}}(J_{\mathrm{F}}^{\mathrm{c}} + J_{\mathrm{DL}}^{\mathrm{c}})$ respectively.

4.3.3 Nondimensionalization

We denote the ambipolar diffusivity of the neutral salt in the dilute limit, the limiting current density and the limiting current as D_{amb0}, J_{lim} and $I_{\mathrm{lim}} = J_{\mathrm{lim}} A$ respectively. They are given by [172, 122]

$$D_{\mathrm{amb0}} = \frac{(z_+ - z_-) D_{+0} D_{-0}}{z_+ D_{+0} - z_- D_{-0}}, \quad J_{\mathrm{lim}} = \frac{2(z_+ - z_-) e \epsilon_{\mathrm{p}} D_{+0} \nu_- c_0}{L}. \tag{4.13}$$

These quantities are used to define appropriate scales for the following nondimensionalization: $\tilde{x} \equiv \frac{x}{L}$, $\tilde{t} \equiv \frac{D_{\mathrm{amb0}} t}{L^2}$, $\tilde{c}_{\pm} \equiv \frac{c_{\pm}}{\nu_{\pm} c_0}$, $\tilde{\beta}_1 \equiv \frac{\beta_1}{\nu_- c_0} = 1 + \frac{\tilde{\rho}_{\mathrm{s}} + |\tilde{\rho}_{\mathrm{s}}|}{2}$, $\tilde{\phi} \equiv \frac{e\phi}{k_{\mathrm{B}} T}$, $\tilde{F}_{\pm} \equiv \frac{L F_{\pm}}{\epsilon_{\mathrm{p}} D_{\mathrm{amb0}} \nu_{\pm} c_0}$, $\tilde{D}_{\pm 0} \equiv \frac{D_{\pm 0}}{D_{\mathrm{amb0}}}$, $\tilde{J} \equiv \frac{J}{J_{\mathrm{lim}}}$, $\tilde{I} \equiv \frac{I}{I_{\mathrm{lim}}}$, $\tilde{\rho}_{\mathrm{s}} \equiv \frac{\rho_{\mathrm{s}}}{z_+ \nu_+ e c_0} = -\frac{\rho_{\mathrm{s}}}{z_- \nu_- e c_0}$, $\tilde{\jmath}_0 \equiv \frac{\epsilon_{\mathrm{p}} j_0}{J_{\mathrm{lim}}}$ and $\tilde{J}_{\mathrm{F}} \equiv \frac{\epsilon_{\mathrm{p}} J_{\mathrm{F}}}{J_{\mathrm{lim}}}$. We note that $\tilde{I} = \tilde{J}$ in 1D. It is also convenient to define the following dimensionless parameters: $\beta_{\mathrm{D}} \equiv -\frac{z_- D_{-0}}{2(z_+ D_{+0} - z_- D_{-0})}$ and $\xi_+ \equiv \frac{\nu_+ c_0}{c_+^{\Theta}}$. ξ_+ is useful for switching between the two different concentration scales for c_+, namely c_0 and c_+^{Θ}. Impedance analysis involves computing the system impedance Z in response to a small-amplitude sinusoidal time-varying perturbation of current or voltage with

angular frequency ω. For ω and Z, we define the following nondimensionalization: $\tilde{\omega} \equiv \frac{L^2\omega}{D_{\mathrm{amb0}}}$ and $\tilde{Z} \equiv \frac{eI_{\mathrm{lim}}Z}{k_{\mathrm{B}}T}$ where $\frac{D_{\mathrm{amb0}}}{L^2}$ is the characteristic diffusion frequency, which is the reciprocal of the characteristic diffusion time $\frac{L^2}{D_{\mathrm{amb0}}}$.

To avoid cluttering the notation, we drop tildes on all dimensionless variables and parameters and the $-$ subscript on $\tilde{c}_-$ and $\tilde{F}_-$ in all following sections unless otherwise stated. To eliminate c_+ from the governing equations and boundary conditions, we substitute the electroneutrality constraint into the charge conservation equation and boundary conditions. Therefore, in terms of c and ϕ, the dimensionless PDEs and electroneutrality constraint are given by

$$\frac{\partial c}{\partial t} + \frac{\partial F}{\partial x} = 0, \quad F = -D_{-0}\left(\frac{\partial c}{\partial x} + z_- c\frac{\partial \phi}{\partial x}\right), \tag{4.14}$$

$$\rho_{\mathrm{s}} = c - c_+, \tag{4.15}$$

$$\frac{\partial J}{\partial x} = 0, \quad J = \beta_{\mathrm{D}}\left\{(D_{-0} - D_{+0})\frac{\partial c}{\partial x} + [z_+ D_{+0}\rho_{\mathrm{s}} - (z_+ D_{+0} - z_- D_{-0})c]\frac{\partial \phi}{\partial x}\right\}. \tag{4.16}$$

In addition, $J(x=0) = J(x=1)$ because of charge conservation and $I = J(x=0) = J(x=1)$ in 1D. The dimensionless boundary conditions and integral constraint are given by

$$\frac{\partial c}{\partial x} + z_- c\frac{\partial \phi}{\partial x}\bigg|_{x=0} = \frac{\partial c}{\partial x} + z_- c\frac{\partial \phi}{\partial x}\bigg|_{x=1} = 0, \tag{4.17}$$

$$\int_0^1 c\,\mathrm{d}x = \beta_1, \tag{4.18}$$

$$J_{\mathrm{F}} = j_0\{\exp(-\alpha_1\eta) - \exp[(2-\alpha_1)\eta]\}, \tag{4.19}$$

$$j_0 = j_0^{\mathrm{ref}}\left[\frac{\xi_+(c-\rho_{\mathrm{s}})}{\hat{c}_+^{\mathrm{ref}}}\right]^{1-\frac{\alpha_1}{2}}, \tag{4.20}$$

$$\Delta\phi^{\mathrm{eq}} = \frac{1}{2}\ln[\xi_+(c-\rho_{\mathrm{s}})] + E^{\Theta}, \tag{4.21}$$

$$-J(x=0) = J_{\mathrm{F}}^{\mathrm{a}}, \quad \phi_{\mathrm{e}}^{\mathrm{a}} = 0, \tag{4.22}$$

$$J(x=1) = J_{\mathrm{F}}^{\mathrm{c}}, \quad \phi_{\mathrm{e}}^{\mathrm{c}} = -V, \quad V \geq 0, \tag{4.23}$$

where $\eta = \Delta\phi - \Delta\phi^{\mathrm{eq}}$ and $\Delta\phi = \phi_{\mathrm{e}} - \phi$.

4.3.4 Perturbations

Throughout this section, we work with dimensionless variables and parameters. We impose sinusoidal perturbations in time t on c and ϕ around the steady state, which is chosen as the base state, and ignore higher order terms of order $\mathcal{O}(\epsilon^2)$

$$c(x,t) = c^{(0)}(x) + \epsilon c^{(1)}(x)\exp(i\omega t) + \mathcal{O}\big(\epsilon^2\big), \tag{4.24}$$

$$\phi(x,t) = \phi^{(0)}(x) + \epsilon \phi^{(1)}(x)\exp(i\omega t) + \mathcal{O}\big(\epsilon^2\big), \tag{4.25}$$

where $\epsilon \ll 1$ is a dimensionless small parameter, ω is the angular frequency, the (0) and (1) superscripts denote steady and perturbed states respectively, and $c^{(1)}$ and $\phi^{(1)}$ are the perturbation amplitudes for c and ϕ respectively. As a result of the perturbations on c and ϕ, other variables in the system are also perturbed with the same frequency ω. Therefore,

$$J(x,t) = J^{(0)}(x) + \epsilon J^{(1)}(x)\exp(i\omega t) + \mathcal{O}\big(\epsilon^2\big), \tag{4.26}$$

$$\psi(t) = \psi^{(0)} + \epsilon \psi^{(1)}\exp(i\omega t) + \mathcal{O}\big(\epsilon^2\big), \tag{4.27}$$

where $\psi \in \{\phi_{\mathrm{e}}, \Delta\phi, \Delta\phi^{\mathrm{eq}}, \eta, j_0, J_{\mathrm{F}}, V, I\}$, and $J^{(1)}$ and $\psi^{(1)}$ are the perturbation amplitudes. We substitute these perturbations into the dimensionless equations in Section 4.3.3 and match terms at $\mathcal{O}(1)$ in Section 4.3.5 and $\mathcal{O}(\epsilon)$ in Section 4.3.6. Matching terms at $\mathcal{O}(1)$ results in solving the system at steady state while matching terms at $\mathcal{O}(\epsilon)$ is equivalent to linearizing the nonlinear PDEs and boundary conditions around the steady state.

4.3.5 Steady state equations

The outcome of matching the PDEs and boundary conditions at $\mathcal{O}(1)$ for the model described in Section 4.3.3 is solving the model at steady state, which is expected because the base state chosen for linearization is the steady state as discussed in Section 4.3.4. The complete list of steady state equations is derived from [122] and provided in Appendix 4.8.1. For galvanostatic conditions in which we apply a current

$I^{(0)}_{\text{applied}}$ on the system, we impose $J^{(0)}(x=1) = I^{(0)}_{\text{applied}}$ and measure $V^{(0)}$. For potentiostatic conditions in which we apply an electric potential $-V^{(0)}$ on the cathode, we impose $\phi_{\text{e}}^{\text{c},(0)} = -V^{(0)}$ and measure $J^{(0)}(x=1)$. At steady state, the current-voltage relation is invertible as illustrated in Figure 10 of [122]. Therefore, for a compatible set of $\left\{J^{(0)}(x=1), V^{(0)}\right\}$, the choice of galvanostatic or potentiostatic conditions does not affect the $c^{(0)}$ and $\phi^{(0)}$ spatial profiles.

As discussed in [122], the $c^{(0)}$ solution is known analytically and can be expressed in terms of the Lambert W function [68]. On the other hand, the $\phi^{(0)}$ solution is known semi-analytically: it is known analytically in terms of the Lambert W function up to an additive constant that is computed numerically. This constant is a function of $I^{(0)}$ and ρ_{s} and is determined by numerically solving the nonlinear Butler-Volmer equations given by Equations 4.57 and 4.58 in Appendix 4.8.1 for the required overpotential to drive the correct amount of Faradaic current density. Regarding the steady state current-voltage relation, $V^{(0)}$ can be arbitrarily large regardless of the sign of ρ_{s} but the maximum value of $I^{(0)}$ that can be achieved depends on the sign of ρ_{s}. When $\rho_{\text{s}} < 0$, the system is capable of achieving OLC, therefore there are no restrictions on how large $I^{(0)}$ can be. For $\rho_{\text{s}} = 0$, as $V^{(0)} \to \infty$, $I^{(0)}$ tends asymptotically towards the limiting current, which is denoted as $I^{\text{BV}}_{\text{lim}}$, whose value is equal to 1. However, when $\rho_{\text{s}} > 0$, the maximum $I^{(0)}$ that can be achieved, which is denoted as $I^{\text{BV}}_{\text{max}}$, is lower than $I^{\text{BV}}_{\text{lim}}$, and $I^{\text{BV}}_{\text{max}}$ decreases as ρ_{s} increases. Hence, a positive volume-averaged background charge density effectively lowers the limiting current. A detailed discussion of how to numerically compute $I^{\text{BV}}_{\text{max}}$ can be found at [122].

4.3.6 Perturbation equations

Matching the PDEs and boundary conditions at $\mathcal{O}(\epsilon)$, we obtain the perturbation equations and boundary conditions that are solved for computing impedance spectra. The perturbation ODEs (ordinary differential equations) are given by

$$\frac{\mathrm{d}^2 c^{(1)}}{\mathrm{d}x^2} + z_- \frac{\mathrm{d}}{\mathrm{d}x}\left(c^{(0)}\frac{\mathrm{d}\phi^{(1)}}{\mathrm{d}x} + \frac{\mathrm{d}\phi^{(0)}}{\mathrm{d}x}c^{(1)}\right) = \frac{i\omega}{D_{-0}}c^{(1)}, \tag{4.28}$$

$$(D_{-0}-D_{+0})\frac{\mathrm{d}^2c^{(1)}}{\mathrm{d}x^2}-(z_+D_{+0}-z_-D_{-0})\frac{\mathrm{d}}{\mathrm{d}x}\left(c^{(0)}\frac{\mathrm{d}\phi^{(1)}}{\mathrm{d}x}+\frac{\mathrm{d}\phi^{(0)}}{\mathrm{d}x}c^{(1)}\right)+z_+D_{+0}\rho_\mathrm{s}\frac{\mathrm{d}^2\phi^{(1)}}{\mathrm{d}x^2}=0, \tag{4.29}$$

and the perturbation current density $J^{(1)}$ is given by

$$J^{(1)}(x)=\beta_\mathrm{D}\left[(D_{-0}-D_{+0})\frac{\mathrm{d}c^{(1)}}{\mathrm{d}x}-(z_+D_{+0}-z_-D_{-0})\left(c^{(0)}\frac{\mathrm{d}\phi^{(1)}}{\mathrm{d}x}+\frac{\mathrm{d}\phi^{(0)}}{\mathrm{d}x}c^{(1)}\right)+z_+D_{+0}\rho_\mathrm{s}\frac{\mathrm{d}\phi^{(1)}}{\mathrm{d}x}\right]. \tag{4.30}$$

Moreover, we require $J^{(1)}(x=0)=J^{(1)}(x=1)$ because of charge conservation and $I^{(1)}=J^{(1)}(x=0)=J^{(1)}(x=1)$ in 1D. The boundary conditions and integral constraint are given by

$$\frac{\mathrm{d}c^{(1)}}{\mathrm{d}x}+z_-\left(c^{(0)}\frac{\mathrm{d}\phi^{(1)}}{\mathrm{d}x}+\frac{\mathrm{d}\phi^{(0)}}{\mathrm{d}x}c^{(1)}\right)\bigg|_{x=0}=\frac{\mathrm{d}c^{(1)}}{\mathrm{d}x}+z_-\left(c^{(0)}\frac{\mathrm{d}\phi^{(1)}}{\mathrm{d}x}+\frac{\mathrm{d}\phi^{(0)}}{\mathrm{d}x}c^{(1)}\right)\bigg|_{x=1}=0, \tag{4.31}$$

$$\int_0^1 c^{(1)}\,\mathrm{d}x=0, \tag{4.32}$$

$$\begin{aligned}J_\mathrm{F}^{(1)}&=j_0^{(0)}\eta^{(1)}\big\{-\alpha_1\exp\big(-\alpha_1\eta^{(0)}\big)-(2-\alpha_1)\exp\big[(2-\alpha_1)\eta^{(0)}\big]\big\}\\&\quad+j_0^{(1)}\big\{\exp\big(-\alpha_1\eta^{(0)}\big)-\exp\big[(2-\alpha_1)\eta^{(0)}\big]\big\},\end{aligned} \tag{4.33}$$

$$j_0^{(1)}=j_0^{(0)}\frac{\big(1-\frac{\alpha_1}{2}\big)c^{(1)}}{c^{(0)}-\rho_\mathrm{s}}, \tag{4.34}$$

$$\Delta\phi^{\mathrm{eq},(1)}=\frac{c^{(1)}}{2(c^{(0)}-\rho_\mathrm{s})}, \tag{4.35}$$

$$-J^{(1)}(x=0)=J_\mathrm{F}^{\mathrm{a},(1)},\quad \phi_\mathrm{e}^{\mathrm{a},(1)}=0, \tag{4.36}$$

$$J^{(1)}(x=1)=J_\mathrm{F}^{\mathrm{c},(1)},\quad \phi_\mathrm{e}^{\mathrm{c},(1)}=-V^{(1)},\quad V^{(1)}\geq 0, \tag{4.37}$$

where $\eta^{(1)}=\Delta\phi^{(1)}-\Delta\phi^{\mathrm{eq},(1)}$ and $\Delta\phi^{(1)}=\phi_\mathrm{e}^{(1)}-\phi^{(1)}$.

As expected, solving the equations at $\mathcal{O}(\epsilon)$ requires knowledge of $\mathcal{O}(1)$ variables, namely $c^{(0)}$, $\frac{\mathrm{d}c^{(0)}}{\mathrm{d}x}$, $\frac{\mathrm{d}\phi^{(0)}}{\mathrm{d}x}$ and $\frac{\mathrm{d}^2\phi^{(0)}}{\mathrm{d}x^2}$. As discussed in Section 4.3.5, $c^{(0)}$ is known analytically while $\phi^{(0)}$ is known analytically up to an additive constant. Therefore, we can compute $c^{(0)}$, $\frac{\mathrm{d}c^{(0)}}{\mathrm{d}x}$, $\frac{\mathrm{d}\phi^{(0)}}{\mathrm{d}x}$ and $\frac{\mathrm{d}^2\phi^{(0)}}{\mathrm{d}x^2}$ analytically and we provide their expressions in Appendix 4.8.2.

4.3.7 Impedance

For galvanostatic EIS (electrochemical impedance spectroscopy) in which we apply a perturbation current of amplitude $I^{(1)}_{\text{applied}}$ on the system, we impose $J^{(1)}(x=1) = I^{(1)}_{\text{applied}}$ and measure $V^{(1)}$. For potentiostatic EIS in which we apply an electric potential of amplitude $-V^{(1)}$ on the cathode, we impose $\phi_{\text{e}}^{\text{c},(1)} = -V^{(1)}$ and measure $J^{(1)}(x=1)$. In both cases, the impedance Z is given by

$$Z(\omega) = \frac{V^{(1)}}{J^{(1)}(x=1)} \tag{4.38}$$

and both cases give the same value of Z for a particular ω. Z is generally a complex-valued function of ω and the impedance spectrum is typically visualized using the Nyquist plot of $-\text{Im}(Z)$ against $\text{Re}(Z)$, the Bode magnitude plot of $\log_{10}|Z|$ against $\log_{10}\omega$, and the Bode phase plot of $-\arg Z$ against $\log_{10}\omega$.

Alternatively, we can use Fourier transforms [182, 244] to arrive at the expression for Z in Equation 4.38, which allows us to interpret the perturbation amplitudes as Fourier transforms of perturbation variables. We first define perturbation variables for the anion concentration and electrolyte electric potential that are of order $\mathcal{O}(\epsilon)$ and ignore higher order terms: $\bar{c}(x,t) = c(x,t) - c^{(0)}(x)$ and $\bar{\phi}(x,t) = \phi(x,t) - \phi^{(0)}(x)$. Similarly, we define $\bar{J}(x,t) = J(x,t) - J^{(0)}(x)$ and $\bar{\psi}(t) = \psi(t) - \psi^{(0)}$. We then substitute these expressions into the equations in Section 4.3.3, match terms at $\mathcal{O}(\epsilon)$, which is equivalent to the linearization of the nonlinear PDEs and boundary conditions around the steady state, and perform Fourier transforms in time t. Denoting the Fourier transforms in time t of the perturbation variables as $\hat{\bar{c}}$, $\hat{\bar{\phi}}$, $\hat{\bar{J}}$ and $\hat{\bar{\psi}}$, we conclude that $\hat{\bar{c}} = c^{(1)}$, $\hat{\bar{\phi}} = \phi^{(1)}$, $\hat{\bar{J}} = J^{(1)}$ and $\hat{\bar{\psi}} = \psi^{(1)}$. Therefore, the perturbation amplitudes are the Fourier transforms of the perturbation variables and Z is the transfer function given by the ratio of the Fourier transform of voltage perturbation to the Fourier transform of current perturbation.

To analyze the impedance spectra, we first rewrite $J_{\mathrm{F}}^{(1)}$ given by Equation 4.33 as

$$J_{\mathrm{F}}^{(1)} = j_0^{(0)}\Big\{\Big\{-\alpha_1 \exp\big(-\alpha_1\eta^{(0)}\big) - (2-\alpha_1)\exp\big[(2-\alpha_1)\eta^{(0)}\big]\Big\}\Delta\phi^{(1)} + 2\exp\big(-\alpha_1\eta^{(0)}\big)\Delta\phi^{\mathrm{eq},(1)}\Big\}. \tag{4.39}$$

Motivated by [231, 232, 27], we generalize the definitions of the Faradaic reaction impedance Z_{F}, charge transfer resistance ρ_{ct} and diffusion impedance Z_{D} for an arbitrary overpotential $\eta^{(0)}$ as

$$Z_{\mathrm{F}} = \rho_{\mathrm{ct}} + Z_{\mathrm{D}}, \tag{4.40}$$

$$Z_{\mathrm{F}} \equiv -\frac{\Delta\phi^{(1)}}{J_{\mathrm{F}}^{(1)}}, \tag{4.41}$$

$$\rho_{\mathrm{ct}} \equiv \frac{1}{j_0^{(0)}\{\alpha_1\exp(-\alpha_1\eta^{(0)}) + (2-\alpha_1)\exp[(2-\alpha_1)\eta^{(0)}]\}}, \tag{4.42}$$

$$\rho_{\mathrm{D}} \equiv \frac{2\exp\big(-\alpha_1\eta^{(0)}\big)}{\alpha_1\exp(-\alpha_1\eta^{(0)}) + (2-\alpha_1)\exp[(2-\alpha_1)\eta^{(0)}]}, \tag{4.43}$$

$$Z_{\mathrm{D}} \equiv -\rho_{\mathrm{D}}\frac{\Delta\phi^{\mathrm{eq},(1)}}{J_{\mathrm{F}}^{(1)}}. \tag{4.44}$$

Because we are primarily interested in studying the impedance spectra at overlimiting currents, which imply high overpotentials, these generalized definitions are useful for separating and analyzing the individual contributions to the total impedance response at such high currents and overpotentials. As $\eta^{(0)} \to 0$ for small overpotentials, we obtain $\rho_{\mathrm{D}} \to 1$ and recover the expressions for Z_{F}, ρ_{ct} and Z_{D} in [231, 232]. In addition, we define the bulk electrolyte impedance Z_{b} as

$$Z_{\mathrm{b}} \equiv -\frac{\Delta\phi^{\mathrm{b},(1)}}{J^{(1)}(x=1)}, \tag{4.45}$$

$$\Delta\phi^{\mathrm{b},(1)} \equiv \phi^{(1)}(x=1) - \phi^{(1)}(x=0), \tag{4.46}$$

where the "b" subscript and superscript denote bulk electrolyte. Therefore, we can break down the total impedance Z into three individual impedances $Z_{\mathrm{F}}^{\mathrm{a}}$, Z_{b} and $Z_{\mathrm{F}}^{\mathrm{c}}$

that are connected in series as

$$Z = Z_{\mathrm{F}}^{\mathrm{a}} + Z_{\mathrm{b}} + Z_{\mathrm{F}}^{\mathrm{c}} = \rho_{\mathrm{ct}}^{\mathrm{a}} + Z_{\mathrm{D}}^{\mathrm{a}} + Z_{\mathrm{b}} + \rho_{\mathrm{ct}}^{\mathrm{c}} + Z_{\mathrm{D}}^{\mathrm{c}} \tag{4.47}$$

where the "a" and "c" superscripts refer to the anode and cathode respectively. Similar to [105], we also define the resistance in the system that is attributed to diffusion both at the electrode/electrolyte interfaces and in the bulk electrolyte as the mass transfer resistance R_{mass}, which is given by

$$R_{\mathrm{mass}} \equiv R_{\mathrm{LF}} - R_{\mathrm{HF}} \tag{4.48}$$

where $R_{\mathrm{LF}} \equiv Z(\omega \to 0)$ and $R_{\mathrm{HF}} \equiv Z(\omega \to \infty)$ are the intercepts on the real axis in the Nyquist plot at $\omega \to 0$ and $\omega \to \infty$ respectively; the LF and HF subscripts denote low and high frequencies respectively. For experiments and numerical simulations that use a minimum frequency ω_{min} that is small but nonzero, we can approximate R_{LF} as $\mathrm{Re}[Z(\omega = \omega_{\mathrm{min}})]$. Similarly, because the maximum frequency ω_{max} used cannot be infinite in both experiments and numerical simulations, if ω_{max} is sufficiently large, we can approximate R_{HF} as $\mathrm{Re}[Z(\omega = \omega_{\mathrm{max}})]$.

As discussed in Section 4.3.2, the model does not include double layer charging effects. If we were to consider double layer charging currents at the anode and cathode, we would connect a capacitor with capacitance $C_{\mathrm{DL}}^{\mathrm{a}}$ in parallel to $Z_{\mathrm{F}}^{\mathrm{a}}$ to form a Randles equivalent circuit [192] for the anode and another capacitor with capacitance $C_{\mathrm{DL}}^{\mathrm{c}}$ in parallel to $Z_{\mathrm{F}}^{\mathrm{c}}$ to form another Randles equivalent circuit for the cathode.

4.4 Model implementation

First and second order spatial derivatives of $c^{(0)}$ and $\phi^{(0)}$ are needed for numerical computations of impedance spectra and they are provided in Appendix 4.8.2. We use MATLAB's `bvp4c` boundary value problem solver to numerically solve the steady state and perturbation equations in Sections 4.3.5 and 4.3.6 respectively. Implementation details for solving the steady state equations are found in Section 3 of [122].

For the perturbation equations, the form of equations that is suitable to be used by the `bvp4c` solver is given in Appendix 4.8.3. We also specify all the Jacobians for the perturbation equations to the `bvp4c` function to increase convergence rate when the nonlinear Butler-Volmer boundary conditions are used. The expressions for these Jacobians are provided in Appendix 4.8.4.

For the steady state solutions, it is computationally fast and convenient to use the analytical and semi-analytical expressions for $c^{(0)}$ and $\phi^{(0)}$ for plotting their steady state spatial profiles. However, when using the `bvp4c` function to solve the perturbation equations, it is computationally slow to use these expressions for repeated evaluation of the required $\mathcal{O}(1)$ variables on the mesh that is adaptively refined. This is because the Lambert W function in MATLAB, which is called `lambertw`, is implemented as a symbolic function in the Symbolic Toolbox and computations involving it are slow [95]. Using Halley's method [68] to numerically compute the Lambert W function, which is implemented by MATLAB as `Lambert_W` and available in the MATLAB File Exchange [162], is slightly faster but does not significantly reduce the time for computing the impedance spectra. Instead, we use `Lambert_W` to compute the analytical and semi-analytical steady state solutions that serve as good initial guesses to the `bvp4c` function that then numerically solves the steady state equations. We subsequently use MATLAB's `deval` function on these numerical solutions to provide the required $\mathcal{O}(1)$ variables via Hermite cubic interpolation. While computing these numerical solutions takes more time than simply using the analytical and semi-analytical solutions, the interpolation performed by the `deval` function is significantly faster than using the symbolic `lambertw` and numerical `Lambert_W` functions, therefore the overall amount of time needed to solve for the impedance spectra is dramatically reduced.

4.5 Results

To generate the results in Sections 4.5.1 and 4.5.2, we consider Butler-Volmer reaction kinetics for copper electrodeposition and electrodissolution, as discussed in

Table 4.1: Dimensional parameters for copper electrodeposition and electrodissolution for AAO membranes at $T = 298\,\mathrm{K}$ and copper(II) sulfate ($CuSO_4$) electrolyte ($\nu_+ = 1, \nu_- = 1, z_+ = 2, z_- = -2$) taken from Table 1 of [122].

Parameter	Value	Notes and references
E^Θ	$0.3419\,\mathrm{V}$	Ref. [110]
D^{m}_{+0}	$7.14 \times 10^{-10}\,\mathrm{m^2/s}$	Ref. [110]
D^{m}_{-0}	$1.065 \times 10^{-9}\,\mathrm{m^2/s}$	Ref. [110]
j_0^{ref}	$2.9\,\mathrm{mA/cm^2}$	Mean of exchange current densities for E electrodes in Table 2 of [157]
c_+^{ref}	$75\,\mathrm{mM}$	Ref. [157]
α_1	0.75	Compromise between 0.5 in [157] and 1.16 in [172]
r_{p}	$175\,\mathrm{nm}$	Mean of product specification of $150\,\mathrm{nm} - 200\,\mathrm{nm}$
L	$60\,\mu\mathrm{m}$	Product specification
ϵ_{p}	0.375	Mean of product specification of $0.25 - 0.50$
r_{e}	$6\,\mathrm{mm}$	Product specification
τ	1	Straight parallel AAO pores
c_+^Θ	$1\,\mathrm{M} = 10^3\,\mathrm{mol/m^3}$	Standard concentration

Section 4.3.2, in an anodic aluminum oxide (AAO) membrane that contains copper(II) sulfate ($CuSO_4$) as the electrolyte. AAO membranes consist of straight parallel cylindrical pores with the same length and pore radius [115], therefore they have a tortuosity $\tau = 1$ and an effective pore size $h_{\mathrm{p}} = \frac{\epsilon_{\mathrm{p}}}{a_{\mathrm{p}}} = \frac{r_{\mathrm{p}}}{2}$ where r_{p} is the pore radius. The electrodes used are circular with a radius r_{e}, therefore their surface area A is given by $A = \pi r_{\mathrm{e}}^2$. All the dimensional parameters used in Sections 4.5.1 and 4.5.2 are taken from Table I of [122], which we reproduce in Table 4.1 for convenience.

4.5.1 Steady state solutions

To analyze the impedance spectra, we need to first understand the steady state $c^{(0)}$ and $\phi^{(0)}$ spatial profiles and how they vary with ρ_{s} and $I^{(0)}$. A more detailed discussion of the steady state solutions is found at [122].

In Figures 4-2 and 4-3, we plot $c^{(0)}$ and $\phi^{(0)}$ against x respectively to demonstrate the effects of varying ρ_{s} and $I^{(0)}$. The ρ_{s} values considered are -0.75, -0.05, 0, 0.05 and 0.75. For $\rho_{\mathrm{s}} = -0.75, -0.05$, we pick $I^{(0)} = 0.75, 1, 2, 3, 4, 5$. For $\rho_{\mathrm{s}} = 0$, we pick $I^{(0)} = 0.75, 0.825, 0.9$ and not $I^{(0)} = I^{\mathrm{BV}}_{\mathrm{lim}} = 1$ because $I^{(0)} = I^{\mathrm{BV}}_{\mathrm{lim}} = 1$

implies $V^{(0)} \to \infty$ that cannot be computed numerically. For $\rho_s = 0.05, 0.75$, we pick $I^{(0)} = 0.75I^{BV}_{max}, 0.825I^{BV}_{max}, 0.9I^{BV}_{max}$. We first observe that regardless of ρ_s, when the current is either underlimiting or limiting, $c^{(0)}$ varies almost linearly with x because ambipolar diffusion is the predominant mechanism for ion transport. For the same reason, features of the $c^{(0)}$ and $\phi^{(0)}$ plots for $\rho_s \geq 0$ are qualitatively the same as each other. On the other hand, when the current is overlimiting for $\rho_s < 0$, anions are depleted near the cathode, and the length of the depletion region increases as $|\rho_s|$ decreases and $I^{(0)}$ increases. In the depletion region, the anion concentration gradient almost vanishes but the electrolyte electric potential gradient is linear, which implies that the electric field is constant. Therefore, the current in the depletion region is predominantly carried by electromigration of the counterions, which are the cations, under a constant electric field, i.e., surface conduction. However, outside the depletion region, the opposite happens as the anion concentration gradient is linear while the electrolyte electric potential gradient almost vanishes, therefore ambipolar diffusion dominates and carries most of the current.

4.5.2 Impedance spectra

The range of frequencies used to generate the impedance spectra is $\omega = 10^{-2}$ to $\omega = 10^{6}$, which spans 8 orders of magnitude, while the ranges of ρ_s and $I^{(0)}$ values used are the same as that used in Section 4.5.1. For these ω, ρ_s and $I^{(0)}$ values, we first plot the total impedance spectra Z in Figure 4-4 before analyzing the individual impedance contributions to Z. For qualitative comparison with the theoretical impedance spectra, we also include in Figure 4-4 the experimental dimensional impedance spectra for copper electrodeposition in a 10 mM copper(II) sulfate ($CuSO_4$) electrolyte in negatively and positively charged AAO membranes, which are labeled as AAO(−) and AAO(+) respectively, taken from Figure 3(a) in [105]. The most striking set of theoretical impedance spectra is the one for $\rho_s = -0.75$ in which we observe that the spectra travel to the left as the current $I^{(0)}$ increases and Z converges to approximately the same real value at a large frequency for high overlimiting currents, i.e., the high frequency horizontal intercept or resistance appears to

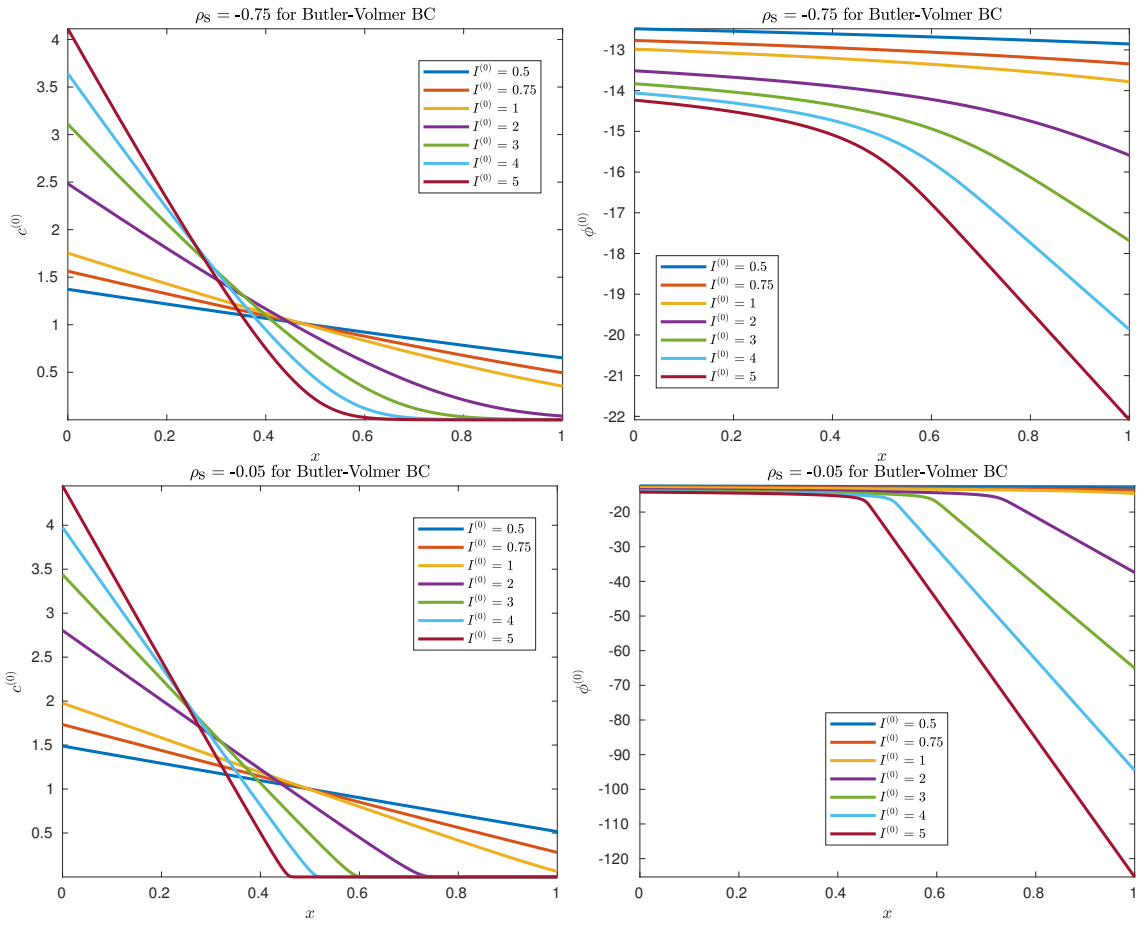

Figure 4-2: Plots of $c^{(0)}$ and $\phi^{(0)}$ against x for $\rho_s = -0.75, -0.05$ and $I^{(0)} = 0.75, 1, 2, 3, 4, 5$ for Butler-Volmer boundary conditions at anode and cathode.

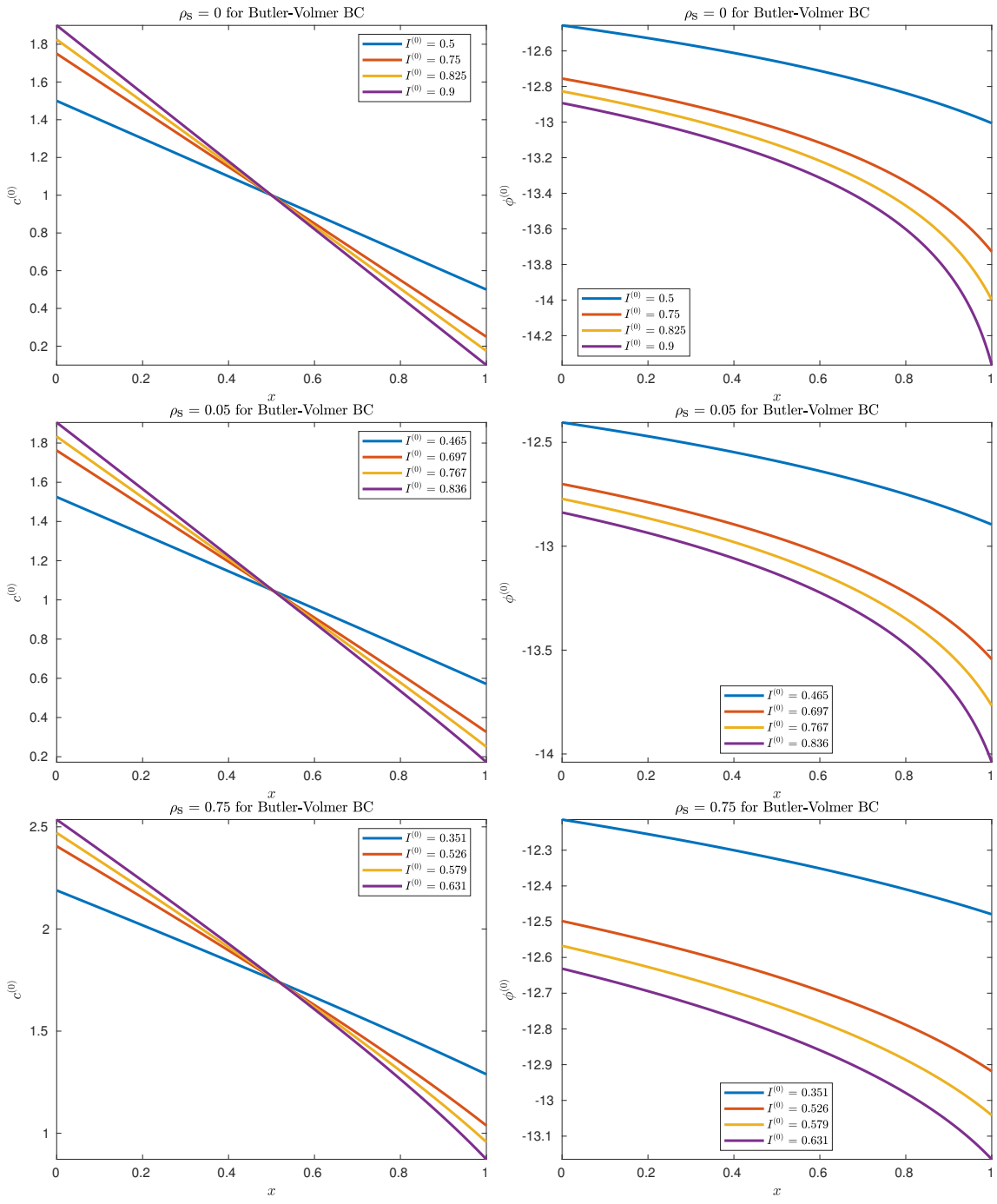

Figure 4-3: Plots of $c^{(0)}$ and $\phi^{(0)}$ against x for 1) $\rho_s = 0$ and $I^{(0)} = 0.75, 0.825, 0.9$ (top row) and 2) $\rho_s = 0.05, 0.75$ and $I^{(0)} = 0.75 I^{\text{BV}}_{\text{max}}, 0.825 I^{\text{BV}}_{\text{max}}, 0.9 I^{\text{BV}}_{\text{max}}$ (second and third rows) for Butler-Volmer boundary conditions at anode and cathode.

be "pinned" when the current is sufficiently large. These features qualitatively agree with the experimental impedance spectra for negatively charged AAO membranes. In stark contrast, the impedance spectra for $\rho_s = -0.05$ travel to the right as the current increases and no horizontal intercepts or resistances appear to be "pinned". Different from the impedance spectra for the negative values of ρ_s, the impedance spectra for $\rho_s = 0$, $\rho_s = 0.05$ and $\rho_s = 0.75$ behave similarly to each other: the spectra increase in "diameter" as the current increases and the high frequency resistance, like that for $\rho_s = -0.75$, is pinned at currents near $I_{\max}^{\mathrm{BV}}$. This behavior is similarly observed in the experimental impedance spectra for positively charged AAO membranes, ignoring the low frequency arcs in the latter that cannot be explained by the model.

The characteristics of the total impedance spectra can be better understood when we analyze the individual impedance components $\rho_{\mathrm{ct}}^{\mathrm{a}}$, $Z_{\mathrm{D}}^{\mathrm{a}}$, Z_{b}, $\rho_{\mathrm{ct}}^{\mathrm{c}}$ and $Z_{\mathrm{D}}^{\mathrm{c}}$ given by Equation 4.47. To this end, in Figures 4-5 to 4-9, we plot $Z_{\mathrm{F}}^{\mathrm{a}}$, $Z_{\mathrm{D}}^{\mathrm{a}}$, $Z_{\mathrm{F}}^{\mathrm{c}}$, $Z_{\mathrm{D}}^{\mathrm{c}}$, Z_{b} and Z for the same ρ_s and $I^{(0)}$ values previously discussed and the $\rho_{\mathrm{ct}}^{\mathrm{a}}$ and $\rho_{\mathrm{ct}}^{\mathrm{c}}$ values are noted in the legends where appropriate. In Figure 4-5 for $\rho_s = -0.75$, we see that the $Z_{\mathrm{F}}^{\mathrm{a}}$ and $Z_{\mathrm{F}}^{\mathrm{c}}$ are dominated by $\rho_{\mathrm{ct}}^{\mathrm{a}}$ and $\rho_{\mathrm{ct}}^{\mathrm{c}}$ respectively because a highly negative ρ_s increases surface conductivity and hence decreases the diffusion impedances $Z_{\mathrm{D}}^{\mathrm{a}}$ and $Z_{\mathrm{D}}^{\mathrm{c}}$. For the same reason, a highly negative ρ_s also decreases the bulk electrolyte impedance Z_{b}. As a result, although Z_{b} always increases with $I^{(0)}$, $\rho_{\mathrm{ct}}^{\mathrm{a}}$ and $\rho_{\mathrm{ct}}^{\mathrm{c}}$ and hence $Z_{\mathrm{F}}^{\mathrm{a}}$ and $Z_{\mathrm{F}}^{\mathrm{c}}$ decrease faster with $I^{(0)}$ such that the total impedance Z overall decreases and travels to the left in the Nyquist plot. Eventually, at a sufficiently high $I^{(0)}$, the competition between these two effects almost balances out and results in Z remaining somewhat stationary and causing the high frequency resistance to be "pinned". On the other hand, for $\rho_s = -0.05$, the additional surface conductivity is not sufficient to overcome the increase in Z_{b} as $I^{(0)}$ increases, therefore Z overall increases and travels to the right in the Nyquist plot in Figure 4-6. For $\rho_s = 0, 0.05, 0.75$ in Figures 4-7, 4-8 and 4-9, the positive background charge density contributes a "negative" surface conductivity and hence causes $Z_{\mathrm{F}}^{\mathrm{a}}$ and $Z_{\mathrm{F}}^{\mathrm{c}}$ to be dominated by $Z_{\mathrm{D}}^{\mathrm{a}}$ and $Z_{\mathrm{D}}^{\mathrm{c}}$ respectively, both of which increase with $I^{(0)}$. Therefore, Z overall increases and this manifests in the impedance spectra increasing in "diameter" as $I^{(0)}$ increases.

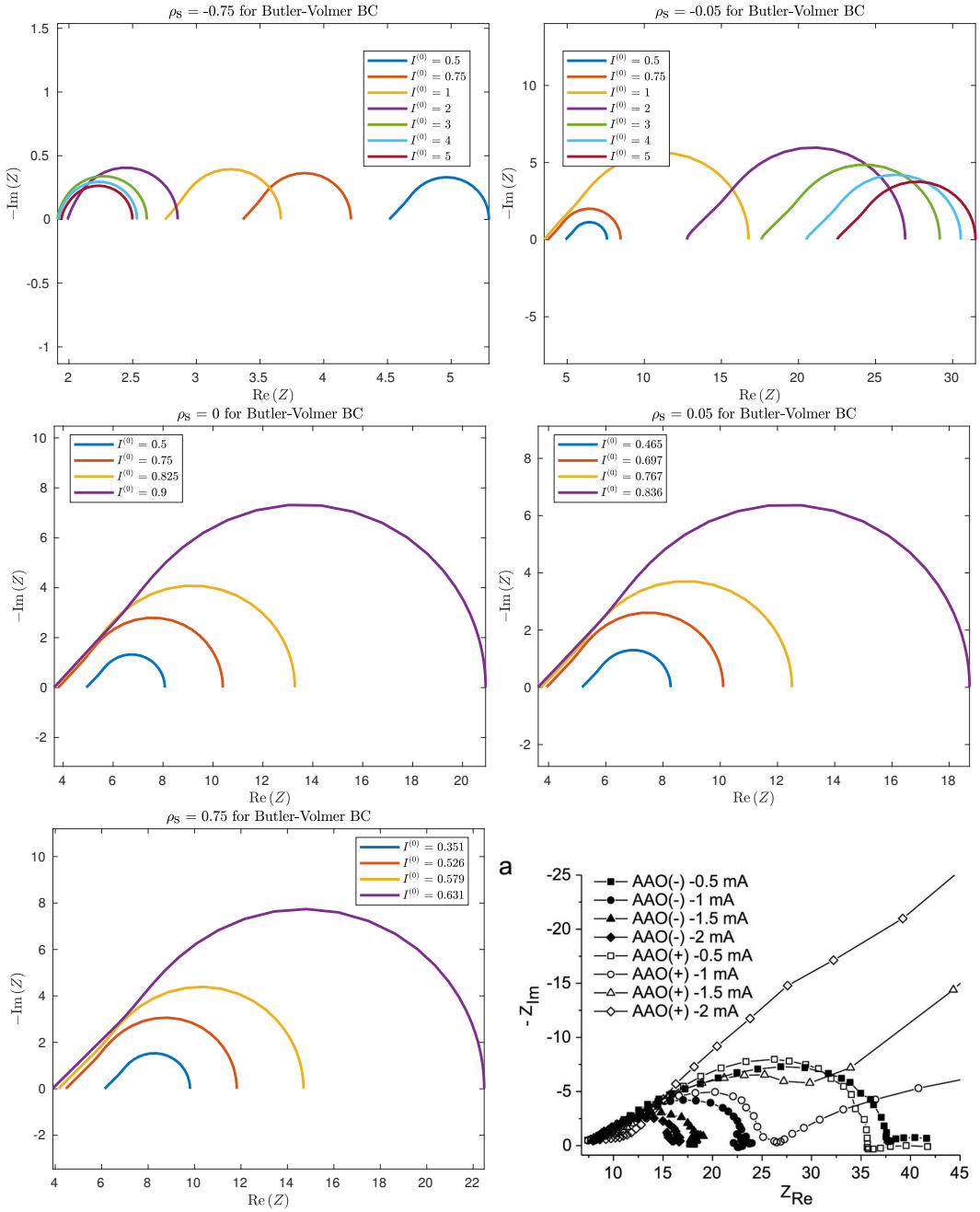

Figure 4-4: Total impedance spectra Z in the form of Nyquist plots for $\rho_s = -0.75, -0.05, 0, 0.05, 0.75$ for Butler-Volmer boundary conditions at anode and cathode in first five plots. For these ρ_s values, the following $I^{(0)}$ values are used: 1) $\rho_s = -0.75, -0.05$: $I^{(0)} = 0.75, 1, 2, 3, 4, 5$, 2) $\rho_s = 0$: $I^{(0)} = 0.75, 0.825, 0.9$, and 3) $\rho_s = 0.05, 0.75$: $I^{(0)} = 0.75 I^{\mathrm{BV}}_{\max}, 0.825 I^{\mathrm{BV}}_{\max}, 0.9 I^{\mathrm{BV}}_{\max}$. Last plot is the experimental dimensional impedance spectra for copper electrodeposition in 10 mM copper(II) sulfate ($CuSO_4$) electrolyte in negatively (AAO(−)) and positively (AAO(+)) charged AAO membranes taken from Figure 3(a) in [105].

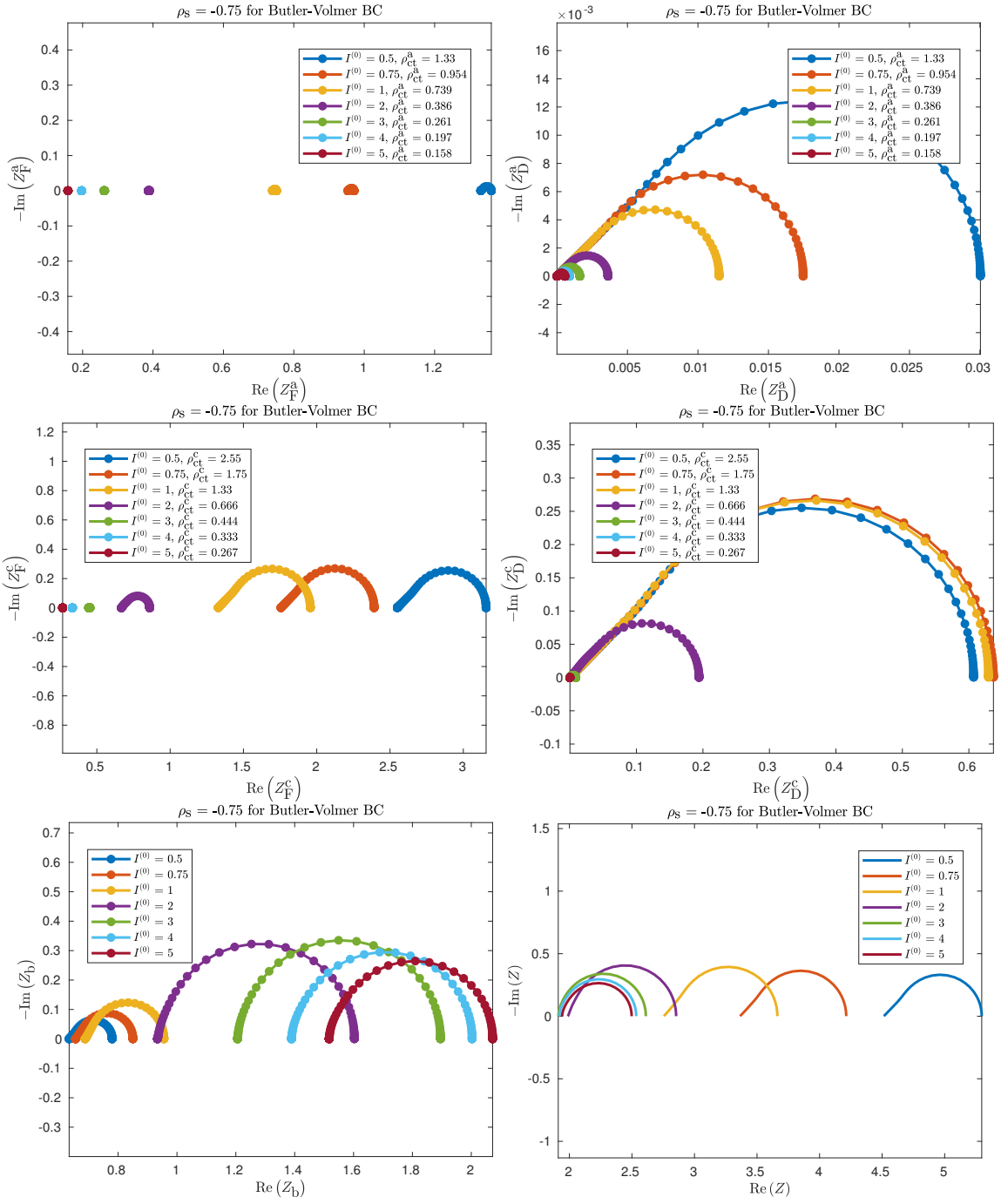

Figure 4-5: Spectra in the form of Nyquist plots for impedance components $Z_{\mathrm{F}}^{\mathrm{a}}$, $Z_{\mathrm{D}}^{\mathrm{a}}$, $Z_{\mathrm{F}}^{\mathrm{c}}$, $Z_{\mathrm{D}}^{\mathrm{c}}$, Z_{b} and Z for $\rho_{\mathrm{s}} = -0.75$ for Butler-Volmer reactions at anode and cathode. $\rho_{\mathrm{ct}}^{\mathrm{a}}$ and $\rho_{\mathrm{ct}}^{\mathrm{c}}$ values are noted in the legends where appropriate.

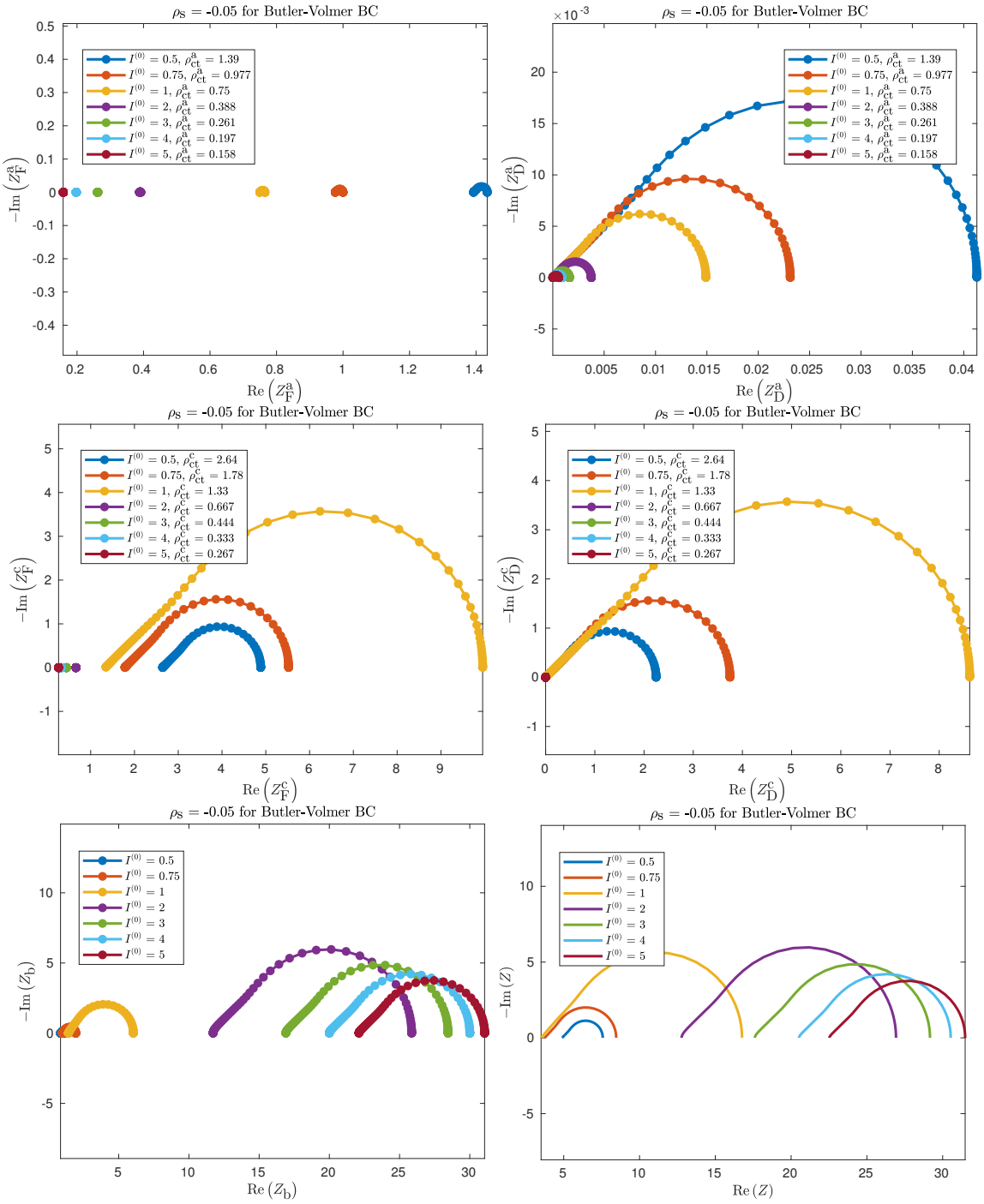

Figure 4-6: Spectra in the form of Nyquist plots for impedance components $Z_{\mathrm{F}}^{\mathrm{a}}$, $Z_{\mathrm{D}}^{\mathrm{a}}$, $Z_{\mathrm{F}}^{\mathrm{c}}$, $Z_{\mathrm{D}}^{\mathrm{c}}$, Z_{b} and Z for $\rho_{\mathrm{s}} = -0.05$ for Butler-Volmer reactions at anode and cathode. $\rho_{\mathrm{ct}}^{\mathrm{a}}$ and $\rho_{\mathrm{ct}}^{\mathrm{c}}$ values are noted in the legends where appropriate.

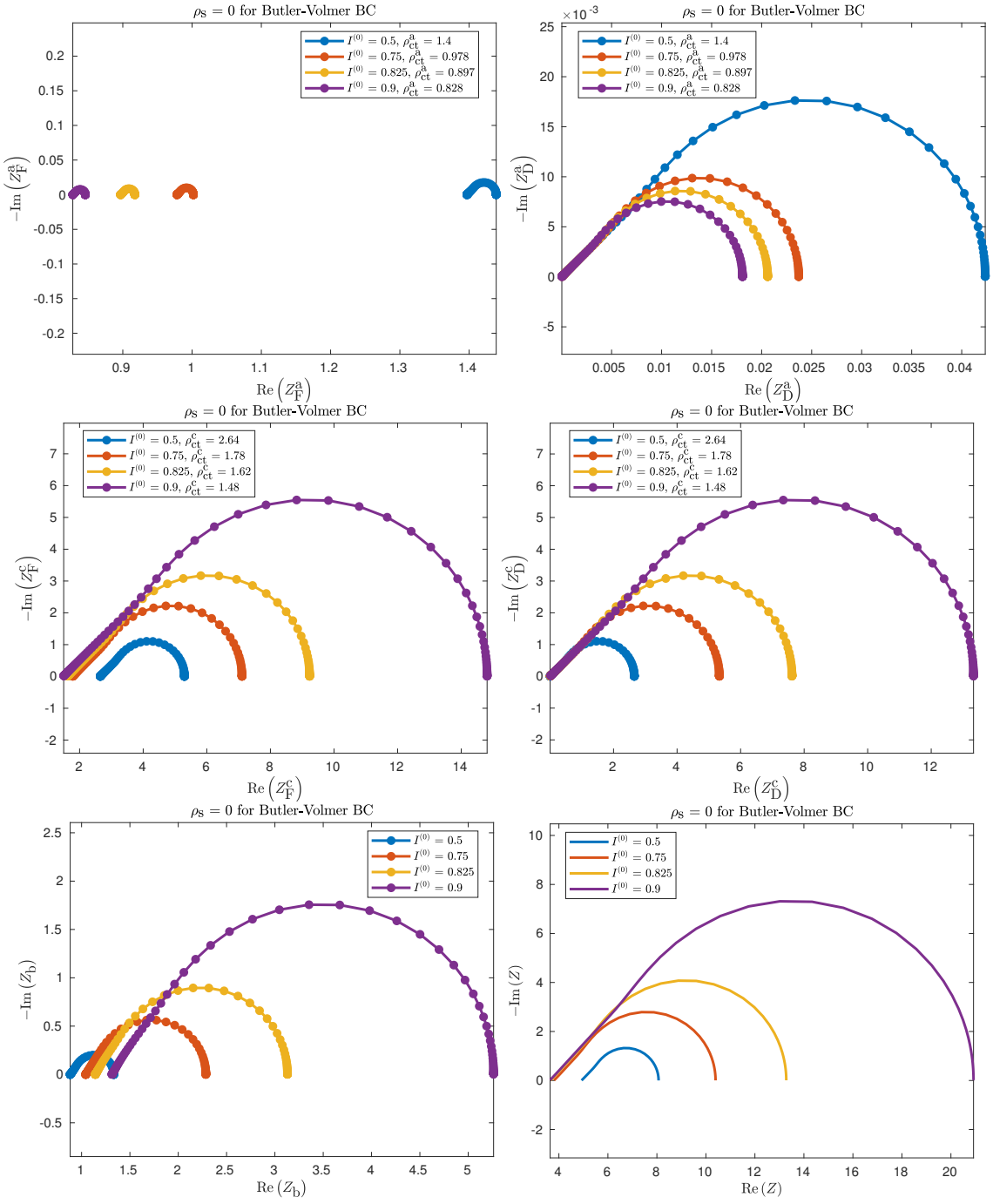

Figure 4-7: Spectra in the form of Nyquist plots for impedance components Z^a_F, Z^a_D, Z^c_F, Z^c_D, Z_b and Z for $\rho_s = 0$ for Butler-Volmer reactions at anode and cathode. ρ^a_{ct} and ρ^c_{ct} values are noted in the legends where appropriate.

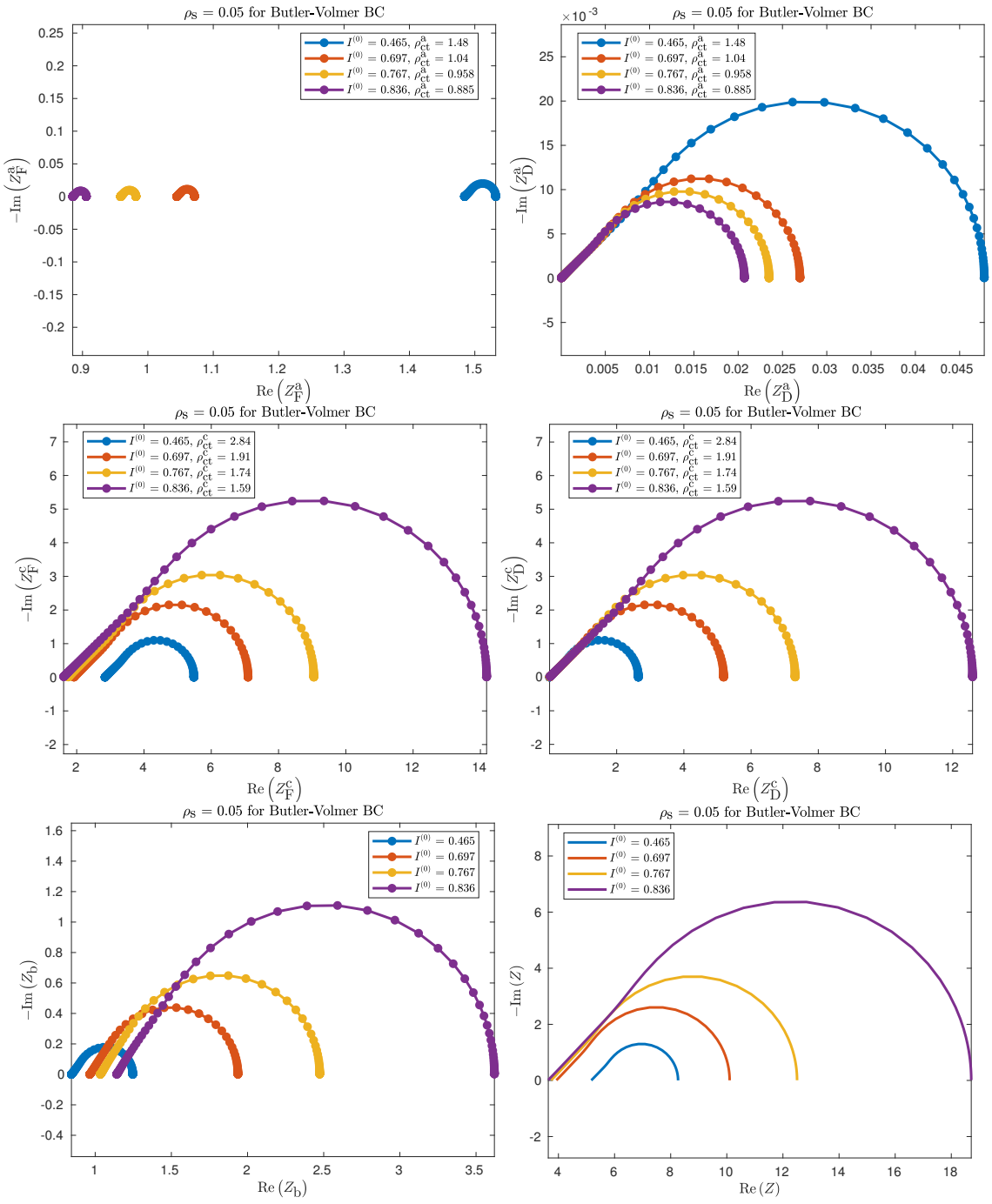

Figure 4-8: Spectra in the form of Nyquist plots for impedance components Z^a_F, Z^a_D, Z^c_F, Z^c_D, Z_b and Z for $\rho_s = 0.05$ for Butler-Volmer reactions at anode and cathode. ρ^a_{ct} and ρ^c_{ct} values are noted in the legends where appropriate.

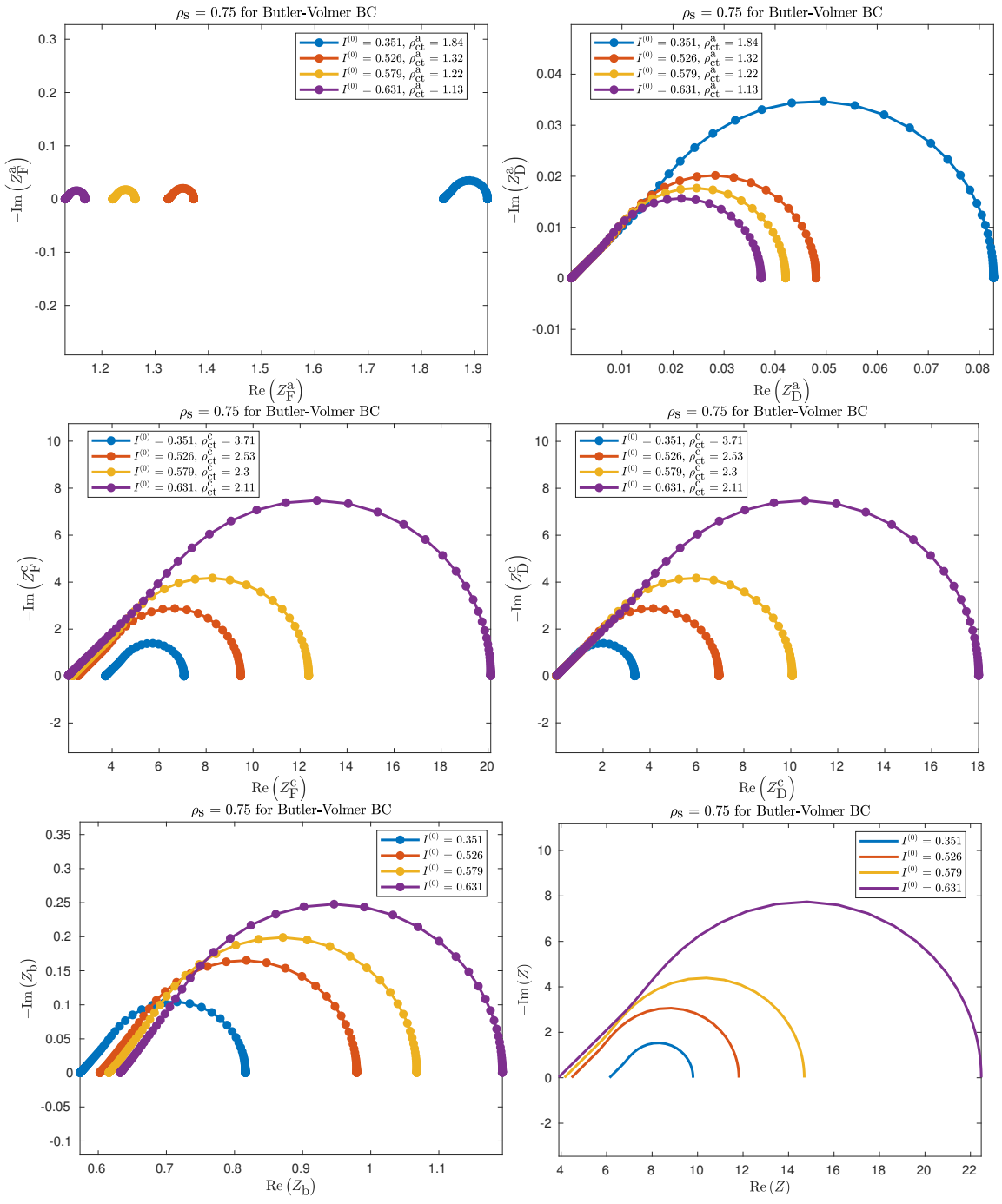

Figure 4-9: Spectra in the form of Nyquist plots for impedance components Z^a_F, Z^a_D, Z^c_F, Z^c_D, Z_b and Z for $\rho_s = 0.75$ for Butler-Volmer reactions at anode and cathode. ρ^a_{ct} and ρ^c_{ct} values are noted in the legends where appropriate.

4.5.3 Parameter estimation for AAO membranes

Using the model, we perform nonlinear least squares fitting with MATLAB's `lsqnonlin` function on the experimental impedance spectra generated for copper electrodeposition and electrodissolution in negatively charged AAO membranes for dimensional currents of 0.5 mA, 1 mA, 1.5 mA and 2 mA shown in Figure 3(a) of [105]. We focus on the negatively charged membranes instead of the positively charged ones because the impedance spectra for the positively charged membranes have some low frequency arcs that our model cannot explain. In addition, the local phase angle of the experimental impedance spectra at high frequencies is significantly smaller than 45°, therefore we add a constant phase element (CPE) in parallel with Z_{F} to form a generalized Randles equivalent circuit [27] at the anode and cathode.

The impedance of the CPE Z_{CPE} is given by $Z_{\mathrm{CPE}} = \frac{A}{(i\omega)^{\alpha}}$ [27] where $A \geq 0$ and $0 \leq \alpha \leq 1$ are CPE parameters that are fitted from experimental impedance spectra. Hence, there are four fitting parameters for the CPEs at the anode and cathode: A^{a}, α^{a}, A^{c} and α^{c} where the "a" and "c" superscripts refer to the anode and cathode respectively. In addition, like our previous work on parameter estimation using the steady state current-voltage relation in Section 4.3 of [122], we pick ρ_{s}, j_0^{ref}, α_1 and ϵ_{p} as fitting parameters; we note that $\tau = 1$ for AAO membranes that have straight parallel pores and τ is therefore not a fitting parameter here. In Figure 4-10, we plot the experimental impedance spectra together with the numerical impedance spectra computed from the fitted parameter values in the form of Nyquist plots, Bode magnitude plots and Bode phase plots. We observe that the numerical impedance spectra generally agree well with the experimental ones, except that the agreement significantly deteriorates for the Nyquist plot at dimensional $I^{(0)} = 2\,\mathrm{mA}$ because the $Z(\omega)$ curve is too "flat" over a reasonably wide range of frequencies.

4.6 Conclusion

We have performed impedance analysis on the leaky membrane model, which is capable of predicting overlimiting current due to surface conduction, that is coupled with

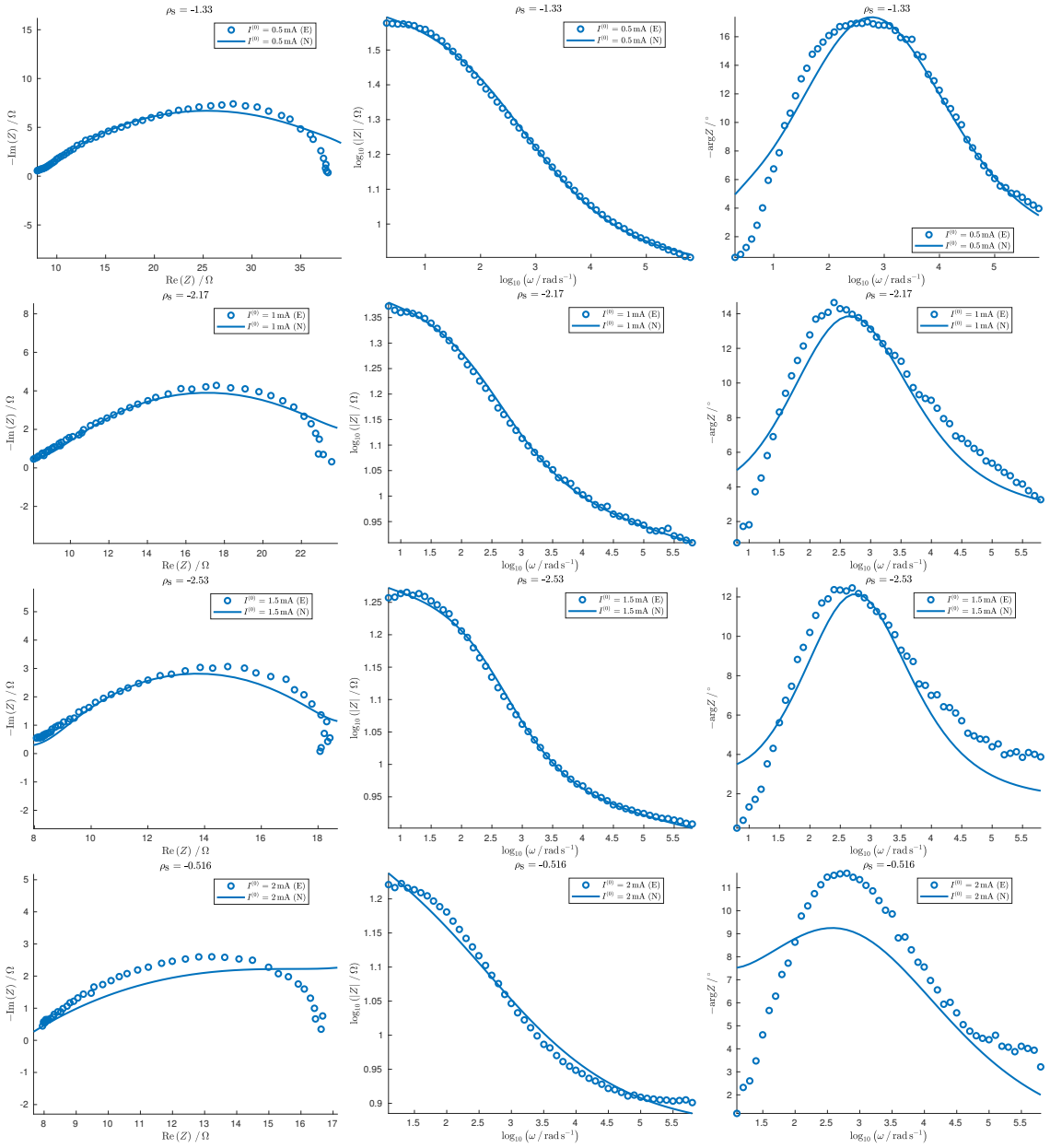

Figure 4-10: Dimensional Nyquist plots, Bode magnitude plots and Bode phase plots for copper electrodeposition and electrodissolution in negatively charged AAO membranes at dimensional $I^{(0)} = 0.5\,\mathrm{mA}, 1\,\mathrm{mA}, 1.5\,\mathrm{mA}, 2\,\mathrm{mA}$. Experimental data are take from Figure 3(a) of [105]. In the legends, (E) stands for experimental data while (N) stands for numerical solution computed from fitted parameter values.

Butler-Volmer reaction kinetics. Through a systematic analysis of the individual components of the total impedance response, we have seen how the impedance spectra for a highly negatively charged membrane qualitatively behave very differently from that for membranes that are weakly negatively charged, neutral or positively charged. Last but not least, we have also performed parameter estimation using experimental data for copper electrodeposition and electrodissolution in negatively charged AAO membranes and obtained a reasonable agreement between the experimental and fitted impedance spectra. One useful extension for future consideration is that instead of using a constant phase element (CPE) at the anode and cathode, we can invert the experimental impedance spectra to obtain the distribution of relaxation times (DRT) [255], which is more physically interpretable than the CPE parameters A and α.

4.7 Acknowledgments

E. Khoo acknowledges support from the National Science Scholarship (PhD) funded by Agency for Science, Technology and Research, Singapore (A*STAR). We also acknowledge J.-H. Han for providing the raw experimental datasets for the impedance spectra.

4.8 Appendix

All variables and parameters in this appendix are dimensionless. Like in the main text, we drop tildes on all dimensionless variables and parameters and the subscript $-$ on $\tilde{c}_-$ unless otherwise stated. The expressions for $c^{(0)}$ and $\phi^{(0)}$ and their associated parameters are taken from [122]. From [122], we define $\alpha_1 \equiv \frac{z_+\rho_s}{z_+-z_-}$ and $\alpha_2 \equiv z_-\alpha_1$ and note that the expression for α_3 used here is given by Equation 44 in [122]. In Sections 4.8.2, 4.8.3, 4.8.4 and 4.8.5, we write the (0) and (1) superscripts, which denote steady and perturbed states respectively, as 0 and 1 subscripts respectively to avoid cluttering the notation.

4.8.1 Steady state equations

The steady state ODEs (ordinary differential equations) are given by

$$\frac{\mathrm{d}^2 c^{(0)}}{\mathrm{d}x^2} + z_- \frac{\mathrm{d}}{\mathrm{d}x}\left(c^{(0)} \frac{\mathrm{d}\phi^{(0)}}{\mathrm{d}x}\right) = 0, \tag{4.49}$$

$$(D_{-0} - D_{+0})\frac{\mathrm{d}^2 c^{(0)}}{\mathrm{d}x^2} - (z_+ D_{+0} - z_- D_{-0})\frac{\mathrm{d}}{\mathrm{d}x}\left(c^{(0)} \frac{\mathrm{d}\phi^{(0)}}{\mathrm{d}x}\right) + z_+ D_{+0}\rho_\mathrm{s} \frac{\mathrm{d}^2 \phi^{(0)}}{\mathrm{d}x^2} = 0, \tag{4.50}$$

and the current density $J^{(0)}$ is given by

$$J^{(0)}(x) = \beta_\mathrm{D}\left[(D_{-0} - D_{+0})\frac{\mathrm{d}c^{(0)}}{\mathrm{d}x} - (z_+ D_{+0} - z_- D_{-0})c^{(0)}\frac{\mathrm{d}\phi^{(0)}}{\mathrm{d}x} + z_+ D_{+0}\rho_\mathrm{s}\frac{\mathrm{d}\phi^{(0)}}{\mathrm{d}x}\right]. \tag{4.51}$$

In addition, $J^{(0)}(x=0) = J^{(0)}(x=1)$ because of charge conservation and $I^{(0)} = J^{(0)}(x=0) = J^{(0)}(x=1)$ in 1D. The boundary conditions and integral constraint are given by

$$\frac{\mathrm{d}c^{(0)}}{\mathrm{d}x} + z_- c^{(0)}\frac{\mathrm{d}\phi^{(0)}}{\mathrm{d}x}\bigg|_{x=0} = \frac{\mathrm{d}c^{(0)}}{\mathrm{d}x} + z_- c^{(0)}\frac{\mathrm{d}\phi^{(0)}}{\mathrm{d}x}\bigg|_{x=1} = 0, \tag{4.52}$$

$$\int_0^1 c^{(0)}\,\mathrm{d}x = \beta_1, \tag{4.53}$$

$$J_\mathrm{F}^{(0)} = j_0^{(0)}\left\{\exp\left(-\alpha_1 \eta^{(0)}\right) - \exp\left[(2-\alpha_1)\eta^{(0)}\right]\right\}, \tag{4.54}$$

$$j_0^{(0)} = j_0^\mathrm{ref}\left[\frac{\xi_+\left(c^{(0)} - \rho_\mathrm{s}\right)}{\hat{c}_+^\mathrm{ref}}\right]^{1-\frac{\alpha_1}{2}}, \tag{4.55}$$

$$\Delta\phi^{\mathrm{eq},(0)} = \frac{1}{2}\ln\left[\xi_+\left(c^{(0)} - \rho_\mathrm{s}\right)\right] + E^\Theta, \tag{4.56}$$

$$-J^{(0)}(x=0) = J_\mathrm{F}^{\mathrm{a},(0)}, \quad \phi_\mathrm{e}^{\mathrm{a},(0)} = 0, \tag{4.57}$$

$$J^{(0)}(x=1) = J_\mathrm{F}^{\mathrm{c},(0)}, \quad \phi_\mathrm{e}^{\mathrm{c},(0)} = -V^{(0)}, \quad V^{(0)} \geq 0, \tag{4.58}$$

where $\eta^{(0)} = \Delta\phi^{(0)} - \Delta\phi^{\mathrm{eq},(0)}$ and $\Delta\phi^{(0)} = \phi_\mathrm{e}^{(0)} - \phi^{(0)}$.

4.8.2 First and second order spatial derivatives

For $\rho_s = 0$,

$$c_0 = \alpha_3 - 2I_0 x, \tag{4.59}$$

$$\frac{\mathrm{d}c_0}{\mathrm{d}x} = -2I_0, \tag{4.60}$$

$$\frac{\mathrm{d}^2 c_0}{\mathrm{d}x^2} = 0, \tag{4.61}$$

$$\phi_0 = -\frac{1}{z_-}\ln\left(\frac{c_0}{\alpha_3}\right) + \alpha_4 = -\frac{1}{z_-}\ln\left(1 - \frac{2I_0}{\alpha_3}x\right) + \alpha_4, \tag{4.62}$$

$$\frac{\mathrm{d}\phi_0}{\mathrm{d}x} = \frac{2I_0}{z_-(\alpha_3 - 2I_0 x)}, \tag{4.63}$$

$$\frac{\mathrm{d}^2\phi_0}{\mathrm{d}x^2} = \frac{4I_0^2}{z_-(\alpha_3 - 2I_0 x)^2}, \tag{4.64}$$

where α_4 is the additive constant discussed in the main text that is a function of I_0 and ρ_s and is determined by numerically solving the Butler-Volmer equations. For $\rho_s \neq 0$,

$$c_0 = -\alpha_1 W\left[-\frac{\alpha_3}{\alpha_1}\exp\left(\frac{2I_0 x - \alpha_3}{\alpha_1}\right)\right], \tag{4.65}$$

$$\frac{\mathrm{d}c_0}{\mathrm{d}x} = \frac{2\alpha_3 I_0}{\alpha_1 \exp\left(-\frac{c_0 + 2I_0 x - \alpha_3}{\alpha_1}\right) - \alpha_3}, \tag{4.66}$$

$$\frac{\mathrm{d}^2 c_0}{\mathrm{d}x^2} = \frac{2\alpha_3 I_0\left(\frac{\mathrm{d}c_0}{\mathrm{d}x} + 2I_0\right)\exp\left(-\frac{c_0 + 2I_0 x - \alpha_3}{\alpha_1}\right)}{\left[\alpha_1 \exp\left(-\frac{c_0 + 2I_0 x - \alpha_3}{\alpha_1}\right) - \alpha_3\right]^2}, \tag{4.67}$$

$$\phi_0 = -\frac{\alpha_1}{\alpha_2}\ln\left(\frac{c_0}{\alpha_3}\right) + \alpha_4 = -\frac{c_0 + 2I_0 x - \alpha_3}{\alpha_2} + \alpha_4, \tag{4.68}$$

$$\frac{\mathrm{d}\phi_0}{\mathrm{d}x} = -\frac{\frac{\mathrm{d}c_0}{\mathrm{d}x} + 2I_0}{\alpha_2}, \tag{4.69}$$

$$\frac{\mathrm{d}^2\phi_0}{\mathrm{d}x^2} = -\frac{1}{\alpha_2}\frac{\mathrm{d}^2 c_0}{\mathrm{d}x^2}, \tag{4.70}$$

where we use the W_0 branch for $\rho_s < 0$ and the W_{-1} branch for $\rho_s > 0$.

4.8.3 Construction of perturbation equations for use in MATLAB

MATLAB's `bvp4c` function solves boundary value problems of the form

$$\frac{\mathrm{d}y}{\mathrm{d}x} = f(x, y, p), \quad y_{\mathrm{BC}} = 0, \tag{4.71}$$

where x is the scalar independent variable, y is the vector of dependent variables, p is the vector of parameters, f is the vector function relating $\frac{\mathrm{d}y}{\mathrm{d}x}$ to x, y and p, and y_{BC} is the vector of boundary conditions. Different boundary conditions result in different expressions for y, p, f and y_{BC}. Throughout this section, we use primes to denote derivatives taken with respect to x. For convenience, we define

$$\gamma_1 = c_0'\phi_1' + \phi_0''c_1 + \phi_0'c_1'. \tag{4.72}$$

We need to include a variable, which is called y_5, in y, that enforces the integral constraint for the conservation of the number of anions. p is needed for galvanostatic EIS (electrochemical impedance spectroscopy) where we impose $J_1(x = 1) = I_{\mathrm{applied},1}$ in order to find V_1 (recall that $\phi^{\mathrm{c}}_{\mathrm{e},1} = -V_1$) while p is not required for potentiostatic EIS where we impose $\phi^{\mathrm{c}}_{\mathrm{e},1} = -V_1$. y and f are given by

$$y = \begin{bmatrix} c_1 \\ c_1' \\ \phi_1 \\ \phi_1' \\ y_5 \end{bmatrix}, \tag{4.73}$$

$$f = \begin{bmatrix} c_1' \\ c_1'' \\ \phi_1' \\ \phi_1'' \\ c_1 \end{bmatrix} = \begin{bmatrix} c_1' \\ \frac{\left[\left(z_+ D_{+0} - z_- D_{-0}\right) c_0 - z_+ D_{+0} \rho_\mathrm{s}\right] \frac{i\omega}{D_{-0}} c_1 + z_+ z_- D_{+0} \rho_\mathrm{s} \gamma_1}{[(z_+ - z_-) c_0 - z_+ \rho_\mathrm{s}] D_{+0}} \\ \phi_1' \\ \frac{\left(D_{-0} - D_{+0}\right) \frac{i\omega}{D_{-0}} c_1 - (z_+ - z_-) D_{+0} \gamma_1}{[(z_+ - z_-) c_0 - z_+ \rho_\mathrm{s}] D_{+0}} \\ c_1 \end{bmatrix}. \tag{4.74}$$

For galvanostatic EIS where we impose $J_1(x=1) = I_{\text{applied},1}$,

$$p = V_1, \tag{4.75}$$

$$y_\mathrm{BC} = \begin{bmatrix} y_5(x=0) \\ J_1(x=0) + J_{\mathrm{F},1}^\mathrm{a} \\ c_1' + z_-(c_0\phi_1' + \phi_0' c_1)|_{x=1} \\ -J_1(x=1) + J_{\mathrm{F},1}^\mathrm{c} \\ y_5(x=1) \\ I_{\text{applied},1} - J_1(x=1) \end{bmatrix}, \tag{4.76}$$

while for potentiostatic EIS where we impose $\phi_{\mathrm{e},1}^\mathrm{c} = -V_1$,

$$y_\mathrm{BC} = \begin{bmatrix} y_5(x=0) \\ J_1(x=0) + J_{\mathrm{F},1}^\mathrm{a} \\ c_1' + z_-(c_0\phi_1' + \phi_0' c_1)|_{x=1} \\ -J_1(x=1) + J_{\mathrm{F},1}^\mathrm{c} \\ y_5(x=1) \end{bmatrix}. \tag{4.77}$$

4.8.4 Jacobians for perturbation equations

To increase convergence rate, we provide Jacobians to the `bvp4c` function. There are two types of Jacobians we can provide: 1) partial derivatives of f with respect to y and p ($\frac{\partial f}{\partial y}$ and $\frac{\partial f}{\partial p}$), and 2) partial derivatives of y_BC with respect to $y(x=0)$, $y(x=1)$ and p ($\frac{\partial y_\mathrm{BC}}{\partial y(x=0)}$, $\frac{\partial y_\mathrm{BC}}{\partial y(x=1)}$ and $\frac{\partial y_\mathrm{BC}}{\partial p}$). For simplicity, the elements of f, y, y_BC, $y(x=0)$

and $y(x=1)$ are written as

$$f = \begin{bmatrix} f_1 \\ f_2 \\ f_3 \\ f_4 \\ f_5 \end{bmatrix}, \tag{4.78}$$

$$y = \begin{bmatrix} y_1 \\ y_2 \\ y_3 \\ y_4 \\ y_5 \end{bmatrix}, \tag{4.79}$$

$$y_{\mathrm{BC}} = \begin{bmatrix} y_{\mathrm{BC},1} \\ y_{\mathrm{BC},2} \\ y_{\mathrm{BC},3} \\ y_{\mathrm{BC},4} \\ y_{\mathrm{BC},5} \end{bmatrix} \quad \text{or} \quad \begin{bmatrix} y_{\mathrm{BC},1} \\ y_{\mathrm{BC},2} \\ y_{\mathrm{BC},3} \\ y_{\mathrm{BC},4} \\ y_{\mathrm{BC},5} \\ y_{\mathrm{BC},6} \end{bmatrix}, \tag{4.80}$$

$$y(x=0) = \begin{bmatrix} y_{0,1} \\ y_{0,2} \\ y_{0,3} \\ y_{0,4} \\ y_{0,5} \end{bmatrix}, \tag{4.81}$$

$$y(x=1) = \begin{bmatrix} y_{1,1} \\ y_{1,2} \\ y_{1,3} \\ y_{1,4} \\ y_{1,5} \end{bmatrix}. \tag{4.82}$$

The nonzero elements of the $\frac{\partial f}{\partial y}$ Jacobian $\in \mathbb{R}^{5\times 5}$ are given by

$$\frac{\partial f_1}{\partial y_2} = 1, \tag{4.83}$$

$$\frac{\partial f_2}{\partial y_1} = \frac{\frac{[(z_+ D_{+0} - z_- D_{-0})c_0 - z_+ D_{+0}\rho_\mathrm{s}]i\omega}{D_{-0}} + z_+ z_- D_{+0}\rho_\mathrm{s}\phi_0''}{[(z_+ - z_-)c_0 - z_+\rho_\mathrm{s}]D_{+0}}, \tag{4.84}$$

$$\frac{\partial f_2}{\partial y_2} = \frac{z_+ z_- D_{+0}\rho_\mathrm{s}\phi_0'}{[(z_+ - z_-)c_0 - z_+\rho_\mathrm{s}]D_{+0}}, \tag{4.85}$$

$$\frac{\partial f_2}{\partial y_4} = \frac{z_+ z_- D_{+0}\rho_\mathrm{s}c_0'}{[(z_+ - z_-)c_0 - z_+\rho_\mathrm{s}]D_{+0}}, \tag{4.86}$$

$$\frac{\partial f_3}{\partial y_4} = 1, \tag{4.87}$$

$$\frac{\partial f_4}{\partial y_1} = \frac{\frac{(D_{-0} - D_{+0})i\omega}{D_{-0}} - (z_+ - z_-)D_{+0}\phi_0''}{[(z_+ - z_-)c_0 - z_+\rho_\mathrm{s}]D_{+0}}, \tag{4.88}$$

$$\frac{\partial f_4}{\partial y_2} = -\frac{(z_+ - z_-)D_{+0}\phi_0'}{[(z_+ - z_-)c_0 - z_+\rho_\mathrm{s}]D_{+0}}, \tag{4.89}$$

$$\frac{\partial f_4}{\partial y_4} = -\frac{(z_+ - z_-)D_{+0}c_0'}{[(z_+ - z_-)c_0 - z_+\rho_\mathrm{s}]D_{+0}}, \tag{4.90}$$

$$\frac{\partial f_5}{\partial y_1} = 1. \tag{4.91}$$

For galvanostatic EIS, the $\frac{\partial f}{\partial p}$ Jacobian $\in \mathbb{R}^{5\times 1}$ is a zero vector. The nonzero elements of the $\frac{\partial y_\mathrm{BC}}{\partial y(x=0)}$ Jacobian ($\in \mathbb{R}^{6\times 5}$ for galvanostatic EIS or $\in \mathbb{R}^{5\times 5}$ for potentiostatic EIS) are given by

$$\frac{\partial y_{\mathrm{BC},1}}{\partial y_{0,5}} = 1, \tag{4.92}$$

$$\frac{\partial y_{\mathrm{BC},2}}{\partial y_{0,1}} = -\beta_\mathrm{D}(z_+ D_{+0} - z_- D_{-0})\phi_0'(x=0) + j_0^\mathrm{ref}\left(\frac{\xi_+}{\hat{c}_+^\mathrm{ref}}\right)^{1-\frac{\alpha_1}{2}}(c_0 - \rho_\mathrm{s})^{-\frac{\alpha_1}{2}}\exp(-\alpha_1\eta_0)\Bigg|_{x=0}, \tag{4.93}$$

$$\frac{\partial y_{\mathrm{BC},2}}{\partial y_{0,2}} = \beta_\mathrm{D}(D_{-0} - D_{+0}), \tag{4.94}$$

$$\frac{\partial y_{\mathrm{BC},2}}{\partial y_{0,3}} = j_0^\mathrm{ref}\left[\frac{\xi_+(c_0 - \rho_\mathrm{s})}{\hat{c}_+^\mathrm{ref}}\right]^{1-\frac{\alpha_1}{2}}\{\alpha_1\exp(-\alpha_1\eta_0) + (2-\alpha_1)\exp[(2-\alpha_1)\eta_0]\}\Bigg|_{x=0}, \tag{4.95}$$

$$\frac{\partial y_{\mathrm{BC},2}}{\partial y_{0,4}} = \beta_\mathrm{D}[-(z_+ D_{+0} - z_- D_{-0})c_0(x=0) + z_+ D_{+0}\rho_\mathrm{s}]. \tag{4.96}$$

For galvanostatic EIS, the nonzero elements of the $\frac{\partial y_{\mathrm{BC}}}{\partial y(x=1)}$ Jacobian $\in \mathbb{R}^{6\times 5}$ are given by

$$\frac{\partial y_{\mathrm{BC},3}}{\partial y_{1,1}} = z_- \phi_0'(x=1), \tag{4.97}$$

$$\frac{\partial y_{\mathrm{BC},3}}{\partial y_{1,2}} = 1, \tag{4.98}$$

$$\frac{\partial y_{\mathrm{BC},3}}{\partial y_{1,4}} = z_- c_0(x=1), \tag{4.99}$$

$$\begin{aligned}\frac{\partial y_{\mathrm{BC},4}}{\partial y_{1,1}} &= \beta_{\mathrm{D}}(z_+ D_{+0} - z_- D_{-0})\phi_0'(x=1) \\ &\quad + j_0^{\mathrm{ref}}\left(\frac{\xi_+}{\hat{c}_+^{\mathrm{ref}}}\right)^{1-\frac{\alpha_1}{2}} (c_0-\rho_{\mathrm{s}})^{-\frac{\alpha_1}{2}} \exp(-\alpha_1\eta_0)\Bigg|_{x=1},\end{aligned} \tag{4.100}$$

$$\frac{\partial y_{\mathrm{BC},4}}{\partial y_{1,2}} = -\beta_{\mathrm{D}}(D_{-0} - D_{+0}), \tag{4.101}$$

$$\frac{\partial y_{\mathrm{BC},4}}{\partial y_{1,3}} = j_0^{\mathrm{ref}}\left[\frac{\xi_+(c_0-\rho_{\mathrm{s}})}{\hat{c}_+^{\mathrm{ref}}}\right]^{1-\frac{\alpha_1}{2}} \{\alpha_1 \exp(-\alpha_1\eta_0) + (2-\alpha_1)\exp[(2-\alpha_1)\eta_0]\}\Bigg|_{x=1}, \tag{4.102}$$

$$\frac{\partial y_{\mathrm{BC},4}}{\partial y_{1,4}} = -\beta_{\mathrm{D}}[-(z_+ D_{+0} - z_- D_{-0})c_0(x=1) + z_+ D_{+0}\rho_{\mathrm{s}}], \tag{4.103}$$

$$\frac{\partial y_{\mathrm{BC},5}}{\partial y_{1,5}} = 1, \tag{4.104}$$

$$\frac{\partial y_{\mathrm{BC},6}}{\partial y_{1,1}} = \beta_{\mathrm{D}}(z_+ D_{+0} - z_- D_{-0})\phi_0'(x=1), \tag{4.105}$$

$$\frac{\partial y_{\mathrm{BC},6}}{\partial y_{1,2}} = -\beta_{\mathrm{D}}(D_{-0} - D_{+0}), \tag{4.106}$$

$$\frac{\partial y_{\mathrm{BC},6}}{\partial y_{1,4}} = -\beta_{\mathrm{D}}[-(z_+ D_{+0} - z_- D_{-0})c_0(x=1) + z_+ D_{+0}\rho_{\mathrm{s}}], \tag{4.107}$$

and the nonzero element of the $\frac{\partial y_{\mathrm{BC}}}{\partial p}$ Jacobian $\in \mathbb{R}^{6\times 1}$ is given by

$$\frac{\partial y_{\mathrm{BC},4}}{\partial p} = j_0^{\mathrm{ref}}\left[\frac{\xi_+(c_0-\rho_{\mathrm{s}})}{\hat{c}_+^{\mathrm{ref}}}\right]^{1-\frac{\alpha_1}{2}} \{\alpha_1 \exp(-\alpha_1\eta_0) + (2-\alpha_1)\exp[(2-\alpha_1)\eta_0]\}\Bigg|_{x=1}, \tag{4.108}$$

while for potentiostatic EIS, the nonzero elements of the $\frac{\partial y_{\mathrm{BC}}}{\partial y(x=1)}$ Jacobian $\in \mathbb{R}^{5\times 5}$ are

given by

$$\frac{\partial y_{\mathrm{BC},3}}{\partial y_{1,1}} = z_- \phi_0'(x=1), \tag{4.109}$$

$$\frac{\partial y_{\mathrm{BC},3}}{\partial y_{1,2}} = 1, \tag{4.110}$$

$$\frac{\partial y_{\mathrm{BC},3}}{\partial y_{1,4}} = z_- c_0(x=1), \tag{4.111}$$

$$\begin{aligned}\frac{\partial y_{\mathrm{BC},4}}{\partial y_{1,1}} &= \beta_{\mathrm{D}}(z_+ D_{+0} - z_- D_{-0})\phi_0'(x=1) \\ &\quad + j_0^{\mathrm{ref}} \left(\frac{\xi_+}{\hat{c}_+^{\mathrm{ref}}}\right)^{1-\frac{\alpha_1}{2}} (c_0 - \rho_{\mathrm{s}})^{-\frac{\alpha_1}{2}} \exp(-\alpha_1 \eta_0)\Bigg|_{x=1},\end{aligned} \tag{4.112}$$

$$\frac{\partial y_{\mathrm{BC},4}}{\partial y_{1,2}} = -\beta_{\mathrm{D}}(D_{-0} - D_{+0}), \tag{4.113}$$

$$\frac{\partial y_{\mathrm{BC},4}}{\partial y_{1,3}} = j_0^{\mathrm{ref}} \left[\frac{\xi_+(c_0 - \rho_{\mathrm{s}})}{\hat{c}_+^{\mathrm{ref}}}\right]^{1-\frac{\alpha_1}{2}} \{\alpha_1 \exp(-\alpha_1 \eta_0) + (2-\alpha_1)\exp[(2-\alpha_1)\eta_0]\}\Bigg|_{x=1}, \tag{4.114}$$

$$\frac{\partial y_{\mathrm{BC},4}}{\partial y_{1,4}} = -\beta_{\mathrm{D}}[-(z_+ D_{+0} - z_- D_{-0})c_0(x=1) + z_+ D_{+0}\rho_{\mathrm{s}}], \tag{4.115}$$

$$\frac{\partial y_{\mathrm{BC},5}}{\partial y_{1,5}} = 1. \tag{4.116}$$

4.8.5 Equations for cases 1 and 2 in Section 4.2 of [122]

For completeness, we provide the dimensionless equations for cases 1 and 2 in Section 4.2 of [122]. For case 1, we consider a reservoir at $x = 0$ and an ideal cation-selective and anion-blocking surface at $x = 1$. For case 2, we consider the anode at $x = 0$ and the cathode at $x = 1$ to be ideal cation-selective and anion-blocking surfaces.

4.8.5.1 Dimensionless equations

4.8.5.1.1 Case 1: reservoir boundary condition at anode The dimensionless boundary conditions are given by

$$c(x=0) = \beta_1, \tag{4.117}$$

$$\phi(x=0) = 0, \tag{4.118}$$

$$\left.\frac{\partial c}{\partial x} + z_- c \frac{\partial \phi}{\partial x}\right|_{x=1} = 0, \tag{4.119}$$

$$\phi(x=1) = -V, \quad V \geq 0. \tag{4.120}$$

At $\mathcal{O}(1)$, the boundary conditions are given by

$$c_0(x=0) = \beta_1, \tag{4.121}$$

$$\phi_0(x=0) = 0, \tag{4.122}$$

$$\left.\frac{\mathrm{d}c_0}{\mathrm{d}x} + z_- c_0 \frac{\mathrm{d}\phi_0}{\mathrm{d}x}\right|_{x=1} = 0, \tag{4.123}$$

$$\phi_0(x=1) = -V_0, \quad V_0 \geq 0. \tag{4.124}$$

At $\mathcal{O}(\epsilon)$, the boundary conditions are given by

$$c_1(x=0) = 0, \tag{4.125}$$

$$\phi_1(x=0) = 0, \tag{4.126}$$

$$\left.\frac{\mathrm{d}c_1}{\mathrm{d}x} + z_- \left(c_0 \frac{\mathrm{d}\phi_1}{\mathrm{d}x} + \frac{\mathrm{d}\phi_0}{\mathrm{d}x} c_1\right)\right|_{x=1} = 0, \tag{4.127}$$

$$\phi_1(x=1) = -V_1, \quad V_1 \geq 0. \tag{4.128}$$

4.8.5.1.2 Case 2: no-anion-flux boundary condition at anode The dimensionless boundary conditions are given by

$$\left.\frac{\partial c}{\partial x} + z_- c \frac{\partial \phi}{\partial x}\right|_{x=0} = \left.\frac{\partial c}{\partial x} + z_- c \frac{\partial \phi}{\partial x}\right|_{x=1} = 0, \tag{4.129}$$

$$\int_0^1 c \, \mathrm{d}x = \beta_1, \tag{4.130}$$

$$\phi(x=0) = 0, \tag{4.131}$$

$$\phi(x=1) = -V, \quad V \geq 0. \tag{4.132}$$

At $\mathcal{O}(1)$, the boundary conditions are given by

$$\frac{\mathrm{d}c_0}{\mathrm{d}x} + z_- c_0 \frac{\mathrm{d}\phi_0}{\mathrm{d}x}\bigg|_{x=0} = \frac{\mathrm{d}c_0}{\mathrm{d}x} + z_- c_0 \frac{\mathrm{d}\phi_0}{\mathrm{d}x}\bigg|_{x=1} = 0, \tag{4.133}$$

$$\int_0^1 c_0 \,\mathrm{d}x = \beta_1, \tag{4.134}$$

$$\phi_0(x=0) = 0, \tag{4.135}$$

$$\phi_0(x=1) = -V_0, \quad V_0 \geq 0. \tag{4.136}$$

At $\mathcal{O}(\epsilon)$, the boundary conditions are given by

$$\frac{\mathrm{d}c_1}{\mathrm{d}x} + z_- \left(c_0 \frac{\mathrm{d}\phi_1}{\mathrm{d}x} + \frac{\mathrm{d}\phi_0}{\mathrm{d}x} c_1 \right)\bigg|_{x=0} = \frac{\mathrm{d}c_1}{\mathrm{d}x} + z_- \left(c_0 \frac{\mathrm{d}\phi_1}{\mathrm{d}x} + \frac{\mathrm{d}\phi_0}{\mathrm{d}x} c_1 \right)\bigg|_{x=1} = 0, \tag{4.137}$$

$$\int_0^1 c_1 \,\mathrm{d}x = 0, \tag{4.138}$$

$$\phi_1(x=0) = 0, \tag{4.139}$$

$$\phi_1(x=1) = -V_1, \quad V_1 \geq 0. \tag{4.140}$$

4.8.5.2 First and second order spatial derivatives

4.8.5.2.1 Case 1: reservoir boundary condition at anode For $\rho_\mathrm{s} = 0$,

$$c_0 = 1 - 2I_0 x, \tag{4.141}$$

$$\frac{\mathrm{d}c_0}{\mathrm{d}x} = -2I_0, \tag{4.142}$$

$$\frac{\mathrm{d}^2 c_0}{\mathrm{d}x^2} = 0, \tag{4.143}$$

$$\phi_0 = -\frac{1}{z_-} \ln c_0 = -\frac{1}{z_-} \ln(1 - 2I_0 x), \tag{4.144}$$

$$\frac{\mathrm{d}\phi_0}{\mathrm{d}x} = \frac{2I_0}{z_-(1 - 2I_0 x)}, \tag{4.145}$$

$$\frac{\mathrm{d}^2 \phi_0}{\mathrm{d}x^2} = \frac{4I_0^2}{z_-(1 - 2I_0 x)^2}. \tag{4.146}$$

For $\rho_s \neq 0$,

$$c_0 = -\alpha_1 W\left[-\frac{\beta_1}{\alpha_1}\exp\left(\frac{2I_0 x - \beta_1}{\alpha_1}\right)\right], \tag{4.147}$$

$$\frac{\mathrm{d}c_0}{\mathrm{d}x} = \frac{2\beta_1 I_0}{\alpha_1 \exp\left(-\frac{c_0+2I_0x-\beta_1}{\alpha_1}\right) - \beta_1}, \tag{4.148}$$

$$\frac{\mathrm{d}^2 c_0}{\mathrm{d}x^2} = \frac{2\beta_1 I_0\left(\frac{\mathrm{d}c_0}{\mathrm{d}x} + 2I_0\right)\exp\left(-\frac{c_0+2I_0x-\beta_1}{\alpha_1}\right)}{\left[\alpha_1 \exp\left(-\frac{c_0+2I_0x-\beta_1}{\alpha_1}\right) - \beta_1\right]^2}, \tag{4.149}$$

$$\phi_0 = -\frac{\alpha_1}{\alpha_2}\ln\left(\frac{c_0}{\beta_1}\right) = -\frac{c_0 + 2I_0 x - \beta_1}{\alpha_2}, \tag{4.150}$$

$$\frac{\mathrm{d}\phi_0}{\mathrm{d}x} = -\frac{\frac{\mathrm{d}c_0}{\mathrm{d}x} + 2I_0}{\alpha_2}, \tag{4.151}$$

$$\frac{\mathrm{d}^2\phi_0}{\mathrm{d}x^2} = -\frac{1}{\alpha_2}\frac{\mathrm{d}^2 c_0}{\mathrm{d}x^2}, \tag{4.152}$$

where we use the W_0 branch for $\rho_s < 0$ and the W_{-1} branch for $\rho_s > 0$.

4.8.5.2.2 Case 2: no-anion-flux boundary condition at anode

For $\rho_s = 0$,

$$c_0 = \alpha_3 - 2I_0 x, \tag{4.153}$$

$$\frac{\mathrm{d}c_0}{\mathrm{d}x} = -2I_0, \tag{4.154}$$

$$\frac{\mathrm{d}^2 c_0}{\mathrm{d}x^2} = 0, \tag{4.155}$$

$$\phi_0 = -\frac{1}{z_-}\ln\left(\frac{c_0}{\alpha_3}\right) = -\frac{1}{z_-}\ln\left(1 - \frac{2I_0}{\alpha_3}x\right), \tag{4.156}$$

$$\frac{\mathrm{d}\phi_0}{\mathrm{d}x} = \frac{2I_0}{z_-(\alpha_3 - 2I_0 x)}, \tag{4.157}$$

$$\frac{\mathrm{d}^2\phi_0}{\mathrm{d}x^2} = \frac{4I_0^2}{z_-(\alpha_3 - 2I_0 x)^2}. \tag{4.158}$$

For $\rho_s \neq 0$,

$$c_0 = -\alpha_1 W\left[-\frac{\alpha_3}{\alpha_1}\exp\left(\frac{2I_0 x - \alpha_3}{\alpha_1}\right)\right], \tag{4.159}$$

$$\frac{\mathrm{d}c_0}{\mathrm{d}x} = \frac{2\alpha_3 I_0}{\alpha_1 \exp\left(-\frac{c_0+2I_0x-\alpha_3}{\alpha_1}\right) - \alpha_3}, \tag{4.160}$$

$$\frac{\mathrm{d}^2 c_0}{\mathrm{d}x^2} = \frac{2\alpha_3 I_0\left(\frac{\mathrm{d}c_0}{\mathrm{d}x} + 2I_0\right)\exp\left(-\frac{c_0+2I_0x-\alpha_3}{\alpha_1}\right)}{\left[\alpha_1\exp\left(-\frac{c_0+2I_0x-\alpha_3}{\alpha_1}\right)-\alpha_3\right]^2}, \tag{4.161}$$

$$\phi_0 = -\frac{\alpha_1}{\alpha_2}\ln\left(\frac{c_0}{\alpha_3}\right) = -\frac{c_0+2I_0x-\alpha_3}{\alpha_2}, \tag{4.162}$$

$$\frac{\mathrm{d}\phi_0}{\mathrm{d}x} = -\frac{\frac{\mathrm{d}c_0}{\mathrm{d}x}+2I_0}{\alpha_2}, \tag{4.163}$$

$$\frac{\mathrm{d}^2\phi_0}{\mathrm{d}x^2} = -\frac{1}{\alpha_2}\frac{\mathrm{d}^2 c_0}{\mathrm{d}x^2}, \tag{4.164}$$

where we use the W_0 branch for $\rho_\mathrm{s} < 0$ and the W_{-1} branch for $\rho_\mathrm{s} > 0$.

4.8.5.3 Construction of perturbation equations for use in MATLAB

4.8.5.3.1 Case 1: reservoir boundary condition at anode p is not required and y and f are given by

$$y = \begin{bmatrix} c_1 \\ c_1' \\ \phi_1 \\ \phi_1' \end{bmatrix}, \tag{4.165}$$

$$f = \begin{bmatrix} c_1' \\ c_1'' \\ \phi_1' \\ \phi_1'' \end{bmatrix} = \begin{bmatrix} c_1' \\ \frac{\left[\left(z_+D_{+0}-z_-D_{-0}\right)c_0 - z_+D_{+0}\rho_\mathrm{s}\right]\frac{i\omega}{D_{-0}}c_1 + z_+z_-D_{+0}\rho_\mathrm{s}\gamma_1}{[(z_+-z_-)c_0-z_+\rho_\mathrm{s}]D_{+0}} \\ \phi_1' \\ \frac{\left(D_{-0}-D_{+0}\right)\frac{i\omega}{D_{-0}}c_1 - (z_+-z_-)D_{+0}\gamma_1}{[(z_+-z_-)c_0-z_+\rho_\mathrm{s}]D_{+0}} \end{bmatrix}. \tag{4.166}$$

For galvanostatic EIS where we impose $J_1(x=1) = I_{\text{applied},1}$,

$$y_\mathrm{BC} = \begin{bmatrix} c_1(x=0) \\ \phi_1(x=0) \\ c_1' + z_-(c_0\phi_1' + \phi_0' c_1)\big|_{x=1} \\ I_{\text{applied},1} - J_1(x=1) \end{bmatrix}, \tag{4.167}$$

while for potentiostatic EIS where we impose $\phi_1(x=1) = -V_1$,

$$y_{\mathrm{BC}} = \begin{bmatrix} c_1(x=0) \\ \phi_1(x=0) \\ c_1' + z_-(c_0\phi_1' + \phi_0' c_1)|_{x=1} \\ \phi_1(x=1) + V_1 \end{bmatrix}. \tag{4.168}$$

4.8.5.3.2 Case 2: no-anion-flux boundary condition at anode We need to include a variable, which is called y_5, in y, that enforces the integral constraint for the conservation of the number of anions. p is not required and y and f are given by

$$y = \begin{bmatrix} c_1 \\ c_1' \\ \phi_1 \\ \phi_1' \\ y_5 \end{bmatrix}, \tag{4.169}$$

$$f = \begin{bmatrix} c_1' \\ c_1'' \\ \phi_1' \\ \phi_1'' \\ c_1 \end{bmatrix} = \begin{bmatrix} c_1' \\ \frac{\left[\left(z_+ D_{+0} - z_- D_{-0}\right)c_0 - z_+ D_{+0}\rho_{\mathrm{s}}\right]\frac{i\omega}{D_{-0}} c_1 + z_+ z_- D_{+0}\rho_{\mathrm{s}}\gamma_1}{[(z_+ - z_-)c_0 - z_+\rho_{\mathrm{s}}]D_{+0}} \\ \phi_1' \\ \frac{\left(D_{-0} - D_{+0}\right)\frac{i\omega}{D_{-0}} c_1 - (z_+ - z_-)D_{+0}\gamma_1}{[(z_+ - z_-)c_0 - z_+\rho_{\mathrm{s}}]D_{+0}} \\ c_1 \end{bmatrix}. \tag{4.170}$$

For galvanostatic EIS where we impose $J_1(x=1) = I_{\mathrm{applied},1}$,

$$y_{\mathrm{BC}} = \begin{bmatrix} y_5(x=0) \\ \phi_1(x=0) \\ c_1' + z_-(c_0\phi_1' + \phi_0' c_1)|_{x=1} \\ I_{\mathrm{applied},1} - J_1(x=1) \\ y_5(x=1) \end{bmatrix}, \tag{4.171}$$

while for potentiostatic EIS where we impose $\phi_1(x=1) = -V_1$,

$$y_{\mathrm{BC}} = \begin{bmatrix} y_5(x=0) \\ \phi_1(x=0) \\ c_1' + z_-(c_0\phi_1' + \phi_0' c_1)|_{x=1} \\ \phi_1(x=1) + V_1 \\ y_5(x=1) \end{bmatrix}. \tag{4.172}$$

4.8.5.4 Jacobians for perturbation equations

For simplicity, the elements of f, y, y_{BC}, $y(x=0)$ and $y(x=1)$ are written as

$$f = \begin{bmatrix} f_1 \\ f_2 \\ f_3 \\ f_4 \end{bmatrix} \quad \text{or} \quad \begin{bmatrix} f_1 \\ f_2 \\ f_3 \\ f_4 \\ f_5 \end{bmatrix}, \tag{4.173}$$

$$y = \begin{bmatrix} y_1 \\ y_2 \\ y_3 \\ y_4 \end{bmatrix} \quad \text{or} \quad \begin{bmatrix} y_1 \\ y_2 \\ y_3 \\ y_4 \\ y_5 \end{bmatrix}, \tag{4.174}$$

$$y_{\mathrm{BC}} = \begin{bmatrix} y_{\mathrm{BC},1} \\ y_{\mathrm{BC},2} \\ y_{\mathrm{BC},3} \\ y_{\mathrm{BC},4} \end{bmatrix} \quad \text{or} \quad \begin{bmatrix} y_{\mathrm{BC},1} \\ y_{\mathrm{BC},2} \\ y_{\mathrm{BC},3} \\ y_{\mathrm{BC},4} \\ y_{\mathrm{BC},5} \end{bmatrix}, \tag{4.175}$$

$$y(x=0) = \begin{bmatrix} y_{0,1} \\ y_{0,2} \\ y_{0,3} \\ y_{0,4} \end{bmatrix} \quad \text{or} \quad \begin{bmatrix} y_{0,1} \\ y_{0,2} \\ y_{0,3} \\ y_{0,4} \\ y_{0,5} \end{bmatrix}, \tag{4.176}$$

$$y(x=1) = \begin{bmatrix} y_{1,1} \\ y_{1,2} \\ y_{1,3} \\ y_{1,4} \end{bmatrix} \quad \text{or} \quad \begin{bmatrix} y_{1,1} \\ y_{1,2} \\ y_{1,3} \\ y_{1,4} \\ y_{1,5} \end{bmatrix}. \tag{4.177}$$

4.8.5.4.1 Case 1: reservoir boundary condition at anode The nonzero elements of the $\frac{\partial f}{\partial y}$ Jacobian $\in \mathbb{R}^{4\times4}$ are given by

$$\frac{\partial f_1}{\partial y_2} = 1, \tag{4.178}$$

$$\frac{\partial f_2}{\partial y_1} = \frac{\frac{[(z_+D_{+0}-z_-D_{-0})c_0-z_+D_{+0}\rho_s]i\omega}{D_{-0}} + z_+z_-D_{+0}\rho_s\phi_0''}{[(z_+-z_-)c_0-z_+\rho_s]D_{+0}}, \tag{4.179}$$

$$\frac{\partial f_2}{\partial y_2} = \frac{z_+z_-D_{+0}\rho_s\phi_0'}{[(z_+-z_-)c_0-z_+\rho_s]D_{+0}}, \tag{4.180}$$

$$\frac{\partial f_2}{\partial y_4} = \frac{z_+z_-D_{+0}\rho_s c_0'}{[(z_+-z_-)c_0-z_+\rho_s]D_{+0}}, \tag{4.181}$$

$$\frac{\partial f_3}{\partial y_4} = 1, \tag{4.182}$$

$$\frac{\partial f_4}{\partial y_1} = \frac{\frac{(D_{-0}-D_{+0})i\omega}{D_{-0}} - (z_+-z_-)D_{+0}\phi_0''}{[(z_+-z_-)c_0-z_+\rho_s]D_{+0}}, \tag{4.183}$$

$$\frac{\partial f_4}{\partial y_2} = -\frac{(z_+-z_-)D_{+0}\phi_0'}{[(z_+-z_-)c_0-z_+\rho_s]D_{+0}}, \tag{4.184}$$

$$\frac{\partial f_4}{\partial y_4} = -\frac{(z_+-z_-)D_{+0}c_0'}{[(z_+-z_-)c_0-z_+\rho_s]D_{+0}}. \tag{4.185}$$

The nonzero elements of the $\frac{\partial y_{BC}}{\partial y(x=0)}$ Jacobian $\in \mathbb{R}^{4\times4}$ are given by

$$\frac{\partial y_{BC,1}}{\partial y_{0,1}} = 1, \tag{4.186}$$

$$\frac{\partial y_{\mathrm{BC},2}}{\partial y_{0,3}} = 1. \tag{4.187}$$

For galvanostatic EIS, the nonzero elements of the $\frac{\partial y_{\mathrm{BC}}}{\partial y(x=1)}$ Jacobian $\in \mathbb{R}^{4\times4}$ are given by

$$\frac{\partial y_{\mathrm{BC},3}}{\partial y_{1,1}} = z_- \phi_0'(x=1), \tag{4.188}$$
$$\frac{\partial y_{\mathrm{BC},3}}{\partial y_{1,2}} = 1, \tag{4.189}$$
$$\frac{\partial y_{\mathrm{BC},3}}{\partial y_{1,4}} = z_- c_0(x=1), \tag{4.190}$$
$$\frac{\partial y_{\mathrm{BC},4}}{\partial y_{1,1}} = \beta_{\mathrm{D}}(z_+ D_{+0} - z_- D_{-0})\phi_0'(x=1), \tag{4.191}$$
$$\frac{\partial y_{\mathrm{BC},4}}{\partial y_{1,2}} = -\beta_{\mathrm{D}}(D_{-0} - D_{+0}), \tag{4.192}$$
$$\frac{\partial y_{\mathrm{BC},4}}{\partial y_{1,4}} = -\beta_{\mathrm{D}}[-(z_+ D_{+0} - z_- D_{-0})c_0(x=1) + z_+ D_{+0}\rho_{\mathrm{s}}], \tag{4.193}$$

while for potentiostatic EIS, the nonzero elements of the $\frac{\partial y_{\mathrm{BC}}}{\partial y(x=1)}$ Jacobian $\in \mathbb{R}^{4\times4}$ are given by

$$\frac{\partial y_{\mathrm{BC},3}}{\partial y_{1,1}} = z_- \phi_0'(x=1), \tag{4.194}$$
$$\frac{\partial y_{\mathrm{BC},3}}{\partial y_{1,2}} = 1, \tag{4.195}$$
$$\frac{\partial y_{\mathrm{BC},3}}{\partial y_{1,4}} = z_- c_0(x=1), \tag{4.196}$$
$$\frac{\partial y_{\mathrm{BC},4}}{\partial y_{1,3}} = 1. \tag{4.197}$$

4.8.5.4.2 Case 2: no-anion-flux boundary condition at anode The nonzero elements of the $\frac{\partial f}{\partial y}$ Jacobian $\in \mathbb{R}^{5\times5}$ are given by

$$\frac{\partial f_1}{\partial y_2} = 1, \tag{4.198}$$
$$\frac{\partial f_2}{\partial y_1} = \frac{\frac{[(z_+ D_{+0} - z_- D_{-0})c_0 - z_+ D_{+0}\rho_{\mathrm{s}}]i\omega}{D_{-0}} + z_+ z_- D_{+0}\rho_{\mathrm{s}}\phi_0''}{[(z_+ - z_-)c_0 - z_+\rho_{\mathrm{s}}]D_{+0}}, \tag{4.199}$$

$$\frac{\partial f_2}{\partial y_2} = \frac{z_+ z_- D_{+0} \rho_\mathrm{s} \phi_0'}{[(z_+ - z_-)c_0 - z_+ \rho_\mathrm{s}] D_{+0}}, \tag{4.200}$$

$$\frac{\partial f_2}{\partial y_4} = \frac{z_+ z_- D_{+0} \rho_\mathrm{s} c_0'}{[(z_+ - z_-)c_0 - z_+ \rho_\mathrm{s}] D_{+0}}, \tag{4.201}$$

$$\frac{\partial f_3}{\partial y_4} = 1, \tag{4.202}$$

$$\frac{\partial f_4}{\partial y_1} = \frac{\frac{(D_{-0} - D_{+0})i\omega}{D_{-0}} - (z_+ - z_-) D_{+0} \phi_0''}{[(z_+ - z_-)c_0 - z_+ \rho_\mathrm{s}] D_{+0}}, \tag{4.203}$$

$$\frac{\partial f_4}{\partial y_2} = -\frac{(z_+ - z_-) D_{+0} \phi_0'}{[(z_+ - z_-)c_0 - z_+ \rho_\mathrm{s}] D_{+0}}, \tag{4.204}$$

$$\frac{\partial f_4}{\partial y_4} = -\frac{(z_+ - z_-) D_{+0} c_0'}{[(z_+ - z_-)c_0 - z_+ \rho_\mathrm{s}] D_{+0}}, \tag{4.205}$$

$$\frac{\partial f_5}{\partial y_1} = 1. \tag{4.206}$$

The nonzero elements of the $\frac{\partial y_\mathrm{BC}}{\partial y(x=0)}$ Jacobian $\in \mathbb{R}^{5\times 5}$ are given by

$$\frac{\partial y_{\mathrm{BC},1}}{\partial y_{0,5}} = 1, \tag{4.207}$$

$$\frac{\partial y_{\mathrm{BC},2}}{\partial y_{0,3}} = 1. \tag{4.208}$$

For galvanostatic EIS, the nonzero elements of the $\frac{\partial y_\mathrm{BC}}{\partial y(x=1)}$ Jacobian $\in \mathbb{R}^{5\times 5}$ are given by

$$\frac{\partial y_{\mathrm{BC},3}}{\partial y_{1,1}} = z_- \phi_0'(x=1), \tag{4.209}$$

$$\frac{\partial y_{\mathrm{BC},3}}{\partial y_{1,2}} = 1, \tag{4.210}$$

$$\frac{\partial y_{\mathrm{BC},3}}{\partial y_{1,4}} = z_- c_0(x=1), \tag{4.211}$$

$$\frac{\partial y_{\mathrm{BC},4}}{\partial y_{1,1}} = \beta_\mathrm{D}(z_+ D_{+0} - z_- D_{-0}) \phi_0'(x=1), \tag{4.212}$$

$$\frac{\partial y_{\mathrm{BC},4}}{\partial y_{1,2}} = -\beta_\mathrm{D}(D_{-0} - D_{+0}), \tag{4.213}$$

$$\frac{\partial y_{\mathrm{BC},4}}{\partial y_{1,4}} = -\beta_\mathrm{D}[-(z_+ D_{+0} - z_- D_{-0}) c_0(x=1) + z_+ D_{+0} \rho_\mathrm{s}], \tag{4.214}$$

$$\frac{\partial y_{\mathrm{BC},5}}{\partial y_{1,5}} = 1, \tag{4.215}$$

while for potentiostatic EIS, the nonzero elements of the $\frac{\partial y_{\mathrm{BC}}}{\partial y(x=1)}$ Jacobian $\in \mathbb{R}^{5\times 5}$ are given by

$$\frac{\partial y_{\mathrm{BC},3}}{\partial y_{1,1}} = z_- \phi_0'(x=1), \tag{4.216}$$

$$\frac{\partial y_{\mathrm{BC},3}}{\partial y_{1,2}} = 1, \tag{4.217}$$

$$\frac{\partial y_{\mathrm{BC},3}}{\partial y_{1,4}} = z_- c_0(x=1), \tag{4.218}$$

$$\frac{\partial y_{\mathrm{BC},4}}{\partial y_{1,3}} = 1, \tag{4.219}$$

$$\frac{\partial y_{\mathrm{BC},5}}{\partial y_{1,5}} = 1. \tag{4.220}$$

Chapter 5

Conclusion

In this thesis, in order to model electrodeposition in charged porous media, we have coupled the leaky membrane model, which is capable of predicting overlimiting current carried by surface conduction, with Butler-Volmer reaction kinetics, which is commonly used for describing electrochemical reactions such as electrodeposition, and analyzed the resulting coupled model in three different ways, namely steady state current-voltage relations and linear sweep voltammetry, linear stability analysis, and impedance analysis. We have also focused on the overlimiting current regime because practical applications such as electroplating of metals and charging of batteries are ideally carried out at as high a current as possible without causing the formation and propagation of dendrites.

In the analysis of steady state current-voltage relations and linear sweep voltammetry, we first derived analytical or semi-analytical expressions for ion concentrations, electric potentials, current-voltage relations and overlimiting conductances at steady state for three different types of experimentally relevant boundary conditions. We then validated the model with experimental steady state current-voltage relations for copper electrodeposition in different nanoporous media. After this model validation, we proceeded to perform linear stability analysis on the model to investigate how the linear stability of the electrode surface depends on key system parameters such as the pore surface charge density, Damköhler number and applied current density. We also further validated the model by comparing theoretical predictions for critical and insta-

bility wavelengths with published experimental data for copper electrodeposition in cellulose nitrate membranes. Finally, we performed impedance analysis on the model to explain experimental impedance spectra obtained for copper electrodeposition in anodic aluminum oxide membranes.

Despite the simplicity of the model, we have been able to analyze it and derive key theoretical predictions that are validated by experimental data and observations. Nonetheless, there are some important extensions that would further generalize the model. First, we have assumed that the ion diffusivities are concentration-independent but this assumption is often not true, especially in concentrated solutions. One straightforward extension in this direction would be to use the Debye-Hückel theory for activity coefficients in dilute solutions. Another important extension is to account for surface adsorption and surface diffusion of adsorbed species, both of which are likely to occur in most electrochemical reaction mechanisms including copper electrodeposition. Last, one major extension that would generalize the model to solid electrolytes used in solid state batteries would be to include additional mechanical effects such as pressure, viscous stress and deformational stress.

Bibliography

[1] Zeeshan Ahmad and Venkatasubramanian Viswanathan. Role of anisotropy in determining stability of electrodeposition at solid-solid interfaces. *Physical Review Materials*, 1(5):055403, October 2017.

[2] Zeeshan Ahmad and Venkatasubramanian Viswanathan. Stability of Electrodeposition at Solid-Solid Interfaces and Implications for Metal Anodes. *Physical Review Letters*, 119(5):056003, August 2017.

[3] Rohan Akolkar. Mathematical model of the dendritic growth during lithium electrodeposition. *Journal of Power Sources*, 232:23–28, June 2013.

[4] Rohan Akolkar. Modeling dendrite growth during lithium electrodeposition at sub-ambient temperature. *Journal of Power Sources*, 246:84–89, January 2014.

[5] Paul Albertus, Susan Babinec, Scott Litzelman, and Aron Newman. Status and challenges in enabling the lithium metal electrode for high-energy and low-cost rechargeable batteries. *Nature Energy*, 3(1):16–21, January 2018.

[6] M. B. Andersen, M. van Soestbergen, A. Mani, H. Bruus, P. M. Biesheuvel, and M. Z. Bazant. Current-Induced Membrane Discharge. *Physical Review Letters*, 109(10):108301, September 2012.

[7] Ryoichi Aogaki. Image Analysis of Morphological Instability in Galvanostatic Electrocrystallization I . General Expression for the Growth Mode of Surface Irregularities. *Journal of The Electrochemical Society*, 129(11):2442–2446, November 1982.

[8] Ryoichi Aogaki. Image Analysis of Morphological Instability in Galvanostatic Electrocrystallization II . Experimental Demonstration of Crystal Growth Behavior. *Journal of The Electrochemical Society*, 129(11):2447–2450, November 1982.

[9] Ryoichi Aogaki, Koichi Kitazawa, Yutaka Kose, and Kazuo Fueki. Theory of powdered crystal formation in electrocrystallization—occurrence of morphological instability at the electrode surface. *Electrochimica Acta*, 25(7):965–972, July 1980.

[10] Ryoichi Aogaki and Tohru Makino. Theory of powdered metal formation in electrochemistry—morphological instability in galvanostatic crystal growth under diffusion control. *Electrochimica Acta*, 26(11):1509–1517, November 1981.

[11] Ryoichi Aogaki and Tohru Makino. Morphological Instability in Nonsteady Galvanostatic Electrodeposition I . Effect of Surface Diffusion of Adatoms. *Journal of The Electrochemical Society*, 131(1):40–46, January 1984.

[12] Ryoichi Aogaki and Tohru Makino. Morphological Instability in Nonsteady Galvanostatic Electrodeposition II . Experimental Demonstration of the Surface Diffusion Effect of Adatoms by Means of Image Analysis. *Journal of The Electrochemical Society*, 131(1):46–51, January 1984.

[13] Ryoichi Aogaki and Tohru Makino. Morphological instability of crystal growth in nonsteady potentiostatic electrodeposition. I. The mechanism of growth of random crystals in metal deposition. *The Journal of Chemical Physics*, 81(4):2154–2163, August 1984.

[14] Ryoichi Aogaki and Tohru Makino. Morphological instability of crystal growth in nonsteady potentiostatic electrodeposition. II. Experimental examination with the image analysis of crystal morphology. *The Journal of Chemical Physics*, 81(4):2164–2168, August 1984.

[15] Nizar Aouina, Hubert Cachet, Catherine Debiemme-chouvy, and Thi Tuyet Mai Tran. Insight into the electroreduction of nitrate ions at a copper electrode, in neutral solution, after determination of their diffusion coefficient by electrochemical impedance spectroscopy. *Electrochimica Acta*, 55(24):7341–7345, October 2010.

[16] F. Argoul, E. Freysz, A. Kuhn, C. Léger, and L. Potin. Interferometric characterization of growth dynamics during dendritic electrodeposition of zinc. *Physical Review E*, 53(2):1777–1788, February 1996.

[17] M. Armand and J.-M. Tarascon. Building better batteries. *Nature*, 451:652, February 2008.

[18] Asghar Aryanfar, Daniel Brooks, Boris V. Merinov, William A. Goddard, Agustín J. Colussi, and Michael R. Hoffmann. Dynamics of Lithium Dendrite Growth and Inhibition: Pulse Charging Experiments and Monte Carlo Calculations. *The Journal of Physical Chemistry Letters*, 5(10):1721–1726, May 2014.

[19] Doron Aurbach, Ella Zinigrad, Yaron Cohen, and Hanan Teller. A short review of failure mechanisms of lithium metal and lithiated graphite anodes in liquid electrolyte solutions. *Solid State Ionics*, 148(3):405–416, June 2002.

[20] Peng Bai and Martin Z. Bazant. Charge transfer kinetics at the solid–solid interface in porous electrodes. *Nature Communications*, 5:3585, April 2014.

[21] Peng Bai, Jinzhao Guo, Miao Wang, Akihiro Kushima, Liang Su, Ju Li, Fikile R. Brushett, and Martin Z. Bazant. Interactions between Lithium Growths and Nanoporous Ceramic Separators. *Joule*, September 2018.

[22] Peng Bai, Ju Li, Fikile R. Brushett, and Martin Z. Bazant. Transition of lithium growth mechanisms in liquid electrolytes. *Energy & Environmental Science*, 9(10):3221–3229, October 2016.

[23] T. C. Banwell and A. Jayakumar. Exact analytical solution for current flow through diode with series resistance. *Electronics Letters*, 36(4):291–292, February 2000.

[24] Allen J. Bard and Larry R. Faulkner. *Electrochemical Methods: Fundamentals and Applications*. Wiley, New York, 2 edition edition, December 2000.

[25] Dale P. Barkey, Rolf H. Muller, and Charles W. Tobias. Roughness Development in Metal Electrodeposition I . Experimental Results. *Journal of The Electrochemical Society*, 136(8):2199–2207, August 1989.

[26] Dale P. Barkey, Rolf H. Muller, and Charles W. Tobias. Roughness Development in Metal Electrodeposition II . Stability Theory. *Journal of The Electrochemical Society*, 136(8):2207–2214, August 1989.

[27] Evgenij Barsoukov and J. Ross Macdonald, editors. *Impedance Spectroscopy: Theory, Experiment, and Applications*. Wiley, Hoboken, NJ, 3 edition edition, May 2018.

[28] J. L. Barton and J. O'M. Bockris. The electrolytic growth of dendrites from ionic solutions. *Proc. R. Soc. Lond. A*, 268(1335):485–505, August 1962.

[29] M. Bazant, K. Chu, and B. Bayly. Current-Voltage Relations for Electrochemical Thin Films. *SIAM Journal on Applied Mathematics*, 65(5):1463–1484, January 2005.

[30] Martin Z. Bazant. Regulation of ramified electrochemical growth by a diffusive wave. *Physical Review E*, 52(2):1903–1914, August 1995.

[31] Martin Z. Bazant. Theory of Chemical Kinetics and Charge Transfer based on Nonequilibrium Thermodynamics. *Accounts of Chemical Research*, 46(5):1144–1160, May 2013.

[32] Martin Z. Bazant. Thermodynamic stability of driven open systems and control of phase separation by electro-autocatalysis. *Faraday Discussions*, 199(0):423–463, July 2017.

[33] Jacob Bear. *Dynamics of Fluids in Porous Media*. Dover Publications, New York, revised edition edition, September 1988.

[34] E. Ben-Jacob, G. Deutscher, P. Garik, Nigel D. Goldenfeld, and Y. Lareah. Formation of a Dense Branching Morphology in Interfacial Growth. *Physical Review Letters*, 57(15):1903–1906, October 1986.

[35] E. Ben-Jacob, P. Garik, and D. Grier. Interfacial pattern formation far from equilibrium. *Superlattices and Microstructures*, 3(6):599–615, January 1987.

[36] E. Ben-Jacob, P. Garik, T. Mueller, and D. Grier. Characterization of morphology transitions in diffusion-controlled systems. *Physical Review A*, 38(3):1370–1380, August 1988.

[37] E. Ben-Jacob, R. Godbey, Nigel D. Goldenfeld, J. Koplik, H. Levine, T. Mueller, and L. M. Sander. Experimental Demonstration of the Role of Anisotropy in Interfacial Pattern Formation. *Physical Review Letters*, 55(12):1315–1318, September 1985.

[38] E. Ben-Jacob, Nigel Goldenfeld, B. G. Kotliar, and J. S. Langer. Pattern Selection in Dendritic Solidification. *Physical Review Letters*, 53(22):2110–2113, November 1984.

[39] E. Ben-Jacob, Nigel Goldenfeld, J. S. Langer, and Gerd Schön. Dynamics of Interfacial Pattern Formation. *Physical Review Letters*, 51(21):1930–1932, November 1983.

[40] E. Ben-Jacob, Nigel Goldenfeld, J. S. Langer, and Gerd Schön. Boundary-layer model of pattern formation in solidification. *Physical Review A*, 29(1):330–340, January 1984.

[41] Eshel Ben-Jacob and Peter Garik. The formation of patterns in non-equilibrium growth. *Nature*, 343(6258):523–530, February 1990.

[42] David Bensimon, Leo P. Kadanoff, Shoudan Liang, Boris I. Shraiman, and Chao Tang. Viscous flows in two dimensions. *Reviews of Modern Physics*, 58(4):977–999, October 1986.

[43] Dawn M. Bernardi and Mark W. Verbrugge. A Mathematical Model of the Solid-Polymer-Electrolyte Fuel Cell. *Journal of The Electrochemical Society*, 139(9):2477–2491, September 1992.

[44] George E. Blomgren. The Development and Future of Lithium Ion Batteries. *Journal of The Electrochemical Society*, 164(1):A5019–A5025, January 2017.

[45] J. O'm Bockris and M. Enyo. Mechanism of electrodeposition and dissolution processes of copper in aqueous solutions. *Transactions of the Faraday Society*, 58(0):1187–1202, January 1962.

[46] R. Bouchet, S. Lascaud, and M. Rosso. An EIS Study of the Anode Li/PEO-LiTFSI of a Li Polymer Battery. *Journal of The Electrochemical Society*, 150(10):A1385–A1389, October 2003.

[47] Bernard A. Boukamp. Electrochemical impedance spectroscopy in solid state ionics: recent advances. *Solid State Ionics*, 169(1):65–73, April 2004.

[48] R. M. Brady and R. C. Ball. Fractal growth of copper electrodeposits. *Nature*, 309(5965):225–229, May 1984.

[49] K. Brandt. Historical development of secondary lithium batteries. *Solid State Ionics*, 69(3):173–183, August 1994.

[50] C Brissot, M Rosso, J. N Chazalviel, P Baudry, and S Lascaud. In situ study of dendritic growth in lithium/PEO-salt/lithium cells. *Electrochimica Acta*, 43(10):1569–1574, April 1998.

[51] C. Brissot, M. Rosso, J. N. Chazalviel, and S. Lascaud. Dendritic growth mechanisms in lithium/polymer cells. *Journal of Power Sources*, 81-82:925–929, September 1999.

[52] C. Brissot, M. Rosso, J.-N. Chazalviel, and S. Lascaud. In Situ Concentration Cartography in the Neighborhood of Dendrites Growing in Lithium/Polymer-Electrolyte/Lithium Cells. *Journal of The Electrochemical Society*, 146(12):4393–4400, December 1999.

[53] C Brissot, M Rosso, J. N Chazalviel, and S Lascaud. Concentration measurements in lithium/polymer–electrolyte/lithium cells during cycling. *Journal of Power Sources*, 94(2):212–218, March 2001.

[54] O. R. Brown and H. R. Thirsk. The rate-determining step in the electrodeposition of copper on copper from aqueous cupric sulphate solutions. *Electrochimica Acta*, 10(4):383–393, April 1965.

[55] Peter G. Bruce, Bruno Scrosati, and Jean-Marie Tarascon. Nanomaterials for Rechargeable Lithium Batteries. *Angewandte Chemie International Edition*, 47(16):2930–2946, April 2008.

[56] Q. BuAli, L. E. Johns, and R. Narayanan. The growth of roughness during electrodeposition. *Electrochimica Acta*, 51(14):2881–2889, March 2006.

[57] Elton J. Cairns and Paul Albertus. Batteries for Electric and Hybrid-Electric Vehicles. *Annual Review of Chemical and Biomolecular Engineering*, 1(1):299–320, 2010.

[58] M. S. Chandrasekar and Malathy Pushpavanam. Pulse and pulse reverse plating—Conceptual, advantages and applications. *Electrochimica Acta*, 53(8):3313–3322, March 2008.

[59] Byoung-Yong Chang and Su-Moon Park. Electrochemical Impedance Spectroscopy. *Annual Review of Analytical Chemistry*, 3(1):207–229, 2010.

[60] J.-N. Chazalviel. Electrochemical aspects of the generation of ramified metallic electrodeposits. *Physical Review A*, 42(12):7355–7367, December 1990.

[61] J. N. Chazalviel, M. Rosso, E. Chassaing, and V. Fleury. A quantitative study of gravity-induced convection in two-dimensional parallel electrodeposition cells. *Journal of Electroanalytical Chemistry*, 407(1):61–73, May 1996.

[62] Chao-Peng Chen and Jacob Jorne. The Dynamics of Morphological Instability during Electrodeposition. *Journal of The Electrochemical Society*, 138(11):3305–3311, November 1991.

[63] Xin-Bing Cheng, Rui Zhang, Chen-Zi Zhao, Fei Wei, Ji-Guang Zhang, and Qiang Zhang. A Review of Solid Electrolyte Interphases on Lithium Metal Anode. *Advanced Science*, 3(3):1500213, March 2016.

[64] Xin-Bing Cheng, Rui Zhang, Chen-Zi Zhao, and Qiang Zhang. Toward Safe Lithium Metal Anode in Rechargeable Batteries: A Review. *Chemical Reviews*, 117(15):10403–10473, August 2017.

[65] Jang Wook Choi and Doron Aurbach. Promise and reality of post-lithium-ion batteries with high energy densities. *Nature Reviews Materials*, 1(4):16013, April 2016.

[66] K. Chu and M. Bazant. Electrochemical Thin Films at and above the Classical Limiting Current. *SIAM Journal on Applied Mathematics*, 65(5):1485–1505, January 2005.

[67] Stephen Cobeldick. ColorBrewer: Attractive and Distinctive Colormaps - File Exchange - MATLAB Central.

[68] R. M. Corless, G. H. Gonnet, D. E. G. Hare, D. J. Jeffrey, and D. E. Knuth. On the LambertW function. *Advances in Computational Mathematics*, 5(1):329–359, December 1996.

[69] John Crank. *Free and Moving Boundary Problems*. Clarendon Press, Oxford Oxfordshire : New York, February 1987.

[70] M. C. Cross and P. C. Hohenberg. Pattern formation outside of equilibrium. *Reviews of Modern Physics*, 65(3):851–1112, July 1993.

[71] William M. Deen. *Analysis of Transport Phenomena*. Oxford University Press, New York, 2 edition edition, October 2011.

[72] Daosheng Deng, E. Victoria Dydek, Ji-Hyung Han, Sven Schlumpberger, Ali Mani, Boris Zaltzman, and Martin Z. Bazant. Overlimiting Current and Shock Electrodialysis in Porous Media. *Langmuir*, 29(52):16167–16177, December 2013.

[73] A. R. Despic, J. Diggle, and J. O'm Bockris. Mechanism of the Formation of Zinc Dendrites. *Journal of The Electrochemical Society*, 115(5):507–508, May 1968.

[74] G. Devaraj, S. Guruviah, and S. K. Seshadri. Pulse plating. *Materials Chemistry and Physics*, 25(5):439–461, August 1990.

[75] J. W. Diggle, A. R. Despic, and J. O'm Bockris. The Mechanism of the Dendritic Electrocrystallization of Zinc. *Journal of The Electrochemical Society*, 116(11):1503–1514, November 1969.

[76] E. Victoria Dydek and Martin Z. Bazant. Nonlinear dynamics of ion concentration polarization in porous media: The leaky membrane model. *AIChE Journal*, 59(9):3539–3555, September 2013.

[77] E. Victoria Dydek, Boris Zaltzman, Isaak Rubinstein, D. S. Deng, Ali Mani, and Martin Z. Bazant. Overlimiting Current in a Microchannel. *Physical Review Letters*, 107(11):118301, September 2011.

[78] J. Elezgaray, C. Léger, and F. Argoul. Linear Stability Analysis of Unsteady Galvanostatic Electrodeposition in the Two-Dimensional Diffusion-Limited Regime. *Journal of The Electrochemical Society*, 145(6):2016–2024, June 1998.

[79] J. Elezgaray, C. Léger, and F. Argoul. Dense Branching Morphology in Electrodeposition Experiments: Characterization and Mean-Field Modeling. *Physical Review Letters*, 84(14):3129–3132, April 2000.

[80] David R. Ely and R. Edwin García. Heterogeneous Nucleation and Growth of Lithium Electrodeposits on Negative Electrodes. *Journal of The Electrochemical Society*, 160(4):A662–A668, January 2013.

[81] J. Erlebacher, P. C. Searson, and K. Sieradzki. Computer simulations of dense-branching patterns. *Physical Review Letters*, 71(20):3311–3314, November 1993.

[82] Vinodkumar Etacheri, Rotem Marom, Ran Elazari, Gregory Salitra, and Doron Aurbach. Challenges in the development of advanced Li-ion batteries: a review. *Energy & Environmental Science*, 4(9):3243–3262, 2011.

[83] S. D. Fabre, D. Guy-Bouyssou, P. Bouillon, F. Le Cras, and C. Delacourt. Charge/Discharge Simulation of an All-Solid-State Thin-Film Battery Using a One-Dimensional Model. *Journal of The Electrochemical Society*, 159(2):A104–A115, January 2011.

[84] Todd R. Ferguson and Martin Z. Bazant. Nonequilibrium Thermodynamics of Porous Electrodes. *Journal of The Electrochemical Society*, 159(12):A1967–A1985, January 2012.

[85] V. Fleury, J.-N. Chazalviel, and M. Rosso. Theory and experimental evidence of electroconvection around electrochemical deposits. *Physical Review Letters*, 68(16):2492–2495, April 1992.

[86] V. Fleury, J.-N. Chazalviel, and M. Rosso. Coupling of drift, diffusion, and electroconvection, in the vicinity of growing electrodeposits. *Physical Review E*, 48(2):1279–1295, August 1993.

[87] V. Fleury, J. N. Chazalviel, M. Rosso, and B. Sapoval. The role of the anions in the growth speed of fractal electrodeposits. *Journal of Electroanalytical Chemistry and Interfacial Electrochemistry*, 290(1):249–255, September 1990.

[88] V. Fleury, J. H. Kaufman, and D. B. Hibbert. Mechanism of a morphology transition in ramified electrochemical growth. *Nature*, 367(6462):435–438, February 1994.

[89] V. Fleury, M. Rosso, and J.-N. Chazalviel. Geometrical aspect of electrodeposition: The Hecker effect. *Physical Review A*, 43(12):6908–6916, June 1991.

[90] V. Fleury, M. Rosso, J.-N. Chazalviel, and B. Sapoval. Experimental aspects of dense morphology in copper electrodeposition. *Physical Review A*, 44(10):6693–6705, November 1991.

[91] Y. Fu, S. Poizeau, A. Bertei, C. Qi, A. Mohanram, J. D. Pietras, and M. Z. Bazant. Heterogeneous electrocatalysis in porous cathodes of solid oxide fuel cells. *Electrochimica Acta*, 159:71–80, March 2015.

[92] Yeqing Fu, Yi Jiang, Sophie Poizeau, Abhijit Dutta, Aravind Mohanram, John D. Pietras, and Martin Z. Bazant. Multicomponent Gas Diffusion in Porous Electrodes. *Journal of The Electrochemical Society*, 162(6):F613–F621, January 2015.

[93] P. Garik, D. Barkey, E. Ben-Jacob, E. Bochner, N. Broxholm, B. Miller, B. Orr, and R. Zamir. Laplace- and diffusion-field-controlled growth in electrochemical deposition. *Physical Review Letters*, 62(23):2703–2706, June 1989.

[94] John Gary and Richard Helgason. A matrix method for ordinary differential eigenvalue problems. *Journal of Computational Physics*, 5(2):169–187, April 1970.

[95] Walter Gautschi. The numerical evaluation of a challenging integral. *Numerical Algorithms*, 49(1-4):187–194, December 2008.

[96] John B. Goodenough and Youngsik Kim. Challenges for Rechargeable Li Batteries. *Chemistry of Materials*, 22(3):587–603, February 2010.

[97] John B. Goodenough and Kyu-Sung Park. The Li-Ion Rechargeable Battery: A Perspective. *Journal of the American Chemical Society*, 135(4):1167–1176, January 2013.

[98] Dimitrios A. Goussis and Arne J. Pearlstein. Removal of infinite eigenvalues in the generalized matrix eigenvalue problem. *Journal of Computational Physics*, 84(1):242–246, September 1989.

[99] D. Grier, E. Ben-Jacob, Roy Clarke, and L. M. Sander. Morphology and Microstructure in Electrochemical Deposition of Zinc. *Physical Review Letters*, 56(12):1264–1267, March 1986.

[100] David G. Grier, David A. Kessler, and L. M. Sander. Stability of the dense radial morphology in diffusive pattern formation. *Physical Review Letters*, 59(20):2315–2318, November 1987.

[101] Mikko Haataja and David J. Srolovitz. Morphological Instability and Additive-Induced Stabilization in Electrodeposition. *Physical Review Letters*, 89(21):215509, November 2002.

[102] Mikko Haataja, David J. Srolovitz, and Andrew B. Bocarsly. Morphological Stability during Electrodeposition I. Steady States and Stability Analysis. *Journal of The Electrochemical Society*, 150(10):C699–C707, October 2003.

[103] Mikko Haataja, David J. Srolovitz, and Andrew B. Bocarsly. Morphological Stability during Electrodeposition II. Additive Effects. *Journal of The Electrochemical Society*, 150(10):C708–C716, October 2003.

[104] P. T. Hammond. Form and Function in Multilayer Assembly: New Applications at the Nanoscale. *Advanced Materials*, 16(15):1271–1293, August 2004.

[105] Ji-Hyung Han, Edwin Khoo, Peng Bai, and Martin Z. Bazant. Over-limiting Current and Control of Dendritic Growth by Surface Conduction in Nanopores. *Scientific Reports*, 4:7056, November 2014.

[106] Ji-Hyung Han, Miao Wang, Peng Bai, Fikile R. Brushett, and Martin Z. Bazant. Dendrite Suppression by Shock Electrodeposition in Charged Porous Media. *Scientific Reports*, 6:28054, June 2016.

[107] Bala S. Haran, Branko N. Popov, and Ralph E. White. Determination of the hydrogen diffusion coefficient in metal hydrides by impedance spectroscopy. *Journal of Power Sources*, 75(1):56–63, September 1998.

[108] Mark Harrower and Cynthia A. Brewer. ColorBrewer.org: An Online Tool for Selecting Colour Schemes for Maps. *The Cartographic Journal*, 40(1):27–37, June 2003.

[109] E Hawkins Cwirko and R. G Carbonell. Transport of electrolytes in charged pores: Analysis using the method of spatial averaging. *Journal of Colloid and Interface Science*, 129(2):513–531, May 1989.

[110] William M. Haynes, editor. *CRC Handbook of Chemistry and Physics, 97th Edition*. CRC Press, 97 edition edition, June 2016.

[111] G. Heidari, S. M. Mousavi Khoie, M. Ebrahimizadeh Abrishami, and M. Javanbakht. Electrodeposition of Cu–Sn alloys: theoretical and experimental approaches. *Journal of Materials Science: Materials in Electronics*, 26(3):1969–1976, March 2015.

[112] G M Homsy. Viscous Fingering in Porous Media. *Annual Review of Fluid Mechanics*, 19(1):271–311, January 1987.

[113] M. E. Huerta Garrido and M. D. Pritzker. EIS and statistical analysis of copper electrodeposition accounting for multi-component transport and reactions. *Journal of Electroanalytical Chemistry*, 594(2):118–132, September 2006.

[114] M. E. Huerta Garrido and M. D. Pritzker. Reply to "Remarks on 'EIS and statistical analysis of copper electrodeposition accounting for multi-component transport and reactions' [M.E. Huerta Garrido, M.D. Pritzker, J. Electroanal. Chem. 594 (2006) 118]" by A. Lasia. *Journal of Electroanalytical Chemistry*, 619–620:183–186, July 2008.

[115] John C. Hulteen and Charles R. Martin. A general template-based method for the preparation of nanomaterials. *Journal of Materials Chemistry*, 7(7):1075–1087, January 1997.

[116] A. Al-Haj Hussein and I. Batarseh. A Review of Charging Algorithms for Nickel and Lithium Battery Chargers. *IEEE Transactions on Vehicular Technology*, 60(3):830–838, March 2011.

[117] John M. Huth, Harry L. Swinney, William D. McCormick, Alexander Kuhn, and Françoise Argoul. Role of convection in thin-layer electrodeposition. *Physical Review E*, 51(4):3444–3458, April 1995.

[118] Amit Jain and Avinashi Kapoor. Exact analytical solutions of the parameters of real solar cells using Lambert W-function. *Solar Energy Materials and Solar Cells*, 81(2):269–277, February 2004.

[119] H. Kahlert, U. Retter, H. Lohse, K. Siegler, and F. Scholz. On the Determination of the Diffusion Coefficients of Electrons and of Potassium Ions in Copper(II) Hexacyanoferrate(II) Composite Electrodes. *The Journal of Physical Chemistry B*, 102(44):8757–8765, October 1998.

[120] Daniel T. Kawano, Matthias Morzfeld, and Fai Ma. The decoupling of second-order linear systems with a singular mass matrix. *Journal of Sound and Vibration*, 332(25):6829–6846, December 2013.

[121] David A. Kessler, Joel Koplik, and Herbert Levine. Pattern selection in fingered growth phenomena. *Advances in Physics*, 37(3):255–339, June 1988.

[122] Edwin Khoo and Martin Z. Bazant. Theory of voltammetry in charged porous media. *Journal of Electroanalytical Chemistry*, 811:105–120, February 2018.

[123] Sung Jae Kim, Ying-Chih Wang, Jeong Hoon Lee, Hongchul Jang, and Jongyoon Han. Concentration Polarization and Nonlinear Electrokinetic Flow near a Nanofluidic Channel. *Physical Review Letters*, 99(4):044501, July 2007.

[124] R. Krishnan, L. E. Johns, and R. Narayanan. Instability in electrodeposition: the critical wavelength. *Electrochimica Acta*, 48(1):1–6, November 2002.

[125] J. J. Krol, M. Wessling, and H. Strathmann. Chronopotentiometry and overlimiting ion transport through monopolar ion exchange membranes. *Journal of Membrane Science*, 162(1–2):155–164, September 1999.

[126] J. J. Krol, M. Wessling, and H. Strathmann. Concentration polarization with monopolar ion exchange membranes: current–voltage curves and water dissociation. *Journal of Membrane Science*, 162(1–2):145–154, September 1999.

[127] Salomea Krzewska. Impedance investigation of the mechanism of copper electrodeposition from acidic perchlorate electrolyte. *Electrochimica Acta*, 42(23):3531–3540, January 1997.

[128] A. Kuhn and F. Argoul. Influence of chemical perturbations on the surface roughness of thin layer electrodeposits. *Fractals*, 01(03):451–459, September 1993.

[129] A. Kuhn and F. Argoul. Revisited experimental analysis of morphological changes in thin-layer electrodeposition. *Journal of Electroanalytical Chemistry*, 371(1):93–100, June 1994.

[130] A. Kuhn and F. Argoul. Spatiotemporal morphological transitions in thin-layer electrodeposition: The Hecker effect. *Physical Review E*, 49(5):4298–4305, May 1994.

[131] Akihiro Kushima, Kang Pyo So, Cong Su, Peng Bai, Nariaki Kuriyama, Takanori Maebashi, Yoshiya Fujiwara, Martin Z. Bazant, and Ju Li. Liquid cell transmission electron microscopy observation of lithium metal growth and dissolution: Root growth, dead lithium and lithium flotsams. *Nano Energy*, 32:271–279, February 2017.

[132] J. S. Langer. Instabilities and pattern formation in crystal growth. *Reviews of Modern Physics*, 52(1):1–28, January 1980.

[133] Andrzej Lasia. Remarks on "EIS and statistical analysis of copper electrodeposition accounting for multi-component transport and reactions" [M.E. Huerta Garrido, M.D. Pritzker, J. Electroanal. Chem. 594 (2006) 118]. *Journal of Electroanalytical Chemistry*, 605(1):77–79, July 2007.

[134] Andrzej Lasia. *Electrochemical Impedance Spectroscopy and its Applications*. Springer, New York, NY, 2014 edition edition, June 2014.

[135] R. LeVeque. *Finite Difference Methods for Ordinary and Partial Differential Equations*. Other Titles in Applied Mathematics. Society for Industrial and Applied Mathematics, January 2007.

[136] M. D. Levi and D. Aurbach. Diffusion Coefficients of Lithium Ions during Intercalation into Graphite Derived from the Simultaneous Measurements and Modeling of Electrochemical Impedance and Potentiostatic Intermittent Titration Characteristics of Thin Graphite Electrodes. *The Journal of Physical Chemistry B*, 101(23):4641–4647, June 1997.

[137] Jun Li, Edward Murphy, Jack Winnick, and Paul A Kohl. The effects of pulse charging on cycling characteristics of commercial lithium-ion batteries. *Journal of Power Sources*, 102(1):302–309, December 2001.

[138] Zhe Li, Jun Huang, Bor Yann Liaw, Viktor Metzler, and Jianbo Zhang. A review of lithium deposition in lithium-ion and lithium metal secondary batteries. *Journal of Power Sources*, 254:168–182, May 2014.

[139] Dingchang Lin, Yayuan Liu, and Yi Cui. Reviving the lithium metal anode for high-energy batteries. *Nature Nanotechnology*, 12(3):194–206, March 2017.

[140] Dingchang Lin, Yayuan Liu, Allen Pei, and Yi Cui. Nanoscale perspective: Materials designs and understandings in lithium metal anodes. *Nano Research*, 10(12):4003–4026, December 2017.

[141] L. Lopez-Tomas, J. Mach, P. P. Trigueros, F. Mas, J. Claret, and F. Sagues. Quasi-twodimensional electrodeposition: a summarized review on morphology and growth mechanisms. *Chaos, Solitons & Fractals*, 6:287–294, January 1995.

[142] Jun Lu, Zhongwei Chen, Feng Pan, Yi Cui, and Khalil Amine. High-Performance Anode Materials for Rechargeable Lithium-Ion Batteries. *Electrochemical Energy Reviews*, 1(1):35–53, March 2018.

[143] C. Léger, J. Elezgaray, and F. Argoul. Experimental Demonstration of Diffusion-Limited Dynamics in Electrodeposition. *Physical Review Letters*, 78(26):5010–5013, June 1997.

[144] C. Léger, J. Elezgaray, and F. Argoul. Dynamical characterization of one-dimensional stationary growth regimes in diffusion-limited electrodeposition processes. *Physical Review E*, 58(6):7700–7709, December 1998.

[145] Christophe Léger, Françoise Argoul, and Martin Z. Bazant. Front Dynamics during Diffusion-Limited Corrosion of Ramified Electrodeposits. *The Journal of Physical Chemistry B*, 103(28):5841–5851, July 1999.

[146] Christophe Léger, Juan Elezgaray, and Françoise Argoul. Internal structure of dense electrodeposits. *Physical Review E*, 61(5):5452–5463, May 2000.

[147] Christophe Léger, Juan Elezgaray, and Françoise Argoul. Probing interfacial dynamics by phase-shift interferometry in thin cell electrodeposition. *Journal of Electroanalytical Chemistry*, 486(2):204–219, May 2000.

[148] Christophe Léger, Laurent Servant, Jean Luc Bruneel, and Françoise Argoul. Growth patterns in electrodeposition. *Physica A: Statistical Mechanics and its Applications*, 263(1):305–314, February 1999.

[149] Digby D. Macdonald. Review of mechanistic analysis by electrochemical impedance spectroscopy. *Electrochimica Acta*, 35(10):1509–1525, October 1990.

[150] Digby D. Macdonald. Reflections on the history of electrochemical impedance spectroscopy. *Electrochimica Acta*, 51(8):1376–1388, January 2006.

[151] J. Ross Macdonald. Impedance spectroscopy and its use in analyzing the steady-state AC response of solid and liquid electrolytes. *Journal of Electroanalytical Chemistry and Interfacial Electrochemistry*, 223(1):25–50, May 1987.

[152] Tohru Makino, Ryoichi Aogaki, and Eiji Niki. Application of morphological instability to the analysis of physical parameters of a metal surface: Adsorption effect of hydrogen on galvanostatic electrodeposition. *The Journal of Chemical Physics*, 81(11):5145–5150, December 1984.

[153] Tohru Makino, Ryoichi Aogaki, and Eiji Niki. Determination of surface parameters of metals by means of image analysis of morphological instability in electrodeposition. *The Journal of Chemical Physics*, 81(11):5137–5144, December 1984.

[154] Ali Mani and Martin Z. Bazant. Deionization shocks in microstructures. *Physical Review E*, 84(6):061504, December 2011.

[155] Ali Mani, Thomas A. Zangle, and Juan G. Santiago. On the Propagation of Concentration Polarization from Microchannel−Nanochannel Interfaces Part I: Analytical Model and Characteristic Analysis. *Langmuir*, 25(6):3898–3908, March 2009.

[156] M. Matsushita, M. Sano, Y. Hayakawa, H. Honjo, and Y. Sawada. Fractal Structures of Zinc Metal Leaves Grown by Electrodeposition. *Physical Review Letters*, 53(3):286–289, July 1984.

[157] E. Mattsson and J. O'm Bockris. Galvanostatic studies of the kinetics of deposition and dissolution in the copper + copper sulphate system. *Transactions of the Faraday Society*, 55(0):1586–1601, January 1959.

[158] Matthew Z. Mayers, Jakub W. Kaminski, and Thomas F. Miller. Suppression of Dendrite Formation via Pulse Charging in Rechargeable Lithium Metal Batteries. *The Journal of Physical Chemistry C*, 116(50):26214–26221, December 2012.

[159] G. B. McFadden, S. R. Coriell, T. P. Moffat, D. Josell, D. Wheeler, W. Schwarzacher, and J. Mallett. A Mechanism for Brightening Linear Stability Analysis of the Curvature-Enhanced Coverage Model. *Journal of The Electrochemical Society*, 150(9):C591–C599, September 2003.

[160] Paul Meakin. Formation of Fractal Clusters and Networks by Irreversible Diffusion-Limited Aggregation. *Physical Review Letters*, 51(13):1119–1122, September 1983.

[161] Mohammad Mirzadeh and Martin Z. Bazant. Electrokinetic Control of Viscous Fingering. *Physical Review Letters*, 119(17):174501, October 2017.

[162] Cleve Moler. The Lambert W Function - File Exchange - MATLAB Central.

[163] Charles Monroe and John Newman. Dendrite Growth in Lithium/Polymer Systems A Propagation Model for Liquid Electrolytes under Galvanostatic Conditions. *Journal of The Electrochemical Society*, 150(10):A1377–A1384, October 2003.

[164] Charles Monroe and John Newman. The Effect of Interfacial Deformation on Electrodeposition Kinetics. *Journal of The Electrochemical Society*, 151(6):A880–A886, June 2004.

[165] Charles Monroe and John Newman. The Impact of Elastic Deformation on Deposition Kinetics at Lithium/Polymer Interfaces. *Journal of The Electrochemical Society*, 152(2):A396–A404, February 2005.

[166] A. A. Moya. Theory of the formation of the electric double layer at the ion exchange membrane–solution interface. *Physical Chemistry Chemical Physics*, 17(7):5207–5218, February 2015.

[167] A. A. Moya, E. Belashova, and P. Sistat. Numerical simulation of linear sweep and large amplitude ac voltammetries of ion-exchange membrane systems. *Journal of Membrane Science*, 474:215–223, January 2015.

[168] W. W. Mullins and R. F. Sekerka. Morphological Stability of a Particle Growing by Diffusion or Heat Flow. *Journal of Applied Physics*, 34(2):323–329, February 1963.

[169] W. W. Mullins and R. F. Sekerka. Stability of a Planar Interface During Solidification of a Dilute Binary Alloy. *Journal of Applied Physics*, 35(2):444–451, February 1964.

[170] Sungmin Nam, Inhee Cho, Joonseong Heo, Geunbae Lim, Martin Z. Bazant, Dustin Jaesuk Moon, Gun Yong Sung, and Sung Jae Kim. Experimental Verification of Overlimiting Current by Surface Conduction and Electro-Osmotic Flow in Microchannels. *Physical Review Letters*, 114(11):114501, March 2015.

[171] P. P. Natsiavas, K. Weinberg, D. Rosato, and M. Ortiz. Effect of prestress on the stability of electrode–electrolyte interfaces during charging in lithium batteries. *Journal of the Mechanics and Physics of Solids*, 95:92–111, October 2016.

[172] John Newman and Karen E. Thomas-Alyea. *Electrochemical Systems, 3rd Edition*. Wiley-Interscience, Hoboken, N.J, 3 edition edition, May 2004.

[173] Christoffer P. Nielsen and Henrik Bruus. Concentration polarization, surface currents, and bulk advection in a microchannel. *Physical Review E*, 90(4):043020, October 2014.

[174] Christoffer P. Nielsen and Henrik Bruus. Morphological instability during steady electrodeposition at overlimiting currents. *Physical Review E*, 92(5):052310, November 2015.

[175] Victor V. Nikonenko, Anna V. Kovalenko, Mahamet K. Urtenov, Natalia D. Pismenskaya, Jongyoon Han, Philippe Sistat, and Gérald Pourcelly. Desalination at overlimiting currents: State-of-the-art and perspectives. *Desalination*, 342:85–106, June 2014.

[176] Victor V. Nikonenko, Natalia D. Pismenskaya, Elena I. Belova, Philippe Sistat, Patrice Huguet, Gérald Pourcelly, and Christian Larchet. Intensive current transfer in membrane systems: Modelling, mechanisms and application in electrodialysis. *Advances in Colloid and Interface Science*, 160(1–2):101–123, October 2010.

[177] Adélcio C. Oliveira, Franco D. R. Amado, and Ruan C. A. Moura. Steady state of ion transport in homopolar ion-exchange membrane: a theoretical study. *Journal of the Brazilian Society of Mechanical Sciences and Engineering*, 38(4):1165–1170, April 2016.

[178] Mark E. Orazem and Bernard Tribollet. *Electrochemical Impedance Spectroscopy*. Wiley, Hoboken, New Jersey, 2 edition edition, April 2017.

[179] William M'F. Orr. The Stability or Instability of the Steady Motions of a Perfect Liquid and of a Viscous Liquid. Part I: A Perfect Liquid. *Proceedings of the Royal Irish Academy. Section A: Mathematical and Physical Sciences*, 27:9–68, 1907.

[180] William M'F. Orr. The Stability or Instability of the Steady Motions of a Perfect Liquid and of a Viscous Liquid. Part II: A Viscous Liquid. *Proceedings of the Royal Irish Academy. Section A: Mathematical and Physical Sciences*, 27:69–138, 1907.

[181] Steven A. Orszag. Accurate solution of the Orr–Sommerfeld stability equation. *Journal of Fluid Mechanics*, 50(4):689–703, December 1971.

[182] Brad Osgood. Stanford Engineering Everywhere | EE261 - The Fourier Transform and its Applications.

[183] M. R. Palacín and A. de Guibert. Why do batteries fail? *Science*, 351(6273):1253292, February 2016.

[184] E. Peled and S. Menkin. Review—SEI: Past, Present and Future. *Journal of The Electrochemical Society*, 164(7):A1703–A1719, January 2017.

[185] G. Peters and J. Wilkinson. $Ax = \lambda Bx$ and the Generalized Eigenproblem. *SIAM Journal on Numerical Analysis*, 7(4):479–492, December 1970.

[186] P. B. Peters, R. van Roij, M. Z. Bazant, and P. M. Biesheuvel. Analysis of electrolyte transport through charged nanopores. *Physical Review E*, 93(5):053108, May 2016.

[187] Robert F. Pierret. *Semiconductor Device Fundamentals*. Addison Wesley, Reading, Mass, 2nd edition edition, April 1996.

[188] A. Pohjoranta, A. Mendelson, and R. Tenno. A copper electrolysis cell model including effects of the ohmic potential loss in the cell. *Electrochimica Acta*, 55(3):1001–1012, January 2010.

[189] Mark D. Pritzker and Thomas Z. Fahidy. Morphological stability of a planar metal electrode during potentiostatic electrodeposition and electrodissolution. *Electrochimica Acta*, 37(1):103–112, January 1992.

[190] B. K. Purushothaman and U. Landau. Rapid Charging of Lithium-Ion Batteries Using Pulsed Currents A Theoretical Analysis. *Journal of The Electrochemical Society*, 153(3):A533–A542, March 2006.

[191] B. K. Purushothaman, P. W. Morrison, and U. Landau. Reducing Mass-Transport Limitations by Application of Special Pulsed Current Modes. *Journal of The Electrochemical Society*, 152(4):J33–J39, April 2005.

[192] J. E. B. Randles. Kinetics of rapid electrode reactions. *Discussions of the Faraday Society*, 1:11–19, January 1947.

[193] Jonathan D. Reid and Allan P. David. Impedance Behavior of a Sulfuric Acid-Cupric Sulfate/Copper Cathode Interface. *Journal of The Electrochemical Society*, 134(6):1389–1394, June 1987.

[194] W. Van Roosbroeck. Theory of the flow of electrons and holes in germanium and other semiconductors. *The Bell System Technical Journal*, 29(4):560–607, October 1950.

[195] M. Rosso, E. Chassaing, J. N. Chazalviel, and T. Gobron. Onset of current-driven concentration instabilities in thin cell electrodeposition with small inter-electrode distance. *Electrochimica Acta*, 47(8):1267–1273, February 2002.

[196] M. Rosso, J. N. Chazalviel, and E. Chassaing. Calculation of the space charge in electrodeposition from a binary electrolyte. *Journal of Electroanalytical Chemistry*, 587(2):323–328, February 2006.

[197] M. Rosso, J. N. Chazalviel, V. Fleury, and E. Chassaing. Experimental evidence for gravity induced motion in the vicinity of ramified electrodeposits. *Electrochimica Acta*, 39(4):507–515, March 1994.

[198] M. Rosso, T. Gobron, C. Brissot, J. N. Chazalviel, and S. Lascaud. Onset of dendritic growth in lithium/polymer cells. *Journal of Power Sources*, 97-98:804–806, July 2001.

[199] Michel Rosso. Electrodeposition from a binary electrolyte: new developments and applications. *Electrochimica Acta*, 53(1):250–256, November 2007.

[200] Michel Rosso, Claire Brissot, Anna Teyssot, Mickaël Dollé, Lucas Sannier, Jean-Marie Tarascon, Renaud Bouchet, and Stéphane Lascaud. Dendrite short-circuit and fuse effect on Li/polymer/Li cells. *Electrochimica Acta*, 51(25):5334–5340, July 2006.

[201] Michel Rosso, Elisabeth Chassaing, Vincent Fleury, and Jean-Noël Chazalviel. Shape evolution of metals electrodeposited from binary electrolytes. *Journal of Electroanalytical Chemistry*, 559:165–173, November 2003.

[202] M. Rostami and F. Xue. Robust Linear Stability Analysis and a New Method for Computing the Action of the Matrix Exponential. *SIAM Journal on Scientific Computing*, pages A3344–A3370, January 2018.

[203] I. Rubinshtein, B. Zaltzman, J. Pretz, and C. Linder. Experimental Verification of the Electroosmotic Mechanism of Overlimiting Conductance Through a Cation Exchange Electrodialysis Membrane. *Russian Journal of Electrochemistry*, 38(8):853–863, August 2002.

[204] I. Rubinstein. *Electro-Diffusion of Ions*. Studies in Applied and Numerical Mathematics. Society for Industrial and Applied Mathematics, January 1990.

[205] I. Rubinstein and B. Zaltzman. Electro-osmotically induced convection at a permselective membrane. *Physical Review E*, 62(2):2238–2251, August 2000.

[206] I. Rubinstein and B. Zaltzman. Convective diffusive mixing in concentration polarization: from Taylor dispersion to surface convection. *Journal of Fluid Mechanics*, 728:239–278, August 2013.

[207] Isaak Rubinstein and Leonid Shtilman. Voltage against current curves of cation exchange membranes. *Journal of the Chemical Society, Faraday Transactions 2: Molecular and Chemical Physics*, 75(0):231–246, January 1979.

[208] S. M. Rubinstein, G. Manukyan, A. Staicu, I. Rubinstein, B. Zaltzman, R. G. H. Lammertink, F. Mugele, and M. Wessling. Direct Observation of a Nonequilibrium Electro-Osmotic Instability. *Physical Review Letters*, 101(23):236101, December 2008.

[209] Riccardo Ruffo, Seung Sae Hong, Candace K. Chan, Robert A. Huggins, and Yi Cui. Impedance Analysis of Silicon Nanowire Lithium Ion Battery Anodes. *The Journal of Physical Chemistry C*, 113(26):11390–11398, July 2009.

[210] John Rumble, editor. *CRC Handbook of Chemistry and Physics, 98th Edition*. CRC Press, Boca Raton London New York, 98 edition edition, June 2017.

[211] H. W. Rösler, F. Maletzki, and E. Staude. Ion transfer across electrodialysis membranes in the overlimiting current range: chronopotentiometric studies. *Journal of Membrane Science*, 72(2):171–179, September 1992.

[212] P. G. Saffman. Viscous fingering in Hele-Shaw cells. *Journal of Fluid Mechanics*, 173:73–94, December 1986.

[213] Philip Geoffrey Saffman and Geoffrey Ingram Taylor. The penetration of a fluid into a porous medium or Hele-Shaw cell containing a more viscous liquid. *Proc. R. Soc. Lond. A*, 245(1242):312–329, June 1958.

[214] Francesc Sagués, Marta Queralt López-Salvans, and Josep Claret. Growth and forms in quasi-two-dimensional electrocrystallization. *Physics Reports*, 337(1):97–115, October 2000.

[215] Henry J. S. Sand. On the Concentration at the Electrodes in a Solution, with special reference to the Liberation of Hydrogen by Electrolysis of a Mixture of Copper Sulphate and Sulphuric Acid. *Proceedings of the Physical Society of London*, 17(1):496, 1899.

[216] F. Savoye, P. Venet, M. Millet, and J. Groot. Impact of Periodic Current Pulses on Li-Ion Battery Performance. *IEEE Transactions on Industrial Electronics*, 59(9):3481–3488, September 2012.

[217] Yasuji Sawada, A. Dougherty, and J. P. Gollub. Dendritic and Fractal Patterns in Electrolytic Metal Deposits. *Physical Review Letters*, 56(12):1260–1263, March 1986.

[218] Jarrod Schiffbauer, Uri Liel, Neta Leibowitz, Sinwook Park, and Gilad Yossifon. Probing space charge and resolving overlimiting current mechanisms at the microchannel-nanochannel interface. *Physical Review E*, 92(1):013001, July 2015.

[219] Sven Schlumpberger. *Shock electrodialysis for water purification and electrostatic correlations in electrolytes*. Thesis, Massachusetts Institute of Technology, 2016.

[220] Sven Schlumpberger and Martin Z. Bazant. Simple Theory of Ionic Activity in Concentrated Electrolytes. *arXiv:1709.03106 [cond-mat, physics:physics]*, September 2017. arXiv: 1709.03106.

[221] Sven Schlumpberger, Nancy B. Lu, Matthew E. Suss, and Martin Z. Bazant. Scalable and Continuous Water Deionization by Shock Electrodialysis. *Environmental Science & Technology Letters*, 2(12):367–372, December 2015.

[222] Nicholas M. Schneider, Jeung Hun Park, Joseph M. Grogan, Daniel A. Steingart, Haim H. Bau, and Frances M. Ross. Nanoscale evolution of interface morphology during electrodeposition. *Nature Communications*, 8(1):2174, December 2017.

[223] W. Schwarzacher. Kinetic roughening of electrodeposited films. *Journal of Physics: Condensed Matter*, 16(26):R859, 2004.

[224] Bruno Scrosati and Jürgen Garche. Lithium batteries: Status, prospects and future. *Journal of Power Sources*, 195(9):2419–2430, May 2010.

[225] R. F. Sekerka. A Stability Function for Explicit Evaluation of the Mullins-Sekerka Interface Stability Criterion. *Journal of Applied Physics*, 36(1):264–268, January 1965.

[226] Weixiang Shen, Thanh Tu Vo, and A. Kapoor. Charging algorithms of lithium-ion batteries: An overview. In *2012 7th IEEE Conference on Industrial Electronics and Applications (ICIEA)*, pages 1567–1572, July 2012.

[227] Philippe Sistat and Gérald Pourcelly. Steady-state ion transport through homopolar ion-exchange membranes: an analytical solution of the Nernst–Planck equations for a 1:1 electrolyte under the electroneutrality assumption. *Journal of Electroanalytical Chemistry*, 460(1–2):53–62, January 1999.

[228] J. H. Sluyters and J. J. C. Oomen. On the impedance of galvanic cells: II. Experimental verification. *Recueil des Travaux Chimiques des Pays-Bas*, 79(10):1101–1110, January 1960.

[229] Seoyun Sohn, Inhee Cho, Soonhyun Kwon, Hyomin Lee, and Sung Jae Kim. Surface Conduction in a Microchannel. *Langmuir*, 34(26):7916–7921, July 2018.

[230] Arnold Sommerfeld. Ein beitrag zur hydrodynamischen erklaerung der turbulenten fluessigkeitsbewegungen. *Atti del*, 4:116–124, 1908.

[231] Juhyun Song and Martin Z. Bazant. Effects of Nanoparticle Geometry and Size Distribution on Diffusion Impedance of Battery Electrodes. *Journal of The Electrochemical Society*, 160(1):A15–A24, January 2013.

[232] Juhyun Song and Martin Z. Bazant. Electrochemical Impedance of a Battery Electrode with Anisotropic Active Particles. *Electrochimica Acta*, 131:214–227, June 2014.

[233] Juhyun Song and Martin Z. Bazant. Electrochemical Impedance Imaging via the Distribution of Diffusion Times. *Physical Review Letters*, 120(11):116001, March 2018.

[234] G. M. Stone, S. A. Mullin, A. A. Teran, D. T. Hallinan, A. M. Minor, A. Hexemer, and N. P. Balsara. Resolution of the Modulus versus Adhesion Dilemma in Solid Polymer Electrolytes for Rechargeable Lithium Metal Batteries. *Journal of The Electrochemical Society*, 159(3):A222–A227, January 2012.

[235] H. Strathmann. Electrodialysis, a mature technology with a multitude of new applications. *Desalination*, 264(3):268–288, December 2010.

[236] Lars-Göran Sundström and Fritz H. Bark. On morphological instability during electrodeposition with a stagnant binary electrolyte. *Electrochimica Acta*, 40(5):599–614, April 1995.

[237] Simon M. Sze and Kwok K. Ng. *Physics of Semiconductor Devices*. Wiley-Interscience, Hoboken, N.J, 3 edition edition, October 2006.

[238] J.-M. Tarascon and M. Armand. Issues and challenges facing rechargeable lithium batteries. *Nature*, 414:359, November 2001.

[239] Anna Teyssot, Céline Belhomme, Renaud Bouchet, Michel Rosso, Stéphane Lascaud, and Michel Armand. Inter-electrode in situ concentration cartography in lithium/polymer electrolyte/lithium cells. *Journal of Electroanalytical Chemistry*, 584(1):70–74, October 2005.

[240] Indrajeet V. Thorat, David E. Stephenson, Nathan A. Zacharias, Karim Zaghib, John N. Harb, and Dean R. Wheeler. Quantifying tortuosity in porous Li-ion battery materials. *Journal of Power Sources*, 188(2):592–600, March 2009.

[241] Mukul D. Tikekar, Lynden A. Archer, and Donald L. Koch. Stability Analysis of Electrodeposition across a Structured Electrolyte with Immobilized Anions. *Journal of The Electrochemical Society*, 161(6):A847–A855, January 2014.

[242] Mukul D. Tikekar, Lynden A. Archer, and Donald L. Koch. Stabilizing electrodeposition in elastic solid electrolytes containing immobilized anions. *Science Advances*, 2(7):e1600320, July 2016.

[243] Mukul D. Tikekar, Snehashis Choudhury, Zhengyuan Tu, and Lynden A. Archer. Design principles for electrolytes and interfaces for stable lithium-metal batteries. *Nature Energy*, 1(9):16114, September 2016.

[244] L. Trefethen. *Spectral Methods in MATLAB*. Software, Environments and Tools. Society for Industrial and Applied Mathematics, January 2000.

[245] Pedro Pablo Trigueros, Josep Claret, Francesc Mas, and Francesc Sagués. Pattern morphologies in zinc electrodeposition. *Journal of Electroanalytical Chemistry and Interfacial Electrochemistry*, 312(1):219–235, August 1991.

[246] Zhengyuan Tu, Pooja Nath, Yingying Lu, Mukul D. Tikekar, and Lynden A. Archer. Nanostructured Electrolytes for Stable Lithium Electrodeposition in Secondary Batteries. *Accounts of Chemical Research*, 48(11):2947–2956, November 2015.

[247] Alan Mathison Turing. The chemical basis of morphogenesis. *Phil. Trans. R. Soc. Lond. B*, 237(641):37–72, August 1952.

[248] J. V. Valério, M. S. Carvalho, and C. Tomei. Filtering the eigenvalues at infinite from the linear stability analysis of incompressible flows. *Journal of Computational Physics*, 227(1):229–243, November 2007.

[249] M. van Soestbergen, P. M. Biesheuvel, and M. Z. Bazant. Diffuse-charge effects on the transient response of electrochemical cells. *Physical Review E*, 81(2):021503, February 2010.

[250] Mark W. Verbrugge and Robert F. Hill. Ion and Solvent Transport in Ion-Exchange Membranes I . A Macrohomogeneous Mathematical Model. *Journal of The Electrochemical Society*, 137(3):886–893, March 1990.

[251] Mark W. Verbrugge and Robert F. Hill. Ion and Solvent Transport in Ion-Exchange Membranes II . A Radiotracer Study of the Sulfuric-Acid, Nation-117 System. *Journal of The Electrochemical Society*, 137(3):893–899, March 1990.

[252] Pallavi Verma, Pascal Maire, and Petr Novák. A review of the features and analyses of the solid electrolyte interphase in Li-ion batteries. *Electrochimica Acta*, 55(22):6332–6341, September 2010.

[253] J. Vetter, P. Novák, M. R. Wagner, C. Veit, K. C. Möller, J. O. Besenhard, M. Winter, M. Wohlfahrt-Mehrens, C. Vogler, and A. Hammouche. Ageing mechanisms in lithium-ion batteries. *Journal of Power Sources*, 147(1):269–281, September 2005.

[254] Tamás Vicsek. Pattern Formation in Diffusion-Limited Aggregation. *Physical Review Letters*, 53(24):2281–2284, December 1984.

[255] Ting Hei Wan, Mattia Saccoccio, Chi Chen, and Francesco Ciucci. Influence of the Discretization Methods on the Distribution of Relaxation Times Deconvolution: Implementing Radial Basis Functions with DRTtools. *Electrochimica Acta*, 184:483–499, December 2015.

[256] Aiping Wang, Sanket Kadam, Hong Li, Siqi Shi, and Yue Qi. Review on modeling of the anode solid electrolyte interphase (SEI) for lithium-ion batteries. *npj Computational Materials*, 4(1):15, March 2018.

[257] Xiao-Lin Wang, Toshinori Tsuru, Shin-ichi Nakao, and Shoji Kimura. Electrolyte transport through nanofiltration membranes by the space-charge model and the comparison with Teorell-Meyer-Sievers model. *Journal of Membrane Science*, 103(1):117–133, July 1995.

[258] E. Warburg. Ueber die Polarisationscapacität des Platins. *Annalen der Physik*, 311(9):125–135, January 1901.

[259] M. Stanley Whittingham. Lithium Batteries and Cathode Materials. *Chemical Reviews*, 104(10):4271–4302, October 2004.

[260] Nicholas Williard, Wei He, Christopher Hendricks, and Michael Pecht. Lessons Learned from the 787 Dreamliner Issue on Lithium-Ion Battery Reliability. *Energies*, 6(9):4682–4695, September 2013.

[261] T. A. Witten and L. M. Sander. Diffusion-Limited Aggregation, a Kinetic Critical Phenomenon. *Physical Review Letters*, 47(19):1400–1403, November 1981.

[262] T. A. Witten and L. M. Sander. Diffusion-limited aggregation. *Physical Review B*, 27(9):5686–5697, May 1983.

[263] Kang Xu. Nonaqueous Liquid Electrolytes for Lithium-Based Rechargeable Batteries. *Chemical Reviews*, 104(10):4303–4418, October 2004.

[264] Wu Xu, Jiulin Wang, Fei Ding, Xilin Chen, Eduard Nasybulin, Yaohui Zhang, and Ji-Guang Zhang. Lithium metal anodes for rechargeable batteries. *Energy & Environmental Science*, 7(2):513–537, January 2014.

[265] Fei Xue. A Solver for the Rightmost Eigenvalues - File Exchange - MATLAB Central.

[266] David Yan, Martin Z. Bazant, P. M. Biesheuvel, Mary C. Pugh, and Francis P. Dawson. Theory of linear sweep voltammetry with diffuse charge: Unsupported electrolytes, thin films, and leaky membranes. *Physical Review E*, 95(3):033303, March 2017.

[267] Andriy Yaroshchuk. Over-limiting currents and deionization "shocks" in current-induced polarization: Local-equilibrium analysis. *Advances in Colloid and Interface Science*, 183–184:68–81, November 2012.

[268] Andriy Yaroshchuk, Emiliy Zholkovskiy, Sergey Pogodin, and Vladimir Baulin. Coupled Concentration Polarization and Electroosmotic Circulation near Micro/Nanointerfaces: Taylor–Aris Model of Hydrodynamic Dispersion and Limits of Its Applicability. *Langmuir*, 27(18):11710–11721, September 2011.

[269] Gilad Yossifon and Hsueh-Chia Chang. Selection of Nonequilibrium Overlimiting Currents: Universal Depletion Layer Formation Dynamics and Vortex Instability. *Physical Review Letters*, 101(25):254501, December 2008.

[270] B. Zaltzman and I. Rubinstein. Electro-osmotic slip and electroconvective instability. *Journal of Fluid Mechanics*, 579:173–226, May 2007.

[271] Thomas A. Zangle, Ali Mani, and Juan G. Santiago. On the Propagation of Concentration Polarization from Microchannel−Nanochannel Interfaces Part II: Numerical and Experimental Study. *Langmuir*, 25(6):3909–3916, March 2009.

[272] Thomas A. Zangle, Ali Mani, and Juan G. Santiago. Effects of Constant Voltage on Time Evolution of Propagating Concentration Polarization. *Analytical Chemistry*, 82(8):3114–3117, April 2010.

[273] Thomas A. Zangle, Ali Mani, and Juan G. Santiago. Theory and experiments of concentration polarization and ion focusing at microchannel and nanochannel interfaces. *Chemical Society Reviews*, 39(3):1014–1035, February 2010.

[274] Yi Zeng, Peng Bai, Raymond B. Smith, and Martin Z. Bazant. Simple formula for asymmetric Marcus–Hush kinetics. *Journal of Electroanalytical Chemistry*, 748:52–57, July 2015.

[275] Yi Zeng, Raymond B. Smith, Peng Bai, and Martin Z. Bazant. Simple formula for Marcus–Hush–Chidsey kinetics. *Journal of Electroanalytical Chemistry*, 735:77–83, December 2014.

[276] Sheng Shui Zhang. The effect of the charging protocol on the cycle life of a Li-ion battery. *Journal of Power Sources*, 161(2):1385–1391, October 2006.

[277] Sheng Shui Zhang. A review on the separators of liquid electrolyte Li-ion batteries. *Journal of Power Sources*, 164(1):351–364, January 2007.